# A Theoretical Study of Ultrafast Phenomena in Complex Atoms

*A Doctoral Thesis by*

Carl Leon Mikael Petersson

*Supervised by*

Fernando Martín


Departamento de Química
Facultad de Ciencias
Universidad Autónoma de Madrid

# Acknowledgements

My sincerest regards go out to all those who have supported me in the creation of this work.

Foremost, I would like to thank my supervisor, Fernando Martín, for giving me the opportunity to write this work. It has been a great blessing to be able to work under such a prolific scientist, and in a group as prominent as the UAM XCHEM one. I have greatly enjoyed working at UAM and thank all my friends there for their support.

Luca Argenti, who acted as my secondary supervisor during the first few years, also has my deepest appreciation. Without his great support and patience, this work would not have been possible.

Both Carlos Marante and Markus Klinker, whom I have worked closely with, and who have been of great help during my studies, also have my deepest gratitude.

Furthermore, my gratitude goes out to Kilian Arteaga, Pedro Fernández, and especially Vicent Borràs, for assisting me in writing the Spanish parts of my thesis.

I am also deeply grateful to the experimental groups we have cooperated with; at Lund, ETH, Université Paris-Saclay, and The Ohio State University; who have offered great input, and helped ground our theoretical musings in reality.

Finally, I am eternally grateful to my family. Their help with proofreading has been extremely helpful, and without their support, I do not know how I would have managed.

# Abstract

The ultrafast movement of electrons is a driving force of chemical reactions, making it a highly desirable avenue for study. This thesis studies such movements, making use of pump-probe methods such as attosecond transient absorption spectroscopy (ATAS) and reconstruction of attosecond beatings by interference of two-photon transitions (RABITT), in complex atomic systems. The main approach used to solve the time-dependent Schrödinger equation (TDSE) was exact, attosecond, full-electron, ab-initio calculations.

Firstly, helium was probed above the second ionisation threshold, where several ionisation channels are open, using accurate ab-initio calculations. Here, the ATAS method was employed to predict beatings between the autoionising $3snp\,^1P^o$ resonances and nearby $^1S^e$ and $^1D^e$ states. More surprisingly, two-photon beatings between the doubly-excited $3s3p$ state and the $^1P^o$ continuum were also observed, demonstrating control of the correlated, two-electron, multi-channel wave packet.

Secondly, two studies of neon were carried out below the second ionisation threshold. The first makes use of ATAS calculations to probe beatings between the autoionising neon states. Using a two-colour, mixed extreme-ultraviolet (XUV) near-infrared (NIR) pump, one-photon beatings between the $2s^{-1}3p\,^1P^o$ and the nearby $2s^{-1}3s\,^1S^e$ and $2s^{-1}3d\,^1D^e$ resonances are observed. Further, one- and two-photon beatings between the autoionising $2s^{-1}3\ell$, $\ell \in \{0, 1\}$ and the $^1P^o$ continuum are predicted.

The second uses the RABITT method to probe the atomic phase in the

vicinity of multiple resonances. This is far from trivial, and interferometric methods have until now been restricted to simpler energy-regions, due to the difficulty of accurately describing the electron correlation associated with the more complex case, making accurate ab-initio calculations needed to guide experiments unavailable. Despite the complex energy-dependence of the phase when several resonances are present, presented results from experiment and ab-initio theory are in excellent agreement. Further, using a simple extension of the Fano model for resonant continua, the contributions of the different involved resonances are disentangled. Such simple models are highly desirable in more advanced systems, where accurate ab-initio calculations are inaccessible.

The ab-initio results of both neon studies were carried out using the newly developed XCHEM methodology, which is thus further validated by the excellent agreement with presented experiments and previous studies.

Finally, a RABITT study of argon in the vicinity of the $3s^{-1}n\ell$ resonances was performed. Angularly resolved, experimental results are presented, showing the anisotropy of the atomic phase in smooth continua as well as the vicinity of resonances. Due to the complexity of the system, no ab-initio results are present. Instead, simpler interferometric models are used to successfully explain the anisotropic behaviour of the phase.

# Resumen

El movimiento ultrarrápido de electrones es la fuerza motriz de las reacciones químicas, por lo cual su estudio resulta muy atractivo. Esta tesis se dedica al estudio de ese tipo de movimientos, utilizando métodos de bombeo y sonda, como espectroscopía de absorción transitoria de attosegundos (ATAS) y reconstrucción de "beatings" de attosegundo por interferencia de transiciones de dos fotones (RABITT), en átomos complejos. El método principal utilizado para resolver de la ecuación de Schrödinger dependiente del tiempo fue la propagación exacta (ab-initio) considerando todos los electrones.

En primer lugar, se investigó el átomo de helio por encima del segundo umbral de ionización, donde existen varios canales de ionización. Aquí, el método de ATAS se empleó para predecir beatings entre las resonancias $3snp\,^1P^o$ y estados $^1S^e$ y $^1D^e$ cercanos. Sorprendentemente, también se observaron beatings de dos fotones, lo cual muestra control del paquete de ondas correlacionado multicanal de dos electrones.

En segundo lugar, dos estudios por debajo del segundo umbral de ionización del neón se llevaron a cabo. El primero utiliza cálculos de ATAS para investigar los beatings entre estados autoionizantes de neón. Utilizando un bombeo de dos colores, radiación ultravioleta extrema (XUV) mezclada con radiación infrarrojo cercano (NIR), es posible observar beatings entre la resonancia del $2s^{-1}3p\,^1P^o$ y las $2s^{-1}3s\,^1S^e$ y $2s^{-1}3d\,^1D^e$. Además, se predicen beatings de uno y dos fotones entre las resonancias autoionizantes $2s^{-1}3\ell$, $\ell \in \{0,1\}$ y el continuo $^1P^o$.

El segundo usa el método de RABITT para estudiar la fase atómica en las cercanías de las resonancias múltiples. Hasta ahora, los métodos interferométricos han estado restringidos a regiones de energía de hasta una resonancia, a causa de las dificultades en llevar a cabo propagaciones exactas (ab-initio), las cuales dependen de la correlación electrónica para describir bien los experimentos.

A pesar de la complejidad de la dependencia de la energía con la fase, debido a la presencia de varias resonancias, los resultados teóricos obtenidos comparan muy bien con los resultados experimentales presentados. Además, usando una extensión del modelo de Fano para continuos resonantes, las contribuciones de las distintas resonancias se han podido resolver. Modelos más simples son necesarios en sistemas más avanzados, donde cálculos ab-initio son inaccesibles.

Los resultados ab-initio presentados en ambos estudios se realizaron con el método XCHEM recientemente propuesto, dando así validez al método.

Finalmente, se realizó un estudio RABITT cerca de las resonancias $3s^{-1}n\ell$ del argón. Se presentan experimentos mostrando la dependencia angular de la fase atómica, tanto en continuos suaves como en las cercanías de resonancias. Debido a la complejidad del sistema, no se presentan resultados ab-initio. En cambio, mediante modelos interferométricos se ha podido explicar el comportamiento anisótropo de la fase.

# Abbreviations

| | |
|---|---|
| **APT** | **A**ttosecond **p**ulse **t**rain |
| **AT** | **A**utler-**T**ownes |
| **ATAS** | **A**ttosecond **t**ransient **a**bsorption **s**pectroscopy |
| **CAP** | **C**omplex **a**bsorption **p**otential |
| **CAS** | **C**omplete **a**ctive **s**pace |
| **DES** | **D**oubly **e**xcited **s**tates |
| **FWHM** | **F**ull **w**idth at **h**alf **m**aximum |
| **GABS** | Combined **Ga**ussian–**B**-**s**pline |
| **HF** | **H**artree-**F**ock |
| **HH** | **H**igh **h**armonic |
| **HHG** | **H**igh **h**armonic **g**eneration |
| **IR** | **I**nfra**r**ed |
| **NIR** | **N**ear **I**nfra**r**ed |
| **PAD** | **P**hotoelectron **a**ngular **d**istribution |
| **PES** | **P**hoto**e**lectron **s**pectrum |
| **PI** | **P**arent **i**on |
| **QCP** | **Q**uantum **C**hemistry **P**ackage |
| **RABITT** | **R**econstruction of **a**tomic **b**eatings by **i**nterference of **t**wo-photon **t**ransitions |
| **SAE** | **S**ingle **A**ctive **E**lectron |

| | |
|---|---|
| **SB** | **S**ide**b**and |
| **SCF** | **S**elf **C**onsistent **F**ield |
| **TDPT** | **T**ime-**d**ependent **p**erturbation **t**heory |
| **TDSE** | **T**ime-**d**ependent **S**chrödinger **e**quation |
| **TISE** | **T**ime-**i**ndependent **S**chrödinger **e**quation |
| **VIS** | **Vis**ible |
| **XUV** | E**x**treme **u**ltra**v**iolet |

# List of Publications

**Barreau**, **L.**, **Petersson C. L. M.**, M. Klinker, A. Camper, C. Marante, T. Gorman, D. Kiesewetter, L. Argenti, P. Agostini, J. González-Vázquez, P. Salières, L. F. DiMauro, and F. Martín (June 2019). "Disentangling Spectral Phases of Interfering Autoionizing States from Attosecond Interferometric Measurements". In: *Phys. Rev. Lett.* 122 (25), p. 253203. DOI: 10.1103/PhysRevLett.122.253203. URL: https://link.aps.org/doi/10.1103/PhysRevLett.122.253203.

**Cirelli**, **C.**, C. Marante, S. Heuser, C. L. M. Petersson, Á. J. Galán, L. Argenti, S. Zhong, D. Busto, M. Isinger, S. Nandi, et al. (2018). "Anisotropic photoemission time delays close to a Fano resonance". In: *Nature Communications* 9.1, p. 955. ISSN: 2041-1723. DOI: 10.1038/s41467-018-03009-1. URL: https://doi.org/10.1038/s41467-018-03009-1.

**Petersson**, **C. L. M.**, L. Argenti, and F. Martín (2017). "Attosecond transient absorption spectroscopy of helium above the N= 2 ionization threshold". In: *Physical Review A* 96.1, p. 013403. DOI: 10.1103/PhysRevA.96.013403. URL: https://journals.aps.org/pra/abstract/10.1103/PhysRevA.96.013403.

# Contents


**I Background** **1**

**1 Introduction** **3**

**2 Light-Matter Interaction** **7**

**II Theory** **13**

**3 Ab-Initio Theory** **15**

3.1 Attosecond Transient Absorption Spectroscopy . . . . . 16

3.1.1 The Transient Absorption Spectrum . . . . . 18

3.1.2 The Bidimensional Spectrum . . . . . 24

3.1.3 Features of the ATAS Spectrum . . . . . 26

3.2 Reconstruction of Attosecond Beatings by Interference of Two-Photon Transitions . . . . . 33

3.2.1 The Sideband Phase . . . . . 40

3.3 Ab-Initio Propagations . . . . . 47

3.3.1 Field-Free Propagation . . . . . 51

3.3.2 Field-Driven Propagation . . . . . 52

3.3.3 Complex Absorption Potential . . . 58
3.4 Extracting Observables . . . 63
3.4.1 The Transient Absorption Spectrum . . . 64
3.4.2 The Photoelectron Spectrum . . . 70

**4 Ab-Initio Bases** **73**
4.1 The B-Spline Helium Basis . . . 74
4.1.1 The Helium Eigenfunctions . . . 75
4.1.2 The B-Spline Basis . . . 77
4.1.3 Diagonalising the Hamiltonian . . . 80
4.2 The XCHEM Basis . . . 82
4.2.1 The Atomic Basis . . . 83
4.2.2 The GABS Hybrid Basis . . . 85
4.2.3 Diagonalising the Hamiltonian . . . 87

**5 Simple Interferometric Models** **89**
5.1 Calculation of the Matrix Elements . . . 90
5.1.1 Transition Amplitudes Between Featureless Continua . . . 92
5.1.2 Fano Formalism and Resonant Transition Amplitudes . . . 93
5.2 Angularly Resolved Atomic Phases . . . 99

**III Results** **103**

**6 Helium** **105**
6.1 ATAS Above the $N = 2$ Threshold . . . 105
6.1.1 The Cross Section . . . 108
6.1.2 The Attosecond Transient Absorption Spectrum . . . 109
6.1.3 The Bidimensional Spectrum . . . 112
6.1.4 Conclusions . . . 113

**7 Neon** **115**
7.1 ATAS Below the Second Threshold . . . . . 116
7.1.1 The Cross Section . . . . . 118
7.1.2 The Attosecond Transient Absorption Spectrum . . . . . 119
7.1.3 The Bidimensional Spectrum . . . . . 121
7.1.4 Conclusions . . . . . 123
7.2 RABITT in the Vicinity of Multiple Resonances . . . . . 123
7.2.1 The Photoelectron Spectrum . . . . . 129
7.2.2 Extracted Phases . . . . . 131
7.2.3 Conclusions . . . . . 134

**8 Argon** **137**
8.1 Anisotropic Time Delays Near a Resonance . . . . . 137
8.1.1 Delay-Integrated Asymmetry Parameters . . . . . 142
8.1.2 Delay-Resolved Asymmetry Parameters . . . . . 144
8.1.3 Angularly Resolved Atomic Delays . . . . . 145
8.1.4 Angularly and Spectrally Resolved Atomic Delays . . . . . 147
8.1.5 Ionisation Paths and Angle-Dependent Atomic Delays . . . 149
8.1.6 Conclusions . . . . . 153

**IV Conclusions** **155**

**9 Conclusions** **157**

**10 Conclusiones** **161**

**V Appendices** **165**

**A Atomic Units** **167**

**B Time-Dependent Perturbation Theory** **169**

**C Numerical Accuracy and Efficiency** **173**
C.1 Accuracy of the Operator Split . . . . . 174
C.1.1 The Strang Splitting . . . . . 175
C.1.2 Addition of the CAP . . . . . 176
C.2 Time Complexity . . . . . 176
C.2.1 Field-Free Propagation . . . . . 177
C.2.2 Field-Driven Propagation . . . . . 178
C.2.3 Complex Absorption Potential . . . . . 180

**Bibliography** **180**

# List of Figures


3.1 A schematic view of the ATAS field . . . 17
3.2 An example of the ATAS spectra . . . 25
3.3 A schematic view of ATAS beatings . . . 29
3.4 A schematic view of slow-varying ATAS fringes . . . 31
3.5 The three-step model of HHG . . . 36
3.6 The composition of the RABITT Field . . . 36
3.7 The RABITT spectrum . . . 39
3.8 The scattering phase and Wigner time delay . . . 46
3.9 The eigenstates of the quenched Hamiltonian . . . 61
3.10 The numerical dipole evolution with and without filters . . . 62
3.11 The short- and long-ranged TAS components . . . 66
3.12 The contributions of the different channels to the PES . . . 70

4.1 The difference between B-Splines of different order . . . 78
4.2 The XCHEM GABS basis . . . 86

6.1 A schematic view of the helium region studied using ATAS . . . 107
6.2 The helium cross-section above the $N = 2$ threshold . . . 108
6.3 The ATAS spectrum above the $N = 2$ threshold of helium . . . 110
6.4 The ATAS spectrum above the $N = 2$ threshold of helium, with the background removed . . . 110
6.5 The bidimensional ATAS spectrum of helium . . . 111

7.1 A schematic view of the neon region studied using ATAS . . . . . 118
7.2 The transient neon cross-section . . . . . 119
7.3 The ATAS spectrum of neon . . . . . 120
7.4 The bidimensional ATAS spectrum of neon . . . . . 122
7.5 A schematic view of the neon region studied using RABITT . . . 125
7.6 The neon RABITT spectrum . . . . . 128
7.7 The one-photon photoelectron yield of $HH_{63}$ . . . . . 130
7.8 The RABITT atomic phase difference of $SB_{62}$ to $SB_{64}$ . . . . . 131
7.9 The resonant contributions to the atomic phase difference of $SB_{64}$ 135

8.1 The spectral distributions of the experimental RABITT pumps . 140
8.2 The argon RABITT spectra . . . . . 141
8.3 Angular photoelectron distributions and $\beta_i$ parameters . . . . . 142
8.4 The time-dependence of the $\beta_2$ parameters . . . . . 144
8.5 The angularly resolved emission delays . . . . . 146
8.6 Emission delays resolved by energy and angle . . . . . 148
8.7 Angular dependence of matrix element amplitudes and phases . 150
8.8 Angular dependence of argon continuum-continuum phases . . 152

# I Background

# Chapter 1

## Introduction

The nature of chemical reactions is largely governed by the motions of bound electrons, making an increased understanding of electron movement in the proper time-scale a highly desirable objective. The movement – referred to as ultrafast – of atomic valence electrons tends to occur in the order of magnitude of attoseconds or a few femtoseconds. Such phenomena can be studied by employing what is known as the pump-probe approach: This approach makes use of two separate laser pulses to interact with the studied system: A high-energy, often extreme ultraviolet (XUV), pulse, referred to as a pump pulse, is used to ionise an atomic system. A second pulse, known as a probe or control pulse, can subsequently be used to extract information about the state of the excited atom. By varying the delay between the two pulses, a time-dependent view of the atom emerges.

These methods have only recently been extended to the domain of attosecond physics, creating a great demand for theory. As it is not yet possible to experimentally extract relevant information without the proper guidance of theory, theory and experiment have to be developed in parallel.

Of the three main attosecond pump-probe methods, in this thesis, two are considered: Attosecond transient absorption spectroscopy (ATAS) and reconstruction of attosecond beatings by interference of two-photon transitions

(RABITT). Both proven themselves capable tools for obtaining information not available outside the field of attosecond science. Furthermore, compared to the third, streaking, both ATAS and RABITT are more wildly used and are associated with a larger amount of available experimental literature data.

ATAS is an extension of transient absorption spectroscopy (TAS), where the probe pulse is introduced in order to modify the absorption spectrum. Although its femtosecond analogy has been in use for over 50 years, it is only recently (Goulielmakis et al. 2010) pump-probe TAS has been extended to the attosecond domain. ATAS is able to track time-resolve electron dynamics and reconstruct electron wave packets, and RABITT enabling measurements of photoemission delays in the order of hundreds of attoseconds.

RABITT was originally (Agostini et al. 2004; Paul et al. 2001) proposed to study the pulses generated by high-harmonic generation (HHG) (Ferray et al. 1988; McPherson et al. 1987), by focusing on smooth, featureless continua. Once the characteristics of one such pulse is known, however it can instead be used to study more complex atomic and molecular regions. With that, RABITT has enabled measurements of photoemission delays in the order of hundreds of attoseconds.

For atoms more complex than hydrogen, the electron movement is a many-body problem, and theoretically impossible to describe exactly. Instead approximative methods need to be employed. Unfortunately, simpler methods, such as the Hartree (1935)-Fock (1930) (HF) self-consistent field (SCF) approach or the single-active electron (SAE) approximation, which reduce the problem by only considering a single electron at a time, fail to accurately account for the much more intertwined electron-electron interaction – what is known as electron-correlation (Hättig et al. 2011). For this reason, more elaborate descriptions are necessary in order to accurately model these systems.

This thesis considers the theory behind the ultrafast movement of electrons in three complex atoms: helium, neon, and argon. These systems are modeled using accurate, full-electron, ab-initio pump-probe calculations; their description enabled through approaches such as a K-matrix (Argenti et al. 2006;

Lindroth et al. 2012) B-spline (Argenti et al. Unpublished) method and the XCHEM (Marante et al. 2014, 2017a,b) method. Although the systems considered here are all noble gas atoms, and can thus hardly be considered reactive, the underlying theory may well be extended to more reactive atomic and molecular systems.

The underlying document is structured as follows: Part I, to which the present chapter pertains, make up the introduction. It also contains chapter 2, in which a basic description of quantum physics, and the interaction between light and atoms, is given. In part II, the main bulk of the theory is described. It consists of three chapters. Firstly, chapter 3 contains information on the specific experimental, attosecond pump-probe methods employed, on the numerical ab-initio propagation used to simulate them, and on how observables are extracted from the system. Secondly, chapter 4 contains information on the bases used during ab-initio propagations. Thirdly and lastly, chapter 5 describes an extension of the Fano (1961) model to two-photon transitions, used to extract information about atomic systems without the need for expensive ab-initio calculations. In part III, the results are given, divided into one chapter for each studied atomic system. Chapter 6 considers helium, chapter 7 neon, and chapter 8 argon. Part IV consists of chapters 9 and 10, which, in English and Spanish respectively, contain a summary of the conclusions of this work. Finally, three appendices are included, located in part V. In appendix A, atomic units are discussed; in appendix B, time-dependent perturbation theory (TDPT) is described; and in appendix C the split accuracy and time complexity of the ab-initio propagation operator is treated.

Throughout this thesis, Hartree (1928) atomic units (au) will be used unless otherwise stated. These are defined by setting the reduced Plank constant $\hbar$, the electron mass $m_e$ the elemental charge $e$, and the Coulomb constant $\frac{1}{4\pi\epsilon_0}$ (where $\epsilon_0$ is the vacuum permittivity) equal to one ($\hbar = m_e = e = 4\pi\epsilon_0 = 1$). This unit system is convenient, as it greatly simplifies many relevant formulas. Several atomic unit conversion factors are given in appendix A.

# Chapter 2

## Light-Matter Interaction

One of the fundamental concepts that distinguishes quantum mechanics from its classical forerunner, is that it does away with the concept of determinism. According to quantum mechanics, the outcome of an experiment can never be predicted with certainty, but only as a probability distribution. Instead of a particle having a fixed position, energy, and location, these quantities may be distributed over several values, their probability being described as a wave-function distribution. Each such quantity $a$ which can be measured – each observable – is associated with a linear operator $\hat{A}$. This operator can be used to extract the expectation value of the quantity as

$$a_{\text{exp}} = \left\langle \hat{A} \right\rangle \equiv \left\langle \Psi \middle| \hat{A} \middle| \Psi \right\rangle, \tag{2.1}$$

for a particle in a state $\left|\Psi\right\rangle$, which has been denoted using Dirac's (1939) bra-ket notation: In this notation, a state may be described by a ket $\left|\Psi\right\rangle$, which is analogous to a column vector in linear algebra. Similarly, and analogously to a row-vector, the bra $\left\langle\Psi\right|$ is the Hermitian transpose of $\left|\Psi\right\rangle$. Bra-ket notation is going to be used throughout this thesis. Once a measurement of the observable $a$ has been carried out, the result will be an eigenvalue of the associated operator $\hat{A}$, with the state function collapsing to the corresponding eigenstate.

Unlike particles in Newtonian mechanics, the movement of quantum mechanical waves are described by the time-dependent Schrödinger (1926) equation (TDSE),

$$i\frac{\partial}{\partial t}\left|\psi(t)\right\rangle = \hat{\mathcal{H}}(\boldsymbol{r},t)\left|\psi(t)\right\rangle, \tag{2.2}$$

which considers the evolution in time $t$, of a state $\left|\psi(t)\right\rangle$; where $\boldsymbol{r}$ is the position and the Hamiltonian operator $\hat{\mathcal{H}}$ is the sum

$$\hat{\mathcal{H}} = \hat{T} + \hat{\mathcal{V}} \tag{2.3}$$

of the kinetic energy operator $\hat{T}$, and the potential energy operator $\hat{\mathcal{V}}$. Equation 2.2 can be solved by defining the time-evolution operator

$$\hat{\mathcal{U}}(\boldsymbol{r};t_1,t_0) = \hat{\mathcal{T}}_o\left\{\exp\left[-i\int_{t_0}^{t_1} dt\ \hat{\mathcal{H}}(\boldsymbol{r},t)\right]\right\} \tag{2.4}$$

between the times $t_0$ and $t_1$, where the time-ordering operator $\hat{\mathcal{T}}_o$ works on the expression within the brackets.

For a single particle, the kinetic energy operator $\hat{T}$ can be written as

$$\hat{T} = \frac{1}{2}\hat{\boldsymbol{p}}^2, \tag{2.5}$$

where $\hat{\boldsymbol{p}}$ is the momentum operator. The operator $\hat{\boldsymbol{p}}$ may be written in terms of the gradient operator $\hat{\boldsymbol{\nabla}} = \left(\partial_x, \partial_y, \partial_z\right)^{\mathsf{T}}$ as $\hat{\boldsymbol{p}} = -i\hat{\boldsymbol{\nabla}}$. The potential energy operator $\hat{\mathcal{V}}$, on the other hand, can be described as a time and space-dependent scalar operator.

For a time-independent Hamiltonian $\hat{\mathcal{H}}$, the Hamiltonian eigenfunctions $\psi(\boldsymbol{r},t)$ can be written as standing waves

$$\left|\psi(t)\right\rangle = \left|\psi\right\rangle\exp(-i\varepsilon t) \tag{2.6}$$

of energy $\varepsilon$, by separating the time-dependent component from the functions

$\left|\psi\right\rangle$, which also are Hamiltonian eigenfunctions. This allows equation 2.2 to be simplified to the eigenvalue problem

$$\varepsilon \left|\psi(t)\right\rangle = \hat{\mathcal{H}}(\boldsymbol{r}, t) \left|\psi(t)\right\rangle, \tag{2.7}$$

known as the time-independent Schrödinger equation (TISE). This mirrors the classical relation $\varepsilon = \varepsilon_{\text{kin}} + \varepsilon_{\text{pot}}$, according to which the total energy can be seen as the sum of the kinetic ($\varepsilon_{\text{kin}}$) and the potential ($\varepsilon_{\text{pot}}$) energy.

In particular, this thesis consider atomic systems – systems consisting of a single nucleus surrounded by several electrons. The simplest atomic system, hydrogen, is described by the Hamiltonian

$$\hat{\mathcal{H}}_0 = \frac{1}{2}\hat{\boldsymbol{p}}^2 - \frac{1}{\|\hat{\boldsymbol{r}}\|} \tag{2.8}$$

in the inertial reference frame of the atomic core, positioned at the origin. The second term – the potential energy – considers the Coulomb attraction between the core and the electron. This is a potential well, to which Hamiltonian eigenfunctions with negative energies can be considered bound.

The bound eigenfunctions can be divided, by the projection $\left\langle \boldsymbol{r} \middle| \psi_{n\ell m} \right\rangle$ onto the position eigenstates $\left|\boldsymbol{r}\right\rangle$, as

$$\left\langle \boldsymbol{r} \middle| \psi_{n\ell m} \right\rangle = R_{n\ell}(r)\, Y_\ell^m(\hat{r}), \tag{2.9}$$

into a radial component $R_{n\ell}(r)$ (where $r = \|\boldsymbol{r}\|$) from the core, and an angular component $Y_\ell^m(\hat{r})$ (where $\hat{r} = \boldsymbol{r}/r$), known as a spherical harmonic. They are defined by three integer quantum numbers: The principal quantum number $n$, the angular momentum $\ell$, and the magnetic quantum number $m$. These are restricted by $n \geq 1$, $0 \leq \ell < n$, and $|m| \leq \ell$. The associated eigenenergies depend as

$$\varepsilon_n = -13.6 \frac{1}{n^2} \text{ eV} \tag{2.10}$$

on $n$. An energy series $\varepsilon_n \propto -1/n^2$ is known as a Rydberg series.

Turning to larger atomic systems, the case is not as simple. For an atom with the atomic number $Z$, the Hamiltonian may be written as

$$\hat{\mathcal{H}}_0 \;=\; -\sum_i \frac{1}{2}\hat{\boldsymbol{p}}_i^2 \;-\; \sum_i \frac{Z}{\left\|\hat{\boldsymbol{r}}_i\right\|} \;+\; \sum_{i,j>i} \frac{1}{\left\|\hat{\boldsymbol{r}}_i - \hat{\boldsymbol{r}}_j\right\|}, \tag{2.11}$$

where $\hat{\boldsymbol{p}}_i$ and $\hat{\boldsymbol{r}}_i$ are the $ith$ electron momentum and position operator, and the third term has been introduced to account for electron-electron repulsion. When more than one electron is present, the TISE has no exact solution, and a numerical approach must be employed.

A state ket $\left|\Psi(t)\right\rangle$ is expressible as a linear combination

$$\left|\Psi(t)\right\rangle \;=\; \sum_i c_i(t)\left|\psi_i\right\rangle \tag{2.12}$$

of Hamiltonian eigenstates. If the Hamiltonian is time-independent, the constants $c_i(t)$ vary as $c_i(t) = c_i(0)\exp(-i\varepsilon_i t)$. When considering interaction between an atom and an external, time-dependent light field; it is therefore convenient to describe the system using the eigenfunctions of the static, atomic Hamiltonian $\hat{\mathcal{H}}_0$, writing the total Hamiltonian as the sum

$$\hat{\mathcal{H}}(t) \;=\; \hat{\mathcal{H}}_0 \;+\; \hat{\mathcal{H}}_I(t) \tag{2.13}$$

of $\hat{\mathcal{H}}_0$ and a time-dependent interaction component $\hat{\mathcal{H}}_I(t)$. The interaction with the electric field can be modeled using the minimal-coupling Hamiltonian

$$\hat{\mathcal{H}}(t) = \sum_i \frac{1}{2}\left[\hat{\boldsymbol{p}}_i + \alpha \boldsymbol{A}(\hat{\boldsymbol{r}}_i, t)\right]^2 \;-\; \Phi(\hat{\boldsymbol{r}}_i, t) \;+\; \hat{\mathcal{V}}_{atom}(\hat{\boldsymbol{r}}_i), \tag{2.14}$$

where $\hat{\mathcal{V}}_{atom}(\hat{\boldsymbol{r}})$ is the atomic potential, $\alpha$ is the fine-structure constant, and the field is defined by the vector potential $\boldsymbol{A}(\boldsymbol{r}, t)$ and the scalar potential $\Phi(\boldsymbol{r}, t)$.

The electric field can be written as

$$\boldsymbol{E}(\boldsymbol{r},t) \;=\; -\frac{\partial \boldsymbol{A}(\boldsymbol{r},t)}{\partial t} \;-\; \boldsymbol{\nabla}\Phi(\boldsymbol{r},t) \tag{2.15}$$

in terms of $\boldsymbol{A}(\boldsymbol{r},t)$ and $\Phi(\hat{\boldsymbol{r}},t)$. As in the case for the global state phase, neither $\boldsymbol{A}(\boldsymbol{r},t)$ nor $\Phi(\hat{\boldsymbol{r}},t)$ are physical observables. Indeed, the Schrödinger equation is invariant under the gauge transformation

$$\begin{cases} \boldsymbol{A}(\boldsymbol{r},t) \;\rightarrow\; \boldsymbol{A}(\boldsymbol{r},t) + \boldsymbol{\nabla}\chi(\boldsymbol{r},t) & \text{(2.16a)} \\ \Phi(\boldsymbol{r},t) \;\rightarrow\; \Phi(\boldsymbol{r},t) - \dfrac{1}{c}\dfrac{\partial}{\partial t}\chi(\boldsymbol{r},t) \quad , & \text{(2.16b)} \\ \Psi(\boldsymbol{r},t) \;\rightarrow\; \Psi(\boldsymbol{r},t)\;\exp(-i\chi(\boldsymbol{r},t)) & \text{(2.16c)} \end{cases}$$

where the scalar function $\chi(\boldsymbol{r},t)$ has been introduced and $c$ is the speed of light. One useful gauge is the Coulomb gauge, defined by setting $\boldsymbol{\nabla}\cdot\boldsymbol{A}(\boldsymbol{r},t) = 0$ and $\Phi(\boldsymbol{r},t) = 0$. In this gauge, $\boldsymbol{A}(\boldsymbol{r},t)$ and $\boldsymbol{\nabla}$ commute – that is, the commutator $\left[\hat{\mathcal{A}},\hat{\mathcal{B}}\right] = \hat{\mathcal{A}}\hat{\mathcal{B}} - \hat{\mathcal{B}}\hat{\mathcal{A}}$ equals the null operator ($[\boldsymbol{A}(\boldsymbol{r},t),\boldsymbol{\nabla}] = \hat{\emptyset}$). For this reason, the expression

$$\hat{\mathcal{H}}_I(t) \;=\; \sum_i -i\alpha\boldsymbol{A}(\hat{\boldsymbol{r}}_i,t)\cdot\hat{\boldsymbol{p}}_i \;+\; \frac{\alpha^2}{2}\boldsymbol{A}^2(\hat{\boldsymbol{r}}_i,t) \tag{2.17}$$

is valid for the interaction Hamiltonian. In order to further simplify this expression, presently consider the external field. The total field can be written as a linear combination of linearly polarised, monochromatic fields. Each such monochromatic field of wavelength $\lambda$ and frequency $\omega$ can be written as

$$\boldsymbol{A}(\boldsymbol{r},t) = \boldsymbol{A}_0\cos\left(\frac{\hat{n}\cdot\boldsymbol{r}}{\lambda} - \omega t + \phi\right), \tag{2.18}$$

where the vector $\boldsymbol{A}_0$ is orthogonal to the direction $\hat{n}$ of the polarization. When considering wavelengths $\lambda$ sufficiently large compared to the studied system, the spacial dependence of this equation can be disregarded, or, rather, incorporated into the constant phase $\phi$. This is known as the dipole approximation.

For comparison, the shortest wavelengths considered here are in the order of magnitude of 300 au – several hundred times larger than the Bohr radius $a_0$ (the average distance between the core and the electron in a hydrogen atom).

Two more gauges may now be considered. Firstly, the Göppert-Mayer transformation, defined by $\chi(t) = -\hat{\boldsymbol{d}} \cdot \boldsymbol{A}(t)$, where $\hat{\boldsymbol{d}} = \sum_i \hat{\boldsymbol{r}}_i$, allows for transformation into the length gauge. In this gauge, the interaction Hamiltonian may be simplified to the expression

$$\hat{\mathcal{H}}_I^L = \boldsymbol{E}(t) \cdot \hat{\boldsymbol{d}}, \tag{2.19}$$

where $\hat{\boldsymbol{d}}$ is known as the length-gauge dipole operator. Throughout this thesis, however, the velocity gauge is used. It has the interaction Hamiltonian

$$\hat{\mathcal{H}}_I^V = \alpha \boldsymbol{A}(t) \cdot \hat{\boldsymbol{\mathcal{P}}}, \tag{2.20}$$

where $\hat{\boldsymbol{\mathcal{P}}}$ is the velocity-gauge dipole operator, and can be arrived at through the gauge transformation $\chi(t) = \frac{N_e}{2} \int_{-\infty}^{t} dt' \boldsymbol{A}^2(t')$, where the sum over the electrons is carried out by multiplication of the total number $N_e$ of electrons.

This thesis only considers only linearly polarised light. Taking the $\hat{z}$ axis to be the polarisation direction, equation 2.20 can be further simplified as

$$\hat{\mathcal{H}}_I^V = \alpha A(t) \hat{\mathcal{P}}, \tag{2.21}$$

by defining $\hat{\mathcal{P}} = \hat{\boldsymbol{\mathcal{P}}} \cdot \hat{z}$ and $A(t) = \boldsymbol{A}(t) \cdot \hat{z}$. The state may now, as suggested in equation 2.12, be described as a linear combination

$$\left|\Psi(t)\right\rangle = \sum_i c_i(t) \left|\psi_i\right\rangle \exp(-i\varepsilon_i t) \tag{2.22}$$

of Hamiltonian eigenstates $\left|\psi_i\right\rangle$, with corresponding eigenenergies $\varepsilon_i$. The values $c_i(t)$ remain constant unless an external field is present, redistributing the state population. It is these basic process which are examined by the time-resolved studies discussed in this work.

# II

# Theory

# Chapter 3

## Ab-Initio Theory

The focus of this work lies on the study of time-dependent electron dynamics in atoms, induced by linearly polarised ultrashort light. Time-dependent electron dynamics, generally referred to as ultrafast phenomena, take place on time-scales on the order of several attoseconds or a few femtoseconds.

Resolving spectra on such time-scales is not without complications. One problem which arises stems from what is known as the Heisenberg uncertainty principle. Although also applicable to other observables, for time- and energy-operators it can be written as

$$\sigma_\varepsilon \cdot \sigma_t \geq \frac{1}{2} \tag{3.1}$$

where $\sigma_\varepsilon$ is the uncertainty (here defined as the variance) in the energy determination, and $\sigma_t$ is that of the time before the system decays, at which point it can be measured (Svanberg 1991).

This imposes strict limitations on the maximum possible resolutions of energy and time. As an illustrative example, demanding a resolution corresponding to an energy-uncertainty as low as $\sigma_\varepsilon = 7 \cdot 10^{-3}$ au – one tenth of the energy-distance between the $2s^{-2}3s3p$ and $2s^{-2}3s4p$ resonances in Helium, a region studied with significantly higher energy resolution as part of this thesis (in Petersson et al. [2017]) – would impose a minimum time uncertainty of

$\sigma_t \approx 1730$as, an uncertainty more than twenty times the time-resolution used in said study!

How, then, can such a precision be achieved? The answer to this question lies in the pump-probe nature of the methods employed in this work. Using two independent laser pulses, it is not so much the time, $t$, which is measured, but rather the time-delay, $\tau$, between said pulses, which is varied to probe time-dependent dynamics, overriding the constraint imposed by the Heisenberg uncertainty principle. (Pollard et al. 1992).

When considering, say, a two-photon absorption process (one photon associated with each pulse), it is not the exact time between the two absorption events that is measured. The times when these events occur are not known – only their time probability distributions, determined by the respective temporal profiles of the pulses. It is thus the entire probability-distributions that are shifted with $\tau$, which can be done with arbitrary precision.

This chapter is dedicated to the theory behind these methods, and the phenomena they probe. Two pump-probe methods are considered: The first, known as attosecond transient absorption spectroscopy (ATAS), is described in section 3.1, and the second, reconstruction of attosecond beatings by interference of two-photon transitions, in section 3.2. These phenomena were theoretically modelled, using accurate, full-electron, numerical ab-initio propagations. The theory behind those propagations is discussed in section 3.3 (although the details behind the basis employed during propagation are given in chapter 4). Finally, section 3.4 complements this discussion by describing how observables can be extracted from the ab-initio propagation.

## 3.1 Attosecond Transient Absorption Spectroscopy

The first probing technique utilised in this thesis is what is known as attosecond transient absorption spectroscopy (ATAS). ATAS was initially used by Goulielmakis et al. (2010) to monitor the ultrafast dynamics involved in the coherent interference of valance-holes in krypton. It has since been used to monitor dynamics resulting from processes such as superpositions of singly excited states in helium (S. Chen et al. 2012, 2013a,b; Chini et al. 2014; Herrmann et al. 2013), and in neon (Beck et al. 2014; Ding et al. 2016; Wang et al. 2013), of doubly excited states in helium (Argenti et al. 2015; Ott et al. 2014), the buildup of Fano (1961) profiles in helium (Kaldun et al. 2016), and hole alignment in neon (Heinrich-Josties et al. 2014). Through this, it has established itself as a trusted tool for monitoring ultrafast atomic as well as molecular processes (Argenti et al. 2015; Beck et al. 2014; Goulielmakis et al. 2010; Ott et al. 2014).

The general concept of ATAS becomes evident when considering the pump-probe setup, illustrated in figure 3.1. The system under observation is excited by what is typically a short, weak, extreme ultraviolet (XUV), pulse (shown in blue in figure 3.1), intended to populate the studied energy-range of the spectrum. A second probe pulse is then used to probe the dynamics of the excited spectrum. By varying the time-delay, $\tau$, between the pulses, the time-evolution of the populated-spectrum, and the corresponding dynamics, can be studied.This

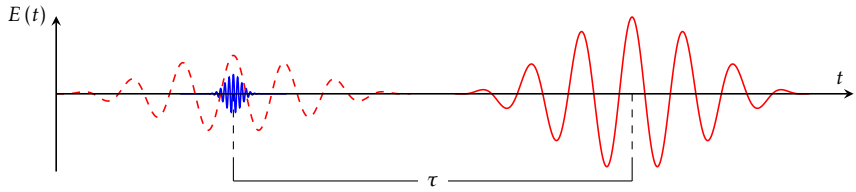


**Figure 3.1:** An illustration of the electric field $E(t)$ of the high-energy pump (blue) and the low-energy probe (fully drawn red) used in ATAS as a function of time $t$. The time delay of the probe with regards to the pump, $\tau$, is varied to resolve the resulting data in time. To study one-photon beatings, a weak, low-energy field (red, dashed) can be added to the pump.

thesis considers the case of an infrared (IR) or visible (VIS) probe (shown in fully drawn red in figure 3.1), stronger than the XUV, but too weak to further drain the ground state.

It should be noted that, using a weak XUV pump as described above, only states which are dipole-connected to the ground state are populated. Although states which are not dipole connected to the ground state may be involved in the dynamics probed by the probe pulse, the time-dependent behaviour of such states is not observed. If such processes *are* to be studied, however, a low-energy component (shown in dashed red in figure 3.1) can be added to the pump (Ding et al. 2016). This component redistributes the population over the excited states – including those not connected to the ground state via one-photon transitions. In this manner, the field-free evolution of such states over the interval between the pump and the probe also becomes relevant. This is already a common practice in femtosecond pump-probe spectroscopy (Petersson et al. 2017).

This work considers both the case where the pump does (see chapter 7.1), and does not (see chapter 6.1), include a low-frequency component.

### 3.1.1 The Transient Absorption Spectrum

In ATAS, the transient absorption spectrum (TAS) is observed. In order to understand the significance of the TAS, and how it can be extracted, consider a beam of light passing through a target medium, along the $x$–axis. Assuming that the target concentration is uniform, the proportion of light absorbed per unit of length will be constant. That is, when passing through a small interval $\partial x$, the relation

$$\frac{\partial I(\omega;x)}{I(\omega;x)} = -c(\omega)\,\partial x, \tag{3.2}$$

where $I(\omega;x)$ is the intensity of the field at frequency $\omega$ after having penetrated a distance of $x$ into the medium, and $c(\omega)$ is the absorbance per length, holds. This relation is known as the Beer-Lambert law (Svanberg 1991). Dividing $c(\omega)$ with the number of atoms per unit of length, $n$, gives an effective atomic cross

section

$$\sigma(\omega) = \frac{c(\omega)}{n}, \tag{3.3}$$

allowing equation 3.2 to be rewritten as

$$\frac{\partial I(\omega;x)}{I(\omega;x)} = -\sigma(\omega)\, n\, \partial x. \tag{3.4}$$

Solving equation 3.4 gives

$$I(\omega;x) = I(\omega;0)\ \exp\left[-\sigma(\omega)\, n\, x\right], \tag{3.5}$$

or, equivalently,

$$\sigma(\omega) = -\frac{1}{nx} \ln\left[\frac{I(\omega;x)}{I(\omega;0)}\right]. \tag{3.6}$$

Using tilde to denote the Fourier transform; the first order Taylor-expansion of equation 3.6 gives

$$\sigma(\omega) = \frac{1}{n\,x}\frac{I(\omega;0) - I(\omega;x)}{I(\omega;0)} = \frac{1}{n\,x}\frac{\left\|\tilde{\boldsymbol{E}}(\omega;0)\right\|^2 - \left\|\tilde{\boldsymbol{E}}(\omega;x)\right\|^2}{\left\|\tilde{\boldsymbol{E}}(\omega;0)\right\|^2}, \tag{3.7}$$

where $\boldsymbol{E}(t;x)$ is the electric field, and the relation $I(\omega) = \left\|\tilde{\boldsymbol{E}}(\omega)\right\|^2$ between the intensity and the norm of the electric field has been used. It is the cross-section $\sigma(\omega)$ which is taken as the TAS-spectrum.

In order to derive an expression for $\sigma(\omega)$, consider Maxwell's equations, written as

$$\nabla \cdot \boldsymbol{D} = 0 \tag{3.8a}$$

$$\nabla \cdot \boldsymbol{B} = 0 \tag{3.8b}$$

$$\nabla \times \boldsymbol{E} = -\frac{1}{c}\frac{\partial}{\partial t}\boldsymbol{B} \tag{3.8c}$$

$$\nabla \times \boldsymbol{H} = \frac{1}{c}\frac{\partial}{\partial t}\boldsymbol{D} \tag{3.8d}$$

in vacuum (where the current-density is zero and no free charges are present), where $\nabla$ is the gradient vector operator, $\boldsymbol{D}$ is the electric displacement, $\boldsymbol{B}$ is the magnetic field, and $\boldsymbol{H}$ is the magnetizing field. Assuming the magnetisation can be neglected, the relations

$$\boldsymbol{D} = \boldsymbol{E} + 4\pi\boldsymbol{P} \tag{3.9a}$$

$$\boldsymbol{H} = \boldsymbol{B} \quad , \tag{3.9b}$$

where $\boldsymbol{P}$ is the polarisation, follow directly from the definitions of $\boldsymbol{D}$ and $\boldsymbol{H}$. Equations 3.8a, 3.8c, 3.8d, 3.9a, and 3.9b, along with the property

$$\nabla \times (\nabla \times \boldsymbol{v}) = \nabla(\nabla \cdot \boldsymbol{v}) - \nabla^2 \boldsymbol{v} \tag{3.10}$$

of the cross product, valid for any arbitrary vector $\boldsymbol{v}$, allows the equation

$$\frac{\partial^2}{\partial t^2}\boldsymbol{D} = 4\pi c^2 \nabla(\nabla \cdot \boldsymbol{P}) + c^2 \nabla^2 \boldsymbol{E} \tag{3.11}$$

to be derived. Together with the second time derivative of equation 3.9a, this gives the expression

$$\left(\nabla^2 - \frac{1}{c^2}\frac{\partial^2}{\partial t^2}\right)\boldsymbol{E} = \frac{4\pi}{c^2}\frac{\partial^2}{\partial t^2}\boldsymbol{P} - 4\pi\nabla(\nabla \cdot \boldsymbol{P}) \tag{3.12}$$

for the wave-propagation.

Additional simplifications of this expression can be made by considering the limitations of the problem studied in this thesis. Firstly, only linearly polarised light – traveling in a predetermined direction here taken as convention to be the $\hat{x}$ axis – is considered, allowing for the simplification

$$\boldsymbol{E}(t;x) = E(t;x)\hat{z} \tag{3.13}$$

to be made, splitting the electric field into the normalised $z$-axis vector $\hat{z}$ and a scalar quantity $E(t;x)$.

Further, the systems treated using this method are helium and neon – both noble gases having an isotropic ground-state. For this reason, the polarisation $\boldsymbol{P}(t) = \boldsymbol{0}$ prior to the arrival of the field. Thus, the only polarisation present will be in the direction of the field, and writing an expression for $\boldsymbol{P}$ analogous to equation 3.13 it can be seen that

$$\boldsymbol{P} = P(t;x)\hat{z} \Rightarrow \boldsymbol{\nabla}\cdot\boldsymbol{P} = 0. \tag{3.14}$$

With this in mind, equation 3.12 can be rewritten as

$$\left(\frac{\partial^2}{\partial x^2} - \frac{1}{c^2}\frac{\partial^2}{\partial t^2}\right)E(t;x) = \frac{4\pi}{c^2}\frac{\partial^2}{\partial t^2}P(t;x) \tag{3.15}$$

in the direction of the field.

Using the expressions

$$E(t;x) = \frac{1}{\sqrt{2\pi}}\int_0^\infty d\omega\,\tilde{E}(\omega;x)\exp\left[i\omega(t-x/c)\right] + \text{c.c.} \tag{3.16}$$

and

$$P(t;x) = \frac{1}{\sqrt{2\pi}}\int_0^\infty d\omega\,\tilde{P}(\omega;x)\exp\left[i\omega(t-x/c)\right] + \text{c.c.} \tag{3.17}$$

of the Fourier-transform, where c.c. denotes the complex conjugate, the frequency distribution of equation 3.15,

$$\left(\frac{\partial^2}{\partial x^2} - 2i\frac{\omega}{c}\frac{\partial}{\partial x}\right)\tilde{E}(\omega;x) = -4\pi\frac{\omega^2}{c^2}\tilde{P}(\omega;x), \tag{3.18}$$

can be derived (Santra et al. 2011).

A third and final limitation must now be introduced. In this work, it is the atom itself, rather than a thick cluster or solid of atoms, that is studied. Thus, the case of a thin, rather than a thick, medium is considered, and the field can be considered as varying slowly during one wavelength, allowing the second-order $x$-derivative in equation 3.18 to be neglected. This allows the further simplification

$$\frac{\partial}{\partial x}\tilde{E}(\omega;x) = -2\pi i\frac{\omega}{c}\tilde{P}(\omega;x), \tag{3.19}$$

to be made. Due to the diluted nature of the observed medium, the polarisation $\tilde{P}(\omega;x) \approx \tilde{P}(\omega)$ can be approximated as constant, allowing the linear approximation

$$\tilde{E}(\omega;x) = \tilde{E}(\omega;0) - 2\pi i\frac{\omega}{c}\tilde{P}(\omega)\,x, \tag{3.20}$$

to be made. Inserting this in equation 3.7 gives

$$\sigma(\omega) = -\frac{1}{n}\frac{4\pi\omega}{c}\mathrm{Im}\left\{\frac{\tilde{P}(\omega)}{\tilde{E}(\omega)}\right\}. \tag{3.21}$$

Since the polarisation corresponds to the total dipole moment, $\tilde{d}(\omega)$, of the $n$ atoms considered, the further simplification

$$\sigma(\omega) = -\frac{4\pi\omega}{c}\mathrm{Im}\left\{\frac{\tilde{d}(\omega)}{\tilde{E}(\omega)}\right\}, \tag{3.22}$$

can be made. This formula can be directly used to calculate the atomic spectrum (Argenti et al. 2015).

It is possible, however, to further simplify this expression in the velocity gauge. In order to do so, consider the relation

$$\frac{\partial}{\partial t}\left\langle \hat{\mathcal{A}} \right\rangle = i\left\langle \left[ \hat{\mathcal{H}}(t), \hat{\mathcal{A}} \right] \right\rangle, \tag{3.23}$$

where $\hat{\mathcal{H}}(t)$ is the total Hamiltonian, is valid for any given time-independent operator $\hat{\mathcal{A}}$ (Ohlén 2005). In the velocity gauge, the Hamiltonian can be written as

$$\hat{\mathcal{H}}(t) = \hat{\mathcal{H}}_0 + \alpha \boldsymbol{A}(t) \cdot \hat{\boldsymbol{\mathcal{P}}}, \tag{3.24}$$

where $\hat{\mathcal{H}}_0$ is the field-free atomic potential, $\alpha$ is the fine-structure constant, and the vectors $\boldsymbol{A}(t)$ and $\hat{\boldsymbol{\mathcal{P}}} = \sum_{i=1}^{N_e} \hat{\boldsymbol{\mathcal{P}}}_i$ contains in all directions, respectively, the field vector potential and the electron canonical moment operator for all $N_e$ electrons. The total dipole momentum operator vector, $\hat{\boldsymbol{d}} = \sum_{i=1}^{N_e} \hat{\boldsymbol{r}}_i$, contains the position vector operators $\hat{\boldsymbol{r}}_i$ for all electrons. Thus, in the velocity gauge, equation 3.23 gives

$$\frac{\partial}{\partial t}\left\langle \hat{\boldsymbol{d}} \right\rangle = i\left\langle \left[ \hat{\mathcal{H}}_0 + \alpha \boldsymbol{A}(t) \cdot \hat{\boldsymbol{\mathcal{P}}}, \hat{\boldsymbol{d}} \right] \right\rangle = \left\langle -\hat{\boldsymbol{\mathcal{P}}} \right\rangle + \left\langle -\alpha N_e \boldsymbol{A}(t) \right\rangle. \tag{3.25}$$

Hence, it can be seen that the dipole moment, written as

$$\frac{\partial}{\partial t} d(t) = -p(t) - \alpha N_e A(t) \tag{3.26}$$

in the direction of the field, can be divided into two components – one corresponding to the electron canonical momentum and the other to the external field. The corresponding frequency-domain expression is

$$\tilde{d}(\omega) = \frac{i}{\omega}\tilde{p}(\omega) + \frac{i\alpha N_e}{\omega}\tilde{A}(\omega). \tag{3.27}$$

This can, together with the relation

$$\tilde{E}(\omega) = -i\frac{\omega}{c}\tilde{A}(\omega), \tag{3.28}$$

be inserted into equation 3.22. As the fraction corresponding to the external-field component to the dipole is real, the expression

$$\sigma(\omega) = \frac{4\pi}{\omega}\mathrm{Im}\left\{\frac{\tilde{p}(\omega)}{\tilde{A}(\omega)}\right\} \tag{3.29}$$

is arrived at. This is the expression which has been used to extract the TAS in this work.

A numerical treatment of the TAS can be found in section 3.4.1. One point from that section which bears repeating here, is that only the dipole response with the ground state is significant enough to be visible in the TAS. For this reason, only states which are dipole-coupled with the ground state are directly observed[1].

By varying the delay $\tau$ between the pulses, a time-resolved TAS $\sigma(\omega_r;\tau)$ can be defined. To provide an illustrative example, parts of such a spectrum, for the case described in chapter 7.1, is shown in figures 3.2a and 3.2c. The system considered is neon. For the energy ranges discussed herein, a $2p$ valence electron can either be excited to ionise said atom, or either one $2s$ or two $2p$ electrons can be excited to give rise to an autoionising resonance (Barreau et al. 2019). This gives rise to a continuum containing several features.

In this case, neon is studied with a mixed XUV-NIR (near infrared) pump and an NIR probe of frequency $\omega_{\mathrm{NIR}} = 0.05879$ au. The corresponding spectrum when no probe pulse is used is denoted as $\sigma_0(\omega_r)$ below.

### 3.1.2 The Bidimensional Spectrum

In order to further study the ATAS spectrum, it is also useful to consider the changes to $\sigma(\omega_r,\tau)$ with $\tau$ in the frequency-, rather than the time-, domain.

[1] In all communications making up part of this thesis which makes use of ATAS, the ground state is of symmetry $^1S^e$. In such cases, only $^1P^o$ states are directly visible.

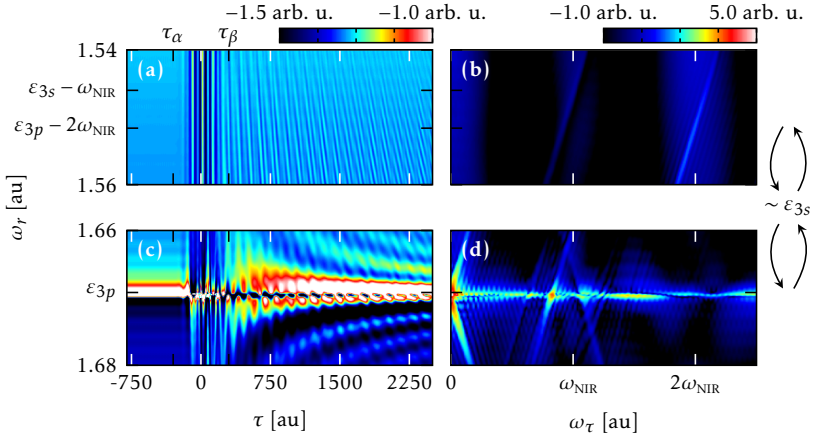


**Figure 3.2:** The natural logarithm of part of the TAS $\ln\{\sigma(\omega_r,\tau)\}$ ((a) and (c)) and the bidimensional spectrum $\ln\{\tilde{\sigma}(\omega_r,\omega_\tau)\}$ ((b) and (d)) discussed in chapter 7.1 Two energy ranges are displayed, one near the $2s^{-1}3p$ (labeled $3p$) resonance ((c) and (d)) and one at lower energies where one- and two-photon beatings (illustrated to the right with arrows) with the $2s^{-1}3s$ (labeled $3s$) and $2s^{-1}3p$ resonances respectively can be found ((a) and (b)). The time-delays are divided into three time-delay intervals using the markers $\tau_\alpha$ and $\tau_\beta$ The nearby $2p^{-2}3s3p$ resonance was excluded from the calculations, providing a clear view of the $2s^{-1}3p$ resonance.

This is done via the Fourier transform

$$\tilde{\sigma}(\omega_r,\omega_\tau) = \int d\tau \left[\sigma(\omega_r,\tau) - \sigma_0(\omega_r)\right] \frac{e^{-i\omega_\tau\tau}}{\sqrt{2\pi}} \tag{3.30}$$

of the TAS. Here the background component $\sigma_0(\omega_r)$ has been removed. To understand why, consider that when integrating over $\tau \in (-\infty,\infty)$, this component corresponds to a Dirac delta function $\sigma_0(\omega_r)\delta_0(\omega_\tau)$; and that when for numerical reasons integrating over a finite interval $\tau \in (-\tau_{\min},\tau_{\max})$, it corresponds to the Fourier transform $\sigma_0(\omega_r)\mathscr{F}\left\{\theta(\tau-\tau_{\min}) - \theta(\tau+\tau_{\max})\right\}$ of a plateau, where $\theta(x)$ is the Heaviside step function. In the former case, the contribution of $\sigma_0(\omega_r)$ is trivial; in the latter, it is unphysical. The Fourier transform in equation 3.30 is here referred to as the bidimensional spectrum. For the same system and energy ranges as figures 3.2a and 3.2c, can be found in figures 3.2b and

3.2d.

As the XUV pump is weak, the frequency-distribution of the dipole response can be written as

$$\tilde{d}(\omega_r) = \int d\omega_e \; \chi(\omega_r, \omega_e) \tilde{E}_{\mathrm{XUV}}(\omega_e), \tag{3.31}$$

where $\tilde{E}_{\mathrm{XUV}}$ is the XUV-component of the field, $\chi(\omega_r, \omega_e)$ is the electric susceptibility of the dressed atom, and $\omega_e$ is used to denote the excitation energy (Argenti et al. 2015). From this, it can be seen that the non-diagonal component $\chi_{nd}(\omega_r, \omega_e)$ of $\chi(\omega_r, \omega_e)$ relates (Argenti et al. 2015) to the bidimensional spectrum as

$$\tilde{\sigma}(\omega_r, \omega_\tau) = \frac{(2\pi)^{3/2}\omega_r}{ic} \left[ \chi_{nd}(\omega_r, \omega_r - \omega_\tau) - \overline{\chi}_{nd}(\omega_r, \omega_r + \omega_\tau) \right], \tag{3.32}$$

where $c$ is the speed of light, the diagonal component having already been removed with the removal of $\sigma_0(\omega_r)$ in equation 3.30.

### 3.1.3 Features of the ATAS Spectrum

The time-delay domain of the TAS can be divided into three different intervals: Using the notation in figure 3.2, these are $\tau_I^- = (-\infty, \tau_\alpha]$, $\tau_I^0 = \left(\tau_\alpha, \tau_\beta\right)$, and $\tau_I^+ = \left[\tau_\beta, \infty\right)$. The regions are selected so that the probe and the XUV component of the pump significantly overlap for $\tau \in \tau_I^0$.

#### Large, Negative Time-Delays

Consider first the case of $\tau \in \tau_I^-$. This region is characterised by the probe arriving before the pump without the two overlapping. Assuming the probe is too weak to not significantly drain the ground state, it will not have any significant effect. Because of this, the relation

$$\tau \in \tau_I^- \Rightarrow \sigma(\omega; \tau) = \sigma_0(\omega) \tag{3.33}$$

is valid in said region.

### Near-Zero Time-Delays

Next, there is the time interval above dubbed $\tau_I^0$. In this region, the atomic system is dressed during excitation.

One phenomenon in particular which was observed as part of this thesis (in Petersson et al. [2017], discussed in chatper 6.1) in this region is the the special case of the Stark effect known as Autler-Townes (1955) (AT) splittings. Although the phenomenon is not clearly visible in figure 3.2, it has previously been observed during ATAS (Argenti et al. 2017; Wu et al. 2016).

AT splittings corresponds to a splitting of the resonance response energy, resulting from the transition between two resonances by a strong (IR, in the case of ATAS) field. This can be illustrated with a very simple model, by considering a two-level system, with two eigenstates, $\left|\psi_\alpha\right\rangle$ and $\left|\psi_\beta\right\rangle$, with complex populations $c_\alpha$ and $c_\beta$, their energies $\omega_\alpha$ and $\omega_\beta$ being separated by an energy $\omega_{\alpha\beta}$ (Wu et al. 2016): Ignoring sub-cycle interactions (what is known as the rotating wave approximation), the time-dependent Schrödinger equation (TDSE) can be written as

$$\frac{\partial}{\partial t}\begin{bmatrix} c_\alpha \\ c_\beta \end{bmatrix} = \begin{pmatrix} 0 & \frac{\Omega(t;\tau)}{2}\exp\left(i\Delta t\right) \\ \frac{\Omega(t;\tau)}{2}\exp\left(-i\Delta t\right) & 0 \end{pmatrix}\begin{bmatrix} c_\alpha \\ c_\beta \end{bmatrix}, \tag{3.34}$$

where $\Delta = \omega_{\mathrm{IR}} - \omega_{\alpha\beta}$ is the detuning and, denoting the total dipole operator $\hat{d}$ and the dressing IR field $E_{\mathrm{IR}}(t;\tau)$,

$$\Omega(t;\tau) = E_{\mathrm{IR}}(t;\tau)\left\langle\psi_\alpha\middle|\hat{d}\middle|\psi_\beta\right\rangle \tag{3.35}$$

is known as the Rabi-frequency. Approximating the field as constant (with a constant Rabi-frequency $\Omega_0 = \Omega(t;\tau)$), this can be solved for $c_\alpha$, giving the result

$$\begin{aligned} c_\alpha(t) \propto & \frac{\widetilde{\Omega}-\Delta}{2\widetilde{\Omega}}\exp\left(\ i\frac{\widetilde{\Omega}+\Delta}{2}t\right) \\ & + \frac{\widetilde{\Omega}+\Delta}{2\widetilde{\Omega}}\exp\left(-i\frac{\widetilde{\Omega}-\Delta}{2}t\right) \end{aligned}, \tag{3.36}$$

where $\widetilde{\Omega} = \sqrt{\Omega_0^2 + \Delta^2}$.

Thus, the population of $\left|\psi_\alpha\right\rangle$ is modified by the IR as

$$\begin{aligned} c_\alpha \exp\left(-i\omega_\alpha t\right) \to & \frac{\widetilde{\Omega}-\Delta}{2\widetilde{\Omega}} c_\alpha \exp\left[-i\left(\omega_\alpha - \tfrac{\widetilde{\Omega}+\Delta}{2}\right)t\right] \\ & + \frac{\widetilde{\Omega}+\Delta}{2\widetilde{\Omega}} c_\alpha \exp\left[-i\left(\omega_\alpha + \tfrac{\widetilde{\Omega}-\Delta}{2}\right)t\right] \end{aligned}, \tag{3.37}$$

splitting the undressed energy eigenvalue into two distinct dressed energy components.

#### Large, Positive Time-Delays

Finally, consider the interval of $\tau \in \tau_I^+$, where the probe arrives after the pump without overlapping. The structure of this region can be divided into two main features (Ding et al. 2016). Firstly, there are the near-vertical, densely packed fringes, which are visible both in figure 3.2a and in figure 3.2c. Secondly, there are the hyperbolic fringes in figure 3.2c, slowly converging towards the nearby $3p$ resonance as $\tau$ increases.

**Induced Attosecond Beatings** The cause of the near-vertical fringes can be understood by considering the paths in the right side of figure 3.3: At the time $t = 0$, the ${}^1P^o$ spectrum – notably near the energies $\varepsilon_{3p}$ and $\varepsilon_\mathrm{F}$ of the $2s^{-1}3p$ resonance and a final state $\left|\psi_\mathrm{F}\right\rangle$ – is populated using the XUV component of the pump. The system is then allowed to propagate freely until the arrival of the probe. During this time the phase difference between the states oscillates with a frequency of $\left|\varepsilon_\mathrm{F} - \varepsilon_{3p}\right|$. When the probe arrives, population is transferred from the resonance to $\left|\psi_\mathrm{F}\right\rangle$ via two-photon stimulated emission, interfering either constructively or destructively depending on the relative phases of the population. This causes beatings of frequency $\left|\varepsilon_\mathrm{F} - \varepsilon_{3p}\right| \approx 2\omega_\mathrm{IR}$ as $\tau$ changes. These beatings are the cause of the local maximum at $\omega_\tau \approx 2\omega_\mathrm{IR}$ in figure 3.2b.

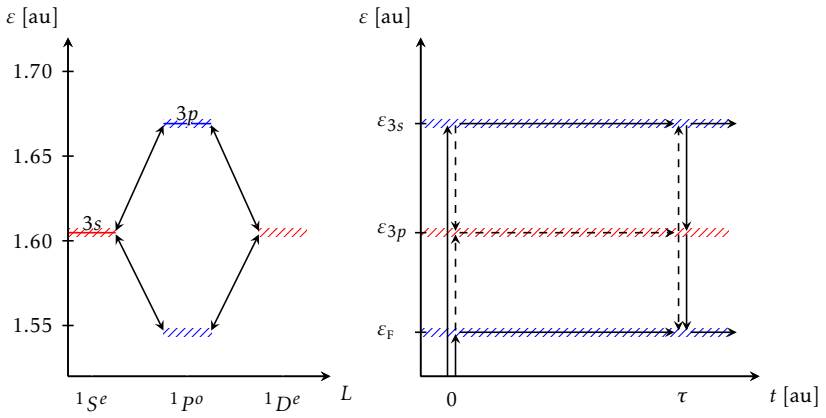


**Figure 3.3:** To the left schematic illustration of the autoionising continuum, including the $2s^{-1}3s$ and $2s^{-1}3p$ resonances (labeled as $3s$ and $3p$ in the figure), below the second threshold of Neon, is shown. Approximate one- and two-photon beatings (illustrated with arrows to the right) induced between the $2s^{-1}3p$ state and lower states using an IR of frequency $\omega_{\text{IR}} = 0.057117$ au are shown with black arrows. The righthand figure show different paths excited electron population can follow over time during ATAS. The pump is centered at $t = 0$, and the probe at $t = \tau$. Dashed paths are only significantly populated if the pump contains a low-energy component.

Due to selection rules, however, only beatings with an even number $k$ of probe photons can be seen when the pump only populates the $L = 1$ spectrum. The dashed arrows in the aforementioned figure show paths which are significantly populated by adding a low-frequency component to the pump. This populates the $2s^{-1}3s$ state. At the time of the arrival of the probe, part of this population is transferred to $\left|\psi_{\text{F}}\right\rangle$ and the $2s^{-1}3p$ resonance via one-photon absorption or stimulated emission. Analogously to the case mentioned above, this causes beatings of frequency $|\varepsilon_{\text{F}} - \varepsilon_{3s}| \approx \omega_{\text{IR}}$. These beatings are visible in figures 3.2b (around $\omega_\tau = \omega_{\text{IR}}$) and 3.2d (slightly above $\omega_\tau = \omega_{\text{IR}}$ for $\omega_r = \varepsilon_{3p}$[2]), in the studied energy ranges.

[2] A peak is also present at $\omega_\tau$ slightly below $\omega_{\text{IR}}$. This is due to the one-photon coupling with the higher $2^{-1}3d$-state, as discussed in chapter 7.1.

To generalise the discussion above, the $k-$photon beating with a given resonance of energy $\varepsilon_{\text{res}}$ can be written as

$$\omega_{\text{beat}} = |\omega_r - \varepsilon_{\text{res}}| \approx k\omega_{\text{IR}}, \tag{3.38}$$

at the response energy $\omega_r$.

Thus, the frequency of the beatings decreases with the energy-distance to the relevant resonance. This can be seen in figures 3.2b and 3.2d: For all the beatings discussed above, an associated local maxima can be found, following a path where $\omega_\tau$ decreases linearly with $|\omega_r - \varepsilon_{\text{res}}|$. The same beatings are visible in $\tilde{\sigma}(\omega_r;\omega_\tau)$ for negative values of $\omega_\tau$, at $\omega_\tau = -|\omega_r - \varepsilon_{\text{res}}|$.

The above reasoning assumes that the energy eigenstates are unperturbed by the external field. However, due to the dressing by the field, the state energies may experience a Stark (1913a,b) shift during the population transfers. The strength of such shifts can be measured by observing the deviation in $\omega_\tau$ of the localised $\tilde{\sigma}(\omega_r;\omega_\tau)$-maxima, from what would be predicted by the above discussion. (Argenti et al. 2015; Freeman et al. 1978, 1987, 1991; Ott et al. 2013; Petersson et al. 2017)

**The Buildup of Fano Profiles** The second feature to be treated is that of the hyperbolic fringes converging towards the $2s^{-1}3p$ state in figure 3.2c. Such fringes are not unique to that resonance, but rather a general trait of resonances populated during ATAS (Argenti et al. 2015; Cheng et al. 2016; Ding et al. 2016).

The cause of such fringes is easily understood with the help of figure 3.4. Figure 3.4a shows the (approximate, see figure text) population of the $\left|2s^{-1}3p\right\rangle$ state for different values of $\tau$ (and for no probe), and figure 3.4b the corresponding spectrum near the $2s^{-1}3p-$resonance to the given time-delay.

First, consider the case when no pulse is used. This is shown in black. At times $t \approx 0$, the mixed XUV-IR pump populates the $\left|2s^{-1}3p\right\rangle$ state. After the

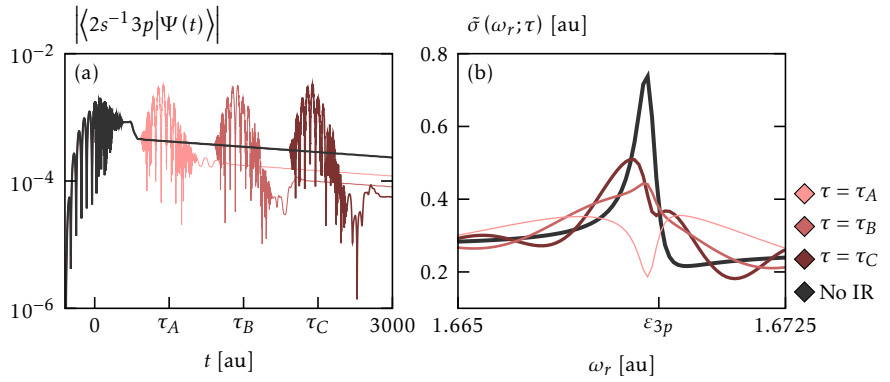


**Figure 3.4:** An illustration of the mechanism behind the slowly varying fringes present in ATAS spectra. In (a), the population of the $\left|2s^{-1}3p\right\rangle$ state is shown for different time-delays (as well as for no probe); in (b) the corresponding spectra are shown. The time-delays considered are: In pink, $\tau_A = 750$ au; in red, $\tau_B = 1500$ au; and in maroon, $\tau_C = 2250$ au. The very thick, black line uses no probe. Note that the $\left|2s^{-1}3p\right\rangle$ state is mixed with the continuum background in the (imperfect) basis used for these propagations. Therefore the projection in (a) is only a projection on to part of $\left|2s^{-1}3p\right\rangle$ – the rest of $\left|2s^{-1}3p\right\rangle$ is distributed over nearby, supposed continuum states.

end of the pump, the population decreases exponentially as

$$\left|\left\langle 2s^{-1}3p\middle|\Psi(t)\right\rangle\right| = \left|c_{3p}\right|\exp\left(-\frac{\Gamma_{3p}}{2}t\right) \tag{3.39}$$

where $c_{3p}$ defines the complex population of the resonance after the end of the pump, and $\Gamma_{3p}$ is the width of the $2s^{-1}3p$ resonance (Ott et al. 2013, 2014). As $\left|\Psi(t)\right\rangle$ evolves in time, the time profile $p(t)$ of the dipole moment emerges, and with it, the corresponding spectral profile $\tilde{p}(\omega)$. From this, the spectrum can be derived via equation 3.29. As can be seen in figure 3.4b, the spectral profile which emerges is that of the well-known Fano (1961) profile, resulting from the interference between the resonance and the smooth background.

What, then, is the effect of the probe? Defining a quantity $\Delta$, defined as the minimal width for which the relation

$$\{\forall t \in \mathbb{R} : E_{\mathrm{IR}}(t;\tau) \neq 0\} \subseteq \left(\tau - \tfrac{\Delta}{2}, \tau + \tfrac{\Delta}{2}\right) \tag{3.40}$$

holds for the temporal IR probe profile $E_{\mathrm{IR}}(t;\tau)$ (at least approximately), it becomes clear that the probe only acts on the system for a limited time. Prior to, as well following, this time interval, the population decays exponentially as described in equation 3.39. With this in mind, equation 3.39 can be generalised to the case where a probe is used as

$$\left|\left\langle 2s^{-1}3p \middle| \Psi(t) \right\rangle\right| = \begin{cases} \left|c_{3p}\right| \exp\left(-\dfrac{\Gamma_{3p}}{2}t\right), & t-\tau \leq -\dfrac{\Delta}{2} & \text{(3.41a)} \\ \Theta(t;\tau) \quad , & |t-\tau| < \dfrac{\Delta}{2}, & \text{(3.41b)} \\ \left|c'_{3p}\right| \exp\left(-\dfrac{\Gamma_{3p}}{2}t\right), & t-\tau \geq \dfrac{\Delta}{2} & \text{(3.41c)} \end{cases}$$

where $\Theta(t;\tau)$ corresponds to the complex behaviour of the $2s^{-1}3p$ population during the dressing of the atom, and $c'_{3p}$ is a complex constant analogous to $c_{3p}$.

Thus, it can be seen that the evolution of the population in equation 3.39 is modified sharply by the dressing of the atom. This is visible for several time-delays, $\tau_A = 750$ au, $\tau_B = 1500$ au, and $\tau_C = 2250$ au, in figure 3.4a. This variation to the resonance population (as well as nearby continuum states) also causes a modification to $p(t)$, and thereby a corresponding modification to $\tilde{p}(\omega)$ and $\sigma(t_0;\tau)$. Such distortion of populations near resonance energies are the cause of the nearby, converging, hyperbolic fringes (Argenti et al. 2015).

Consider now the influence of the time-delay on the distortion of the resonances. It is immediately obvious that the time-evolution of the system converges towards the field-free case as $\tau$ increases. Thus, the limit

$$\lim_{\tau\to\infty} \sigma(\omega;\tau) \to \sigma_0(\omega) \tag{3.42}$$

holds. This follows necessarily from equation 3.41, irrespectively of circumstances relating to the contingent nature of $\Theta(t;\tau)$. This is the cause of the hyperbolic fringes converging towards their corresponding resonance energy. Figure 3.4b illustrates this trend well. As the time-delay is increased, the resonance profile – originally completely obscured – is slowly restored. This can be interpreted as ATAS allowing monitoring of the resonance Fano profile buildup (Kaldun et al. 2016).

In figure 3.2c, it is clear that the hyperbolic fringes have a significantly lower frequency (along the $\tau$-axis) than the near-vertical ones. As the energy approaches that of the resonances, the frequency decreases even further, with the limit of zero when $\omega_r = \varepsilon_{3p}$. That is, as the fringes approach the resonance, they become parallel to the $\tau$ axis. This can be seen for $\omega_\tau \approx 0$ in 3.2d, where local maxima can be found for both $\omega_r < \varepsilon_{3p}$ and $\omega_r > \varepsilon_{3p}$. As $\omega_r$ approaches $\varepsilon_{3p}$, these maxima approach zero.

## 3.2 Reconstruction of Attosecond Beatings by Interference of Two-Photon Transitions

The second technique considered in this thesis is the interferometric technique known as reconstruction of attosecond beatings by interference of two-photon transitions (RABITT).

In smooth, excited continua, RABITT has proven to be efficient in probing photo-emission delays, both angularly integrated (Schultze et al. 2010) and resolved (Cirelli et al. 2018; Heuser et al. 2016). Although this is not possible close to resonances (Argenti et al. 2017; Sabbar et al. 2015), it can still be used to probe transition amplitudes and spectral phases in resonant regions (Busto et al. 2018; Gruson et al. 2016; Kotur et al. 2016).

Although the complex dynamics involved in RABITT largely limits it to the study of simpler continua, it has not only been successfully used to study atomic (Cattaneo et al. 2016; Guénot et al. 2014; Palatchi et al. 2014; Swoboda et al. 2010) dynamics, but also molecular (Caillat et al. 2011; Cattaneo et al. 2018; Haessler et al. 2009; Huppert et al. 2016), solid (Cavalieri et al. 2007; Neppl et al. 2015; Swoboda et al. 2010; Tao et al. 2016), and fine-structure (Jordan et al. 2017) ones. The great utility of RABITT has given rise to significant amounts of theoretical work, with the aim of forging an underlying theoretical framework (Dahlström et al. 2012b; Feist et al. 2014; Kheifets 2013; Moore et al. 2011; Pazourek et al. 2015).

RABITT was originally proposed to validate the method for extreme ultraviolet (XUV) pulse generation known as high harmonic generation (HHG) (Agostini et al. 2004; Paul et al. 2001), and uses an extreme ultraviolet attosecond pulse train (XUV-APT) generated via HHG as a pump. Thus, in order to understand RABITT, it is convenient to first briefly comment on the nature of HHG.

HHG, developed by Ferray et al. (1988) and McPherson et al. (1987), involves using a strong, low-energy field to populate high energy states of an electron

system (here taken to be atomic). As the system returns to its ground state, it emits high frequency light.

The most common model used to simplify and describe the dynamics underlying HHG is known as the three-step model (developed by Corkum [1993], Krause et al. [1992], and Schafer et al. [1993]), and is illustrated in figure 3.5. As the name suggests, the three-step model divides the HHG process into three separate steps.

The first step, known as "tunnelling" (shown in figure 3.5a), consists of the atomic potential being modified by the IR-interaction potential to the extent that the electron may free itself from the atomic potential via tunneling.

During the second step, called "propagation" (shown in figure 3.5b), the electron is accelerated in the IR field, gaining energy. As the IR field changes sign (every half-cycle), the electron is accelerated back towards the atomic core.

The final step of "recombination" (shown in figure 3.5c) consists of the excited population returning to the ground state, and, in doing so, emitting high-frequency light.

Although higher energies are possible in a non-classical view; assuming that the electron follows a classical path during the propagation step, it can reach a maximum energy around $I_p + 3.2U_p$ (Agostini et al. 2004; Lewenstein et al. 1994), where $I_p$ is the atomic ionisation potential and the ponderomotive energy

$$U_p = \frac{I_{\mathrm{IR}}^{\mathrm{HHG}}}{4\omega_{\mathrm{IR}}^2}, \tag{3.43}$$

is the cycle-averaged kinetic energy of a free electron in the driving IR field of frequency $\omega_{\mathrm{IR}}$ and intensity $I_{\mathrm{IR}}^{\mathrm{HHG}}$ (Gapanov et al. 1958).

It immediately becomes clear from the three-step model that the process of generating high-frequency is repeated (alternatingly spatially inverted in the direction of the IR) once every half-cycle of the dressing IR. This allows the

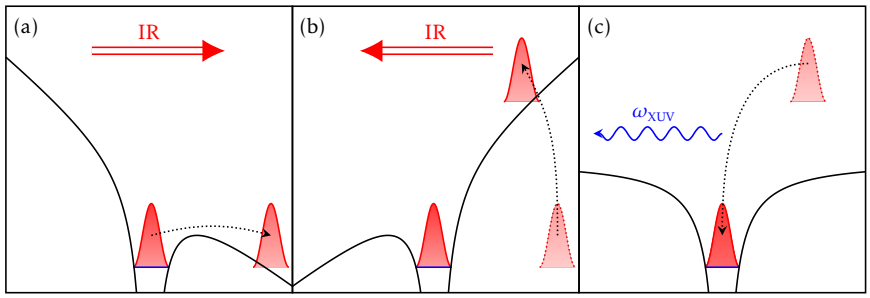


**Figure 3.5:** An illustration of the Three-step model, used to provide a simple explanation of the mechanism behind HHG. (a) Tunneling: The electron tunnels out of the field-distorted atomic potential. (b) Propagation: The electron gains energy from the IR field. (c) Recombination: The electron, brought back to the atomic core, falls back into a bound state, and emits an XUV photon.

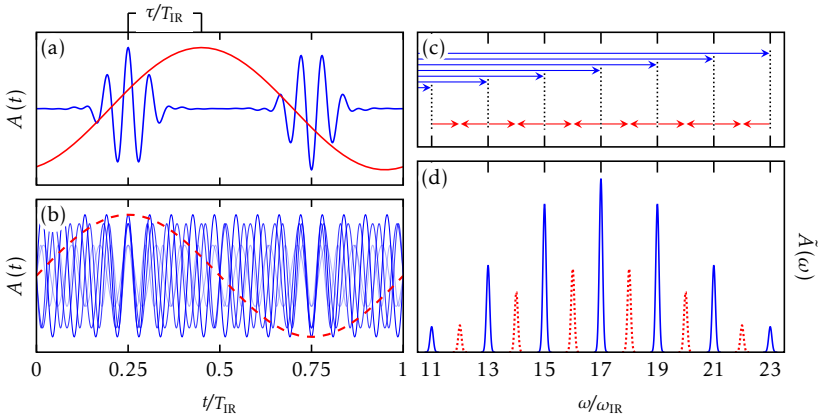


**Figure 3.6:** An illustration of a typical external field used during RABITT. In (a), the XUV-APT pump (blue) is shown along with the IR probe (red) – shifted by a time-delay $\tau$ – during one period $\tau$ of the IR field. In (b), the overtones of the driving IR (dashed red) composing the XUV-APT are shown (blue). In both (a) and (b) the IR fields have been normalised to be comparable to the XUV fields. Different paths available via absorption of one XUV photon (blue) and either emission or absorption of one IR photon (red) are shown in (c). These paths allows the population of states corresponding to the spectral profile shown in (d), where the blue peaks may be populated using only an XUV-APT photon, while the red, dotted ones also require an IR photon.

vector potential of the generated high-energy field to be written on the form

$$A_{\mathrm{XUV}}(t) = A_0^{\mathrm{APT}}(t) \sum_{i=-\infty}^{\infty} (-1)^i f\left(t - \tfrac{i\pi}{\omega_{\mathrm{IR}}}\right), \tag{3.44}$$

where $A_0^{\mathrm{APT}}(t)$ is the slow-varying APT-envelope, and $f(t)$ the single-pulse envelope (Jiménez-Galán et al. 2013). This can be seen in figure 3.6a, where one such APT is shown in blue.

Presently consider the same problem from a second perspective: As the electron gains energy in the field, it does so by absorbing quanta of energy from the field (Schafer et al. 1993). For an approximately monochromatic driving IR, these photonic energies are equal to the central IR frequency, $\omega_{\mathrm{IR}}$. Consequently, the distance in energy between the ground state and the distributed excited population corresponds to the (high) harmonics (HH) of the IR. Due to selection rules, each absorption of a photon corresponds to a change in total angular momentum of $L \rightarrow L \pm 1$, and only the absorption of an odd number of photons can result in a total change in $L$ of $\pm 1$. Because of this, and because of selection rules during the emission of the XUV (as the atom returns to the ground state), only the odd harmonics are emitted (Ben-Tal et al. 1993).

Equation 3.44 can be rewritten (Jiménez-Galán et al. 2013) as

$$A_{\mathrm{XUV}}(t) = \sqrt{\frac{8}{\pi}}\, \omega_{\mathrm{IR}}\, A_0^{\mathrm{APT}}(t) \sum_{j \in \mathbb{N} \setminus 2\mathbb{N}} \left|\tilde{f}(j\,\omega_{\mathrm{IR}})\right| \cos\left(j\,\omega_{\mathrm{IR}} t + \phi_j\right), \tag{3.45}$$

where $\phi_j$ is the spectral phase of the $jth$ harmonic, and only odd values $j$ are included, to reflect the division of the field into its spectral components. The division of the APT of figure 3.6a is shown in figure 3.6b in the temporal domain and in figure 3.6d in the spectral domain.

The figure illustrates how, due to only odd frequencies being included (and assuming $\phi_j \approx 0$), all harmonics interfere constructively once every half-cycle of the field, and are antisymmetric every half cycle. This reflects the picture of the field as a being composed of a train of attosecond pulses, every other spatially

inverted, emerging from the three-step model.

Using a many-cycle XUV-APT taking the general form discussed up until now as a pump (which is the case of RABITT, even if it is not directly generated using HHG), only odd harmonics of the driving IR can be reached. In RABITT, however, a secondary component – an IR probe with the same central frequency as that used during HHG XUV-APT generation, with a time-delay $\tau$ – is introduced. It can be written as

$$A_{\mathrm{IR}}(t;\tau) = A_0^{\mathrm{IR}}(t-\tau)\cos\left[\omega_{\mathrm{IR}}(t-\tau)\right], \tag{3.46}$$

where $A_0^{\mathrm{IR}}(t)$ is the pulse envelope. Here, the IR phase has been neglected – or, rather, it is incorporated in $\omega_{\mathrm{IR}}\tau$. This is an approximation due to $A_0^{\mathrm{IR}}(t)$ envelope also depending on $\tau$, but is a reasonable one, as the exact position of the long, overlapping pulse envelopes can be neglected during RABITT.

This is shown in figure 3.6a. Using this component, it is also possible to populate the even harmonics, known as sidebands (SB), using one pump- and one probe photon, as illustrated in figures 3.6c and 3.6d. Such sidebands are observed during RABITT.

Consider now the intensity of the $2nth$ sideband, $\mathrm{SB}_{2n}$. Assuming both the harmonic below ($\mathrm{HH}_{2n-1}$) and the one above ($\mathrm{HH}_{2n+1}$) $\mathrm{SB}_{2n}$ are significantly populated, population is transferred to the sideband via both harmonics. Once the harmonics are populated by the XUV-APT, the populations of $\mathrm{HH}_{2n+1}$ and $\mathrm{HH}_{2n-1}$ oscillate with frequencies separated by their energy-separation of $2\omega_{\mathrm{IR}}$. When the IR probe populates $\mathrm{SB}_{2n}$ (a process which can be delayed by varying $\tau$), the two paths interfere. Denoting the amplitude of the population transferred to $\mathrm{SB}_{2n}$ from $\mathrm{HH}_{2n-1}$ and $\mathrm{HH}_{2n+1}$ as $\mathcal{A}_{2n}^{-}$ and $\mathcal{A}_{2n}^{+}$, the intensity of $\mathrm{SB}_{2n}$ can be written as

$$\begin{aligned} I_{2n}(\tau) &= \left|\mathcal{A}_{2n}^{-}(\tau) + \mathcal{A}_{2n}^{+}(\tau)\right|^2 \\ &= \left|\mathcal{A}_{2n}^{-}\right|^2 + \left|\mathcal{A}_{2n}^{+}\right|^2 + 2\left|\mathcal{A}_{2n}^{-}\mathcal{A}_{2n}^{+}\right|\cos\left(2\omega_{\mathrm{IR}}\tau + \Delta\phi_{2n}\right) \end{aligned}, \tag{3.47}$$

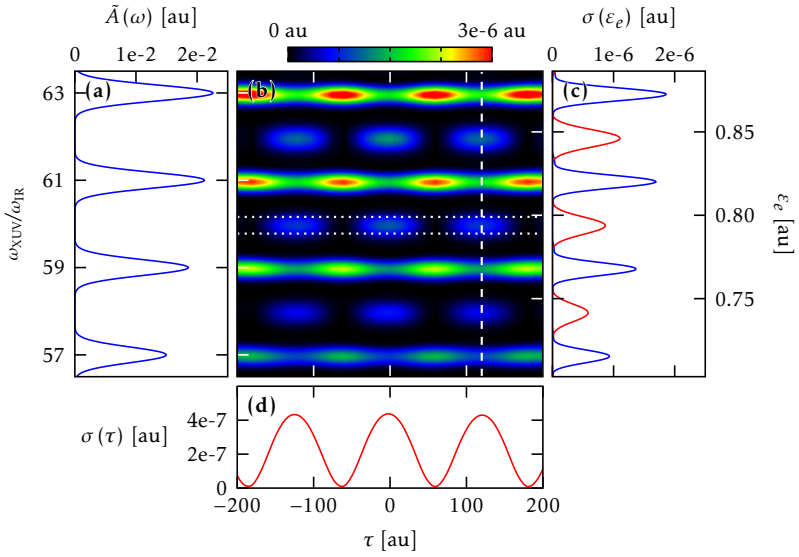


**Figure 3.7:** An illustration of the RABITT spectrum. In (a), the pump APT-XUV used to excite the system (neon) is shown. Together with an IR probe corresponding to its base frequency of $\omega_{IR} = 0.026179$ au and time delay $\tau$, it gives rise to the spectrum shown in (b). A cross section of the spectrum for $\tau = 120$ au (indicated with a dashed line in figure (b)) can be seen in shown in figure (c). It has been separated by total angular momentum $L$, into ${}^1P^o$ (blue) and ${}^1S^e$ and ${}^1D^e$ (red). In (d), the cross section of $SB_{60}$ is shown, integrated over an energy range of 0.01 au (shown in figure (b) with dotted lines).

where the last term corresponds to the interference between the paths (Gruson et al. 2016), and the sideband phase $\Delta\phi_{2n}$ is discussed in detail in section 3.2.1.

These beatings are clearly visible in figure 3.7b, which shows a representative neon RABITT spectrum between $HH_{57}$ and $HH_{63}$; populated by the XUV-APT shown in figure 3.7a. As the IR is shifted in time, the intensity of the sidebands oscillate in an approximately sinusoidal pattern. This is also visible in the cross section of $SB_{60}$ in figure 3.7d.

It has already been mentioned that the sidebands are populated through population transfer from the harmonics. Because of this, the population of the corresponding harmonics is also drained. This gives, as is visible in figure 3.7b,

a sinusoidal pattern also for the harmonic, although one shifted by a phase of $\pi$ so that the harmonic maxima coincide with the sideband minima.

One last, important point is illustrated by figure 3.7: Due to selection rules, the sidebands – ionised via a two-photon process – do not have a dipole beating with the ground state. This is visible in subfigure 3.7c, where a cross section of the spectrum has been divided by total momentum. The sidebands are entirely restricted to the ${}^1S^e$ and ${}^1D^e$ symmetries, the ground state of neon being of symmetry ${}^1S^e$. For this reason, RABITT sidebands are not visible using transient absorption spectroscopy (TAS), which can only directly monitor states with a dipole connection to the ground state (see section 3.4.1 for more details); making it a non-viable method for extracting RABITT spectra. Instead, photo-electron spectroscopy (PES) can be used (Jiménez-Galán et al. 2013), a method described in more detail in section 3.4.2. It is this method which has been used to extract the RABITT spectrum in the present work.

### 3.2.1 The Sideband Phase

The RABITT process as it has been described above can be divided into three steps. First, at a time $t_{\mathrm{XUV}}$, an XUV pump photon is absorbed, populating an intermediate harmonic state of energy $\varepsilon_i$ (and corresponding frequency $\omega_i$). Secondly, it is allowed to evolved freely, until absorbing a second photon, at a time $t_{\mathrm{IR}}$. This absorption is the third step, populating the sideband using an IR probe photon, delayed by a time $\tau$.

The two-photon behaviour is captured by second order perturbation[3] by the interaction Hamiltonian, expressed in the velocity gauge as

$$\hat{\mathcal{H}}_I(t) = \alpha \left[A_{\mathrm{IR}}(t;\tau) + A_{\mathrm{XUV}}(t)\right] \hat{\mathcal{P}}, \tag{3.48}$$

where $\alpha$ is the fine structure constant, $A_{\mathrm{XUV}}(t)$ and $A_{\mathrm{IR}}(t;\tau)$ are the vector potentials of the XUV pump and the IR probe, respectively, and $\hat{\mathcal{P}}$ is the dipole

[3] Time-dependent perturbation theory (TDPT) is described in more detail in appendix B.

operator. In the velocity gauge, this gives the transition amplitude

$$\begin{aligned}\mathcal{A}_{2n} = -i \int\int dt_{\mathrm{IR}}\, dt_{\mathrm{XUV}}\; A_{\mathrm{IR}}(t_{\mathrm{IR}};\tau)\; A_{\mathrm{XUV}}(t_{\mathrm{XUV}}) \\ \times \left\langle \mathrm{SB}_{2n}\right| \alpha\hat{\mathcal{P}}\,\hat{\mathcal{G}}^{+}(t_{\mathrm{IR}} - t_{\mathrm{XUV}})\,\alpha\hat{\mathcal{P}}\left|\psi_0\right\rangle \exp\left(-i\left[\omega_{2n} - \omega_0\right]t\right)\end{aligned} \tag{3.49}$$

between the ground state $\left|\psi_0\right\rangle$ of frequency $\omega_0$, and a final sideband state $\left|\mathrm{SB}_{2n}\right\rangle$ of frequency $\omega_{2n}$ (Jiménez-Galán et al. 2016), where the operator

$$\hat{\mathcal{G}}^{+}(t) = \begin{cases} -i\exp\left(-i\hat{\mathcal{H}}_0 t\right) & ,\ t \geq 0 \\ 0 & ,\ t < 0 \end{cases} \tag{3.50}$$

is known as the retarded Green function and corresponds to both the sequentiality of the processes and the propagation with the field-free, atomic potential $\hat{\mathcal{H}}_0$ between the absorption of the two photons.

In equation 3.49, only paths corresponding to absorption of an XUV photon, followed by absorption or emission by an IR photon is included – paths corresponding to absorption or emission of two IR or XUV photons have been excluded, as have paths which entails the IR photon being emitted or absorbed before that of the XUV.

In the frequency domain, equation 3.49 can be written as

$$\mathcal{A}_{2n} = \int d\varepsilon_i\, \tilde{A}_{\mathrm{IR}}(\omega_{2n} - \omega_i;\tau)\, \tilde{A}_{\mathrm{XUV}}(\omega_i - \omega_0)\, \mathcal{M}^{(2)}_{2n}(\varepsilon_i), \tag{3.51}$$

where $\omega_{2n}$ is the frequency corresponding to the energy of $\mathrm{SB}_{2n}$, $\omega_0$ that corresponding to the ground state frequency, and

$$\mathcal{M}^{(2)}_{2n}(\varepsilon_i) = \left\langle \mathrm{SB}_{2n}\right| \alpha\hat{\mathcal{P}}\,\widetilde{\hat{\mathcal{G}}^{+}}(\varepsilon_i)\,\alpha\hat{\mathcal{P}}\left|\psi_0\right\rangle \tag{3.52}$$

is the two-photon matrix element corresponding to transitions from the ground state to $SB_{2n}$, using the Fourier transform

$$\widetilde{\hat{\mathcal{G}}^{+}}(\varepsilon) = \mathscr{F}\left\{\hat{\mathcal{G}}^{+}(t)\right\} = \frac{1}{\varepsilon - \hat{\mathcal{H}}_0 + i0^{+}}, \tag{3.53}$$

of the retarded Green function. Restricting the integral in equation 3.51 to only considered paths via the nearby harmonics, the corresponding amplitudes

$$\mathcal{A}^{\pm}_{2n} = \int_{\mathrm{HH}_{2n\pm1}} d\varepsilon_i \; \tilde{A}_{\mathrm{IR}}(\omega_{2n} - \omega_i; \tau) \; \tilde{A}_{\mathrm{XUV}}(\omega_i - \omega_0) \; \mathcal{M}^{(2)}_{2n}(\varepsilon_i), \tag{3.54}$$

are derived.

Consider now the interference term of equation 3.47. It can be rewritten explicitly as

$$\mathcal{A}^{-}_{2n}\overline{\mathcal{A}^{+}_{2n}} + \overline{\mathcal{A}^{-}_{2n}}\mathcal{A}^{+}_{2n} = 2\left|\mathcal{A}^{-}_{2n}\mathcal{A}^{+}_{2n}\right|\cos\left(\arg\{\mathcal{A}^{+}_{2n}\} - \arg\{\mathcal{A}^{-}_{2n}\}\right). \tag{3.55}$$

Thus, the frequency and phase of the beatings depend on the phase-difference between the paths. This can be further evaluated by considering $\mathcal{A}^{\pm}_{2n}$.

In order to do so, each harmonic phase is approximated as independent of energy, allowing for the approximation

$$\tilde{A}_{\mathrm{IR}} = \left|\tilde{A}_{\mathrm{IR}}\right| \exp(i\omega_{\mathrm{IR}}\tau) \tag{3.56a}$$

$$\tilde{A}_{2n\pm1} = \left|\tilde{A}_{2n\pm1}\right| \exp(-i\phi_{2n\pm1}) \tag{3.56b}$$

to be made, ignoring the negative-frequency components. The sideband intensity can now be rewritten as

$$I_{2n} = \left|\tilde{A}_{2n-1}\tilde{A}_{\mathrm{IR}}\mathcal{M}^{-}_{2n} + \tilde{A}_{2n+1}\overline{\tilde{A}_{\mathrm{IR}}}\mathcal{M}^{+}_{2n}\right|, \tag{3.57}$$

and the transition amplitudes as

$$\mathcal{A}_{2n}^{\pm} = \exp(\mp i\omega_{\mathrm{IR}}\tau) \times \exp(-i\phi_{2n\pm1}) \times \mathcal{M}_{2n}^{\pm}, \tag{3.58}$$

where

$$\mathcal{M}_{2n}^{\pm} = \int_{\mathrm{HH}_{2n\pm1}} d\omega_i \left|\tilde{A}_{\mathrm{IR}}(\omega_{2n}-\omega_i;0)\,\tilde{A}_{\mathrm{XUV}}(\omega_i-\omega_0)\right| \mathcal{M}_{2n}^{(2)}(\varepsilon_i) \tag{3.59}$$

is the two-photon matrix element corresponding to all different paths from the ground state to $\mathrm{SB}_{2n}$ via $\mathrm{HH}_{2n\pm1}$. The phase

$$\phi_{2n\pm1}^{\mathrm{At}} = -\arg\left\{\mathcal{M}_{2n}^{\pm}\right\}, \tag{3.60}$$

of the matrix element is known as the atomic phase. As is explored in chapter 5, the matrix elements $\mathcal{M}_{2n}^{\pm}$ can be described via approximate models, in order to analytically calculate the atomic phase.

The interference term can now be written as

$$\mathcal{A}_{2n}^{-}\overline{\mathcal{A}_{2n}^{+}} + \overline{\mathcal{A}_{2n}^{-}}\mathcal{A}_{2n}^{+} = 2\left|\mathcal{A}_{2n}^{-}\mathcal{A}_{2n}\right|\cos\left(2\omega_{\mathrm{IR}}\tau + \Delta\phi_{2n}^{\mathrm{APT}} + \Delta\phi_{2n}^{\mathrm{At}}\right), \tag{3.61}$$

where the quantities

$$\Delta\phi_{2n}^{\mathrm{APT}} = \phi_{2n+1} - \phi_{2n-1} \tag{3.62a}$$

$$\Delta\phi_{2n}^{\mathrm{At}} = \phi_{2n+1}^{\mathrm{At}} - \phi_{2n-1}^{\mathrm{At}} \tag{3.62b}$$

are known, respectively, as the spectral phase difference (or attochirp) and the atomic phase difference. As discussed in more detail in chapter 5, the atomic phase varies not only with energy, but also with emission angle (Cirelli et al. 2018; Hammond et al. 2016). This is caused by interference of final symmetries with different angular distributions (Argenti et al. 2017; Heuser et al. 2016).

Here an important digression needs to be made: the definitions introduced in equation 3.62 are not universal. Indeed, several different definitions are used,

including ones relying on inverting the order of the harmonics in equation 3.62 (i.e. $\Delta\phi_{2n}^{\mathrm{APT}} = \phi_{2n-1} - \phi_{2n+1}$ and $\Delta\phi_{2n}^{\mathrm{At}} = \phi_{2n-1}^{\mathrm{At}} - \phi_{2n+1}^{\mathrm{At}}$ [Barreau et al. 2019]) and inverting the sign of the time delay $\tau$ (the sideband beating oscillating as $\cos[2\omega_{\mathrm{IR}}\tau - \Delta\phi_{2n}^{\mathrm{APT}} - \Delta\phi_{2n}^{\mathrm{At}}]$ [Cirelli et al. 2018]). Importantly, *the convention introduced here will be used consistently throughout this thesis*. This is true even when discussing those RABITT studies composing part of this thesis which in the original communication uses a separate convention (i.e., all of them).

The convention in equation 3.62 was selected to satisfy three criteria. The first is to avoid minus signs between the phases in equation 3.61; the second is to keep the spectral phase in equation 3.45 positive; and the third is to keep the definitions of $\Delta\phi_{2n}^{\mathrm{APT}}$ and $\Delta\phi_{2n}^{\mathrm{At}}$ consistent, both being defined as the upper harmonic component minus that of the lower harmonic.

#### Emission Time Delays

As already has been noted, for the slowly varying, many-cycle pulse envelopes used during RABITT, a pulse time-delay is approximately equivalent to a phase shift in the time-domain. In this spirit, the interference term of equation 3.47 can be rewritten as

$$\mathcal{A}_{2n}^{-}\overline{\mathcal{A}_{2n}^{+}} + \overline{\mathcal{A}_{2n}^{-}}\mathcal{A}_{2n}^{+} = 2\left|\mathcal{A}_{2n}^{-}\mathcal{A}_{2n}\right|\cos\left(2\omega_{\mathrm{IR}}\left[\tau - \tau_{2n}\right]\right), \tag{3.63}$$

by introducing (Locher et al. 2015; Lucchini et al. 2015) a photo-emission delay

$$\tau_{2n} = -\frac{\Delta\phi_{2n}}{2\omega_{\mathrm{IR}}}. \tag{3.64}$$

With the two components of $\Delta\phi_{2n}$ defined in equation 3.62, this time-delay can be divided into two components: The attochirp time-delay component,

$$\tau_{2n}^{\mathrm{APT}} = -\frac{\Delta\phi_{2n}^{\mathrm{APT}}}{2\omega_{\mathrm{IR}}}, \tag{3.65}$$

which depends on the APT; and the atomic one,

$$\tau_{2n}^{\mathrm{At}} = -\frac{\Delta\phi_{2n}^{\mathrm{At}}}{2\omega_{\mathrm{IR}}}, \tag{3.66}$$

which depends on the transition matrix elements.

As shown by Dahlström et al. (2013), if the intermediate wave packet is asymptotic, the atomic time-delay can further be divided into two components by considering the two-photon matrix element. The phase of said matrix element, corresponding to an intermediate continuum of angular momentum $\ell_{\mathrm{I}}$, can be written as

$$\arg\left\{\mathcal{M}_{2n}^{\pm,\ell_{\mathrm{I}}}\right\} = \frac{\pi}{2}\left(2-\ell_{\mathrm{I}}\right) + \phi_{\mathrm{cc}}^{2n,\pm} + \eta^{2n\pm1} + \arg\left\{Y_{\ell_{\mathrm{F}}}^{m_0}\left(\hat{\Omega}_{\mathrm{F}}\right)\right\}, \tag{3.67}$$

where $\phi_{\mathrm{cc}}^{2n,\pm}$ arises from the IR-induced continuum-continuum transition in the vicinity of a Coulomb potential; $\eta^{2n\pm1}$ is the scattering phase of the intermediate state; and $Y_{\ell_{\mathrm{F}}}^{m_0}\left(\hat{\Omega}_{\mathrm{F}}\right)$ is the spherical harmonic, associated with the magnetic quantum number $m_0$ of the initial (ground) state and the angular momentum $\ell_{\mathrm{F}}$ of the final state, in the direction $\hat{\Omega}_{\mathrm{F}}$ of the final state electron. Complying with the definition of $\mathcal{M}_{2n}^{\pm}$ in equation 3.59, all quantities in equation 3.67 should be considered as corresponding to the path integrated in energy over the intermediate harmonic.

The atomic time delay is proportional to the phase-difference between the upper and lower harmonic paths to the sideband. Thus, when computing said delay, the only non-vanishing components present in equation 3.67 are those that differ between the two paths, giving the equation

$$\tau_{2n}^{\mathrm{At}} = \frac{\phi_{\mathrm{cc}}^{2n,+} - \phi_{\mathrm{cc}}^{2n,-}}{2\omega_{\mathrm{IR}}} + \frac{\eta^{2n+1} - \eta^{2n-1}}{2\omega_{\mathrm{IR}}}, \tag{3.68}$$

allowing the further division of $\tau_{2n}^{\mathrm{At}}$ into two distinct components. (Dahlström et al. 2012a, 2013)

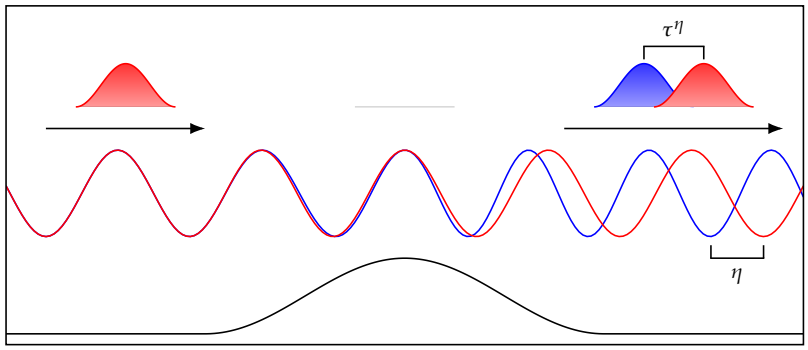


**Figure 3.8:** An illustration of the scattering phase and the associated Wigner time-delay. An incoming plane wave function (red), scattered of a localised potential, will have its phase modified (blue) by a scattering phase $\eta$. For a wave-packet, shown above in the same colors, this corresponds to a time-delay $\tau^\eta$.

The first component,

$$\tau^{\mathrm{cc}}_{2n} = \frac{\phi^{2n,+}_{\mathrm{cc}} - \phi^{2n,-}_{\mathrm{cc}}}{2\omega_{\mathrm{IR}}}, \tag{3.69}$$

is the measurement-induced continuum-continuum delay. The second term,

$$\tau^{\eta}_{2n} = \frac{\eta^{2n+1} - \eta^{2n-1}}{2\omega_{\mathrm{IR}}}, \tag{3.70}$$

originates in the energy-variance of the scattering phase of the intermediate resonance.

In order to further comment on $\tau^{\eta}_{2n}$, it may be useful to consider a related phenomenon – that of electron-scattering. An incoming electron wave of energy $\varepsilon$, scattering of a localised potential, experiences a phase-shift equal to the (scattering-channel dependent) scattering-phase $\eta(\varepsilon)$. This is illustrated for a plane-wave in figure 3.8. As shown by Eisenbud, Smith (1960) and Wigner (1955), this incurs a scattering- (or Wigner) time delay

$$\tau^{\eta}(\varepsilon) = 2\frac{\partial \eta}{\partial \varepsilon} \tag{3.71}$$

of the scattered particle, visualised for a wave-packet in figure 3.8. This time-delay corresponds to the retardation of the electron caused by the interaction with the potential. Such a delay can be negative (in the case of a negative, accelerating potential), but due to sequentiality of the processes, the constraint

$$\tau^{\eta} \geq -\frac{v}{2a} \tag{3.72}$$

is imposed on $\tau^{\eta}$ for the case of a particle of speed $v$ by a localised potential with an effective radius $a$ (Wigner 1955). To rephrase this constraint, it is not possible for the particle to leave the localised potential before entering it.

This can be directly compared to equation 3.70, with the limit

$$\lim_{\omega_{\mathrm{IR}} \to 0} \tau^{\eta}_{2n} \to \frac{1}{2}\tau^{\eta}(\varepsilon_{2n}), \tag{3.73}$$

holding for the sideband energy $\varepsilon_{2n}$ (and infinitely narrow harmonics). Indeed, photoionisation is often referred to as a half-scattering problem. Consequently, $\tau^{\eta}_{2n}$ is considered an effective Wigner time delay (Dahlström et al. 2013; Pazourek et al. 2015).

Two more observations pertinent to the time-delay are worth considering. Firstly, equation 3.67 considers the case of one intermediate scattering continuum. If several intermediate continua are involved, the total contribution of the different continua shoud be considered.

Secondly, equation 3.67 is based on the assumption of the intermediate state being asymptotic. This is not necessarily the case, one counter-example being in the presence of intermediate resonances. This can introduce an additional component to the effective Wigner time-delay, sufficiently negative to violate the constraint in equation 3.72, making the interpretation as a Wigner time-delay highly questionable (Argenti et al. 2017; Sabbar et al. 2015).

## 3.3 Ab-Initio Propagations

A core component of this work is the theoretical study of time-dependent phenomena. Several studies forming part of this thesis utilise accurate, full-electron ab-initio numerical propagations to provide theoretical predictions of the unfolding of such phenomena. In this context, ab-initio refers to time-propagations of a system initially located in the ground state.

All such propagation were carried out in a finite box in the velocity gauge, using PETSc libraries (Balay et al. 1997, 2014). The Krylov method described below, utilised in the ab-initio propagations of Petersson et al. (2017), was implemented using LAPACK libraries (Anderson et al. 1999). This section outlines the details of the numerical methods employed to this end.

The propagator is constructed from the time-dependent Schrödinger equation (TDSE),

$$i\frac{\partial}{\partial t}\Big|\Psi(t)\Big\rangle = \hat{\mathcal{H}}(t)\Big|\Psi(t)\Big\rangle, \tag{3.74}$$

where $\Big|\Psi(t)\Big\rangle$ is the state ket, and $\hat{\mathcal{H}}(t)$ the Hamiltonian, both at time $t$. The solution to this equation can be written as

$$\Big|\Psi(t+dt)\Big\rangle \approx \exp\Big[-i\,dt\,\hat{\mathcal{H}}(t)\Big]\Big|\Psi(t)\Big\rangle, \tag{3.75}$$

for sufficiently small step sizes $dt$. From this, an infinitesimal time propagation operator

$$\hat{\mathcal{U}}(t;dt) = \exp\Big[-i\,dt\hat{\mathcal{H}}(t)\Big], \tag{3.76}$$

can be defined.

In order to further study the time propagation operator $\hat{\mathcal{U}}(t;dt)$, consider the Hamiltonian, $\hat{\mathcal{H}}(t)$, itself. A more complete treatment of the basis can be found in chapter 4. Here, it will suffice to briefly describe the different components making up the Hamiltonian.

The first component, denoted $\hat{\mathcal{H}}_0$, is the time-independent Hamiltonian corresponding to the kinetic energy and atomic potential. It is the basis of size $N$ of the orthonormal eigenkets of this operator, $\left|\psi_i\right\rangle$, $i \in \{0, 1, \ldots, N-1\}$, with corresponding eigenenergies $\varepsilon_i$ and eigenfrequencies $\omega_i$, in which the propagation is performed.

Secondly, a component corresponding to the interaction with the field is included. Using the dipole approximation in the velocity gauge, this component can be written as $\alpha A(t)\hat{\mathcal{P}}$; where $\alpha$ is the fine structure constant, $A(t)$ the field vector potential, and $\hat{\mathcal{P}}$ the dipole in the direction of the field.

As the propagations take place in a finite box, some boundary conditions need to be enforced for a maximum radius $R_{\max}$. As such boundary conditions are unphysical, they may cause equally unphysical reflections. For this reason, the third and final component of the Hamiltonian, a complex absorption potential (CAP) $\hat{\mathcal{V}}_{\text{CAP}}$, is introduced. This potential is designed to absorb the state population near the boundary of the box, to avoid the aforementioned unphysical reflections.

Dividing $\hat{\mathcal{H}}(t)$ into its different components, it can be written as

$$\hat{\mathcal{H}}(t) = \hat{\mathcal{H}}_0 + \alpha A(t)\hat{\mathcal{P}} + \hat{\mathcal{V}}_{\text{CAP}}, \tag{3.77}$$

at a given time $t$. Inserting equation 3.77 into equation 3.76 results in the step operator

$$\hat{\mathcal{U}}(t; dt) \approx \exp\left(-i\,dt\left[\hat{\mathcal{H}}_0 + \alpha A(t)\hat{\mathcal{P}} + \hat{\mathcal{V}}_{\text{CAP}}\right]\right). \tag{3.78}$$

For two operators $\hat{\mathcal{A}}$ and $\hat{\mathcal{B}}$, the relation $e^{\hat{\mathcal{A}}+\hat{\mathcal{B}}} = e^{\hat{\mathcal{A}}}e^{\hat{\mathcal{B}}}$, which holds for scalar exponents, is generally only satisfied if $\hat{\mathcal{A}}$ and $\hat{\mathcal{B}}$ commute. However, the

midpoint, split operator approximation

$$\hat{\mathcal{U}}(t;dt) \approx \exp\left[-i\,dt\,\hat{\mathcal{V}}_{\text{CAP}}\right] \tag{3.79a}$$

$$\times \exp\left[-i\frac{dt}{2}\hat{\mathcal{H}}_0\right] \tag{3.79b}$$

$$\times \exp\left[-i\,dt\,A\left(t+\frac{dt}{2}\right)\hat{\mathcal{P}}\right] \tag{3.79c}$$

$$\times \exp\left[-i\frac{dt}{2}\hat{\mathcal{H}}_0\right] \tag{3.79d}$$

can be made, allowing the propagation to be done sequentially for each operator. If $\hat{\mathcal{V}}_{\text{CAP}} = \hat{\emptyset}$ equals the null operator, the splitting is a second order approximation and is known as a Strang (1968) splitting. The splitting with the $\hat{\mathcal{V}}_{\text{CAP}}$ operator, on the other hand, is a first order approximation. However, as the purpose of the CAP is to pragmatically counter reflections in the region of the box boundaries, rather than to accurately represent the complex electron dynamics close to the core (where $\hat{\mathcal{V}}_{\text{CAP}} = \hat{\emptyset}$), this is of lesser importance. The order of the respective splittings can be derived at using Taylor expansions, as is show in section C.1.

Precision of approximation methods aside, the philosophy behind equation 3.79 can be described as follows: Since the field-interaction operator is the only time-dependent component of the propagation, it is computed in the middle of the time step – first half the field-free propagation is performed, then, before the other half is performed, the field-interaction step operator is applied. At the end of each time step, the CAP cleans up the population found near the box border.

The time step operator has thus been defined using three main components. The first, corresponding to equation 3.79a, is the CAP, which is introduced to prevent reflections. Secondly there is the field-free component, divided into equations 3.79b and 3.79d, which each correspond to half of the propagation

using the atomic- and box potential. Finally, shown in equation 3.79c is the driven component, corresponding to the interaction with the field. More information about each part of the time-step operator, listed in the order to which they are applied to $\left|\Psi(t)\right\rangle$, can be found in sections 3.3.1 to 3.3.3.

### 3.3.1 Field-Free Propagation

The first component of the propagator to be considered is the one corresponding to the box potential – here dubbed the field-free component. Having already been introduced in equations 3.79b and 3.79d, this time-independent component of the propagator is written as

$$\hat{\mathcal{U}}_{\mathrm{FF}}(dt) = \exp\left(-i\,dt\,\hat{\mathcal{H}}_0\right). \tag{3.80}$$

Inserting the identity operator $\hat{\mathcal{I}}$ into the Maclaurin expansion of $\hat{\mathcal{U}}_{\mathrm{FF}}(dt)$ in the basis of $\hat{\mathcal{H}}_0$ eigenstates gives the expression

$$\begin{aligned}
\hat{\mathcal{U}}_{\mathrm{FF}}(dt)\,\hat{\mathcal{I}}\left|\Psi(t)\right\rangle &= \sum_{j=0}^{N-1}\sum_{k=0}^{\infty}\frac{(-i\,dt)^k}{k!}\hat{\mathcal{H}}_0^k\left|\psi_j\right\rangle\!\left\langle\psi_j\right|\Psi(t)\right\rangle \\
&= \sum_{j=0}^{N-1}\sum_{k=0}^{\infty}\frac{(-i\,dt)^k}{k!}\,\omega_j^k\left|\psi_j\right\rangle\!\left\langle\psi_j\right|\Psi(t)\right\rangle. \\
&= \sum_{j=0}^{N-1}\exp\left(-i\,dt\,\omega_j\right)\left|\psi_j\right\rangle\!\left\langle\psi_j\right|\Psi(t)\right\rangle
\end{aligned} \tag{3.81}$$

Since the ab-initio calculations are performed in the eigenbasis of $\hat{\mathcal{H}}_0$ of size $N$, spanned by the orthonormal eigenkets $\left|\psi_i\right\rangle$ with the corresponding eigenfrequencies $\omega_i$; it becomes clear that $\hat{\mathcal{U}}_{\mathrm{FF}}(dt)$ can be applied ket-wise, via multiplication of a set of $N$ scalars $\exp\left(-i\,dt\,\omega_j\right)$, where $j \in \{0,1,\ldots,N-1\}$. The time complexity of this method is treated in appendix C.2.1.

### 3.3.2 Field-Driven Propagation

Presently consider the field-interaction operator

$$\hat{\mathcal{U}}_{\mathrm{I}}(t;dt) = \exp\left[-i\,dt\,\alpha A\left(t+\frac{dt}{2}\right)\hat{\mathcal{P}}\right], \tag{3.82}$$

shown above in equation 3.79c. There are two reasons why propagation using this operator is more complex than the field-free propagation. Firstly, the exponent of the propagator is dependent on the field. This means that the operator needs to be recalculated every time the field strength changes. Secondly, since the propagation is not carried out in the basis of $\hat{\mathcal{P}}$, it cannot be performed for $\hat{\mathcal{U}}_{\mathrm{I}}(t;dt)$ in the same, simple eigvalue-wise manner as for $\hat{\mathcal{U}}_{\mathrm{FF}}(dt)$.

Below, two methods for solving this problem are presented, one using a Krylov method approximation and the other using an exact solution. The respective time complexities of both these methods are considered and compared in appendix C.2.2.

#### Using a Krylov Method

The first method used in this thesis (Petersson et al. 2017) to calculate the field-driven propagation employs what is known as a Krylov method (Saad 1992). In order to apply $\hat{\mathcal{U}}_{\mathrm{I}}(t;dt)$ to $\left|\Psi(t)\right\rangle$, an orthonormal set of kets

$$\begin{cases} \left|\xi_i\right\rangle = \dfrac{1}{N_i}\,\left|\Psi(t)\right\rangle & ,\ i=0 \qquad (3.83a) \\ \left|\xi_i\right\rangle = \dfrac{1}{N_i}\left(\left|\xi_i'\right\rangle - \displaystyle\sum_{j=0}^{i-1}\left|\xi_j\right\rangle\!\left\langle\xi_j\middle|\xi_i'\right\rangle\right) & ,\ i>0 \qquad (3.83b) \end{cases}$$

is defined, where $N_i$ are normalisation constants and the non-orthonormal help kets

$$\left|\xi_i'\right\rangle = -i\,dt\,\alpha A\left(t+\frac{dt}{2}\right)\hat{\mathcal{P}}\left|\xi_{i-1}\right\rangle \tag{3.84}$$

are used. The subspace spanned by the first $n$ of the kets defined in equation 3.83, $\mathcal{K}_n$, is known as the Krylov subspace of order $n$. It should be noted that

$$\forall j \in \{0,1,\ldots,n-1\} \;:\; \left[-i\,dt\,\alpha A\left(t+\frac{dt}{2}\right)\hat{\mathcal{P}}\right]^j \left|\Psi(t)\right\rangle \in \mathcal{K}_n, \tag{3.85}$$

follows from the definition of the $\mathcal{K}_n$.

Using the Maclaurin expansion

$$\exp\left[-i\,dt\,\alpha A\left(t+\frac{dt}{2}\right)\hat{\mathcal{P}}\right] = \sum_{j=0}^{\infty}\frac{\left[-i\,dt\,\alpha A\left(t+\frac{dt}{2}\right)\right]^j}{j!}\hat{\mathcal{P}}^j, \tag{3.86}$$

it becomes clear from equation 3.85 that $\left|\Psi(t)\right\rangle$ and $\hat{\mathcal{U}}_{\mathrm{I}}(t;dt)\left|\Psi(t)\right\rangle$ are both contained within $\mathcal{K}_\infty$. The result of the application of the propagator on the state vector can therefore be represented entirely as a linear combination of Krylov vectors. Further more, it also becomes clear that the approximative *nth* partial sum of the Maclaurin expansion,

$$\exp\left[-i\,dt\,\alpha A\left(t+\frac{dt}{2}\right)\hat{\mathcal{P}}\right] \approx \sum_{j=0}^{n}\frac{\left[-i\,dt\,\alpha A\left(t+\frac{dt}{2}\right)\right]^j}{j!}\hat{\mathcal{P}}^j, \tag{3.87}$$

is contained within $\mathcal{K}_{n+1}$. This approximation can be rewritten as

$$\hat{\mathcal{U}}_{\mathrm{I}}^n(t;dt) \;=\; \sum_{i=0}^{n-1}\sum_{j=0}^{n-1}\left|\xi_i\right\rangle\!\left\langle\xi_i\right|\hat{\mathcal{U}}_{\mathrm{I}}(t;dt)\left|\xi_j\right\rangle\!\left\langle\xi_j\right| \tag{3.88}$$

by inserting the minimal identity operator in $\mathcal{K}_n$ on both sides of $\hat{\mathcal{U}}_{\mathrm{I}}(t;dt)$. Applying $\hat{\mathcal{U}}_{\mathrm{I}}^n(t;dt)$ to $\left|\Psi(t)\right\rangle$ and using $\left\langle\xi_i\middle|\Psi(t)\right\rangle = \delta_{i,0}$, where $\delta_{i,j}$ is the Kronecker

delta, gives

$$\hat{\mathcal{U}}_{\mathrm{I}}^{n}(t;dt)\left|\Psi(t)\right\rangle = \sum_{j=0}^{n-1}\left|\xi_j\right\rangle\left\langle\xi_j\right|\hat{\mathcal{U}}_{\mathrm{I}}(t;dt)\left|\xi_0\right\rangle. \tag{3.89}$$

The exponent of $\hat{\mathcal{U}}_{\mathrm{I}}(t;dt)$ is easily projected onto $\mathcal{K}_n$. Indeed, the relation

$$\left\langle\xi_j\right| - i\,dt\,\alpha A\left(t+\tfrac{dt}{2}\right)\hat{\mathcal{P}}\left|\xi_i\right\rangle = \begin{cases} \left\langle\xi_j\middle|\xi_i'\right\rangle\,, & j \le i & \text{(3.90a)}\\ N_{i+1} \quad\,, & j = i+1 & \text{(3.90b)}\\ 0 \qquad\,, & j > i+1 & \text{(3.90c)}\end{cases}$$

of the relevant operator elements follows directly from equations 3.83 and 3.84! With this in mind, it is possible to efficiently (depending on the order $n$ of $\mathcal{K}_n$) build and diagonalise the operator

$$-i\,dt\,\alpha A\left(t+\frac{dt}{2}\right)\hat{\mathcal{P}} \approx \sum_{i=0}^{n-1}\lambda_{nt,i}\left|\alpha_{nt,i}\right\rangle\left\langle\alpha_{nt,i}\right| \tag{3.91}$$

into eigenvalues $\lambda_{nt,i}$ and eigenkets $\left|\alpha_{nt,i}\right\rangle$ in the Krylov subspace of order $n$ at time $t$. Equation 3.89 can then be rewritten as

$$\hat{\mathcal{U}}_{\mathrm{I}}^{n}(t;dt)\left|\Psi(t)\right\rangle = \sum_{i=0}^{n-1}\sum_{j=0}^{n-1}e^{\lambda_{nt,j}}\left|\xi_i\right\rangle\left\langle\xi_i\middle|\alpha_{nt,j}\right\rangle\left\langle\alpha_{nt,j}\middle|\xi_0\right\rangle, \tag{3.92}$$

which is the form of the equation used during the numerical calculations.

**Convergence of the Krylov Subspace** The accuracy of the above described method is highly dependent on the number of terms included in the Maclaurin expansion 3.87, and therefore also on the order $n$ of $\mathcal{K}_n$. This means that the accuracy of the method increases with $n$, giving an incentive to increase the order of the $\mathcal{K}_n$. But this is not the only factor in play – the computational cost must also be considered. Indeed, the very purpose of employing a Krylov

method is to avoid diagonalising, at each time step, the exponent of $\hat{\mathcal{U}}_{\mathrm{I}}(t;dt)$ in too large a basis. It is also important to limit the number of Krylov vectors created; this since their creation, and projecting the exponent of $\hat{\mathcal{U}}_{\mathrm{I}}(t;dt)$ onto the space they span, requires computational time. Because of this, two criteria, to be discussed below, for the convergence of the $\mathcal{K}_n$ were defined. The subspace $\mathcal{K}_n$ is considered as having converged after one or both of these criteria are fulfilled.

Discussion of the first convergence test should be prefaced by the note that the Krylov subspace of size $n$ has converged completely when $\mathcal{K}_n = \mathcal{K}_{n+1}$. In this limit, $\left|\xi_n\right\rangle$, used to define $\mathcal{K}_{n+1} \cap \mathcal{K}_n^{\perp}$, tends towards the null ket $\left|0\right\rangle$. The equivalent limit of $N_n$ is $N_n \to 0$. At this point, further increasing the size of the Krylov space is redundant.

Indeed, choosing $dt$ correctly, a larger Krylov space would not yield a significant improvement in precision, even for small, non-zero values of $N_n$. Choosing $dt$ so that the relation

$$\forall j : \left| -i\,dt\,\alpha A\left(t + \frac{dt}{2}\right)\lambda_j \right| \ll 1, \tag{3.93}$$

where $\lambda_j,\ j \in \{0, 1, \ldots, N-1\}$ are the eigenvalues of $\hat{\mathcal{P}}$, is valid for the exponent of $\hat{\mathcal{U}}_{\mathrm{I}}(t;dt)$; the effect of each extra term included in the Krylov expansion is significantly smaller than that of the last. Thus, if $N_n$ is very small, increasing the order of the Krylov space will scarcely improve accuracy.

The first convergence criterion is defined accordingly:

*The Krylov space $\mathcal{K}_n$ is considered to have converged if*

$$N_n < e^1_{\mathrm{lim}}, \tag{3.94}$$

*where the real, positive $e^1_{\mathrm{lim}} \approx 0$ is the limit below which $N_n$ is approximated as 0.*

The second convergence criterion is arrived at from the opposite perspective –

instead of being based on the part of the Maclaurin expansion yet to be added, the part already calculated is considered.

It has already been commented upon that for sufficiently small values of $dt$ (or, equivalently, sufficiently small exponents of $\hat{\mathcal{U}}_{\mathrm{I}}(t;dt)$), increasing the order of $\mathcal{K}_n$ will only provide a correction of much smaller magnitude than the changes to $\left|\Psi(t)\right\rangle$ that can already be performed in $\mathcal{K}_n$.

Therefore, if $\left|\Psi(t)\right\rangle$ remains essentially unchanged after applying the *nth* partial sum of the Maclaurin expansion, it can be assumed that further expanding $\mathcal{K}_n$ will have little to no effect. This is the basis for the second convergence criterion:

*Denote the change to* $\left|\Psi(t)\right\rangle$ *due application of* $\hat{\mathcal{U}}_I^n(t;dt)$ *as*

$$\left|\delta\Psi^n(t)\right\rangle = \left[\,\hat{\mathcal{U}}_I^n(t;dt) - \hat{\mathcal{I}}\,\right]\left|\Psi(t)\right\rangle. \tag{3.95}$$

*The Krylov space* $\mathcal{K}_n$ *is considered to have converged if the norm of* $\left|\delta\Psi^n(t)\right\rangle$ *fulfills the relation*

$$\left\langle\delta\Psi^n(t)\middle|\delta\Psi^n(t)\right\rangle < e_{\mathrm{lim}}^2, \tag{3.96}$$

*for a real, positive threshold* $e_{\mathrm{lim}}^2 \approx 0$.

Finally, it should be mentioned that a maximum dimension $n_{\mathrm{max}}$ is imposed. If $\mathcal{K}_{n_{max}}$ fulfills neither of the aforementioned criteria, the method is considered as not having converged, and returns an error[4].

#### Exact Solution

The major complication with the laser-interaction component of the propagation results from $\hat{\mathcal{P}}$ not being diagonal in the basis used for propagation. Because of this, the exponent of $\hat{\mathcal{U}}_{\mathrm{I}}(t;dt)$, $-i\,dt\,\alpha A\left(t+\frac{dt}{2}\right)\hat{\mathcal{P}}$, needs to be diagonalised

[4]For all studies discussed in this thesis, $n_{max} = 21$, and $e_{\mathrm{lim}}^1 = e_{\mathrm{lim}}^2 = 10^{-20}$. Orders $n > 7$ of $\mathcal{K}_n$ were seldom used.

prior to applying the propagation operator. However, since the only non-scalar component of said exponent is $\hat{\mathcal{P}}$, its eigenbasis is the same as that of $\hat{\mathcal{P}}$. In light of this, the Krylov-method described above is cast in a rather absurd light – its purpose is simply to diagonalise the time-independent operator $\hat{\mathcal{P}}$ in a different basis at each time step.

Such a diagonalisation, even in the comparatively large eigenbasis of $\hat{\mathcal{H}}_0$ (used for propagation), could instead be performed prior to performing the propagations. Thus, by writing $\hat{\mathcal{P}}$ using its orthonormal eigenkets $\left|\alpha_i\right\rangle$ and corresponding eigenvalues $\lambda_i$,

$$\hat{\mathcal{P}} = \sum_{i=0}^{M-1} \lambda_i \left|\alpha_i\right\rangle\!\left\langle\alpha_i\right|, \tag{3.97}$$

where $M$ is the size of the eigenbasis of $\hat{\mathcal{P}}$, a second solution emerges. Using this form, and the orthonormality of the eigenkets $\left|\alpha_i\right\rangle$, the Maclaurin expansion of the propagation operator can be expanded as

$$\begin{aligned}
\hat{\mathcal{U}}_{\mathrm{I}}(t;dt) - \hat{\mathcal{I}} &= \left( \sum_{j=0}^{\infty} \frac{\left[-i\,dt\,\alpha A\left(t+\frac{dt}{2}\right)\right]^j}{j!} \hat{\mathcal{P}}^j \right) - \hat{\mathcal{I}} \\
&= \sum_{k=0}^{M-1} \sum_{j=1}^{\infty} \frac{\left[-i\,dt\,\alpha A\left(t+\frac{dt}{2}\right)\right]^j}{j!} \lambda_k^j \left(\left|\alpha_k\right\rangle\!\left\langle\alpha_k\right|\right)^j \quad , \\
&= \sum_{k=0}^{M-1} \left|\alpha_k\right\rangle \left\{ \exp\left[-i\,dt\,\alpha A\left(t+\frac{dt}{2}\right)\lambda_k\right] - 1 \right\} \left\langle\alpha_k\right|
\end{aligned} \tag{3.98}$$

where $\hat{\mathcal{I}}$ is the identity operator. This gives an expression analogous to equation 3.81, and the propagator can be rewritten as

$$\hat{\mathcal{U}}_{\mathrm{I}}(t;dt) = \hat{\mathcal{I}} + \sum_{j=0}^{M-1} \left|\alpha_j\right\rangle \left\{ \exp\left[-i\,dt\,\alpha A\left(t+\frac{dt}{2}\right)\lambda_j\right] - 1 \right\} \left\langle\alpha_j\right|. \tag{3.99}$$

This means that, after diagonalising $\hat{\mathcal{P}}$, the state ket can be projected onto the basis of $\hat{\mathcal{P}}$, propagated via ket-wise multiplication of a set of $M$ time-dependent scalars, and then be projected back.

### 3.3.3 Complex Absorption Potential

After an electron breaks free of the atomic potential, its wave function will diffuse away from the atom indefinitely. In practice, however, it is impossible to simulate an infinite system, and thus it is necessary to limit the radial basis.

Since only the dynamics of the electrons in the atom are of interest, the basis is restricted to a box defined by a maximum distance from the origin. This does however present a problem, as the box boundaries, here introduced using the Dirichlet boundary condition

$$\left\langle r = R_{\max} \middle| \Psi(dt) \right\rangle = 0, \tag{3.100}$$

for the distance $r$ to the nucleus can cause unphysical reflections. To avoid this, a Complex Absorption Potential (CAP) $\hat{\mathcal{V}}_{\text{CAP}}$ is introduced, corresponding to a time-independent propagation operator

$$\hat{\mathcal{U}}_{\text{CAP}}(dt) = \exp\left(-i\,dt\,\hat{\mathcal{V}}_{\text{CAP}}\right), \tag{3.101}$$

according to equation 3.79a, in order to absorb the wave function near the border of the box, consequently minimising reflections. In this work $\hat{\mathcal{V}}_{\text{CAP}}$ is structured as

$$\hat{\mathcal{V}}_{\text{CAP}} = \sum_{\alpha,i} \int_0^\infty dr_i \; v(r_i) \left|\alpha, r_i\right\rangle\!\left\langle \alpha, r_i\right|, \tag{3.102}$$

where $r_i$ is the distance $r$ of the $ith$ active electron from the core, and $\alpha$ is the scattering channel. The function $v(r)$ is chosen as

$$v(r) = \begin{cases} 0, \ r \leq R_{\text{CAP}} \\ c_{\text{CAP}} (r - R_{\text{CAP}})^2, \ r > R_{\text{CAP}} \end{cases}, \tag{3.103}$$

and contains two adjustable coefficients, a radius $R_{\text{CAP}}$ and complex constant $c_{\text{CAP}}$, which are equal for all electrons.With this value of $v(r)$, $\hat{\mathcal{V}}_{\text{CAP}}$ corresponds to a quadratic, spherically symmetric potential starting at $r = R_{\text{max}}$. It fulfills the criterion of continuity of $v(r)$ and $\frac{\partial}{\partial r} v(r)$ in order avoid causing unphysical reflections.

In order to further study the CAP, consider the eigenkets $\left|\psi_i^Q\right\rangle$, with the corresponding eigenenergies $\varepsilon_i^Q$ and eigenfrequencies $\omega_i^Q$, of what is known as the quenched Hamiltonian, $\hat{\mathcal{H}}_Q$, defined as

$$\hat{\mathcal{H}}_Q = \hat{\mathcal{H}}_0 + \hat{\mathcal{V}}_{\text{CAP}}. \tag{3.104}$$

Since $\hat{\mathcal{H}}_0$, being a Hamiltonian operator, is Hermitian, its eigenvalues are real, along with any expectation value $\left\langle \hat{\mathcal{H}}_0 \right\rangle$. However, since $\hat{\mathcal{V}}_{\text{CAP}}$ is not a physical potential, but rather a theoretical construct designed to minimise numerical artifacts, it does not need to obey such rules. This allows for the possibility of non-real eigenenergies of $\hat{\mathcal{H}}_Q$. Defining the real, non-negative scalar

$$\rho_i^{\text{CAP}} = \sum_{\alpha} \sum_{j} \int_{R_{\text{CAP}}}^{\infty} dr_j \left(r_j - R_{\text{CAP}}\right)^2 \left|\left\langle \alpha, r_j \middle| \psi_i^Q \right\rangle\right|^2, \tag{3.105}$$

describing the overlap between the CAP and $\left|\psi_i^Q\right\rangle$; the imaginary part of $\varepsilon_i^Q$ can be calculated as

$$\begin{aligned}\mathrm{Im}\left\{\varepsilon_i^Q\right\} &= \mathrm{Im}\left\{\left\langle\psi_i^Q\middle|\hat{\mathcal{H}}_Q\middle|\psi_i^Q\right\rangle\right\} \\ &= \mathrm{Im}\left\{\left\langle\psi_i^Q\middle|\hat{\mathcal{V}}_{\mathrm{CAP}}\middle|\psi_i^Q\right\rangle\right\}, \\ &= \mathrm{Im}\left\{c_{\mathrm{CAP}}\right\}\rho_i^{\mathrm{CAP}}\end{aligned} \tag{3.106}$$

which only has an imaginary contribution if $c_{\mathrm{CAP}}$ does.

The norm of given eigenket of $\hat{\mathcal{H}}_Q$ is modified by a factor

$$\sqrt{\frac{\left|\left\langle\psi_i^Q\middle|\hat{\mathcal{U}}_{\mathrm{CAP}}^\dagger(dt)\hat{\mathcal{U}}_{\mathrm{CAP}}(dt)\middle|\psi_i^Q\right\rangle\right|}{\left|\left\langle\psi_i^Q\middle|\psi_i^Q\right\rangle\right|}} = \exp\left(dt\,\mathrm{Im}\left\{c_{\mathrm{CAP}}\right\}\rho_i^{\mathrm{CAP}}\right) \tag{3.107}$$

with each application of $\hat{\mathcal{U}}_{\mathrm{CAP}}(dt)$. Selecting $\mathrm{Im}\{c_{\mathrm{CAP}}\} < 0$, it can thus be seen that $\hat{\mathcal{U}}_{\mathrm{CAP}}(dt)$ gradually drains the states which overlap the CAP.

The eigenvalues of $\hat{\mathcal{H}}_Q$ for one case where $\mathrm{Im}\{c_{\mathrm{CAP}}\} < 0$ are shown in figure 3.9. Electrons in bound states and autoionising resonances are mainly restricted to positions near the atomic core. Because of this they barely overlap with the CAP, and the perturbation of these states due to $\hat{\mathcal{V}}_{\mathrm{CAP}}$ is minimal. This is visible in figure 3.9, where for these states, located below each ionisation threshold, the imaginary part of $\varepsilon_i^Q$ is zero for the bound states and small for the autoionizing resonances.

This can also be conceptualized as follows: The complex part of the CAP represents the possibility of one or more electrons[5] leaving the studied system. This is easily understood when considering that the CAP causes the disappearance of electrons approaching the box boundary, rather than allowing them to be reflected back. As shown by equation 3.107, the rate of disappearance is proportional to the imaginary part of the energy eigenvalue. As a bound electron never may leave the atom, the negative part of their corresponding

[5] In this thesis, only one-electron ionisation is considered.

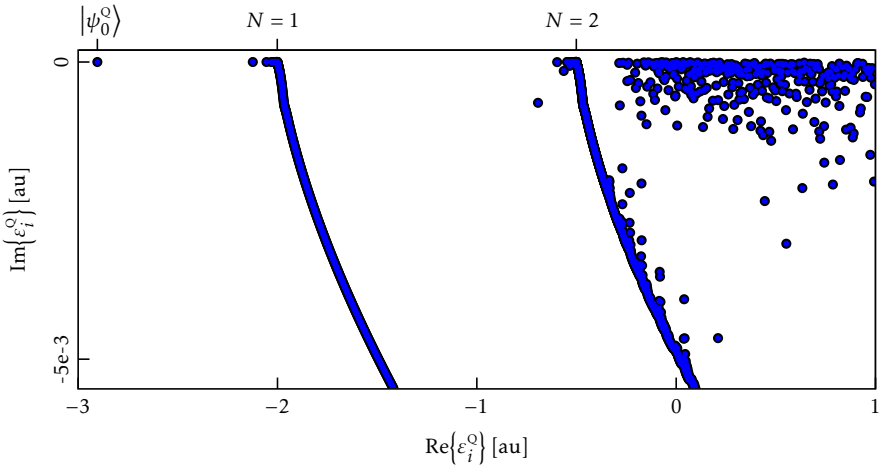


**Figure 3.9:** The location of the energy eigenvalues of the quenched Hamiltonian of helium in the complex plane, for the basis used in (Petersson et al. 2017); where $R_{\max} = 1200$, and the CAP coefficients are $R_{\mathrm{CAP}} = 1000$, and $c_{\mathrm{CAP}} = -(1+5i)\times 10^{-4}$. The energies of the groundstate, $|\psi_0^Q\rangle$, and the first and second thresholds, $N = 1$ and $N = 2$, have been marked.

quenched energy eigenvalues should be zero. Autoionising states, however, decay into the continuum, having a lifetime inversely proportional to their widths Γ (Ott et al. 2013, 2014), and thus have a negative component – albeit one small enough to barely be noticeable in figure 3.9.

Now consider the continuum states. After each ionisation threshold, several series of such states are present, each corresponding to a scattering channel. These have a significant imaginary component to their energy, increasing with the electron energy. Using the same conceptualisation as used for the bound and autoionising states, the imaginary part is proportional to the speed at which the electron leaves the system. For a free electron, this view implies the proportionality

$$\mathrm{Im}\left\{\varepsilon^Q\right\} \propto v_e = \sqrt{2\,\varepsilon_{kin}^Q} \tag{3.108}$$

between the imaginary part of the electron energy $\varepsilon^Q$ and speed $v_e$; with $v_e$ also

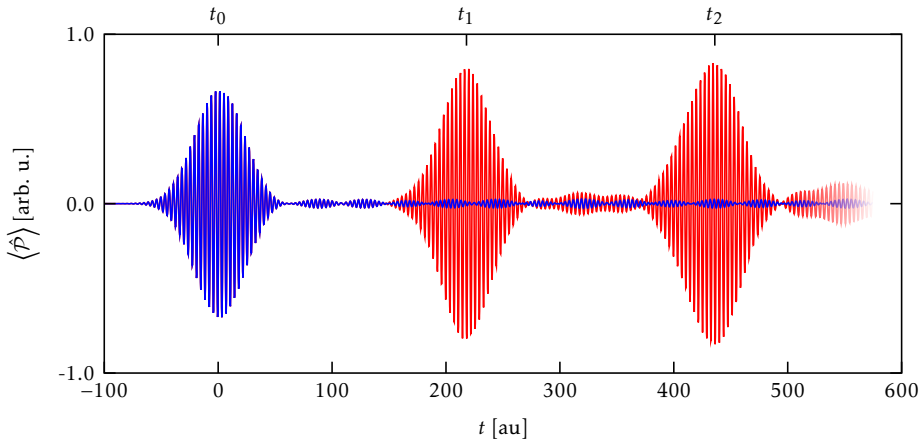


**Figure 3.10:** An illustrative example of the effect of the CAP, exemplified by its effects on the dipole expectation value $\langle\hat{\mathcal{P}}\rangle$ as a function of time. A short, weak XUV pulse centered at time $t = t_0$ excites Neon from the ground state in a small box of $R_{\max} = 150$. In red, the evolution of $\langle\hat{\mathcal{P}}\rangle$ for the case when no CAP is used is shown; whereas in blue, the corresponding data is shown for the case of when a CAP defined by $R_{\text{CAP}} = 100$ and $c_{\text{CAP}} = -(1 + 5i) \times 10^{-4}$. As the system evolves, reflections are visible at times near $t = t_1$ and $t = t_2$ when no filter is used.

implicitly the square root of the electron kinetic energy $\varepsilon^{\text{Q}}_{kin}$. Since the $\varepsilon^{\text{Q}}_{kin}$ is the energy of the electron above the threshold, $\text{Im}\{\varepsilon^{\text{Q}}\} \propto \langle\hat{\mathcal{V}}_{\text{CAP}}\rangle$ will increase with the energy. This is also illustrated in figure 3.9.

A real component can also be introduced to $c_{\text{CAP}}$ to further adjust the potential. Adding a negative real part of $c_{\text{CAP}}$, as is the case in figure 3.9, will for distances above $R_{\max}$ from the core create a negative potential, increasing in magnitude as the distance from the core increases. This will accelerate, away from the core, electrons appearing at these radii, further preventing reflections.

The effects of the filters are illustrated in figure 3.10, where the effects of the CAP on the evolution of the dipole expectation value are shown. After the system is excited, the part of the electron wave function which is found in autoionising and continuum states travels away from the atomic nucleus. After reaching the box boundary, it is either absorbed by the CAP or reflected back.

These reflections cause the discrepancy between the two curves emerging at times around $t = t_1$. After each time it has been reflected back and passes the nucleus, the wave function is once again reflected by the boundary. This is the cause of the periodicity of the reflections shown in figure 3.10.

In this thesis $\hat{\mathcal{U}}_{\text{CAP}}(dt)$ is implemented in a manner analogous to the exact solution to the driven part of the TDSE, shown in equation 3.99. The derivation of said equation need not be repeated here; instead, it suffices to repeat that by diagonalising $\hat{\mathcal{V}}_{\text{CAP}}$ in the basis of $\hat{\mathcal{H}}_0$ as

$$\hat{\mathcal{V}}_{\text{CAP}} = \sum_{i=0}^{K-1} \xi_i \left|\chi_i\right\rangle\!\left\langle\chi_i\right|, \tag{3.109}$$

to get its $K$ eigenkets $\left|\chi_i\right\rangle$ and corresponding eigenvalues $\xi_i$, it is possible to write the CAP propagation operator as

$$\hat{\mathcal{U}}_{\text{CAP}}(dt) = \hat{\mathcal{I}} + \sum_{j=0}^{K-1} \left|\chi_j\right\rangle\!\left\{ \exp\left(-i\,dt\,\xi_j\right) - 1 \right\}\!\left\langle\chi_j\right|. \tag{3.110}$$

Like for the case of $\hat{\mathcal{U}}_{\text{I}}(t; dt)$, the state ket can be projected onto the basis of $\hat{\mathcal{V}}_{\text{CAP}}$, then propagated via ket-wise multiplication by a series of $K$ scalars, before being projected back. One difference that does exist is that the relevant scalars are not time-dependent, and need not be recalculated every time step. The time complexity of the application of $\hat{\mathcal{U}}_{\text{CAP}}(dt)$ is treated in appendix C.2.3.

## 3.4 Extracting Observables

This thesis treats electron dynamics in atomic systems. Section 3.3 outlines the numerical ab-initio methodology by which such dynamics are described in this work. By itself, however, such calculations give only an incomplete picture of the experimental procedure – after the dynamics have been allowed to run their course, there is a need to extract information regarding them. In this work, this is done using two methods: The first method used, transient absorption spectroscopy (TAS), consists in observing the light emitted by the excited atomic system due to dipole-beatings; and the second, photo-electron spectroscopy (PES), in observing the distribution of electrons leaving the atomic system.

A complication with TAS, is that it is only capable, as shown in section 3.4.1, of observing states dipole-coupled to the ground state (only ${}^1P^o$ states for the cases studied in this work). Although this restriction can be seen as a serious limitation, it also provides a clearer view of the states which indeed are visible, by removing features that might otherwise clutter the spectrum. (Petersson et al. 2017)

Conversely, a drawback of PES is that large, charged particles may experience strong distortions prior to reaching the detector (Kaldun et al. 2014), which is not the case for light. For this reason, TAS is capable of achieving a significantly higher resolution than PES (Eppink et al. 1997; Ullrich et al. 2003a). As shown in section 3.4.2, during numerical calculations a low Hamiltonian eigenvalue density also puts constraint on the PES resolution.

### 3.4.1 The Transient Absorption Spectrum

As derived in section 3.1.1, the TAS can be expressed by the equation

$$\sigma(\omega) = \frac{4\pi}{\omega}\mathrm{Im}\left\{\frac{\tilde{p}(\omega)}{\tilde{A}(\omega)}\right\} \tag{3.111}$$

in the velocity gauge. Since the frequency-distribution $\tilde{A}(\omega)$ is known (the external field being input data for the ab-initio propagation), the only non-trivial quantity in equation 3.29 is the Fourier transform $\tilde{p}(\omega)$ of the (electron) dipole moment $p(t)$.

#### Calculation of the Electron Momentum

In order to evaluate $\tilde{p}(\omega)$, $p(t)$ is split as

$$p(t) = p^{-}(t) + p^{+}(t) \tag{3.112}$$

into a short-ranged component $p^{-}(t)$ and a long ranged component $p^{+}(t)$. As illustrated in figure 3.11a, they are separated as

$$p^{-}(t) = p(t)\left[1 - \Phi\left(\frac{t - t_{\Phi}}{\tau_{\Phi}}\right)\right] \tag{3.113a}$$

$$p^{+}(t) = p(t) \quad \Phi\left(\frac{t - t_{\Phi}}{\tau_{\Phi}}\right) \tag{3.113b}$$

by a smooth step function $\Phi(t)$. The step function position and width are defined, respectively, by the quantities $t_{\Phi}$ and $\tau_{\Phi}$. Since the Fourier transform is linear, it can be applied individually to $p^{-}(t)$ and $p^{+}(t)$, before adding the two quantities to get

$$\tilde{p}(\omega) = \tilde{p}^{-}(\omega) + \tilde{p}^{+}(\omega). \tag{3.114}$$

This is illustrated in figure 3.11b, where the contributions of $\tilde{p}^{-}(\omega)$ and $\tilde{p}^{+}(\omega)$ to $\tilde{p}(\omega)$ are shown. From the same figure, it is clear that the shape of the spectrum background mainly is determined by the short-ranged component, whereas the sharper spectral features are mainly restricted to the long-ranged one. This is reasonable, as such features are associated with the long-lived autoionising resonances.

In order to evaluate $\tilde{p}(\omega)$, the two components $\tilde{p}^{-}(\omega)$ and $\tilde{p}^{+}(\omega)$ may now be considered individually.

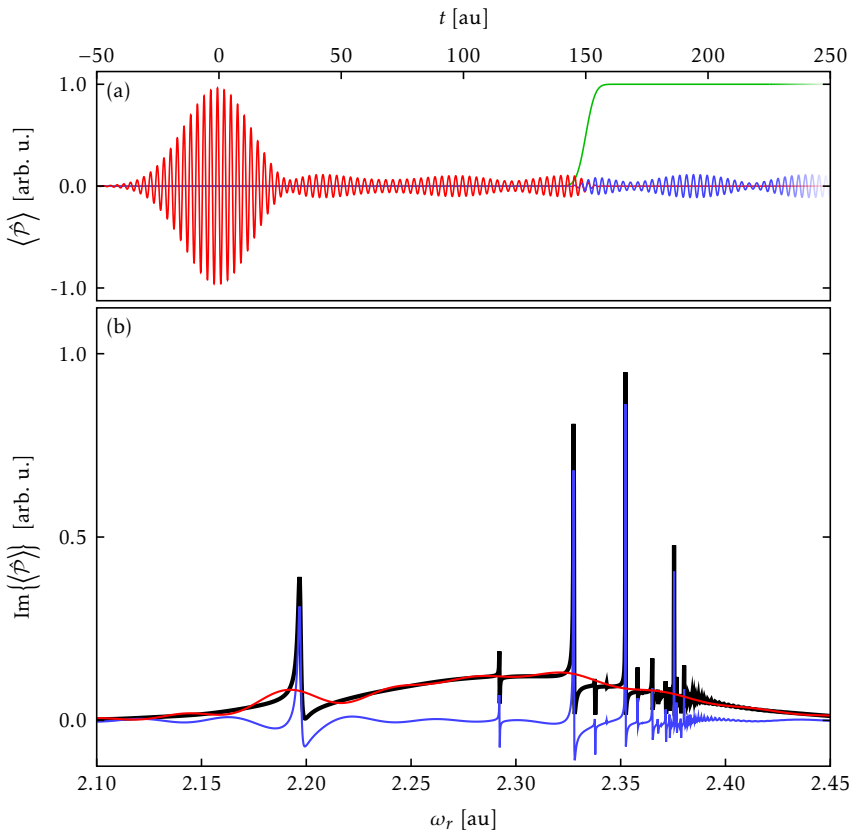


**Figure 3.11:** An illustration of the separation of the electron momentum (of Helium ionised by an extreme ultraviolet attosecond pulse) into a short-ranged (in red) and a long-ranged (in blue) component, both in (a) the temporal and (b) spectral plane. In (a), the step function used to distinguish between the two is shown in green. The sum of the spectral distribution of the two contributions is shown in (b) in black.

**Evaluation of the Short-Ranged Component** As this work treats ab-initio propagations from the energy ground state, and no energy-eigenstate has a dipole beating with itself, the electron momentum is zero at the initial time $T_0$ of the ab-initio calculations prior to the system being affected by the electric field. Selecting $t_\Phi$ and $\tau_\Phi$ so that the approximation

$$1 - \Phi\left(\frac{T_1 - t_\Phi}{\tau_\Phi}\right) \approx 0 \tag{3.115}$$

can be made at the final simulation time $T_1$, the relation

$$\left\{ \forall t \in \mathbb{R} \,:\, p^-(t) \neq 0 \right\} \subseteq \left( T_0,\, T_1 \right) \tag{3.116}$$

holds. Bearing this in mind, the Fourier transform

$$\tilde{p}^-(\omega) = \int_{T_0}^{T_1} dt \left[1 - \Phi\left(\frac{t - t_\Phi}{\tau_\Phi}\right)\right] p(t) \tag{3.117}$$

can be used to numerically calculate the spectral profile $\tilde{p}^-(\omega)$ of $p^-(t)$.

**Evaluation of the Long-Ranged Component** With no external field present, the state ket will evolve freely in the eigenstates $\left|\psi_j^{\mathrm{Q}}\right\rangle$ of the field-free, quenched Hamiltonian, with corresponding eigenfrequencies $\omega_i^{\mathrm{Q}}$. The quenched Hamiltonian (discussed in more detail in section 3.3.3) corresponds to the atomic potential, modified by a potential component which takes the finite lifetimes of the non-bound states into account by adding an imaginary component to $\omega_i^{\mathrm{Q}}$. The evolution of the state ket $\left|\Psi(t)\right\rangle$, from a time $t_0$ after the field has terminated, can be written as

$$\left|\Psi(t)\right\rangle = \sum_j c_j(t_0) \exp\left(-i\omega_j^{\mathrm{Q}}[t - t_0]\right) \left|\psi_j^{\mathrm{Q}}\right\rangle, \tag{3.118}$$

where the complex projection amplitudes

$$c_j(t) = \left\langle \psi_j^{\mathrm{Q}}(t) \middle| \Psi(t) \right\rangle \tag{3.119}$$

give the population distribution at a time $t$ after the cessation of the field.

The expectation value $p(t)$ of the electron dipole operator can, after the field has terminated, be written as

$$\begin{aligned} p(t) &= \sum_{j,k} \left\langle \Psi(t) \middle| \psi_j^{\mathrm{Q}} \right\rangle \left\langle \psi_j^{\mathrm{Q}} \middle| \hat{\mathcal{P}} \middle| \psi_k^{\mathrm{Q}} \right\rangle \left\langle \psi_k^{\mathrm{Q}} \middle| \Psi(t) \right\rangle \\ &= \sum_{j,k} \overline{c_j}(t_0) P_{jk} c_k(t_0) \exp\Big( -i\, \omega_{kj}^{\mathrm{Q}} [t - t_0] \Big), \end{aligned} \tag{3.120}$$

where

$$P_{jk} = \left\langle \psi_j^{\mathrm{Q}} \middle| \hat{\mathcal{P}} \middle| \psi_k^{\mathrm{Q}} \right\rangle, \tag{3.121}$$

are the matrix elements of $\hat{\mathcal{P}}$ corresponding to the beating between them, and the quantity

$$\omega_{kj}^{\mathrm{Q}} = \omega_k^{\mathrm{Q}} - \overline{\omega}_j^{\mathrm{Q}} \tag{3.122}$$

has been introduced.

The long-ranged component of $p(t)$ can now be rewritten as

$$p^+(t) = \Phi\left( \frac{t - t_\Phi}{\tau_\Phi} \right) \sum_{j,k} \overline{c_j}(t_0) P_{jk} c_k(t_0) \exp\Big( -i\, \omega_{kj}^{\mathrm{Q}} [t - t_\Phi] \Big). \tag{3.123}$$

Selecting the step function

$$\Phi(t) = \frac{1}{\sqrt{2\pi}} \int_{-\infty}^{t} dt' \exp\left(-t'^2\right), \tag{3.124}$$

it is possible to evaluate the Fourier transform of $p^+(t)$ analytically. Doing so, after selecting $t_0 = t_\Phi$ and denoting $c_i(t_\Phi) = c_i^\Phi$, gives the result

$$\tilde{p}^+(t) = \frac{\exp(-i\omega t_\Phi)}{\sqrt{2\pi} i} \sum_{j,k} \overline{c}_j^\Phi P_{jk} c_k^\Phi \frac{\exp\Big( -[\omega + \omega_{kj}^{\mathrm{Q}}]^2 \tau_\Phi^2 / 2 \Big)}{\omega + \omega_{kj}^{\mathrm{Q}}}, \tag{3.125}$$

which can be used to evaluate the frequency-distribution of the long-ranged

component of the linear electron momentum. As this is done via addition of all the elements of the matrix $P_{ij}$, the calculation is of time-complexity $\mathcal{O}\left(N^2\right)$, where $N$ is the size of the (quenched) basis. However, unless the external field is capable of significantly draining the ground state (which is not a case considered in this thesis), this can be significantly improved upon. This is because the non-ground state population magnitudes, $|c_i|$, $i \neq 0$, are significantly smaller than the ground state population magnitude $|c_0|$. Therefore, the components of equation 3.125 not corresponding to to beatings with the ground state can be disregarded, decreasing the time-complexity of the problem to $\mathcal{O}\left(2N^{^1P^o}\right) = \mathcal{O}\left(N^{^1P^o}\right)$, where $N^{^1P^o}$ is the number of states of symmetry $^1P^o$.

From this line of reasoning, the final expression,

$$\tilde{p}^+(\omega) = \frac{\exp(-i\omega t_\Phi)}{\sqrt{2\pi}i} \sum_{\{j:P_{0j}\neq 0\}} \begin{aligned} &\overline{c}_0^\Phi P_{0j} c_j^\Phi \frac{\exp\left(-[\omega+\omega_{j0}^{\mathrm{Q}}]^2\tau_\Phi^2/2\right)}{\omega+\omega_{j0}^{\mathrm{Q}}} \\ &+\overline{c}_j^\Phi P_{j0} c_0^\Phi \frac{\exp\left(-[\omega+\omega_{0j}^{\mathrm{Q}}]^2\tau_\Phi^2/2\right)}{\omega+\omega_{0j}^{\mathrm{Q}}} \end{aligned}, \tag{3.126}$$

of the electron momentum, can be arrived at. It now becomes clear that only states with a dipole-beating with the ground state can be monitored (Petersson et al. 2017).

Lastly, it may be interesting to add that, while the change to the energy eigenvalues due to the quenching of the Hamiltonian provides only a slight correction to $\tilde{p}^-(\omega)$ (assuming sufficiently short simulation times), it is absolutely vital for $\tilde{p}^+(\omega)$. This is because the excited electron distribution requires time to reach the complex absorption potential (CAP). By properly selecting $t_\Phi$ and $\tau_\Phi$, the CAP is not even required during the propagation. However, disregarding the CAP during the calculation of $p^+(\omega)$ is not possible. Doing so would give the non-bound states an unphysical spectral distribution, equal to that of a Dirac delta function (that is, they would have an infinite lifetime and an associated [Ott et al. 2013, 2014] infinitesimal spectral width).

### 3.4.2 The Photoelectron Spectrum

Unlike the TAS, which considers the light emitted by an atom, the PES registers the distribution of electrons leaving the atomic system, decaying into ionisation scattering channels. This process is not emulated by the box Hamiltonian eigenstates (which, due to Dirichlet boundary conditions, does not allow electrons to leave the atomic system). However, an approximation of the channel PES-distribution can be extracted directly by projection onto the Hamiltonian eigenstate, as these approximately correspond to scattering channels (Argenti et al. 2013a). This gives the expression

$$P_L^{\alpha_L}(\varepsilon_e) = \left|\left\langle \psi_{L\alpha_L\varepsilon_e} \middle| \Psi(t) \right\rangle\right|^2 \tag{3.127}$$

for the population $P_L^{\alpha_L}$, denoting electron energy $\varepsilon_e$, the total angular momentum $L$, and the scattering channel index $\alpha_L$, and where $\left|\psi_{L\alpha_L\varepsilon}\right\rangle$ is the corresponding, unbound, Hamiltonian eigenket.

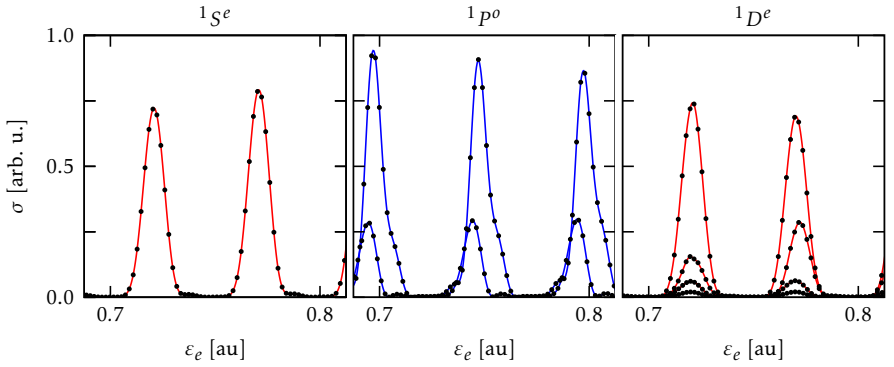


**Figure 3.12:** An illustration of the different (pseudo-) channels of the PES of neon above the first ionisation threshold. The three figures correspond to the $^1S^e$, $^1P^o$ and $^1D^e$ symmetries. The respective symmetries include one, two, and four channels each. Each channel has been (quadratically) interpolated (in red and blue) between the Hamiltonian eigenstates (shown as black dots).

To get the total population $P_L(\varepsilon)$ for a given $L$–value, or that, $P(\varepsilon)$, for all $L$ values, it is possible to sum over the relevant channels as

$$P(\varepsilon) = \sum_L P_L(\varepsilon), \;\; P_L(\varepsilon) = \sum_{\alpha_L} P_L^{\alpha_L}(\varepsilon). \tag{3.128}$$

The different components of a RABITT-like spectrum is shown in figure 3.12. From the figure, it becomes immediately clear that, since the spectrum has been interpolated, the Hamiltonian eigenstate-density is a limiting factor for the energy resolution. Because of this, the size of the basis may need to be increased when resolution is lacking, creating a potential conflict between increasing resolution on the one hand, and minimising computational time and memory on the other.

#### Angularly Resolved Photoelectron Spectra

Presently consider the problem of resolving the PES not only energetically, but also angularly. This can be done by through projection onto the detector eigenstates $\left|\psi^{(-)}_{\alpha;\varepsilon\hat{\Omega}_e}\right\rangle$ of well defined energy $\varepsilon$ and emission angle $\hat{\Omega}_e$ (Marante et al. 2014). These states $\left|\psi^{(-)}_{\alpha;\varepsilon\hat{\Omega}_e}\right\rangle$ of a channel $\alpha$ may be expressed employing a partial wave expansion

$$\left|\psi^{(-)}_{\alpha;\varepsilon\hat{\Omega}_e}\right\rangle = \sum_{\substack{LM \\ \ell_e m_e}} C^{LM}_{\ell_e m_e, \ell_{\mathrm{PI}} m_{\mathrm{PI}}} \left|\psi^{(-),L}_{\alpha;\varepsilon\ell_e m_e}\right\rangle \times \overline{Y^{m_e}_{\ell_e}}\left(\hat{\Omega}_e\right) \times \exp\left[-i\left(\sigma_{\ell_e} - \frac{\ell_e \pi}{2}\right)\right] \tag{3.129}$$

into the energy eigenstates $\left|\psi^{(-),L}_{\alpha;\varepsilon\ell_e m_e}\right\rangle$ which fulfill incoming boundary conditions (García 1992); where $Y^{m_e}_{\ell_e}\left(\hat{\Omega}_e\right)$ is the spherical harmonic associated with the electron angular momentum $\ell_e$ with projection $m_e$, $\sigma_{\ell_e}$ is the Coulomb phase shift (Dill 1976), $L$ is the total angular momentum with projection $M$, and $C^{LM}_{\ell_e m_e, \ell_{\mathrm{PI}} m_{\mathrm{PI}}}$ are Clebsch-Gordan coefficients. The angularly differentiated cross section may now be calculated as an incoherent sum

$$P\left(\varepsilon, \hat{\Omega}_e\right) = \sum_\alpha \left|\left\langle \psi^{(-)}_{\alpha;\varepsilon\hat{\Omega}_e} \middle| \Psi(t)\right\rangle\right|^2 \tag{3.130}$$

over the unresolved channels $\alpha$.

# Chapter 4

## Ab-Initio Bases

In chapter 3.3, a methodology for solving the multi-photon time-dependent Schrödinger equation (TDSE) is described. This is achieved by propagation in the basis of the eigenstates of the atomic Hamiltonian $\hat{\mathcal{H}}_0$. Therefore, it presupposes that the time-independent Schrödinger equation (TISE) already has been solved.

Under the electrostatic approximation, the multi-electron atomic Hamiltonian operator can be written as

$$\hat{\mathcal{H}}_0 = -\sum_i \frac{1}{2}\hat{\mathbf{\nabla}}_i^2 - \sum_i \frac{Z}{\left\|\hat{\boldsymbol{r}}_i\right\|} + \sum_{i,j>i} \frac{1}{\left\|\hat{\boldsymbol{r}}_i - \hat{\boldsymbol{r}}_j\right\|} \tag{4.1}$$

where $Z$ is the nuclear charge, $\hat{\mathbf{\nabla}}_i$ is the $ith$ electron gradient operator, $\hat{\boldsymbol{r}}_i$ is the corresponding position operator, and the nucleus is located at the origin. The three sums in equation 4.1 correspond, respectively, to (i) the electron kinetic energy, (ii) the Coulomb nuclear-electron interaction potential, and (iii) the Coulomb electron-electron interaction potential.

For non hydrogen-like systems (i.e. systems containing $N_e \geq 2$ electrons), no exact solution exists to this problem. Instead, approximative methods need to be employed. One first step to create such an approximation is to only consider one

electron simultaneously, which can be done through the single-active electron (SAE) or the more advanced Hartree (1935)-Fock (1930) (HF) method. The HF method uses a single Slater (1929) determinant to describe the system wave function – the simplest way to to describe an antisymmetric many-particle wave function. This allows the $ith$ electron wave function to be described as an eigenfunction of the Fock-operator

$$\hat{\mathcal{F}}_i = -\frac{1}{2}\hat{\boldsymbol{\nabla}}_i^2 + \frac{Z}{\|\hat{\boldsymbol{r}}_i\|} + \hat{\mathcal{V}}_i^{\mathrm{MF}} \tag{4.2}$$

where $\hat{\mathcal{V}}_i^{\mathrm{MF}}$ is a mean-field potential operator which describes the electron-electron interaction.

Unfortunately, the HF method is not necessarily adequate when describing multi-electron systems; as it (through the mean-field approximation) disregards the tendency of electrons to avoid coinciding with each other, and it dismisses the possibility of more than one Slater determinant being needed. Such effects are known as electron correlation (Hättig et al. 2011), and are vital when describing multi-particle atomic and molecular systems.

Because of the importance of electron correlation, atomic models need to go beyond HF and SAE approximations. This chapter outlines the methodologies utilised for creating the matrix elements necessary to describe the system during ab-initio propagations. Two separate methodologies were employed. In section 4.1, the basis used when describing helium is discussed. In section 4.2, a summary of the XCHEM basis – here used for ab-initio propagations in neon – is given.

## 4.1 The B-Spline Helium Basis

The first basis to be discussed in this chapter was used to describe the single-ionisation region of helium, as described in chapter 6. The program uses a numerical close-coupling (CC) basis to describe the single-ionisation process, while electron correlation is accounted for using a set of localised channel eigenstates (LC). These states are described as a linear combination of B-splines – compact support functions well adapted to describe bound as well as continuum states (Bachau et al. 2001).

The methodology discussed herein has already proven itself capable of describing helium in a non-B-spline basis (Argenti et al. 2013b), and has also been extended to more complex atoms (Argenti et al. 2006). Separately from the study discussed in the results section of this thesis; a time-dependent implementation of the helium basis discussed in this section has previously been used to recreate attosecond transient absorption spectroscopy of doubly excited states (Argenti et al. 2012), as well as to study reconstruction and control of doubly-excited wave packets (Ott et al. 2012), in helium.

The information discussed herein is to be published by Argenti et al. (Unpublished), and is printed here with permission.

### 4.1.1 The Helium Eigenfunctions

In the present methodology, the helium atomic states are expanded in two distinct sets of basis functions: The long ranged asymptotic behaviour is described by a set $\left\{\left|{}^{\mathrm{CC}}\phi^{\Gamma}_{\alpha i}\right\rangle\right\}$ of CC channel functions, defined by a channel $\alpha$ and an index $i$; while the short-ranged correlated behaviour is described by a set $\left\{\left|{}^{\mathrm{LC}}\phi^{\Gamma}_{i}\right\rangle\right\}$ of LCs with index $i$. The symmetry label $\Gamma = (\Pi, S, \Sigma, L, M)$ contains the parity $\Pi$, the total spin $S$ with projection $\Sigma$, and the total angular momentum $L$ with the projection $M$.

Here, the quantity $\boldsymbol{x}_i \equiv (\boldsymbol{r}_i, \zeta_i)$ will be defined for the $ith$ electron as containing its position $\boldsymbol{r}$ (defined by a direction $\hat{r}$ and distance $r$ from the core) and spin $\zeta$. Using the index PI for the bound, parent ion (PI), electron and $e$ for the excited electron, the CC functions can be written as

$$ {}^{\mathrm{CC}}\phi^{\Gamma}_{\alpha i}(\boldsymbol{x}_{\mathrm{PI}}, \boldsymbol{x}_e) \;=\; \Theta_{S\Sigma}(\zeta_{\mathrm{PI}}, \zeta_e) \times \hat{\mathcal{A}} \left\{ R_{N_{\mathrm{PI}}\ell_{\mathrm{PI}}}(r_{\mathrm{PI}}) \times \frac{u_{\ell_\alpha i}(r_e)}{r_e} \times \mathcal{Y}^{LM}_{\ell_{\mathrm{PI}}\ell_e}(\hat{r}_{\mathrm{PI}}, \hat{r}_e) \right\} \quad (4.3) $$

for the case when the PI electron has the principal quantum number $N_{\mathrm{PI}}$, by splitting the wave function into components corresponding to the radial, angular, spin dependency of the state: The radial part is defined by a bound radial hydrogen eigenfunction $R_{n\ell}(r)$ and the arbitrary reduced radial component $u_i(r)$ of the excited electron. The angular part consists of a bipolar spherical harmonic

$$ \mathcal{Y}^{LM}_{\ell_1\ell_2}(\hat{r}_1, \hat{r}_2) = \sum_{m_1 m_2} C^{LM}_{\ell_1 m_1, \ell_2 m_2} Y^{m_1}_{\ell_1}(\hat{r}_1)\, Y^{m_2}_{\ell_2}(\hat{r}_2), \quad (4.4) $$

where $Y^{m_i}_{\ell_i}(\hat{r}_i)$ is a spherical harmonic and $C^{LM}_{\ell_1 m_1, \ell_2 m_2}$ the Clebsch–Gordan coefficient. The spin component is defined by the two-electron spin function

$$ \Theta_{S\Sigma}(\zeta_1, \zeta_2) = \sum_{\substack{\sigma_1 = \pm 1/2 \\ \sigma_2 = \pm 1/2}} C^{S\Sigma}_{1/2\,\sigma_1, 1/2\,\sigma_2}\; {}^2\chi_{\sigma_1}(\zeta_1)\; {}^2\chi_{\sigma_2}(\zeta_2), \quad (4.5) $$

where ${}^2\chi_\sigma(\zeta)$ is the one-electron spin function. Finally, $\hat{\mathcal{A}}$ is the antisymmetrizer, working on the expression within the brackets.

Unfortunately, the CC function defined in equation 4.3 does not give rise to a complete two-electron basis, as it is incapable of of reproducing the sharp spatial modulation caused by electron coalescence. For this reason, a complementary LC basis

$$ {}^{\mathrm{LC}}\phi^{\Gamma}_{\alpha i}(\boldsymbol{x}_1, \boldsymbol{x}_2) = \; N_i\, \Theta_{S\Sigma}(\zeta_1, \zeta_2) \times \hat{\mathcal{A}} \left\{ \frac{\varphi_{n_1\ell_1}(r_1)\, \varphi_{n_2\ell_2}(r_2)}{r_1 r_2} \times \mathcal{Y}^{LM}_{\ell_1\ell_2}(\hat{r}_1, \hat{r}_2) \right\} \quad (4.6) $$

is introduced, normalised by the constants $N_i$, where the reduced radial orbits

$\varphi_{nl}(r)$ are confined to a radius where both electrons have significant probability density.

The $\Gamma$ electron wave function $\left|\phi^{\Gamma}\right\rangle$ can now be written as a linear combination

$$\left|\phi^{\Gamma}\right\rangle = \sum_{\alpha i} c^{\Gamma}_{\alpha i} \left|{}^{\mathrm{CC}}\phi^{\Gamma}_{\alpha i}\right\rangle + \sum_{j} b^{\Gamma}_{j} \left|{}^{\mathrm{LC}}\phi^{\Gamma}_{i}\right\rangle \tag{4.7}$$

of the CC and LC basis functions.

### 4.1.2 The B-Spline Basis

When constructing the basis, the reduced radial electron components present in equations 4.3 and 4.6 are here described as a linear combination of B-Splines. B-Splines are a set of compact functions which has proven itself well suited to represent bound, Rydberg, as well as continuum molecular and atomic orbitals orbitals (Bachau et al. 2001).

B-splines are real functions which belongs to the class $\mathcal{C}^{\infty}$ of infinitely differentiable functions on all points except a predefined set $\{\xi_i\}$ of nodes, here assumed to be ordered as $\xi_{i+1} \geq \xi_i$. Using these nodes, the B-splines of order $k$ can be defined recursively as

$$B^k_i(r) = \begin{cases} \theta_{\xi_i}(r) \cdot \theta_{\xi_{i+1}}(-r) & , \; k = 1 \qquad (4.8a) \\ \dfrac{(r-\xi_i)\cdot B^{k-1}_i(r)}{\xi_{i+k-1}-\xi_i} - \dfrac{(r-\xi_{i+k})\cdot B^{k-1}_{i+1}(r)}{\xi_{i+k}-\xi_{i+1}}, & k > 1 \qquad (4.8b) \end{cases}$$

where the Heaviside step function $\theta_{r_0}(r) = \theta(r - r_0)$ is used to define the first order B-spline as a plateau. The result of this equation can be seen in figure 4.1, which show B-splines of the lower orders $k \in \{1, 2, 3, 4, 5\}$.

The set $\{\xi_i\}$ can be defined as to give rise to intervals of zero length – that is, containing values of $i$ for which $\xi_i = \xi_{i+1}$. When $j$ nodes coincide, i.e. $\xi_i = \xi_{i+1} = \cdots = \xi_{i+j-1}$, the $k - jth$ derivative may be discontinuous at $r = \xi_i$.

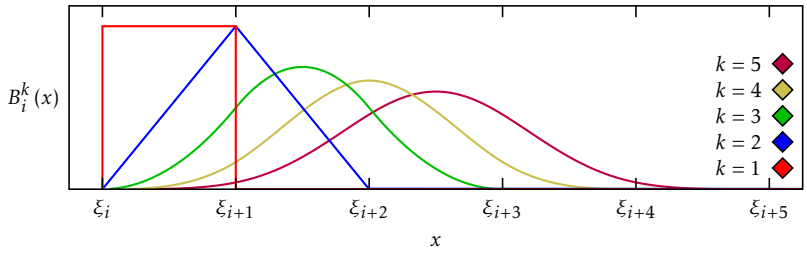


**Figure 4.1:** The difference between B-Splines of different order $k$. As can be seen, increasing $k$ makes for smoother, broader B-spline functions.

Otherwise, only the $k-1th$ derivative is. In order to ensure that the B-splines assume finite values at the boundaries of the studied continuum, the end nodes need to be $k$ times degenerate.

From equation 4.8, it becomes clear that a given B-spline $B_i^k(r)$ only is non-zero only in the interval of $r \in (\xi_i, \xi_{i+k})$. Thus, the B-spline have a banded representation, contributing to making algorithms solving linear systems in this basis numerically stable. The value of $k$ must be chosen with this in mind: Despite the capability of B-splines of describing high-order functions improving with $k$; increasing the value of $k$ will also increase the B-spline overlap, increasing the degree to which the error when solving the linear equation propagates through the system.

The present basis is constructed using two distinct B-spline bases: one for the localised and one for the continuum orbitals. The localised basis is used to describe both PI and localised channel states. It is defined using a set $\left\{\xi_i^{\mathrm{L}}\right\}$ of nodes which increase linearly with $r$ until reaching a radius comparable to the size of the largest, most energetic PI considered (usually in the order of tens of Bohr radii). The continuum B-spline basis node set $\left\{\xi_i^{\mathrm{C}}\right\}$ contains both the localised (that is, $\left\{\xi_i^{\mathrm{L}}\right\} \subsetneq \left\{\xi_i^{\mathrm{C}}\right\}$) and a set of equidistant nodes (generally of the order of 0.5 au) reaching the box-boundary. Enforcing the condition of $\left\{\xi_i^{\mathrm{C}}\right\} \subsetneq \left\{\xi_i^{\mathrm{L}}\right\}$ makes the localised B-spline space an exact subspace of the continuum B-spline space, which preserves the numerical stability of the basis

(Argenti et al. 2006).

It should be noted that the reduced radial components $\varphi_{n\ell}(r)$ need to fulfill the regularity condition

$$\lim_{r\to 0} \varphi_{n\ell}(r) \to 0 \tag{4.9}$$

at the origin. This is explicitly satisfied by eliminating the first $\ell + 1$ B-splines, as

$$\varphi_{n\ell}(r) = \sum_{i>\ell+1} c_{n\ell;i} B_i^k(r), \tag{4.10}$$

for angular momenta $\ell \leq 4$.

The PI radial orbitals present in equation 4.3 are computed by diagonalising the hydrogenic singly-ionised helium (i.e. $He^+$) Hamiltonian. The PIs with a principal quantum number $N_{\text{PI}}$ and angular momentum $\ell_{\text{PI}}$ can then be coupled to orbitals from the continuum B-spline space orthogonal to those PI orbitals with lower principal quantum number $n < N_{\text{PI}}$ and those with $n = N_{\text{PI}}$ and $\ell < \ell_{\text{PI}}$, in order to avoid redundancies. The localised channel are composed of self-consistent-field (SCF) orbitals that diagonalise an effective one-particle Hartree-Fock (HF) Hamiltonian, describing the $1s^2$ ground state of helium with the addition of a single positive charge potential working on the space orthogonal to the $1s$ orbital. Further avoiding redundancies – this time between the CC and LC channels – and allowing the hydrogenic and SCF orbital to be treated separately, the CC projection operator

$$^{\text{CC}}\hat{\mathcal{P}}^{\Gamma} = \sum_{\alpha i} \left|{}^{\text{CC}}\phi^{\Gamma}_{\alpha i}\right\rangle\left\langle{}^{\text{CC}}\phi^{\Gamma}_{\alpha i}\right| \tag{4.11}$$

of the space spanned by the CC channels is diagonalised in the LC basis. States whose eigenvalues equals 1 (to within a certain precision) are removed from the LC basis, being already represented in the CC one. This gives rise to a conditioned LC (CLC) space, linearly independent from the CC space.

### 4.1.3 Diagonalising the Hamiltonian

With the above reasoning in mind, the diagonalisation of the Hamiltonian will now be discussed. It is carried out in two separate parts – firstly, the diagonalisation of the bound states will be discussed; secondly, that of the non-bound ones.

#### Bound Energy Eigenstate

In order to calculate the bound energy eigenstates, the basis

$$\left|\phi^{\Gamma}_{b,i}\right\rangle = \left\{\left|{}^{\mathrm{CLC}}\phi^{\Gamma}_{j}\right\rangle\right\} \cup \bigcup_{\alpha}\left\{\left|{}^{\mathrm{CC}}\overline{\phi}^{\Gamma}_{\alpha k}\right\rangle\right\} \tag{4.12}$$

is defined, comprised of the CLC states $\left|{}^{\mathrm{CLC}}\phi^{\Gamma}_{i}\right\rangle$ and the CC functions $\left|{}^{\mathrm{CC}}\overline{\phi}^{\Gamma}_{\alpha i}\right\rangle$ which have had the last B-spline eliminated (enforcing Dirichlet boundary conditions). In this basis, the Hamiltonian can be diagonalised as

$$\hat{\mathcal{H}}_0\left|\psi^{\Gamma}_{b,i}\right\rangle = \varepsilon^{\Gamma}_{b,i}\left|\psi^{\Gamma}_{b,i}\right\rangle \tag{4.13}$$

to give the bound energy eigenvalues $\varepsilon^{\Gamma}_{b,i}$ and associated eigenkets $\left|\psi^{\Gamma}_{b,i}\right\rangle$ of index $i$.

#### Non-Bound Eigenstates Eigenstate and the K-Matrix Method

Although many methods capable of solving the present multi-channel problem within the close-coupling ansatz (Carette et al. 2013; Nikolopoulos et al. 2001; Zatsarinny et al. 2013) exist (a comprehensive list of which can be found in [Argenti et al. 2013a]), the basis discussed herein is computed using the K-matrix method. The K-matrix method is discussed in more detail in (Argenti et al. 2006; Lindroth et al. 2012), but will here be explained briefly.

As a first step, the Hamiltonian is diagonalised in the subspace of CC states $\left|{}^{\mathrm{CC}}\overline{\phi}^{\Gamma}_{\alpha i}\right\rangle$ independently for each channel $\alpha$. This eigenvalue problem can be

written as

$$\hat{\mathcal{H}}_0 \left| {}^{\mathrm{PWC}}\phi^{\Gamma}_{\alpha i} \right\rangle = \varepsilon^{\Gamma}_{\mathrm{PWC},i} \left| {}^{\mathrm{PWC}}\phi^{\Gamma}_{\alpha i} \right\rangle, \tag{4.14}$$

and gives rise to the normalised so-called partial-wave channel (PWC) functions $\left| {}^{\mathrm{PWC}}\phi^{\Gamma}_{\alpha i} \right\rangle$ of energy $\varepsilon^{\Gamma}_{\mathrm{PWC},i}$.

Below the channel threshold, the energies $\varepsilon^{\Gamma}_{\mathrm{PWC},i}$ correspond to an approximate discrete Rydberg series converging towards the threshold; while above, they consist of continuum energies in the $\alpha$ channel. The below-threshold states correspond to a fixed $\ell$ electron bound by a PI in a given state. The above-threshold states are stationary states in which asymptotically free electrons scatter elastically of a PI in a given state, giving rise to a probability amplitude which vanishes at the box boundary. Compared to a regular Coulomb function with the same angular momentum and asymptotic energy, it exhibits a channel phase shift $\delta_{\alpha i}$.

Using these states along with the CLC ones a scattering Hamiltonian $\hat{\mathcal{H}}^{\Gamma}_{\mathrm{SC}}$ can now be defined as

$$\hat{\mathcal{H}}^{\Gamma}_{\mathrm{SC}} = \sum_{\alpha} \sum\!\!\!\!\!\!\int_i d\varepsilon^{\Gamma}_i \; \varepsilon^{\Gamma}_i \left| \phi^{\Gamma}_{\alpha\varepsilon_i} \right\rangle \left\langle \phi^{\Gamma}_{\alpha\varepsilon_i} \right|, \tag{4.15}$$

where the states $\left| \phi^{\Gamma}_{\alpha\varepsilon} \right\rangle$ of energy $\varepsilon^{\Gamma}_i$ include both CLC and PWC states. Under the realistic assumption that the elastic channels are asymptotically decoupled, the scattering Hamiltonian $\hat{\mathcal{H}}^{\Gamma}_{\mathrm{SC}}$ is approximately equal to the atomic Hamiltonian $\hat{\mathcal{H}}_0$ at large distances $r$ from the nucleus. The effect of $\hat{\mathcal{V}}^{\Gamma} = \hat{\mathcal{H}}_0 - \hat{\mathcal{H}}^{\Gamma}_{\mathrm{SC}}$ can thus be seen as a short-ranged perturbation, and the Hamiltonian multichannel scattering-eigenstates can be calculated as a solutions to the Lippmann-Schwinger equation (LSE)

$$\left| \psi^{\mathcal{P}}_{\Gamma,\alpha\varepsilon} \right\rangle = \left| \phi^{\Gamma}_{\alpha\varepsilon} \right\rangle + \frac{\mathcal{P}}{\varepsilon - \hat{\mathcal{H}}^{\Gamma}_{\mathrm{SC}}} \hat{\mathcal{V}}^{\Gamma} \left| \psi^{\mathcal{P}}_{\Gamma,\alpha\varepsilon} \right\rangle \tag{4.16}$$

where $\beta$ is restricted to channels open at the energy $\varepsilon$. Inserting equation 4.15 into the LSE gives the results

$$\left|\psi^{\mathcal{P}}_{\Gamma,\alpha\varepsilon}\right\rangle = \left|\phi^{\Gamma}_{\alpha\varepsilon}\right\rangle + \sum_{\beta}\!\!\!\!\!\!\int d\varepsilon' \left|\phi^{\Gamma}_{\alpha\varepsilon'}\right\rangle \frac{\mathcal{P}}{\varepsilon-\varepsilon'} \underline{\mathrm{K}}^{\beta\varepsilon'}_{\alpha\varepsilon} \tag{4.17}$$

where $\underline{\mathrm{K}}^{\beta\varepsilon'}_{\Gamma,\alpha\varepsilon} = \left\langle \phi^{\Gamma}_{\beta\varepsilon'} \middle| \hat{\mathcal{V}}^{\Gamma} \middle| \psi^{\mathcal{P}}_{\Gamma,\alpha\varepsilon} \right\rangle$ are the matrix elements of the off-shell reaction matrix $\underline{\mathrm{K}}$, which varies smoothly with the upper energy index $\varepsilon$.

Enforcing the condition of $\left|\psi^{\mathcal{P}}_{\Gamma,\alpha\varepsilon}\right\rangle$ being a $\hat{\mathcal{H}}_0$ eigenfunction, a condition which can be written as

$$\left\langle \phi^{\Gamma}_{\beta\varepsilon'} \middle| \varepsilon - \hat{\mathcal{H}}_0 \middle| \psi^{\mathcal{P}}_{\Gamma,\alpha\varepsilon} \right\rangle = 0, \ \forall \beta, \varepsilon' \tag{4.18}$$

equation 4.17 can be solved. This is is done by solving the system

$$\underline{\mathrm{K}}^{\gamma\varepsilon''}_{\Gamma,\alpha\varepsilon} - \sum_{\beta}\!\!\!\!\!\!\int d\varepsilon' \, \underline{\mathrm{V}}^{\gamma\varepsilon''}_{\Gamma,\beta\varepsilon'}(\varepsilon) \frac{\mathcal{P}}{\varepsilon'-\varepsilon''} \underline{\mathrm{K}}^{\gamma\varepsilon''}_{\Gamma,\alpha\varepsilon} = \underline{\mathrm{V}}^{\gamma\varepsilon''}_{\Gamma,\alpha\varepsilon}(\varepsilon) \tag{4.19}$$

of integral equations for $\underline{\mathrm{K}}$, where the continuum-continuum matrix elements

$$\underline{\mathrm{V}}^{\beta\varepsilon'}_{\Gamma,\alpha\varepsilon}(\varepsilon'') = \left\langle \beta\varepsilon' \middle| \varepsilon'' - \hat{\mathcal{H}}_0 \middle| \alpha\varepsilon \right\rangle \tag{4.20}$$

and $\underline{\mathrm{K}}^{\beta\varepsilon'}_{\Gamma,\alpha\varepsilon}$ are interpolated along their discretised energy indices. The scattering states of a given spherical symmetry fulfilling incoming boundary conditions may now be obtained as a sum

$$\left|\psi^{-}_{\Gamma,\alpha\varepsilon}\right\rangle = \sum_{\beta} \left|\psi^{\mathcal{P}}_{\Gamma,\beta\varepsilon}\right\rangle \frac{1}{1 - i\pi \underline{\mathrm{K}}^{\beta\varepsilon}_{\Gamma,\alpha\varepsilon}} \exp\left[-i\left(\sigma_{\ell_\alpha} + \delta_\alpha + \frac{\pi\ell_\alpha}{2}\right)\right], \tag{4.21}$$

where $\ell_\alpha$ is the excited electron angular momentum, $\sigma_{\ell_\alpha}$ the associated Coulomb phaseshift, and $\delta_\alpha$ the channel phase shift.

## 4.2 The XCHEM Basis

Ab-initio modelling of the time-dependent behaviour of the attosecond processes discussed in this thesis requires accurate treatment of both the short-ranged structure of the studied atom, and the long-ranged ionisation continuum. Well established and sophisticated quantum chemistry packages (QCPs) – such as MOLCAS (Aquilante et al. 2016) and MOLPRO (Werner et al. 2012) – capable of describing bound atomic and molecular states are already commercially available. Such QCPs, however, are ill suited for describing the long-ranged electron continuum.

This is the central focus of the XCHEM (Marante et al. 2014, 2017a,b) approach. By combining sophisticated QCP implementations with a B-spline scattering basis, it allows the accurate treatment of single-ionisation processes in many-electron molecules and atoms. As part of this thesis, the studies discussed in chapter 7 were carried out using a time-dependent implementation of the XCHEM methodology. Below, a summary of the concept of XCHEM, as described by Marante et al. (2014, 2017a,b), is presented.

### 4.2.1 The Atomic Basis

In the XCHEM approach, several distinct radial ranges are considered. The total scattering wave function of energy $\varepsilon$ in the $\alpha$ continuum is written as a linear combination

$$\left|\Psi^{-}_{\alpha\varepsilon}\right\rangle = \sum_{i} c_{i,\alpha\varepsilon}\left|\mathcal{N}_i\right\rangle + \sum_{\beta}\sum_{i} c_{\beta i,\alpha\varepsilon}\left|\overline{\Upsilon}_{\beta i}\right\rangle \tag{4.22}$$

of close-ranged states $\left|\mathcal{N}_i\right\rangle$, describing the case when all $N_e$ electrons constrained within a radius $R_0$; and extended-channel functions $\left|\overline{\Upsilon}_{\beta i}\right\rangle$ which consider the case when one (here assumed to be the last, $N_e th$) electron is at a position

$r_{N_e} > R_0$. They can be written as a product

$$\overline{\Upsilon}_{\alpha i}(\{\boldsymbol{x}_i\}) \;=\; N_{\alpha i}\,\hat{\mathcal{A}}\,\Upsilon_\alpha\left(\boldsymbol{r}_1,\boldsymbol{r}_2,\ldots,\boldsymbol{r}_{N_e-1},\hat{r}_{N_e},\zeta_{N_e}\right)\times\varphi_i\left(r_{N_e}\right), \tag{4.23}$$

between the asymptotically decoupled wave functions $\Upsilon_\alpha$ and the free electron radial wave function $\varphi_i$; where $\hat{\mathcal{A}}$ is the antisymmetriser, and $\boldsymbol{x}_i$ contain the position $\boldsymbol{r}_i$ (of magnitude $r_i$ and direction $\hat{r}_i$) and spin $\zeta_i$ of the $ith$ electron.

The functions $\Upsilon_\alpha$ are obtained by coupling the antisymmetrised parent ion (PI) wave functions ${}^{2S_{\rm PI}+1}\Phi_{\Sigma_{\rm PI}}$ (of total spin $S_{\rm PI}$ with projection $\Sigma_{\rm PI}$), to the emitted electron spin function ${}^2\chi_\sigma\left(\zeta_{N_e}\right)$ (where $\sigma_{N_e}$ is the electron spin projection), while factorising the emitted electron (with direction $\hat{r}_{N_e}$) spherical harmonics $Y^{\ell_{N_e}}_{m_{N_e}}\left(\hat{r}_{N_e}\right)$ (where $\ell_{N_e}$ is the emitted electron angular momentum with projection $m_{N_e}$). This coupling can be written as

$$\Upsilon_\alpha\left(\boldsymbol{r}_1,\boldsymbol{r}_2,\ldots,\boldsymbol{r}_{N_e-1},\hat{r}_{N_e},\zeta_{N_e}\right)=^{2S+1}\left[\Phi\;\otimes\;{}^2\chi\left(\zeta_{N_e}\right)\right]_\Sigma\times Y^{\ell_{N_e}}_{m_{N_e}}\left(\hat{r}_{N_e}\right), \tag{4.24}$$

where $S$ is the total spin with projection $\Sigma$.

The PI wave functions, as well as the localised bound states, can all be well described by the QCPs. These make use of a Gaussian basis set in order to model the inner structure of a molecule (or atom, as is the case considered here). While Gaussian functions are apt for such a purpose, they have the disadvantage of quickly vanishing at large radii. This problem is solved in the XCHEM approach by utilising a combined Gaussian–B-spline (GABS) basis. Using a GABS basis, the short-ranged dynamics are described using QCP Gaussian functions, while the scattering states are described using B-splines; allowing the use of the highly advanced QCP molecular descriptions, while circumnavigating the shortcomings associated with a Gaussian basis.

### 4.2.2 The GABS Hybrid Basis

The XCHEM approach employs three distinct sets of functions in order to construct its basis: (i) a localised Gaussian basis $\left\{\left|{}^{L}\mathcal{G}_i\right\rangle\right\}$, (ii) a diffuse, even tempered, monocentric Gaussian basis $\left\{\left|{}^{M}\mathcal{G}_i\right\rangle\right\}$, and (iii) a monocentric B-spline scattering basis $\left\{\left|\mathcal{B}_i\right\rangle\right\}$. The localised basis $\left\{\left|{}^{L}\mathcal{G}_i\right\rangle\right\}$ is calculated by QCPs. For molecular systems, $\left\{\left|{}^{L}\mathcal{G}_i\right\rangle\right\}$ is a polycentric basis centered at the atomic cores, while for the atomic systems discussed herein it is monocentric. It is the monocentric component $\left\{\left|{}^{M}\mathcal{G}_i\right\rangle\right\} \cup \left\{\left|\mathcal{B}_j\right\rangle\right\}$ which constitutes the GABS basis (Marante et al. 2014).

The radial GABS basis is illustrated in figure 4.2. The B-splines begin at $r = R_0$. This region of $r \in [0, R_0]$ the QCP basis can be found along with the monocentric Gaussian functions. A second radius, $R_1$, has been marked in the figure. Beyond this point, at $r \in [R_1, \infty)$, the Gaussian basis can be approximated as zero, and only the B-spline scattering basis is present. Between these points, for $r \in (R_0, R_1)$, both monocentric bases overlap, bridging the gap between the QCP and scattering functions.

#### GABS Basis Functions

As already mentioned, the GABS basis is composed of one B-spline and one Gaussian basis set. The concept and advantages of B-splines is already discussed in section 4.1.2, and need not be discussed in detail here. Hence, only the monocentric Gaussian basis functions remain to be discussed.

Their radial component can be written on the form

$$ {}^{M}\mathcal{G}^{\ell m}_{K\alpha}(\boldsymbol{r}) \;=\; N_{\alpha K}\frac{g_{\alpha K}(r)}{r}, \tag{4.25} $$

where several new indices and functions have been introduced: The radial distribution is defined by the function

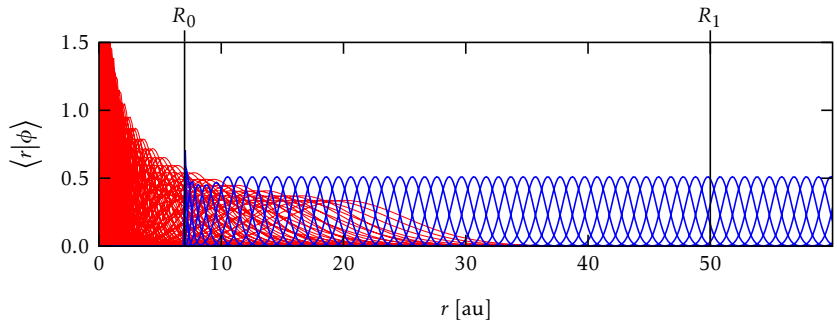


**Figure 4.2:** The radial GABS basis functions $|\phi_i\rangle$. In red, the Gaussian functions $|\phi\rangle \in \{|^L\mathcal{G}_j\rangle\}$ are shown, while the B-splines $|\phi_i\rangle \in \{|\mathcal{B}_i\rangle\}$ are shown in blue. The distance $r$ from the nucleus can be divided into three sections, by $R_0 = 7$ au and $R_1 = 50$ au: For $r < R_0$, no B-Splines are present, while the Gaussian functions are vanishingly small for $r > R_1$. At $r \in [R_0, R_1]$, the diffuse monocentric Gaussian functions $\{|^M\mathcal{G}_i\rangle\}$ overlap the B-Splines $\{|\mathcal{B}_i\rangle\}$.

$$g_{\alpha K}(r) = r^{K+1} \exp\left(-\alpha r^2\right), \tag{4.26}$$

defined by the variables $\alpha$ and $K$. The exponents $\alpha$ make up a discrete set $\alpha \in \{\alpha_1, \alpha_2, \ldots, \alpha_{N_\alpha}\}$, created from the geometric series

$$\alpha_n = \alpha_1 \beta^{n-1}, \; n \in \{0, 1, \ldots, N_\alpha\} \tag{4.27}$$

derived from two constants $\alpha_1$ and $\beta$. Only values $K \in \{\ell, \ell+2, \ell+4, \ldots\}$ of $K$ are considered, where the restriction of $K \geq \ell$ ensures regularity at the origin. Finally, the basis set is normalised as

$$\int_0^\infty dr \, N_{\alpha K}^2 \, g_{\alpha K}^2(r) = 1, \tag{4.28}$$

by using the constants $N_{\alpha K}$.

Presently consider the case of combining the Gaussian and B-spline bases. Both Gaussian and B-splines are well-conditioned basis sets. Combining the two, however, may give rise to linear dependencies. For this purpose, the

$\{|\mathcal{G}_i\rangle\} = \{|{}^L\mathcal{G}_i\rangle\} \cup \{|{}^M\mathcal{G}_j\rangle\}$ projection operator

$$\hat{\mathcal{P}}_{\mathcal{G}} = \sum_i |\mathcal{G}_i\rangle\langle\mathcal{G}_i| \tag{4.29}$$

is diagonalised in the B-spline basis. States with an eigenvalue of 1 (to a certain precision) are then removed from the B-spline basis. From the remaining basis functions, the GABS basis can now be formed as $\{|\chi_i\rangle\} = \{|\mathcal{G}_j\rangle\} \cup \{|\mathcal{B}_k\rangle\}$. In order to ensure that the basis function is zero at the boundary, the last B-spline can be removed from $\{|\chi_i\rangle\}$. The resulting basis will be denoted as $\{|\overline{\chi}_i\rangle\}$. Projection onto this basis enforces Dirichlet boundary conditions.

### 4.2.3 Diagonalising the Hamiltonian

Diagonalising the atomic Hamiltonian $\hat{\mathcal{H}}_0$ in $\{|\overline{\chi}_i\rangle\}$ is an adequate method for calculating the bound Rydberg states, which are constrained near the atomic core far from the box boundary. The same, however, can not be said for the free electron states – in the infinite potential well described by $\{|\overline{\chi}_i\rangle\}$, only a discrete number of the continuous set of free-electron eigenenergies will be represented. Writing the Hamiltonian eigenstates of energy $\varepsilon$ on the form

$$|\psi_{\alpha\varepsilon}\rangle = \sum_{i=1} c_{\alpha\varepsilon,i}|\overline{\chi}_i\rangle + b_{\alpha\varepsilon}|\mathcal{B}_{N_B}\rangle, \tag{4.30}$$

all eigenstates can be considered. The ones for which $b_\varepsilon \neq 0$ are solutions to the equation

$$\langle\overline{\chi}_i|\varepsilon - \hat{\mathcal{H}}_0|\psi_{\alpha\varepsilon}\rangle = 0, \ \forall i. \tag{4.31}$$

These solutions can be written as a function

$$|\psi_{\alpha\varepsilon}\rangle = b_{\alpha\varepsilon}\left[\hat{I} + \sum_{i,j}|\overline{\chi}_i\rangle\langle\overline{\chi}_i|\frac{1}{\varepsilon - \hat{\mathcal{H}}_0}|\overline{\chi}_j\rangle\langle\overline{\chi}_j|\left(\hat{\mathcal{H}}_0 - \varepsilon\right)\right]|\mathcal{B}_{N_B}\rangle, \tag{4.32}$$

where the value of $b_{\alpha\varepsilon}$ functions as an effective normalisation constant.

# Chapter 5

## Simple Interferometric Models

As part of this work, the method of reconstruction of attosecond beatings by interference of two-photon transitions (RABITT), described in detail in chapter 3.2, has been used to study atomic systems. More specifically, it has been used to extract what is known as the atomic phase.

RABITT can accurately be described using time-dependent ab-initio propagations. In more complex systems, where these are unavailable, simpler models can instead be used. This was the case with argon, discussed in chapter 8.1, which was treated prior to the XCHEM methodology (explained in chapter 4.2) was ready to be used for ab-initio calculations. Even when ab-initio treatments of the system are available, however, such models may be highly useful for providing physical insight.

RABITT is a pump-probe experiment which employs an extreme ultraviolet (XUV) pump consisting of the odd high harmonics (HH) of the infrared (IR) probe. Together, one XUV and one IR pump is used to reach the even harmonics, known as sidebands (SB). The interference between the paths via the upper and lower harmonics oscillate with the pump-probe time-delay. This oscillation is shifted by the atomic phase difference, written as

$$\Delta\phi^{\mathrm{At}}_{2n} = \phi^{\mathrm{At}}_{2n+1} - \phi^{\mathrm{At}}_{2n-1} \tag{5.1}$$

for the $2nth$ sideband, where $\phi^{\mathrm{At}}_{2n\pm1}$ is the atomic phases of $\mathrm{SB}_{2n}$ corresponding to the path via $\mathrm{HH}_{2n\pm1}$. It was defined in equation 3.60 as

$$\phi^{\mathrm{At}}_{2n\pm1} = -\arg\left\{\mathcal{M}^{\pm}_{2n}\right\}, \tag{5.2}$$

where $\mathcal{M}^{\pm}_{2n}$ is the two-photon matrix element $\mathcal{M}^{(2)}_{2n}(\varepsilon_i)$ from the ground state of energy $\varepsilon_0$ to sideband $\mathrm{SB}_{2n}$ of energy $\varepsilon_{2n}$, averaged over harmonic $\mathrm{HH}_{2n\pm1}$ as

$$\mathcal{M}^{\pm}_{2n} = \int_{\mathrm{HH}_{2n\pm1}} d\varepsilon_i \left|\tilde{F}_{\mathrm{IR}}(\varepsilon_{2n}-\varepsilon_i)\,\tilde{F}_{\mathrm{XUV}}(\varepsilon_i-\varepsilon_0)\right| \mathcal{M}^{(2)}_{2n}(\varepsilon_i), \tag{5.3}$$

where $\tilde{F}_{\mathrm{XUV}}(\omega)$ and $\tilde{F}_{\mathrm{IR}}(\omega)$ are the spectral profiles of the XUV and IR fields, respectively.

Hence, knowing the dipole matrix elements, the atomic phases can also be calculated. A simple model dedicated to this purpose, based on the Fano (1961) model of resonant continua, was developed by Jiménez-Galán et al. (2016). It models the Hamiltonian

$$\hat{\mathcal{H}}(t) = \hat{\mathcal{H}}_0 + F(t)\hat{\mathcal{O}}, \tag{5.4}$$

by using second-order time-dependent perturbation theory (TDPT) (described in appendix B), considering the perturbation of the field-free Hamiltonian $\hat{\mathcal{H}}_0$ by the time-dependent interaction component $F(t)\hat{\mathcal{O}}$, where $\hat{\mathcal{O}}$ is the appropriate dipole operator in the direction of the field $F(t)$. In chapter 3.2 the velocity gauge expression $\hat{\mathcal{O}} = \alpha\hat{\mathcal{P}}$ of the interaction component is used, where $\alpha$ is the fine structure constant and $\hat{\mathcal{P}}$ the velocity gauge dipole.

The aforementioned model was employed as part of several RABITT studies making up part of this thesis. Below, it is discussed in greater detail. Section 5.1 shows how the two-photon matrix elements can be calculated using TDPT, while section 5.2 outlines the dependence of the atomic phase on photoelectron emission angle.

## 5.1 Calculation of the Matrix Elements

The two-photon matrix element between an initial state $\left|\psi_0\right\rangle$ and a final state $\left|\psi_{\mathrm{F}}\right\rangle$ via an intermediate energy $\varepsilon_i$ can, using TDPT, be written on the general form

$$\mathcal{M}_{\mathrm{F}}^{(2)}(\varepsilon_i) = \left\langle \psi_{\mathrm{F}} \middle| \hat{\mathcal{O}}\, \widetilde{\hat{\mathcal{G}}^{+}}(\varepsilon_i)\, \hat{\mathcal{O}} \middle| \psi_0 \right\rangle, \tag{5.5}$$

where

$$\widetilde{\hat{\mathcal{G}}^{+}}(\varepsilon) = \frac{1}{\varepsilon - \hat{\mathcal{H}}_0 + i0^{+}}, \tag{5.6}$$

is the frequency distribution of the retarded Green function. Expanding this function in energy eigenstates allows equation 5.5 to be rewritten as

$$\mathcal{M}_{\mathrm{F}}^{(2)}(\varepsilon_i) = \sum\!\!\!\!\!\!\int_{\mathrm{I}} d\varepsilon_{\mathrm{I}} \frac{\mathcal{O}_{\mathrm{I}}^{\mathrm{F}} \mathcal{O}_{0}^{\mathrm{I}}}{\varepsilon_i - \varepsilon_{\mathrm{I}} + i0^{+}}, \tag{5.7}$$

where $\mathcal{O}_0^{\mathrm{I}}$ is the one-photon matrix element connecting the ground state to an intermediate state $\left|\psi_{\mathrm{I}}\right\rangle$ with energy $\varepsilon_{\mathrm{I}}$, which in turn is connected to the final state by the matrix element $\mathcal{O}_{\mathrm{I}}^{\mathrm{F}}$. States not contained in the intermediate continua need not be considered in the expansion, as their contribution becomes zero due to dipole connection rules.

Here, a note regarding the intermediate states $\left|\psi_{\mathrm{I}}\right\rangle$ should be made. By Jiménez-Galán et al. (2016), the matrix element is divided into two distinct components – one corresponding to the transition via unbound state and one to that via bound resonances. In this work, only energies far above the ionisation threshold are treated. Due to this restriction, only intermediate unbound and autoionising states will be considered.

### 5.1.1 Transition Amplitudes Between Featureless Continua

In order to further explore the above matrix element, it is convenient to begin by considering the simple case when both the intermediate and the final states are featureless continua $\left|\alpha\varepsilon\right\rangle$, defined by their energy $\varepsilon$ and the set $\alpha$ of non-energy quantum numbers. The two-photon matrix element to the final state $\left|\alpha_{\mathrm{F}}\varepsilon_{\mathrm{F}}\right\rangle$ via the intermediate state $\left|\alpha_{\mathrm{I}}\varepsilon_{\mathrm{I}}\right\rangle$ can be written as

$$\mathcal{M}^{(2)}_{\mathrm{F},\alpha_{\mathrm{I}}}(\varepsilon_i) = \int d\varepsilon_{\mathrm{I}} \frac{\mathcal{O}^{\alpha_{\mathrm{F}}\varepsilon_{\mathrm{F}}}_{\alpha_{\mathrm{I}}\varepsilon_{\mathrm{I}}}\,\mathcal{O}^{\alpha_{\mathrm{I}}\varepsilon_{\mathrm{I}}}_{0}}{\varepsilon_i - \varepsilon_{\mathrm{I}} + i0^{+}}, \tag{5.8}$$

where $\mathcal{O}^{\alpha_{\mathrm{I}}\varepsilon_{\mathrm{I}}}_{0}$ and $\mathcal{O}^{\alpha_{\mathrm{F}}\varepsilon_{F}}_{\alpha_{\mathrm{I}}\varepsilon_{\mathrm{I}}}$ are equivalent to $\mathcal{O}^{\mathrm{I}}_{0}$ and $\mathcal{O}^{\mathrm{F}}_{\mathrm{I}}$.

Regarding $\mathcal{O}^{\alpha_{\mathrm{F}}\varepsilon_{\mathrm{F}}}_{\alpha_{\mathrm{I}}\varepsilon_{\mathrm{I}}}$, it should be noted that the dipole transition matrix elements between free-electron states are near zero unless the states are degenerate. This becomes clear when considering the case of plane waves, as these are eigenstates of the dipole operator. By the same token, the dipole elements between the pure continuum states $\left|\alpha\varepsilon\right\rangle$ considered here are nearly diagonal – although not fully so, as they are affected by the atomic potential.

With this in mind, an integral

$$\overline{\mathcal{O}}^{\alpha_{\mathrm{F}}}_{\alpha_{\mathrm{I}}}(\varepsilon_{\mathrm{F}}) = \int\limits_{\varepsilon_{\mathrm{F}}-\Delta}^{\varepsilon_{\mathrm{F}}+\Delta} d\varepsilon_{\mathrm{I}} \left\langle \alpha_{\mathrm{F}}\varepsilon_{\mathrm{F}}\middle|\mathcal{O}\middle|\alpha_{\mathrm{I}}\varepsilon_{\mathrm{I}}\right\rangle, \tag{5.9}$$

can be defined for a small quantity $\Delta$, in order to enable the approximation

$$\left\langle \alpha_{\mathrm{F}}\varepsilon_{\mathrm{F}}\middle|\mathcal{O}\middle|\alpha_{\mathrm{I}}\varepsilon_{\mathrm{I}}\right\rangle \approx \overline{\mathcal{O}}^{\alpha_{\mathrm{F}}}_{\alpha_{\mathrm{I}}}(\varepsilon_{\mathrm{F}})\,\delta(\varepsilon_{\mathrm{F}} - \varepsilon_{\mathrm{I}}), \tag{5.10}$$

where $\delta(x)$ is the Dirac delta. Now, the equation 5.8 can be approximated as

$$\mathcal{M}^{(2)}_{\mathrm{F},\alpha_{\mathrm{I}}}(\varepsilon_i) \approx \frac{\overline{\mathcal{O}}^{\alpha_{\mathrm{F}}}_{\alpha_{\mathrm{I}}}(\varepsilon_{\mathrm{F}})\,\mathcal{O}^{\varepsilon_{\mathrm{F}}\alpha_{\mathrm{I}}}_{0}}{\varepsilon_i - \varepsilon_{\mathrm{F}} + i0^{+}}. \tag{5.11}$$

The case of non-ground state resonant states remains to be considered.

### 5.1.2 Fano Formalism and Resonant Transition Amplitudes

In order to expand the above formulation to the case of non-ground state resonances, a simple version of the Fano (1961) approach will be employed. In order to do so, presently consider the case of a resonance $\left|n\right\rangle$ of energy $\varepsilon_n$ in a pure energy continuum $\left|\alpha\varepsilon\right\rangle$ with eigenenergies $\varepsilon$, where the index $\alpha$ contains non-energy quantum numbers commuting with $\hat{\mathcal{H}}_0$. With this notation, the system

$$\varepsilon_n = \left\langle n \left|\hat{\mathcal{H}}_0\right| n \right\rangle \tag{5.12a}$$

$${}^{\alpha}\mathcal{V}_{\varepsilon}^{n} = \left\langle n \left|\hat{\mathcal{H}}_0\right|\alpha\varepsilon\right\rangle = \overline{\left\langle\alpha\varepsilon\left|\hat{\mathcal{H}}_0\right| n \right\rangle} = \overline{{}^{\alpha}\mathcal{V}_{n}^{\varepsilon}} \tag{5.12b}$$

$$\varepsilon = \left\langle\alpha\varepsilon\left|\hat{\mathcal{H}}_0\right|\alpha\varepsilon\right\rangle \tag{5.12c}$$

of equations can be introduced, by defining the new transition matrix elements ${}^{\alpha}\mathcal{V}_{\varepsilon}^{n} = \overline{{}^{\alpha}\mathcal{V}_{n}^{\varepsilon}}$.

Using this notation, two more quantities are defined. The first, $\Delta_n(\varepsilon)$, is an energy shift of the resonance $\left|n\right\rangle$. It can be expressed as

$$\Delta_n(\varepsilon) = \mathcal{P}\int d\varepsilon' \frac{\left|{}^{\alpha}\mathcal{V}_{n}^{\varepsilon'}\right|^2}{\varepsilon - \varepsilon'}. \tag{5.13}$$

where $\mathcal{P}$ signifies the principal part of the integral. The second is the resonance width $\Gamma_n(\varepsilon)$, calculated as

$$\Gamma_n(\varepsilon) = 2\pi\left|{}^{\alpha}\mathcal{V}_{n}^{\varepsilon}\right|^2. \tag{5.14}$$

Assuming ${}^{\alpha}\mathcal{V}_{n}^{\varepsilon}$ can be considered as independent of energy, these can be approximated as constant. For convenience, several new quantities will be defined as $\overline{{}^{\alpha}\mathcal{V}^{n}} = {}^{\alpha}\mathcal{V}_{n} = {}^{\alpha}\mathcal{V}_{n}^{\varepsilon_n} \approx {}^{\alpha}\mathcal{V}_{n}^{\varepsilon}$, $\Delta_n = \Delta_n(\varepsilon_n) \approx \Delta_n(\varepsilon)$ and $\Gamma_n = \Gamma_n(\varepsilon_n) \approx \Gamma_n(\varepsilon)$.

Deploying this notation, the continuum eigenstates of $\hat{\mathcal{H}}_0$ can be written as

$$\left|\psi^n_{\alpha\varepsilon}\right\rangle = \left|\alpha\varepsilon\right\rangle + \left(\left|n\right\rangle + \int d\varepsilon' \left|\alpha\varepsilon'\right\rangle \frac{{}^{\alpha}\mathcal{V}_n}{\varepsilon - \varepsilon' + i0^+}\right) \frac{{}^{\alpha}\mathcal{V}^n}{\varepsilon - \tilde{\varepsilon}_n}, \tag{5.15}$$

normalised as $\left\langle \psi^n_{\alpha\varepsilon} \middle| \psi^n_{\alpha\varepsilon'} \right\rangle = \delta(\varepsilon - \varepsilon')$, where the complex energy

$$\tilde{\varepsilon}_n = \varepsilon_n + \Delta_n - i\frac{\Gamma_n}{2} \tag{5.16}$$

has been shifted by $\Delta_n$ and has a pole in the negative imaginary plane at $i\Gamma_n/2$. Equation 5.15 can further be reformulated by dividing it into a pure continuum component $\left|\alpha\varepsilon\right\rangle$, and a resonance-tainted component

$$\left|\tilde{n}_\varepsilon\right\rangle = \left|n\right\rangle + P\int d\varepsilon' \left|\alpha\varepsilon'\right\rangle \frac{{}^{\alpha}\mathcal{V}_n}{\varepsilon - \varepsilon'}, \tag{5.17}$$

This allows the eigenstate to be rewritten as

$$\left|\psi^n_{\alpha\varepsilon}\right\rangle = \frac{\epsilon_n(\varepsilon)}{\epsilon_n(\varepsilon) + i}\left|\alpha\varepsilon\right\rangle + \frac{1}{\pi\,{}^{\alpha}\mathcal{V}_n}\frac{1}{\epsilon_n(\varepsilon) + i}\left|\tilde{n}_\varepsilon\right\rangle. \tag{5.18}$$

where

$$\epsilon_n(\varepsilon) = 2\frac{\varepsilon - \varepsilon_n - \Delta_n}{\Gamma_n} \tag{5.19}$$

is known as the reduced energy variable.

Presently consider a resonant state $\left|m\right\rangle$ dipole-connected to the continuum $\left|\alpha\varepsilon\right\rangle$ in which $\left|\psi^n_{\alpha\varepsilon}\right\rangle$ is located (i.e. $\forall\varepsilon : \mathcal{O}^{\alpha\varepsilon}_m \neq 0$ in the relevant region). From equation 5.18, the transition operator element from $\left|m\right\rangle$ to $\left|\psi^n_{\alpha\varepsilon}\right\rangle$ can be determined as following the well-known behaviour

$$\mathcal{O}^{\alpha n\varepsilon}_m = \frac{\epsilon_n(\varepsilon) + q^{\alpha\tilde{n}\varepsilon}_m}{\epsilon_n(\varepsilon) - i}\mathcal{O}^{\alpha\varepsilon}_m, \tag{5.20}$$

where

$$q_m^{\alpha\tilde{n}\varepsilon} = \frac{1}{\pi\,{}^{\alpha}\mathcal{V}_n} \frac{\left\langle \tilde{n}_\varepsilon \middle| \hat{\mathcal{O}} \middle| m \right\rangle}{\left\langle \alpha\,\varepsilon \middle| \hat{\mathcal{O}} \middle| m \right\rangle} \tag{5.21}$$

is the associated Fano profile parameter, approximated as constant in the region of interest. The energy index can be removed by defining $q_m^{\alpha\tilde{n}} = q_m^{\alpha\tilde{n}\varepsilon_n} \approx q_m^{\alpha\tilde{n}\varepsilon}$, in order to follow the convention laid out for $\Gamma_n$ and $\Delta_n$.

With this background as a foundation, further extensions of $\mathcal{M}^{(2)}_{\mathrm{F},\alpha_\mathrm{I}}(\varepsilon_i)$ may be constructed. These extensions will be divided into three cases. Firstly, the case of intermediate resonances will be considered. Secondly, the case of final resonances will be treated. Finally, the case when both intermediate and final resonances are present will be briefly discussed.

#### The Case of an Intermediate Resonance

When an intermediate resonance is present, the transition amplitude from the ground state to the intermediate continuum is readily given by equation 5.20. As such, only the matrix elements between excited states remain to be calculated.

First consider the transition from the ground state to the intermediate continuum. Analogously to equation 5.20, it can be written as

$$\mathcal{O}_0^{\alpha_\mathrm{I} n_\mathrm{I} \varepsilon_\mathrm{I}} = \left\langle \psi^{n_\mathrm{I}}_{\alpha_\mathrm{I}\varepsilon_\mathrm{I}} \middle| \hat{\mathcal{O}} \middle| \psi_0 \right\rangle = \frac{\epsilon_{n_\mathrm{I}}(\varepsilon_\mathrm{I}) + q_0^{\alpha_\mathrm{I}\tilde{n}_\mathrm{I}}}{\epsilon_{n_\mathrm{I}}(\varepsilon_\mathrm{I}) - i} \mathcal{O}_0^{\alpha_\mathrm{I}\varepsilon_\mathrm{I}}. \tag{5.22}$$

With this concluded, the element $\mathcal{O}^{\alpha_\mathrm{F}\varepsilon_\mathrm{F}}_{\alpha_\mathrm{I} n_\mathrm{I}\varepsilon_\mathrm{I}}$, corresponding to the transition between excited states, remains to be treated.

This matrix element can be further divided into three distinct components: One pure continuum component, one resonance-tainted component, and one resonant component. These correspond to the three kets shown in the right-hand side of equation 5.15.

The pure continuum transition has already been calculated in equation 5.10, and need not be treated again here. As such, the first component to be

considered is the tainted continuum component. It can be calculated as

$$\int d\varepsilon_{\mathrm{I}}' \frac{\left\langle \alpha_{\mathrm{F}}\varepsilon_{\mathrm{F}}\middle|\hat{\mathcal{O}}\middle|\alpha_{\mathrm{I}}\varepsilon_{\mathrm{I}}'\right\rangle}{\varepsilon_{\mathrm{I}}-\varepsilon_{\mathrm{I}}'+i0^{+}} \frac{\left|{}^{\alpha_{\mathrm{I}}}\mathcal{V}_{n_{\mathrm{I}}}\right|^{2}}{\varepsilon_{i}-\tilde{\varepsilon}_{n_{\mathrm{I}}}} = \frac{1}{\pi}\frac{1}{\epsilon_{n_{\mathrm{I}}}(\varepsilon_{\mathrm{I}})+i}\frac{\overline{\mathcal{O}}_{\alpha_{\mathrm{I}}}^{\alpha_{\mathrm{F}}}}{\varepsilon_{\mathrm{I}}-\varepsilon_{\mathrm{F}}+i0^{+}}, \tag{5.23}$$

by assuming that the approximation of $\overline{\mathcal{O}}_{\alpha_{\mathrm{I}}}^{\alpha_{\mathrm{F}}} \approx \overline{\mathcal{O}}_{\alpha_{\mathrm{I}}}^{\alpha_{\mathrm{F}}}(\varepsilon_{\mathrm{F}})$ as energy-independent can be made. Lastly, the resonant component should be considered. It can be written as

$$\left\langle \alpha_{\mathrm{F}}\varepsilon_{\mathrm{F}}\middle|\hat{\mathcal{O}}\middle|n_{\mathrm{I}}\right\rangle \frac{{}^{\alpha_{\mathrm{I}}}\mathcal{V}^{n_{\mathrm{I}}}}{\varepsilon_{\mathrm{I}}-\tilde{\varepsilon}_{n}} = \frac{1}{\pi\,{}^{\alpha_{\mathrm{I}}}\mathcal{V}_{n_{\mathrm{I}}}}\frac{1}{\epsilon_{n_{\mathrm{I}}}(\varepsilon_{\mathrm{I}})+i}\mathcal{O}_{n_{\mathrm{I}}}^{\alpha_{\mathrm{F}}}. \tag{5.24}$$

Together, this gives the form

$$\mathcal{O}_{\alpha_{\mathrm{I}}n_{\mathrm{I}}\varepsilon_{\mathrm{I}}}^{\alpha_{\mathrm{F}}\varepsilon_{\mathrm{F}}} = \delta(\varepsilon_{\mathrm{F}}-\varepsilon_{\mathrm{I}})\overline{\mathcal{O}}_{\alpha_{\mathrm{I}}}^{\alpha_{\mathrm{F}}} + \frac{1}{\pi}\frac{1}{\epsilon_{n_{\mathrm{I}}}(\varepsilon_{\mathrm{I}})+i}\left(\frac{1}{\varepsilon_{\mathrm{I}}-\varepsilon_{\mathrm{F}}+i0^{+}} + \frac{\mathcal{O}_{n_{\mathrm{I}}}^{\alpha_{\mathrm{F}}}}{{}^{\alpha_{\mathrm{I}}}\mathcal{V}_{n_{\mathrm{I}}}\overline{\mathcal{O}}_{\alpha_{\mathrm{I}}}^{\alpha_{\mathrm{F}}}}\right)\overline{\mathcal{O}}_{\alpha_{\mathrm{I}}}^{\alpha_{\mathrm{F}}} \tag{5.25}$$

of the matrix element. It may be noted that the quantity

$$\gamma_{\alpha_{\mathrm{I}}n_{\mathrm{I}}\varepsilon_{\mathrm{I}}}^{\alpha_{\mathrm{F}}\varepsilon_{\mathrm{F}}} = \left(\varepsilon_{\mathrm{I}}-\varepsilon_{\mathrm{F}}\right)\frac{\mathcal{O}_{n_{\mathrm{I}}}^{\alpha_{\mathrm{F}}}}{{}^{\alpha_{\mathrm{I}}}\mathcal{V}_{n_{\mathrm{I}}}\overline{\mathcal{O}}_{\alpha_{\mathrm{I}}}^{\alpha_{\mathrm{F}}}} \tag{5.26}$$

describes the relative strength of the two paths to the final continuum via the intermediate resonant state – the direct path and that via the tainted continuum.

The calculated matrix element can now be inserted into the equation

$$\mathcal{M}_{\mathrm{F},\alpha_{\mathrm{I}}n_{\mathrm{I}}}^{(2)}(\varepsilon_{i}) = \int d\varepsilon_{\mathrm{I}}\frac{\mathcal{O}_{\alpha_{\mathrm{I}}n_{\mathrm{I}}\varepsilon_{\mathrm{I}}}^{\alpha_{\mathrm{F}}\varepsilon_{\mathrm{F}}}\mathcal{O}_{0}^{\alpha_{\mathrm{I}}n_{\mathrm{I}}\varepsilon_{\mathrm{I}}}}{\varepsilon_{i}-\varepsilon_{\mathrm{I}}+i0^{+}}, \tag{5.27}$$

to, after integration, give the two-photon matrix element. The delta-component of the integral can be computed directly; whereas the remaining part, having a pole in the lower part of the complex plane, can be evaluated via a contour integral encompassing the negative half of the imaginary plane. In order to do this, the dipole matrix elements $\mathcal{O}_{n}^{\alpha\varepsilon}$ connecting the resonances to pure continua are approximated as constant, removing the energy index as $\mathcal{O}_{n}^{\alpha} \approx \mathcal{O}_{n}^{\alpha\varepsilon}$. This

gives the final expression

$$\mathcal{M}^{(2)}_{\mathrm{F},\alpha_\mathrm{I}}(\varepsilon_i) = \frac{\epsilon_{n_\mathrm{I}}(\varepsilon_i) + q_0^{\alpha_\mathrm{I}\tilde{n}_\mathrm{I}}\left(1 - \gamma^{\alpha_\mathrm{F}\varepsilon_\mathrm{F}}_{\alpha_\mathrm{I}n_\mathrm{I}\varepsilon_i}\right) + i\gamma^{\alpha_\mathrm{F}\varepsilon_\mathrm{F}}_{\alpha_\mathrm{I}n_\mathrm{I}\varepsilon_i}}{\epsilon_{n_\mathrm{I}}(\varepsilon_i) + i} \frac{\overline{\mathcal{O}}^{\alpha_\mathrm{F}}_{\alpha_\mathrm{I}}\mathcal{O}^{\alpha_\mathrm{I}}_0}{\varepsilon_i - \varepsilon_\mathrm{F}} \tag{5.28}$$

of the matrix element.

Presently consider the transition from the intermediate to the final state. The transition from the intermediate autoionising resonance implies two electron transitions (one electron returning to the core, with the other being ejected into the continuum), while the continuum-continuum transition implies only one. As such, $\gamma^{\alpha_\mathrm{F}\varepsilon_\mathrm{F}}_{\alpha_\mathrm{I}n_\mathrm{I}\varepsilon_\mathrm{I}}$ may be assumed to be small. Approximating $\gamma^{\alpha_\mathrm{F}\varepsilon_\mathrm{F}}_{\alpha_\mathrm{I}n_\mathrm{I}\varepsilon_\mathrm{I}}$ as zero, the matrix element simplifies to

$$\mathcal{M}^{(2)}_{\mathrm{F},\alpha_\mathrm{I}}(\varepsilon_i) = \frac{\epsilon_{n_\mathrm{I}}(\varepsilon_i) + q_0^{\alpha_\mathrm{I}\tilde{n}_\mathrm{I}}}{\epsilon_{n_\mathrm{I}}(\varepsilon_i) + i} \frac{\overline{\mathcal{O}}^{\alpha_\mathrm{F}}_{\alpha_\mathrm{I}}\mathcal{O}^{\alpha_\mathrm{I}}_0}{\varepsilon_i - \varepsilon_\mathrm{F}}. \tag{5.29}$$

This assumption is throughout the studies composing this thesis.

#### The Case of a Final Resonance

The matrix elements for the case of a final resonance can be computed in a manner largely analogous to those computed above for the case corresponding to an intermediate resonance.

As for the case of intermediate resonances, the matrix element between the ground state and the intermediate continuum will be considered first. As no intermediate resonance is present, the slow-varying quantity $\mathcal{O}^{\alpha_\mathrm{I}}_0$ will be used.

Now consider the matrix element between the excited states. As for the case of an intermediate resonance, the various components of the transition between excited states can be considered separately. The pure continuum-continuum component is identical to that of the aforementioned case, and can be derived from equation 5.10. The other components are not.

Now consider the tainted continuum component. Performing, like for with the case of an intermediate resonance, the approximation $\overline{\mathcal{O}}^{\alpha_\mathrm{F}}_{\alpha_\mathrm{I}} \approx \overline{\mathcal{O}}^{\alpha_\mathrm{F}}_{\alpha_\mathrm{I}}(\varepsilon_\mathrm{F})$, it can

be written as

$$\int d\varepsilon_{\mathrm{F}}' \frac{\left\langle \alpha_{\mathrm{F}} \varepsilon_{\mathrm{F}}' \middle| \hat{\mathcal{O}} \middle| \alpha_{\mathrm{I}} \varepsilon_{\mathrm{I}} \right\rangle}{\varepsilon_{\mathrm{F}} - \varepsilon_{\mathrm{F}}' + i0^-} \frac{\left| {}^{\alpha_{\mathrm{I}}}\mathcal{V}^{n_{\mathrm{I}}} \right|^2}{\varepsilon_{\mathrm{I}} - \tilde{\varepsilon}^*_{n_{\mathrm{F}}}} = \frac{1}{\pi} \frac{1}{\epsilon_{n_{\mathrm{F}}}(\varepsilon_{\mathrm{F}}) - i} \frac{\overline{\mathcal{O}}^{\alpha_{\mathrm{F}}}_{\alpha_{\mathrm{I}}}}{\varepsilon_{\mathrm{I}} - \varepsilon_{\mathrm{F}} - i0^-}, \tag{5.30}$$

which leaves the resonant component. It can be calculated as

$$\left\langle n_{\mathrm{F}} \middle| \hat{\mathcal{O}} \middle| \alpha_{\mathrm{I}} \varepsilon_{\mathrm{I}} \right\rangle \frac{{}^{\alpha_{\mathrm{F}}}\mathcal{V}_{n_{\mathrm{F}}}}{\varepsilon - \tilde{\varepsilon}^*_{n_{\mathrm{F}}}} = \frac{1}{\pi} \frac{1}{{}^{\alpha_{\mathrm{F}}}\mathcal{V}^{n_{\mathrm{F}}}} \frac{1}{\epsilon_{n_{\mathrm{F}}}(\varepsilon_{\mathrm{F}}) - i} \mathcal{O}^{n_{\mathrm{F}}}_{\alpha_{\mathrm{I}}}. \tag{5.31}$$

These equations can now be combined to get the expression

$$\mathcal{O}^{\alpha_{\mathrm{F}} n_{\mathrm{F}} \varepsilon_{\mathrm{F}}}_{\alpha_{\mathrm{I}} \varepsilon_{\mathrm{I}}} = \delta(\varepsilon_{\mathrm{F}} - \varepsilon_{\mathrm{I}}) \overline{\mathcal{O}}^{\alpha_{\mathrm{F}}}_{\alpha_{\mathrm{I}}} + \frac{1}{\pi} \frac{1}{\epsilon_{n_{\mathrm{F}}}(\varepsilon_{\mathrm{F}}) - i} \left( \frac{1}{\varepsilon_{\mathrm{I}} - \varepsilon_{\mathrm{F}} - i0^+} + \frac{\mathcal{O}^{n_{\mathrm{F}}}_{\alpha_{\mathrm{I}}}}{{}^{\alpha_{\mathrm{F}}}\mathcal{V}^{n_{\mathrm{F}}} \overline{\mathcal{O}}^{\alpha_{\mathrm{F}}}_{\alpha_{\mathrm{I}}}} \right) \overline{\mathcal{O}}^{\alpha_{\mathrm{F}}}_{\alpha_{\mathrm{I}}} \tag{5.32}$$

for the matrix element of the second photon. Analogously to $\gamma^{\alpha_{\mathrm{F}} \varepsilon_{\mathrm{F}}}_{\alpha_{\mathrm{I}} n_{\mathrm{I}} \varepsilon_{\mathrm{I}}}$, the quantity

$$\gamma^{\alpha_{\mathrm{F}} n_{\mathrm{F}} \varepsilon_{\mathrm{F}}}_{\alpha_{\mathrm{I}} \varepsilon_{\mathrm{I}}} = \left( \varepsilon_{\mathrm{I}} - \varepsilon_{\mathrm{F}} \right) \frac{\mathcal{O}^{n_{\mathrm{F}}}_{\alpha_{\mathrm{F}}}}{{}^{\alpha_{\mathrm{I}}}\mathcal{V}^{n_{\mathrm{F}}} \overline{\mathcal{O}}^{\alpha_{\mathrm{F}}}_{\alpha_{\mathrm{I}}}} \tag{5.33}$$

describes the relative strength of the ionisation path corresponding to the final resonance versus that corresponding to the tainted continuum.

The two-photon matrix element can now be calculated. This is done in a similar way as was done when considering an intermediate resonance: The delta function is integral is evaluated directly, while the non-delta function is integrated using a closed integral containing the upper half of the complex plane, during which $\mathcal{O}^{\alpha\varepsilon}_n \approx \mathcal{O}^{\alpha}_n$ is approximated as constant. This gives the form

$$\mathcal{M}^{(2)}_{\mathrm{F},\alpha_{\mathrm{I}}}(\varepsilon_i) = \frac{\epsilon_{n_{\mathrm{F}}}(\varepsilon_i) + i\left(1 + \gamma^{\alpha_{\mathrm{F}} n_{\mathrm{F}} \varepsilon_{\mathrm{F}}}_{\alpha_{\mathrm{I}} \varepsilon_i}\right)}{\epsilon_{n_{\mathrm{F}}}(\varepsilon_i) - i} \frac{\overline{\mathcal{O}}^{\alpha_{\mathrm{F}}}_{\alpha_{\mathrm{I}}} \mathcal{O}^{\alpha_{\mathrm{I}}}_0}{\varepsilon_i - \varepsilon_{\mathrm{F}}} \tag{5.34}$$

of the matrix element. Approximating, again, $\gamma_{\alpha_I \varepsilon_I}^{\alpha_F n_F \varepsilon_F} = 0$, the simpler form

$$\mathcal{M}^{(2)}_{F,\alpha_I}(\varepsilon_i) = \frac{\epsilon_{n_F}(\varepsilon_F) + i}{\epsilon_{n_F}(\varepsilon_F) - i} \frac{\overline{\mathcal{O}}^{\alpha_F}_{\alpha_I} \mathcal{O}^{\alpha_I}_0}{\varepsilon_i - \varepsilon_F} \tag{5.35}$$

of the matrix element is obtained.

#### Combining Final and Intermediate Resonances

The case when both intermediate and final resonances are present will now be briefly considered. This case introduces several new components, present in the derivations of neither equation 5.28 nor 5.34, to the matrix element. These are as follows: the coupling between the tainted continua components, the connections between the excited resonances, and the respective resonance couplings to the continuum tainted by the opposite excited resonance. On top of this, the intermediate resonance needs to be taken into account when calculating the one-photon matrix element between the ground- and intermediate state, unlike what was done in the derivation of equation 5.34.

This case is relevant to neither of the studies, respectively discussed in chapter 7.2 and chapter 8.1, discussed as part of this thesis which used the models discussed in this chapter. As such, this case need not be treated in detail here. The full formulation is given by equation 68 in Jiménez-Galán et al. (2016).

However, as noted in Barreau et al. (2019), the single-resonance matrix element can be extended to the case of multiple non-overlapping resonances by addition of the non-background components associated with the different resonances. Thus, the equations presented here should be sufficient to model the case when each resonance may be considered independenlty

## 5.2 Angularly Resolved Atomic Phases

As a consequence of interactions between final scattering continua, the atomic phase may vary with the emitted electron direction (Cirelli et al. 2018; Heuser et al. 2016). In this work, the anisotropic behaviour of the atomic phase is studied for the case when a linearly polarised field ionises a noble-gas atom. Due to symmetry, the only variation present will be with the direction of the inclination $\theta$ with regards to the field. Thus, no resolution with regards to the corresponding azimuth $\varphi$ is required, and the angularly resolved intensity of sideband (SB) $2n$ can be calculated as the incoherent sum

$$\mathcal{I}_{2n}(\theta) = \sum\nolimits_{m_\mathrm{F}} \left| \mathcal{A}^{-}_{2n,m_\mathrm{F}}(\theta,\varphi) + \mathcal{A}^{+}_{2n,m_\mathrm{F}}(\theta,\varphi) \right|^2, \tag{5.36}$$

of angularly resolved transition amplitudes $\mathcal{A}^{\pm}_{2n,m_\mathrm{F}}(\theta,\varphi)$ corresponding to a final of electron magnetic quantum number $m_\mathrm{F}$.

The amplitudes $\mathcal{A}^{\pm}_{2n,m_\mathrm{F}}(\theta,\varphi)$ can be calculated by integrating the angularly resolved, two-photon matrix element $\mathcal{M}^{(2)}_{2n,m_\mathrm{F}}(\varepsilon_i;\theta,\varphi)$ with a given $m_\mathrm{F}$ over different intermediate energies $\varepsilon_i$. Said matrix element can be calculated using a coherent sum

$$\mathcal{M}^{(2)}_{2n,m_\mathrm{F}}(\varepsilon_i;\theta,\varphi) = \sum\nolimits_{\ell_\mathrm{F}} \mathcal{M}^{(2)}_{2n,l_\mathrm{F},m_\mathrm{F}}(\varepsilon_i) \times Y^{m_\mathrm{F}}_{\ell_\mathrm{F}}(\theta,\varphi), \tag{5.37}$$

over different final electron angular momenta $\ell_\mathrm{F}$ (Cirelli et al. 2018).

The systems treated here using the RABITT method are noble gases with the outer shell configuration $ns^2np^6$, $n \in \{2,3\}$, leading to emitted electrons of symmetry $p$ and $f$. Further, since only linearly polarised light is used, the relation $m_\mathrm{PI} = -m_\mathrm{F}$ between the parent ion (PI) magnetic quantum number $m_\mathrm{PI}$ and $m_\mathrm{F}$. Since the PI below the second ionisation threshold has a configuration $ns^2np^5$, $m_\mathrm{F}$ can be restricted to $m_\mathrm{F} \in \{-1,0,1\}$.

Expanding the squares of the sum in equation 5.36 gives the expression

$$\begin{aligned}\mathcal{I}_{2n}(\theta) = \sum\nolimits_{m_\mathrm{F}} &\left|\mathcal{A}^{-}_{2n,m_\mathrm{F}}(\theta,\varphi)\right|^2 + \quad \left|\mathcal{A}^{+}_{2n,m_\mathrm{F}}(\theta,\varphi)\right|^2 + \\ &\left|\mathcal{A}^{-}_{2n,m_\mathrm{F}}(\theta,\varphi)\,\mathcal{A}^{+}_{2n,m_\mathrm{F}}(\theta,\varphi)\right| \cos\left(2\omega_\mathrm{IR}\tau + \Delta\phi^{\mathrm{At}}_{2n,m_\mathrm{F}}\right)\end{aligned} \tag{5.38}$$

of the sideband amplitude, where $\omega_\mathrm{IR}$ is the IR frequency, and $\tau$ the pump-probe delay, and $\Delta\phi^{\mathrm{At}}_{2n,\mathrm{PI}}$ is the channel-specific atomic phase. As can be seen in equation 5.37, the cases of $m_\mathrm{PI} = \pm 1$ are identical. Remembering that only $m_\mathrm{F} \in \{-1, 0, 1\}$ needs to be treated, the equation

$$\Delta\phi^{\mathrm{At}}_{2n}\left(\hat{\Omega}\right) = \arctan \frac{2\left|\mathcal{A}^{-}_{2n,1}\mathcal{A}^{+}_{2n,1}\right| \sin\left(\Delta\phi^{\mathrm{At}}_{2n,1}\right) + \left|\mathcal{A}^{-}_{2n,0}\mathcal{A}^{+}_{2n,0}\right| \sin\left(\Delta\phi^{\mathrm{At}}_{2n,0}\right)}{2\left|\mathcal{A}^{-}_{2n,1}\mathcal{A}^{+}_{2n,1}\right| \cos\left(\Delta\phi^{\mathrm{At}}_{2n,1}\right) + \left|\mathcal{A}^{-}_{2n,0}\mathcal{A}^{+}_{2n,0}\right| \cos\left(\Delta\phi^{\mathrm{At}}_{2n,0}\right)}, \tag{5.39}$$

can be used to calculate the angularly dependent expression of $\Delta\phi^{\mathrm{At}}_{2n}$ (Cirelli et al. 2018).

# III

# Results

# Chapter 6

## Helium

Helium is first atomic system treated in this work. More precisely, the regions above the second ionisation threshold are considered. The chapter describes the study published as Petersson et al. (2017), discussed in section 6.1.

The ab-initio results presented in this chapter were derived by solving the time-dependent Schrödinger equation (TDSE) in the helium basis described in chapter 4.1; according to the methodology described in chapter 3.3, the associated Krylov method being used to solve the interaction component of the Hamiltonian. The propagations were performed in a box of 1200 au, containing a complex absorption potential (CAP) starting at a radius of $R_{\mathrm{CAP}} = 1000$ au, with a filter coefficient of $c_{\mathrm{CAP}} = -(1+5i)\times 10^{-4}$ au. Further, only total angular momenta of $L \leq 2$ were considered, excluding processes involving symmetries above ${}^1D^e$.

As it is the first noble gas, containing two protons and electrons, below, doubly excited (DES) autoionising states will be mainly described on the form of $n\ell n'\ell'$, where $n$ and $n'$ are the principal quantum numbers, and $\ell$ and $\ell'$ are the electron angular momenta, of the two electrons. A more complete classification of DESs can be found in Feagin et al. (1986), Herrick et al. (1980), Herrick et al. (1975), Lin (1984, 1986), and Tanner et al. (2000).

## 6.1 ATAS Above the $N = 2$ Threshold

The first and only study treated in this chapter used attosecond transient absorption spectroscopy (ATAS) to study helium above the second ($N = 2$) ionisation threshold. It was published in Physical Review A as Petersson et al. (2017).

The doubly excited states (DES) of the $sp^+_{2,n}\,{}^1P^o$ series below the $N = 2$ threshold of helium have previously been investigated via ATAS, using an extreme ultraviolet (XUV) pump and a visible (VIS) probe (Argenti et al. 2015; Ott et al. 2014). This revealed Autler-Townes (AT) splittings of the $2s2p\,{}^1P^o$ state, the lowest autoionising ${}^1P^o$ state, due to coupling with the $2s2p\,{}^1S^e$ state; as well as continuous inversions of the Fano profiles of higher $sp^+_{2,n}\,{}^1P^o$, states as the intensity of the dressing VIS increases.

So far, ATAS studies of electric coherence in helium have been restricted to regions below the $N = 2$ threshold, where the only parent ion possible after ionisation is the cationic ground state $He^+(1s)$. The present study seeks to apply the method to the autoionising region above the $N = 2$ threshold, where, apart from $He^+(1s)$, ionisation leads to the excited parent ions $He^+(2s)$ and $He^+(2p)$. In doing so, it extends the study of resonant features in transient absorption spectra (TAS) from the single channel to the multichannel case, which is a more common case in complex systems.

The studied system is shown in figure 6.1. As a pump, a weak attosecond XUV pulse is employed. It has a central frequency of $\omega_{\text{XUV}} = 2.5$ au, a spectral full width at half maximum (FWHM) of 0.18 au, and an intensity of $I_{\text{XUV}} = 1e11\,\frac{\text{W}}{\text{cm}^2}$. The probe is comprised of a moderately intensive femtosecond infrared (IR) pulse, with a central frequency of $\omega_{\text{IR}} = 0.057117$ au (corresponding to a wavelength of 798 nm), a spectral FWHM of 0.025 au, and an intensity of $I_{\text{IR}} = 4e12\,\frac{\text{W}}{\text{cm}^2}$. The laser parameters employed here are similar to those utilised in the aforementioned experiment by Argenti et al. (2015) and Ott et al. (2014). The time delay between the pump and the probe was varied, by increments of 84 as, from −10 fs to 20 fs.

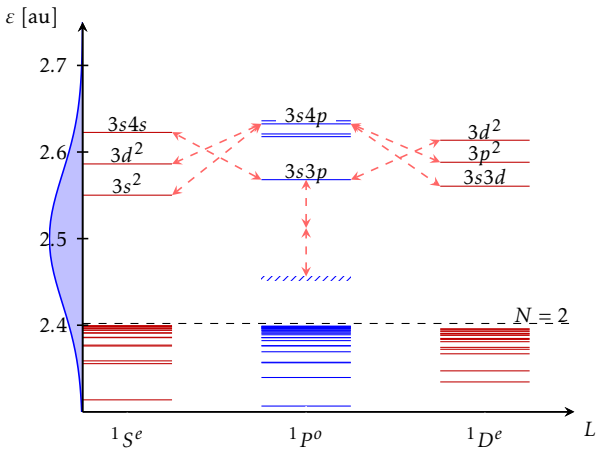


**Figure 6.1:** A schematic illustration of the studied energy region of helium. In blue and red, autoionising resonances of the $^1S^e$, $^1P^o$, and $^1D^e$ symmetries are shown (Burgers et al. 1995; M.-K. Chen 1997; Rost et al. 1997). The $N = 2$ threshold is shown as a dashed line. Additionally, the $^1P^o$ non-resonant continuum located two IR photons below the $3s3p$ spectrum is shown with diagonal stripes. The excited $^1P^o$ spectrum is ionised by an XUV probe with the frequency distribution shown to the left. It has a frequency of $\omega_{\text{XUV}} = 2.5$ au and a FWHM of 0.18 au. Transitions nearly resonant with the frequency of $\omega_{\text{IR}} = 0.057115$ au of the IR (with a FWHM of 0.025 au) are shown with arrows. It should be noted that the resonance labels used here (Martín et al. 1991) are only approximate. The figure is republished with modifications from Fig. 1 in Petersson et al. (2017).

Compared to the single-channel case, the resonances observed above the $N = 2$ threshold are broader and less bright, as would be predicted by dipole-transition propensity rules of two-electron atoms (Rost et al. 1997). Even so, in the results presented here, IR-induced, single-photon beatings between the $3s4p\,^1P^o$ DES and the resonant $3\ell 3\ell'\,^1S^e$ and $^1D^e$ states are observed. These beatings are illustrated in figure 6.1. Also illustrated in figure 6.1 are the two-photon beatings between the $3snp\,^1P^o$, $n = 3, 4$ DESs and the $^1P^o$ continuum just above the $N = 2$ threshold, leading to the formation of a multichannel, correlated two-electron wave packet. Both effects strongly distort the $3snp$ Fano profiles, which vary with the time delay. As such, they demonstrate control of the multichannel resonant profiles in the same way as has been demonstrated by Argenti et al. (2015) and Ott et al. (2014) for the single-channel case.

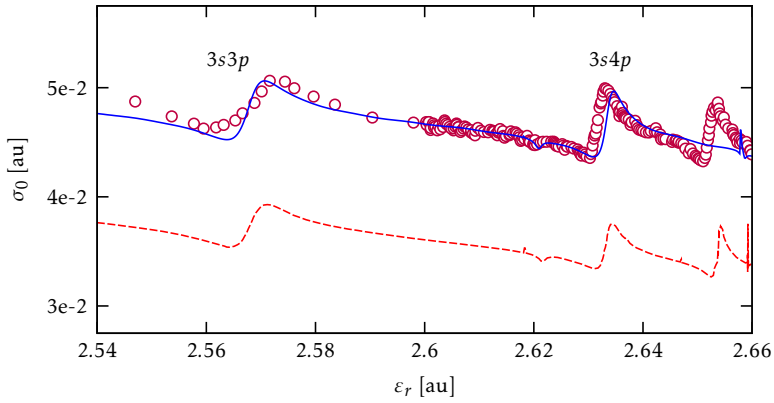


**Figure 6.2:** The cross section $\sigma_0(\varepsilon_r)$, as a function of the response energy $\varepsilon_r$, in the studied region of helium. In blue, the calculated spectrum is shown. For comparison, similar data from the available literature is shown. In dashed red, the results from a comparable, theoretical spectrum, calculated by Moccia et al. (1991), is shown; and, with circles, an experimental spectrum published by Menzel et al. (1996), renormalised. This figure is here republished with modifications from Fig. 2 in Petersson et al. (2017).

### 6.1.1 The Cross Section

In order to validate the quality of the basis in the relevant energy region above the $N = 2$ threshold, the field-free spectrum $\sigma_0(\omega_r)$ was calculated and compared to available experimental (Menzel et al. 1996), and theoretical (Moccia et al. 1991), data. The result of this can be found in figure 6.2. As can be seen, up to around 2.65 au, the results presented here are in excellent agreement especially with the theoretical reference results. In particular, the Fano profiles approximately corresponding to the $3s3p$ and $3s4p$ members of the dominant series of DES are clearly visible[1].

[1] It may be noted, however, that, due to static correlation, DESs can not be modeled exactly using independent-particle single-configuration representations.

### 6.1.2 The Attosecond Transient Absorption Spectrum

The calculated attosecond transient absorption spectrum $\sigma(\varepsilon_r, \tau)$ is shown as a function of the response energy $\varepsilon_r$ and the pump-probe time delay $\tau$ in figure 6.3. Negative time delays correspond to the IR probe arriving prior to the pump.

Due to the low frequency and intensity of the probe, the system remains unaffected until the arrival of the XUV, so that, when the probe arrives before the pump, $\sigma(\omega_r, \tau) = \sigma_0(\omega_r)$. The features visible in this region are thus easily mapped onto figure 6.2. The main features are the bright $3snp$, $n = 3, 4$ DESs. Removing this background, the time-dependent features of the spectrum become even more lucid, as seen in figure 6.4.

When $\tau$ increases, the pulses start to overlap. As this happens, the $3s3p\ ^1P^o$ resonance experience AT splittings due to coupling with the higher energy $3s4s\ ^1S^e$ and $3d^2\ ^1D^e$ dark states. This is especially clear in figure 6.4, after removing the background, where there is a clear broadening of the $3s3p$ resonance for delays of $\tau \approx 0$. Similar features were found, even for quite low intensities, below the $N = 2$ threshold by Argenti et al. (2015), due to couplings between the $2p^2\ ^1S^e$ state and $2p^+_{2,n}\ ^1P^o$ states. For the lowest such state, $2s2p$, this is visible at even lower intensities. Due to the higher density of dark states, the splittings presented in this work are more involved than those found below the $N = 2$ threshold.

For positive values of $\tau$, when the probe arrives after the pump, two main features, both typical of the ATAS spectrum (Ding et al. 2016) are visible.

Firstly, there is the transversal hyperbolic fringes slowly converging towards nearby resonances. This is most clearly visible for the $3s3p$ and $3s4p$ resonances. These result from the sharp modulation in population experienced by the states due to the probe. As the time delay increases, the time-evolution of the dipole converges to the field-free case, and, with it, so does the spectrum. Thus, it can be seen that these fringes trends towards the resonances with an increase in $\tau$.

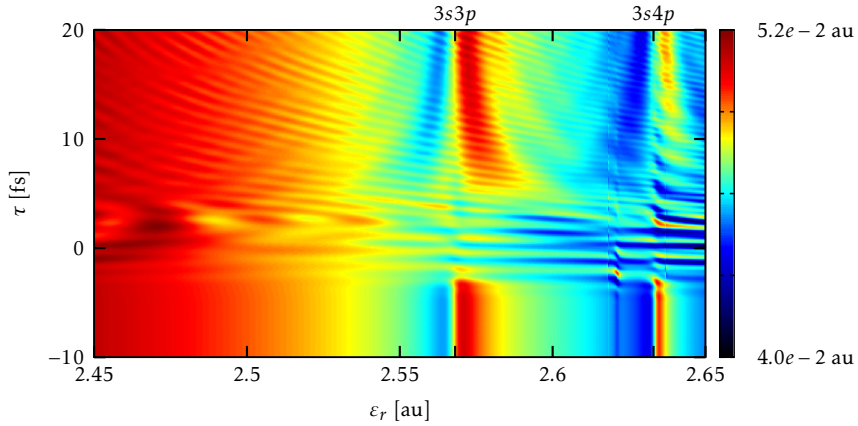


**Figure 6.3:** The ATAS spectrum above the $N = 2$ threshold of helium. The abscissa shows the response energy $\varepsilon_r$ and the ordinate shows the time delay $\tau$ of the probe. This figure is here republished with modifications from Fig. 3 in Petersson et al. (2017).

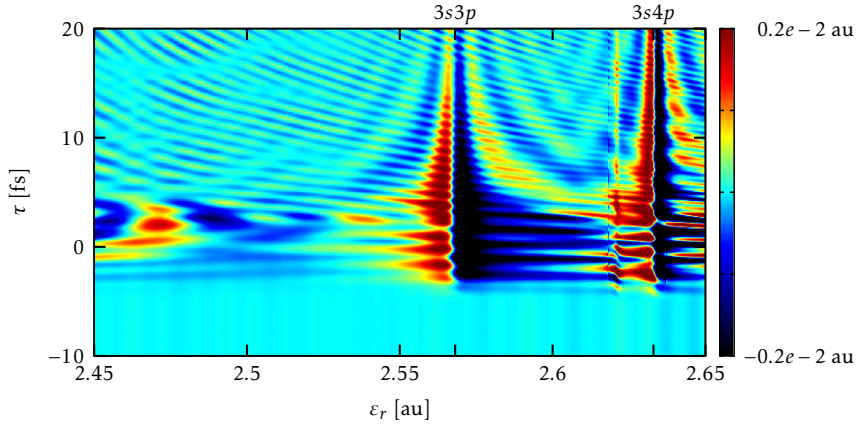


**Figure 6.4:** The ATAS spectrum above the $N = 2$ threshold of helium, with the background removed. The abscissa shows the response energy $\varepsilon_r$ and the ordinate shows the time delay $\tau$ of the probe. Save for the removal of the time-independent component, this figure is identical to figure 6.3.

Another well-known feature of the ATAS spectrum also present is the densely packed transversal fringes visible in figure 6.3. These arise from interference between direct ionisation by one XUV photon and the resonantly enhanced excitation by one XUV photon and subsequent absorption or emission of several IR photons via intermediate states. For the case of a $k$ IR photon exchange after excitation to an intermediate resonance $3snp$ of energy $\varepsilon_{3snp}$, these fringes have an frequency of $\left|\varepsilon_r - \varepsilon_{3snp}\right| \approx k\omega_{\mathrm{IR}}$ at the response energy $\varepsilon_r$. These beatings can be further studied by considering the bidimensional spectrum.

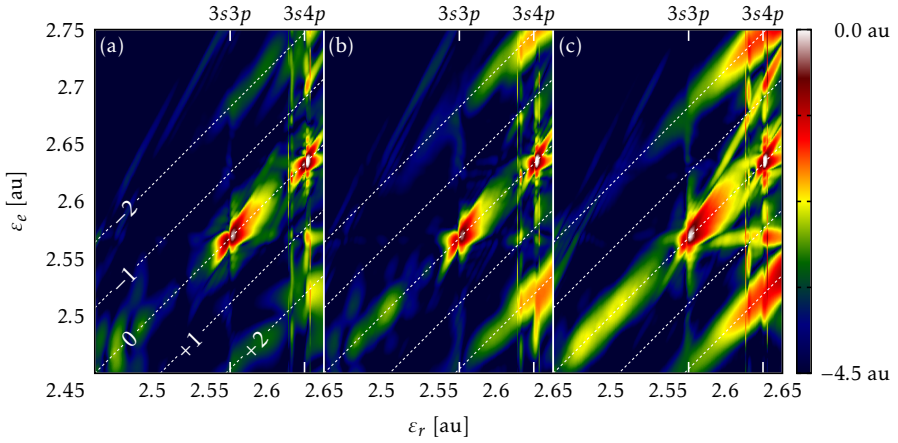


**Figure 6.5:** In (a), the natural logarithm $\ln|\tilde{\sigma}(\varepsilon_r, \varepsilon_e - \varepsilon_r)|$ of the bidimensional spectrum above the $N = 2$ threshold of helium is shown. The abscissa shows the response energy $\varepsilon_r$, and the ordinate shows the excitation energy $\varepsilon_e$. The diagonal, dashed lines are separated by $\omega_{IR}$. Maxima near these lines correspond to the number indicated by their respective labels of absorbed (positive) and emitted (negative) photons. Both (b) and (c) show similar plots for artificial cases. In (b), the ${}^1S^e$ (excluding the ground state) has been artificially removed during propagation. In (c), the same has been done to the ${}^1D^e$ spectrum. This figure is here republished with modifications from Fig. 4 in Petersson et al. (2017).

### 6.1.3 The Bidimensional Spectrum

Figure 6.5a shows the logarithm of the absolute value of the bidimensional spectrum, $\tilde{\sigma}(\varepsilon_r, \varepsilon_e - \varepsilon_r)$, where $\varepsilon_e$ is the excitation energy. Prior to applying the fast Fourier transform to $\sigma(\omega_r, \tau)$, the spectrum was switched off with a smooth step function at high $\tau$. Although this limits the resolution of the spectrum along the $\varepsilon_e$ axis, the main features remain visible.

The dashed lines in the figure indicate a net exchange of an integer number of IR photons. On the $\varepsilon_r = \varepsilon_e$ diagonal, corresponding to a net absorption of zero IR photons, both the $3s3p$ and the $3s4p$ states are seen.

At the lines indicating a net exchange of one IR photon, beatings at the response energy of the $3s4p\ ^1P^o$ state can be observed. These peaks are visibly shifted away from the dashed lines, indicating a Stark shift. Such beatings are only possible if both the states involved are populated by the pump (i.e., dipole connected to the ground state) as well as dipole connected to each other. Although these criteria are, on the surface, contradictory, it is possible for the dressed states to be modified by the field to take on a component of a different symmetry (as an example, Argenti et al. [2015] observed the $2p^2\ ^1S^e$ state taking on a $^1P^o$ component). Thus, these beatings have several possible origins. They may be due to beatings between (i) the $3s4p$ state and lower $^1S^e$ and $^1D^e$ states, (ii) the $3s3p$ state and higher $^1S^e$ and $^1D^e$ states, or (iii) beatings between the dressed $3s3p$ and $3s4p$ states; or a combination thereof. Several of these potential beatings are indicated with arrows in figure 6.1.

Turning to the lines in figure 6.5 indicating a net exchange of two IR photons, several more features are visible. Here, beatings between the $3s3p\ ^1P^o$ and $3s4p\ ^1P^o$ states, with the $^1P^o$ continuum of lower energy (of $\omega_e \approx 2.45$ au and $\omega_e \approx 2.52$ au, respectively). These beatings also leave a mark by populating the nonresonant continuum, contributing to a maximum at $\omega_r \approx \omega_e$ for low energies.

To gain deeper insight into these beatings, consider figures 6.5b and 6.5c.

These are analogous to figure 6.5a, but with the $^1S^e$ symmetry (in 6.5b) and $^1D^e$ symmetry (in 6.5c), respectively, artificially removed during the propagations. Although these calculations are not physical, they can be used to determine to what extent the beatings observed in figure 6.5a are due to the $^1S^e$ and $^1P^e$ states.

After removal of the $^1S^e$ states, the main difference from the physical case is the decrease of the one-photon beatings visible at a response energy of $\varepsilon_r \approx \varepsilon_{3s4p}$. The same is not seen when the $^1D^e$ states are excluded, confirming that the majority of the one-photon beating occur with states of the $^1S^e$, rather than the $^1D^e$, symmetry.

All other structures discussed above are even more pronounced in both figure 6.5b and figure 6.5c than in figure 6.5a. This shows that both the $^1S^e$ and the $^1D^e$ symmetries are significantly involved in all these features.

### 6.1.4 Conclusions

In the present study, ATAS has been used to examine helium above the $N = 2$ threshold, where several ionisation channels are open. By using an XUV pump and an IR probe, with parameters similar to those employed by Argenti et al. (2015) and Ott et al. (2014), it is possible to induce sizable resonant one-photon transitions between the $3s4p\ ^1P^o$ state and lower $3\ell^2\ ^1S^e$ and $3\ell^2\ ^1D^e$ states. Furthermore, two-photon beatings between the $3s3p\ ^1P^o$ and $3s4p\ ^1P^o$ states and the lower $^1P^o$ continuum were observed, leading to the formation of a multichannel two-electron correlated wave packet. Thus, like for resonances lying below the $N = 2$ threshold, it is possible to control the multichannel two-electron correlated wave packet.

Multichannel ionisation continua are the rule, rather than the exception, in most atoms and molecules. The results discussed here, however, show that the additional complications brought by the opening of additional continua should not pose major challenges. The only feature observed here, which so far has not been observed for the single-channel case, is the two-photon beatings

between autoionising resonances and the pure continuum. One limitation that was observed here, however, is that some features may not be unambiguously attributed to specific processes, but may rather have multiple causes. Such features could be further studied by adding an IR component to the pump, which is a standard practice in femtosecond pump-probe spectroscopy and was implemented for the case of neon, as part of in another study discussed in this work, namely the study discussed in chapter 7.1.

# Chapter 7

## Neon

The second atom treated in this thesis is neon, which has been analyzed using accurate ab-initio calculations. This was done between the first and second ionisation thresholds. Neon, being the second noble gas, has the full $2s^2 2p^6$ valence shell configuration. In the studied energy region, this leads to several autoionising resonances. Specifically, the $2s^1 2p^6 n\ell$- and $2s^2 2p^4 3s3p$-resonances are relevant to the discussion below[1].

The propagations introduced in this chapter were carried out in an XCHEM combined Gaussian B-spline (GABS) basis – the XCHEM approach being able to accurately describe electron correlation in the ionisation continuum of many-electron systems.

The basis used was designed to include ${}^1S^e$, ${}^1P^o$, ${}^1D^e$, and ${}^1F^o$ symmetries. Continuum states including four different parent ions (PI) were considered. These PI correspond to the electron configurations $1s^2 2s^1 2p^6$ and $1s^2 2s^2 2p^5$, which were augmented by an additional electron to create neutral states. The PI wave functions were calculated through a state average CAS(7,14) calculation

[1] It should be mentioned that the $2s^2 2p^4 3s3p$ resonance was not included in the ab-initio calculations presented below. This is because the $N$ electron basis is built by augmenting the $N-1$ electron parent ion (PI) states (with $2s^2 2p^5$ and $2s2p^6$ configurations) with the excited electron. This will be discussed in the context of the individual studies below, when it appears to be relevant for the presented results.

(i.e. a complete active space 7 electrons distributed between 14 orbitals) which included all configurations, subject to spin and symmetry restrictions, for seven electrons distributed over the $2s$, $2p$, $3s$, $3p$, $3d$ and $4s$ orbitals, with the $1s$ orbital always being doubly occupied. The PI orbitals were represented by a standard cc-pVQZ (Dunning 1989) basis of localised Gaussian functions. The monocentric Gaussian functions were built from an even-tempered sequence of 22 exponents. The XCHEM methodology is described in more detail in section 4.2.

In section 7.1, neon is studied using attosecond transient absorption spectroscopy (ATAS). Although not yet published, it is currently the subject of a manuscript that is being prepared. In section 7.2, reconstruction of attosecond beatings by interference of two-photon transitions (RABITT) is used to study neon below the second ionisation threshold, showing the possibility of extending the method to multi-resonance regions. This study was originally published as Barreau et al. (2019).

## 7.1 ATAS Below the Second Threshold

The first neon study making up part of this thesis employs attosecond transient absorption spectroscopy (ATAS) to probe energies above the first ionisation threshold. In order to study beatings with states not dipole-connected to the ground state, a combined extreme ultraviolet (XUV) near-infrared (NIR) pump is used. This method was previously used by Ding et al. (2016), who used experiment and R-matrix ab-initio calculations to study one-photon beatings between the $2s^{-1}3p\,^1P^o$ with nearby $^1S^e$ and $^1D^e$ resonances. In this study, a similar theoretical setup is employed to further study the same autoionising region, in order to test the validity of the XCHEM approach. It is currently the subject of a manuscript that is being prepared.

A schematic illustration of the studied system can be found in figure 7.1. Several $2s^{-1}n\ell$ resonances (below referred to as $n\ell$), visible in the figure, are relevant to the discussion below. The $2p^{-2}3s3p$ resonance was not included in the calculations, and will not be visible in the data presented below.

The laser parameters used are similar to those used by Ding et al. (2016): The XUV has a central frequency of $\omega_{\text{XUV}} = 1.71$ au and a spectral full width at half maximum (FWHM) of 0.22 au. The NIR has a frequency of $\omega_{\text{NIR}} = 0.0588$ au, and a spectral FWHM of 0.02 au, corresponding to a temporal FWHM of 7.3 fs. The intensity of the NIR probe is $2 \cdot 10^{12}\ \frac{\text{W}^2}{\text{cm}^2}$, while the NIR pump intensity used is $2 \cdot 10^{11}\ \frac{\text{W}^2}{\text{cm}^2}$. The time-delay $\tau$ was varied between $-20$ fs and 60 fs.

Like what was observed by Ding et al. (2016), the ATAS spectrum showed one-photon beatings between the $3p\,^1P^o$ resonance and the nearby $3s\,^1S^e$ and $3d\,^1D^e$ resonances. Further, both one- and two-photon beatings between the nonresonant $^1P^o$ continuum and nearby resonances are observed.

While Ding et al. (2016) used a combination of experiment and R-matrix calculations to carry out their study, here, the ab-intio calculations presented here made use of an XCHEM basis. The XCHEM methodology is described in more detail in chapter 4.2. Here, a basis of 600 au was used, with B-splines

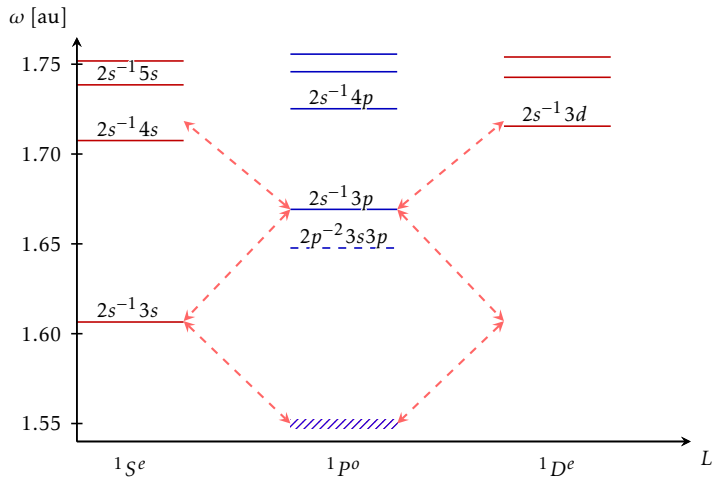


**Figure 7.1:** A schematic illustration of the studied autoionising neon resonances. In blue and red, the autoionising resonances of the $^1S^e$, $^1P^o$, and $^1D^e$ symmetries are shown. The given values are extracted from the XCHEM basis used during propagation. The $2p^{-2}3s3p$ resonance, which was not included in the XCHEM calculations, is marked with a dashed line. It is taken from Schulz et al. (1996), and shifted to align the XCHEM and reference $2s^{-1}3p$ resonance positions. The area marked with diagonal stripes exhibit one- and two-photon beatings. The black arrows show relevant near-resonant NIR transitions. Although the NIR frequency is $\omega_{\text{NIR}} = 0.058$ au, the arrows connected to the $3p$ resonance are designed to correspond to the beatings in figure 7.4.

of order $k = 7$ and a node separation of 2 au starting at 7 au, following the specifications described in the beginning of this chapter. Further, a complex absorption potential (CAP) starting at $R_{\text{CAP}} = 400$ au with a filter coefficient of $c_{\text{CAP}} = -4i \cdot 10^{-4}$ au was used.

### 7.1.1 The Cross Section

As a validation of the basis used in this work, the field-free spectrum calculated with an XUV pump is shown in figure 7.2, together with experimental literature results. In both cases, the background shape is comparable. Further, the Fano profiles corresponding to the $np$ series of resonances is clearly well represented.

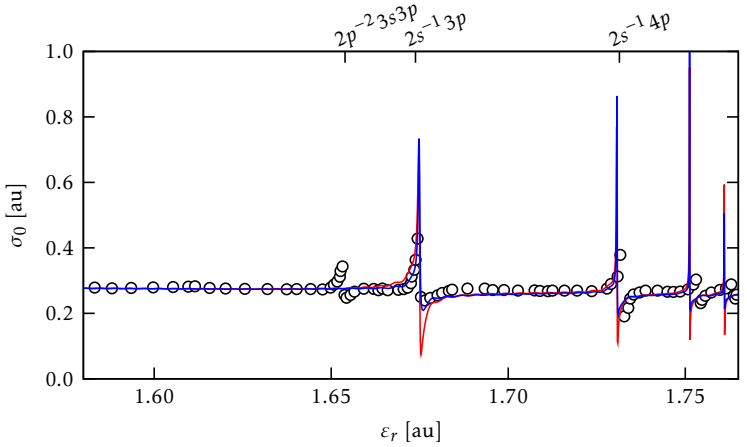


**Figure 7.2:** The neon spectrum. In red, the cross section calculated using only the XUV component of the pump is shown as a function of the response frequency $\omega_r$. In blue, the corresponding value using the full XUV-NIR pump is shown. For comparison, the black circles show experimental literature values (Ding et al. 2016), measured using a comparable XUV pump. These have been normalised in order to be comparable to the presented XCHEM data. The calculated data has been shifted by $5.5e - 3$ au to approximately align the $3p$ resonances.

The main difference between the calculated XCHEM data and experiment is the $3s3p$ resonance, which is missing in the data calculated here. As noted in the introduction, this is due to the corresponding PI not being included.

Figure 7.2 also shows the corresponding spectrum when using the combined XUV-NIR pump. While the NIR component somewhat obscures the Fano profiles, the general shape of the spectrum is kept consistent. As the main purpose of the low-frequency pump component is to populate the ${}^1S^e$ and ${}^1D^e$ symmetries, this is what would be desired and expected.

### 7.1.2 The Attosecond Transient Absorption Spectrum

In figure 7.3, the ATAS spectrum $\sigma(\omega_r, \tau)$ is shown. With the exception of the missing $3s3p$ resonance, the same features discussed by Ding et al. (2016) can

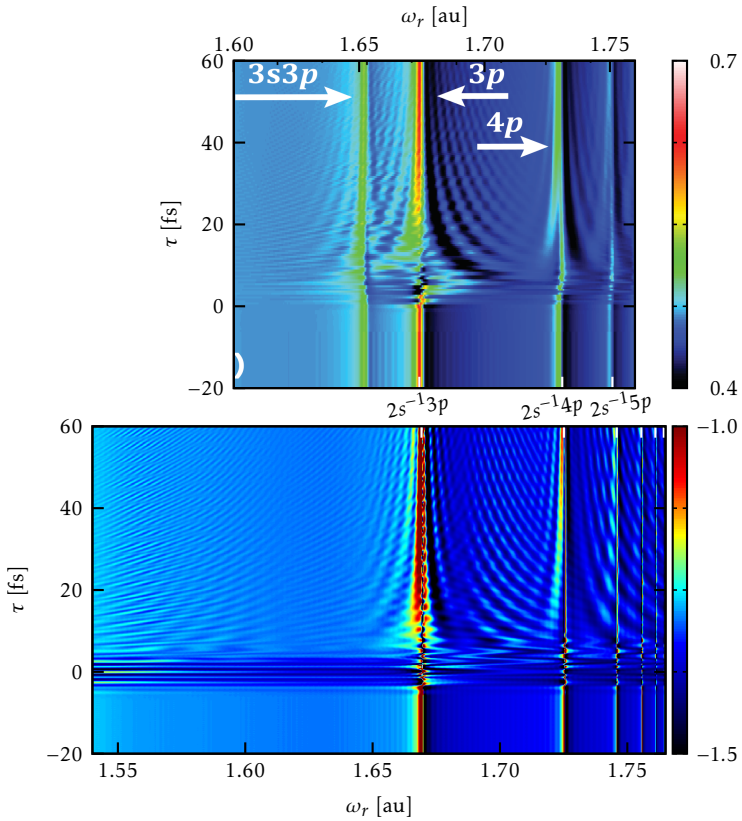


**Figure 7.3:** The neon ATAS spectrum. The lower panel shows the results of the ab-initio, XCHEM calculations. The upper panel shows literature reference data from R-matrix calculations (Ding et al. 2016). The abscissa shows the response frequency $\omega_r$, while the ordinate shows the pump-probe time delay $\tau$. The $^1P^o$ $2s^{-1}np$ series of resonances is visible, and $2s^{-1}np$, $n \in \{3,4,5\}$ resonances have been labeled.

be seen:

For significant negative time-delays $\tau$, the NIR control pulse arrives before the pump. Due to the low probe intensity, it is incapable of exciting the atom, leading to a $\tau$-independent spectrum.

At significant positive delays, two main features, characteristic of ATAS spectra, are present: Firstly, near the resonances, hyperbolic, slow-varying fringes (corresponding to the buildup of the Fano resonance profiles) can be seen. This is most clearly visible for the $3p$ and $4p$ resonances. Secondly, throughout the figure, rapid hyperbolic fringes can be seen. These fringes are indicative of interference between the population ionised directly by the probe and that which has, after excitation by the probe, absorbed or emitted a non-zero net amount of probe photons. For a net absorption of $k$ photons, resonantly enhanced by a resonance $n\ell$ located at a position $\varepsilon_{n\ell}$, such a beating, appearing at a response frequency of $\omega_r$, will have a frequency of $\omega_\tau = |\omega_r - \varepsilon_{n\ell}| \approx k\omega_{\text{NIR}}$. In order to further study these beatings, the bidimensional spectrum will be studied.

### 7.1.3 The Bidimensional Spectrum

Figure 7.4 shows the logarithm of the bidimensional spectrum. Here, at large time-delays, the spectrum was cut off before applying the fast Fourier transform.

The dashed, horizontal lines in the figure correspond to a net exchange of an even number of probe photons. With these lines in mind, the features present at the response energy of $\omega_r \approx 1.55$ au are worth considering. Here, two distinct beatings with the continuum can be seen, both enhanced by dotted lines.

Firstly, a two-photon beating resonantly enhanced by the $3p$ state is present. As is shown in figure 7.1, this beating may well be resonantly enhanced by the $3s$ resonance. Secondly, a weaker, one-photon beating with the $3s$ resonance is visible. For the version of ATAS which employs a weak XUV probe, which was employed in chapter 6.1, no such beating would be present. In the present

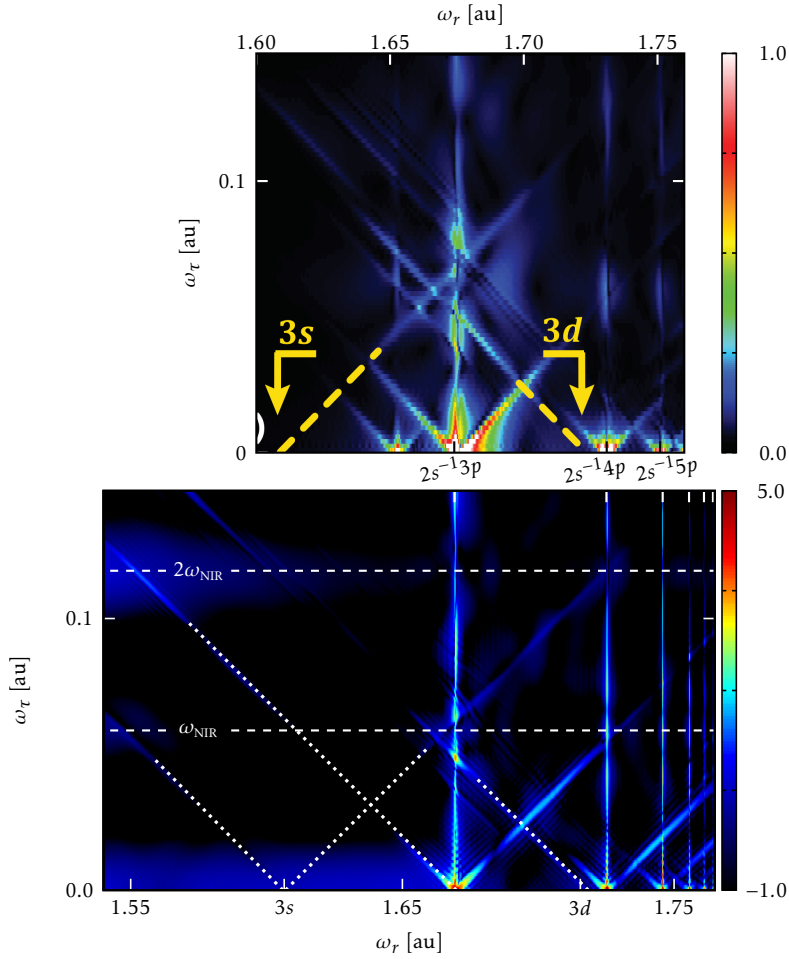


**Figure 7.4:** The bidimensional spectrum $\bar{\sigma}(\omega_e, \omega_\tau)$. The lower panel shows the natural logarithm of the results of the ab-initio, XCHEM calculations. The upper panel shows literature reference data from R-matrix calculations (Ding et al. 2016). The abscissa shows the response frequency $\omega_r$, and the ordinate the Fourier frequency $\omega_\tau$. Several $^1P^o np$ resonances are directly observed and marked, while the $^1S^e 3s$ and $^1D^e 3d$ states, also marked, are indirectly observed through their interactions with $^1P^o$ symmetry states. The horizontal, dashed lines correspond to one- and two-photon beatings. The diagonal, dotted lines have been added to enunciate several one-photon beatings $3p\ ^1P^o$ state and nearby $^1S^e$ and $^1D^e$ states, as well as one- and two-photon beatings between the $3s\ ^1S^e$ and $3p\ ^1P^o$ states and the $^1P^o$ continuum.

work, however, a mixed XUV-NIR pump is employed, allowing the probe to populate the ${}^1S^e$ and ${}^1D^e$ continua, giving rise to one-photon beatings.

Further more, in agreement with what was observed by Ding et al. (2016), two local maxima indicating one-photon beatings are present at response energies $\omega_r \approx \varepsilon_{3p}$ near the $3p$ resonance. As can be seen in figure 7.1, these features are attributable to beatings with the $3s$ and $3d$ states, in correspondence to what was concluded by Ding et al. (2016). In figure 7.4, these beatings are emphasised with dotted lines.

### 7.1.4 Conclusions

To conclude, in the current study, the well-established ATAS method has been used to study neon above the first ionisation threshold. Using a mixed XUV-NIR pump, beatings with states not dipole-connected to the ground state are observed. This allowed beatings between the $3p\,{}^1P^o$ resonances and the $3s\,{}^1S^e$ and $3d\,{}^1D^e$ resonances, similarly to what was observed by Ding et al. (2016). By extending the observed region to lower energies, resonantly enhanced both one- and two-photon beatings with the continuum were observed.

The results presented here show excellent agreement with previous experiment and theory (Ding et al. 2016), and thereby further serves to validate the XCHEM methodology.

## 7.2 RABITT in the Vicinity of Multiple Resonances

The next study to be discussed herein pertains to the extension of interferometric measurements – in particular reconstruction of attosecond beatings by interference of two-photon transitions (RABITT) – to energy regions which include multiple resonances. The study was originally published in Physical Review Letters as Barreau et al. (2019).

Although, as noted in chapter 3.2, RABITT has been very successful in measuring the spectral atomic phases in systems such as molecules and solids, as well as atoms; these studies have so far been restricted to energy-regions containing one or no resonances. Corresponding conditions are easily met in simpler systems, like helium (Gruson et al. 2016), as well as by carefully choosing studied energy ranges in more complex atoms, like argon (Kotur et al. 2016).

In many-electron systems, though, this is the exception rather than the rule, as their resonances tend to be more tightly packed. For these atoms, performing accurate, full-electron, time-dependent theoretical calculations would be needed to guide experiment. Such calculations, however, are extremely difficult to carry out, as they require the accurate treatment of electron correlation in the populated continuum.

For these cases, where more accurate calculations are unavailable, simpler models, capable of filling their role, disentangling the contributions of the different states, are highly desirable.

In the present study, RABITT is used to study the autoionising region of neon below the second ionisation threshold, where several autoionising resonances are present, using both accurate attosecond interferometric experiments and ab-initio full-electron time-dependent calculations. In addition to this, a simple model, based on the theory presented in chapter 5, has been used to successfully disentangle the contributions of distinct resonances.

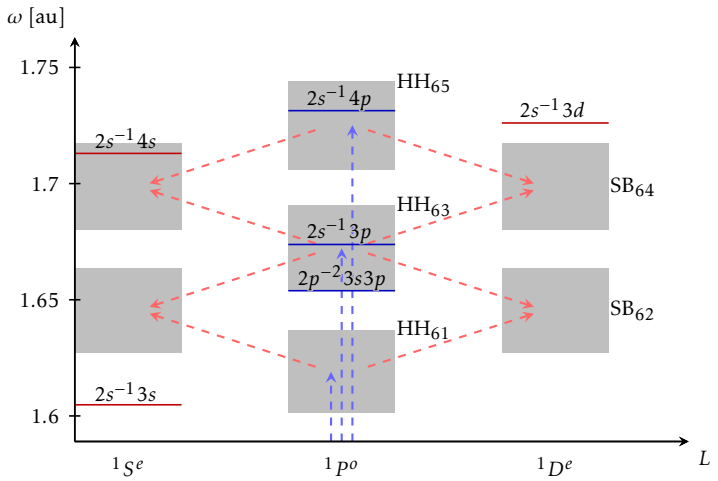


**Figure 7.5:** A schematic view of the neon region, including relevant resonance energies, studied using RABITT. The abscissa shows the state symmetry while the ordinate gives the excitation frequency $\omega$, where . The harmonics, $HH_{61}$, $HH_{63}$, and $HH_{65}$, are populated using a single XUV-APT pump photon, shown in blue; after which that population is transferred to sidebands $SB_{62}$ to $SB_{64}$ with an IR photon. The harmonic and sideband positions were varied over the areas shown in gray, by varying the driving IR frequency. This figure is here republished with modifications from Fig. 2 in Barreau et al. (2019).

A schematic illustration of the studied region can be seen in figure 7.5. The infrared (IR) probe frequency was varied between $\omega_{IR} = 0.0262$ au and $\omega_{IR} = 0.0268$ au, corresponding to wavelengths of around $\lambda_{IR} = 1700$ nm. In total, 16 driving frequencies were used in the experiment and 33 in the theory. In the experiment, for each delay $10^4$ laser shots were averaged. It is the harmonics of this IR frequency that make up the extreme ultraviolet (XUV) attosecond pulse-train (XUV-APT) which was used as the RABITT pump. The IR probe intensity was selected as $I_{IR} \approx 2 \cdot 10^{10} \frac{W}{cm^2}$.

Two sidebands (SBs) are considered during this study – namely $SB_{62}$, and $SB_{64}$. These are populated by the nearby high harmonics (HHs) $HH_{61}$, $HH_{63}$, and $HH_{65}$. As the IR frequency is shifted, so are the associated harmonics and sidebands. As is illustrated in figure 7.5, as the energy is shifted, several

resonances become involved in the two-photon transitions. While $SB_{62}$ will be affected mainly by the $3p$ resonance, $SB_{64}$ is affected by several resonances – namely the $3p$, $4p$, and $4s$ ones. The experimental positions of these resonances are shown in figure 7.5, as well as being referenced below, and are, along with the corresponding resonance widths, taken from Schulz et al. (1996) in the case of the $^1P^o$ symmetry and from Min et al. (2008) in the case of the $^1S^e$ and $^1D^e$ symmetries.

Given a time-delay $\tau$, the $2nth$ RABITT sidebands are populated by interference between $\mathcal{A}^-_{2n}(\tau)$ and $\mathcal{A}^+_{2n}(\tau)$ – the populations transferred via the lower and upper harmonic, respectively. For each driving frequency, the sideband signal was, after integration over an energy range 0.01 au, fitted to the equation, equivalent to equation 3.47,

$$I_{2n}(\tau) = \left|\mathcal{A}^-_{2n}\right|^2 + \left|\mathcal{A}^+_{2n}\right|^2 + \left|\mathcal{A}^-_{2n}\mathcal{A}^+_{2n}\right| \cos\left(2\omega_{\mathrm{IR}}\tau + \Delta\phi_{2n}\right), \tag{7.1}$$

where $\Delta\phi_{2n} = \Delta\phi^{\mathrm{APT}}_{2n} + \Delta\phi^{\mathrm{At}}_{2n}$ contains both the phase $\Delta\phi^{\mathrm{APT}}_{2n}$ related to the APT attochirp and the atomic phase difference $\Delta\phi^{\mathrm{At}}_{2n}$. Thus, in order to derive $\Delta\phi^{\mathrm{At}}_{2n}$, $\Delta\phi^{\mathrm{APT}}_{2n}$ needs to be calculated and subtracted. For the ab-initio theory, this was done by designing the pulses so that $\Delta\phi^{\mathrm{APT}}_{2n} = 0$. For the experiment, it was obtained from a linear fit of the phases of the oscillations of the non-resonant sidebands as a function of energy (Mairesse et al. 2003). The calculated value, 18 $\frac{\mathrm{as}}{\mathrm{eV}}$, is fairly independent of the driving IR frequency and is in very good agreement with calculations of the recombination time for the short trajectories using Lewenstein's (1994) model.

The physical system was theoretically described solving the time-dependent Schrödinger equation (TDSE) according to the methodology described in chapter 3.3, with the exact solution employed for the interaction component. The propagation basis was described using the XCHEM approach, discussed in chapter 4.2, according to the specifications laid out in the introduction to this chapter. The XCHEM B-splines were chosen to be of order $k = 7$, with a node separation of 0.8 au, and were restricted to radii between 7 au and 2000 au. The

resonance positions calculated by XCHEM are not identical to those obtained through literature. To compensate for this, all theoretical results presented below have been shifted upwards in energy by $4.6 \cdot 10^{-3}$ au. This value has been chosen to make the theoretical and experimental $3p$ resonance positions coincide.

The experimental study was performed on The Ohio State University attosecond beamline, where a 1 kHz repetition rate Ti:sapphire laser (SpitFire) of 12 mJ energy was used to pump an optical parameter amplifier (HE-TOPAS). The 1.5 mJ 60 fs idler pulses were split into two arms at the entrance of a Mach-Zehnder interferometer with an 8 mm-diameter silver holed mirror. For the high-harmonic generation (HHG), the outer part (of intensity $I \approx 1.1 \cdot 10^{14}\ \frac{\mathrm{W}}{\mathrm{cm}^2}$) was focused into a $CO_2$ (carbon dioxide) gas jet with a lens of focal length $f = 500$ mm. The remaining IR is spatially filtered by an iris. The generated XUV-APT was focused with a toroidal gold mirror in a neon gas jet in the interaction region of a 1 m long magnetic bottle electron spectrometer (MBES). The inner part of the beam is delayed by propagating in a glass wedge on a piezoelectric translation and recombined with the XUV-APT on a 6mm diameter silver holed mirror. Both beams were spatially and temporally overlapped in the source region of the MBES to induce two-colour two-photon ionisation.

Finally, a simple model has been used to describe the variation of the atomic phase difference for both $SB_{62}$ and $SB_{64}$, making it possible to disentangle the phase contributions from the involved autoionising states, which in turn allows for the extraction of information about individual resonances directly from experiment. The model was developed according to theory described in more detail in chapter 5. Such models are vital to interpreting interferometric experiments in more complex systems, where accurate ab-initio calculations are unavailable.

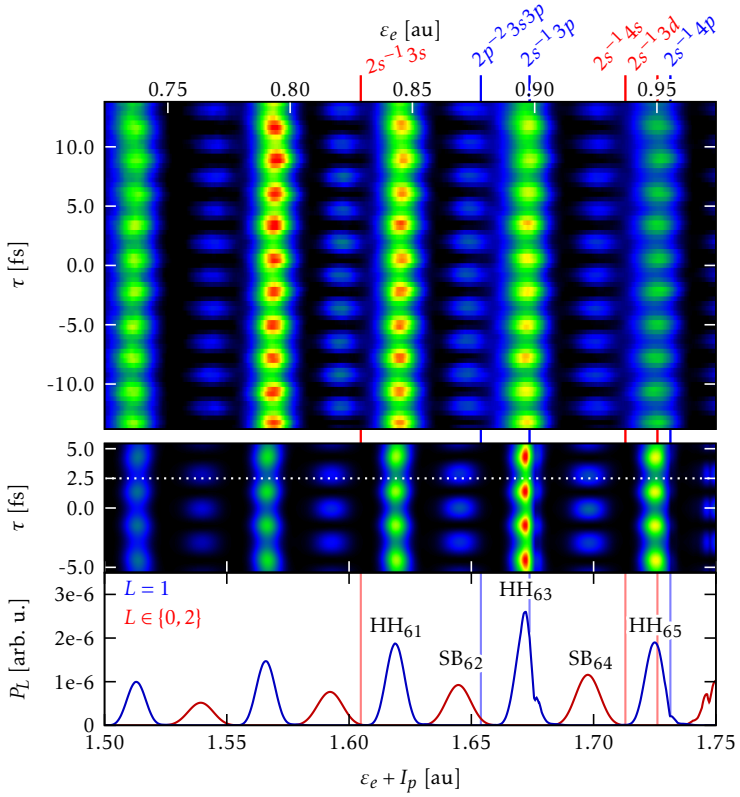


**Figure 7.6:** A sample RABITT PES $P$, for a selected IR frequency of $\omega_{\text{IR}} \approx 2.65 \cdot 10^{-2}$ au, corresponding to a wavelength of $\lambda_{\text{IR}} \approx 1718$ nm. Two spectra are shown – in the upper panel, the experimental spectrum can be seen, whereas the middle panel contains the theoretical spectrum. The bottom panel contains – divided by the symmetry $L$ into $L = 1$ (in blue) and $L \in \{0, 2\}$ (in red) – a cross section $P_L$ of the theoretical spectrum for a time delay of $\tau = 2.5$ au. Lastly, several relevant resonances have been marked. They are colour coded in the same manner as $P_L$ – according to their symmetry. The time-delay $\tau$ is for both RABITT spectra shown on the corresponding ordinate, whereas for all figures the abscissa gives both the photoelectron energy $\varepsilon_e$ and the energy distance $\varepsilon_e + I_p$ to the ground state, where $I_p$ is the ionisation potential. The illustrated region is chosen to contain both studied sidebands and their respective neighbouring harmonics.

### 7.2.1 The Photoelectron Spectrum

A representative RABITT photoelectron spectrum (PES) can be seen in figure 7.6, for a driving IR energy of $\omega_{\text{IR}} \approx 2.65 \cdot 10^{-2}$ au. All such spectra were extracted as functions of the photoelectron energy $\varepsilon_e$ and time delay $\tau$ between the pulses. The spectrum is shown both for the theoretical and experimental case. From comparing the two, it can be concluded that the two spectra are quite similar, as both theory and experiment display comparable harmonic and sideband positions, as well as oscillatory frequency.

Figure 7.6 also contains the PES for a time delay of $\tau = 2.5$ au. It is divided by symmetry, showing in blue the ${}^1P^o$ symmetry, and in red the ${}^1S^e$ and ${}^1D^e$ symmetries. Since the ground state of neon belongs to the ${}^1S^e$ symmetry; one would predict the harmonics, populated by a one-photon process, to be located in the ${}^1P^o$; while the sidebands, being the result of two-photon processes, to be contained within the ${}^1S^e$ and ${}^1D^e$ symmetries. As can be seen in the lower panel of figure 7.6, this is exactly what is found in the present calculations.

One final note should be made in regards to figure 7.6. The maximum delay between the pulses shown for the experimental value is 13.8 fs, while the corresponding value for the theoretical data is closer to 5.44 fs. This is due to higher time delays not being considered in the theoretical calculations, as instead of including filters in the propagations, the total propagation time was restricted so that the propagation was stopped before reflections could be seen. This also required a shorter pulse length to be employed – one of 12 fs, as opposed to the experimental one of 60 fs.

A second comparison between theory and experiment can be found in figure 7.7. It shows the XUV-APT photoelectron yield of $\text{HH}_{63}$ as a function of energy, integrated over an energy range 0.01au. Along with the experimental and ab-initio data, the figure also shows the result of first order time-dependent perturbation theory (TDPT)[2]. It was calculated by integration of the transition

[2] TDPT is described in appendix B.

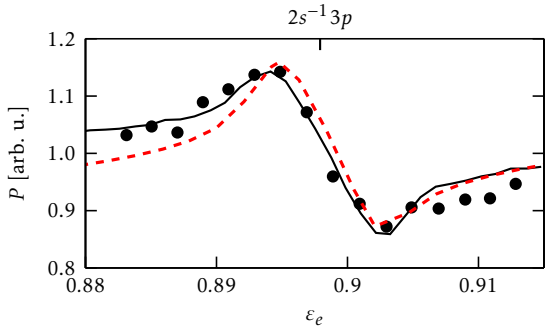


**Figure 7.7:** The one-photon photoelectron yield of $HH_{63}$, near the $3p$ resonance, as a function of the photoelectron energy $\varepsilon_e$, integrated in energy over a width of 0.01au. The experimental results are marked with black dots, while the theoretical ones are shown by the fully drawn, black line. The dashed red line has been calculated using first order perturbation theory. The respective spectra have been normalised to be comparable.

amplitude from the ground state $\left|\psi_0\right\rangle$ with energy $\varepsilon_0$ over final states $\left|\psi_{L\alpha_L\varepsilon}\right\rangle$ of energy $\varepsilon$, belonging to the scattering channel $\alpha_L$ of total angular momentum $L$, as a sum

$$P(\varepsilon_e) = \sum_{\alpha_1} \int_{\varepsilon_e-\delta/2}^{\varepsilon_e+\delta/2} d\varepsilon \left|\tilde{A}_{\mathrm{XUV}}(\varepsilon-\varepsilon_0)\right| \left|\left\langle \psi_{1\alpha_1\varepsilon}\middle|\alpha\hat{\mathcal{P}}\middle|\psi_0\right\rangle\right|^2, \tag{7.2}$$

over ${}^1P^o$ (i.e. $L=1$) states, where $\tilde{A}_{\mathrm{XUV}}$ is the frequency distribution of the XUV vector potential, $\delta = 0.01$ au is the integration width, $\alpha$ is the fine structure constant, and $\hat{\mathcal{P}}$ is the dipole operator. The values of the operator $\hat{\mathcal{P}}$ were identical to those used during propagation.

All three data sets in figure 7.7 display a smooth Fano (1961) profile as they pass over the $3p$ resonance. In this figure as well, excellent agreement between the theory and experiment can be seen.

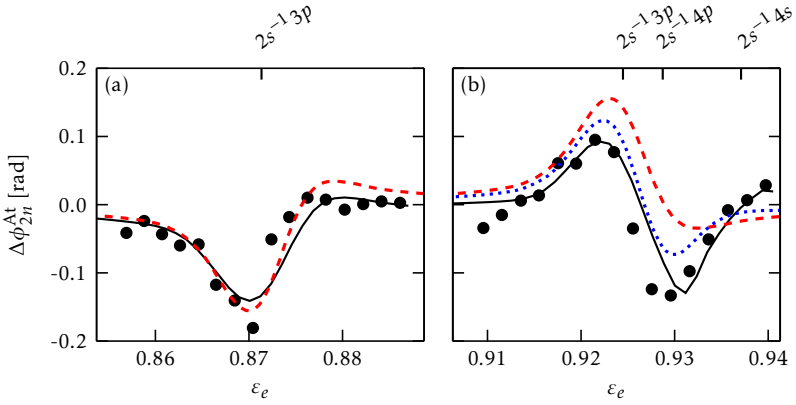


**Figure 7.8:** The RABITT atomic phase difference $\Delta\phi_{2n}^{\mathrm{At}}$ of (a) $\mathrm{SB}_{62}$ and (b) $\mathrm{SB}_{64}$, extracted both from experiment (black dots) and ab-initio theory (continuous black line), shown as functions of the photoelectron energy $\varepsilon_e$. The result of two implementations of the simple model discussed in chapter 5 is also shown: one considering only the $3p$ resonance (in dashed red) and one, only shown for $\mathrm{SB}_{64}$, considering both the $3p$ and the $4p$ resonance (in dotted blue).

### 7.2.2 Extracted Phases

Presently consider anew the atomic phase, written as $\Delta\phi_{2n}^{\mathrm{At}}$ for the $\mathrm{SB}_{2n}$. Figure 7.8 shows the energy-variance of both $\Delta\phi_{62}^{\mathrm{At}}$ (in figure 7.8a) and $\Delta\phi_{64}^{\mathrm{At}}$ (in figure 7.8b) for experiment as well as for ab-initio theory. For both sidebands, the agreement between theory and experiment is excellent.

The results obtained here are much less pronounced than those obtained in previous studies of helium (Gruson et al. 2016) and argon (Kotur et al. 2016). This can be attributed to the spectral width of the involved resonances – the $3p$ resonance having the largest width of $\Gamma_{3p} \approx 5.9 \cdot 10^{-4}$ au – being significantly smaller than both the harmonic width ($\approx 1.1 \cdot 10^{-2}$ au) and the MBES resolution ($\approx 9.2 \cdot 10^{-3}$ au). It may be noted that, due to the narrow harmonic width, the phase variance could not be extracted via Rainbow RABITT.

In figure 7.8a, it is observed that, as the energy approaches $\varepsilon_{3p}$, $\Delta\phi_{62}^{\mathrm{At}}$ decreases by 0.15 rad, before once again increasing to its initial value. What, then,

causes this behaviour? Since the atomic phase (as defined in chapter 3.2.1) corresponds to the phase difference between the two-photon matrix elements averaged over the lower and upper harmonic, respectively; this question can be answered by considering said matrix elements. It is thus convenient to consider the model for two-photon matrix elements discussed in chapter 5.1.

For $SB_{62}$, no resonances need be taken into account when considering intermediate energies close to the energy $\varepsilon_{61}$ of $HH_{61}$; and only one, $3p$, when considering those close to the energy $\varepsilon_{63}$ of $HH_{63}$. These special cases are respectively described by equations 5.11 and 5.29. Thus, denoting the matrix element to the $SB_{2n}$ via an intermediate energy $\varepsilon_i$ as $\mathcal{M}^{(2)}_{2n}(\varepsilon_i)$, and removing the slow-varying background, the matrix elements to $SB_{62}$ can be written as

$$\mathcal{M}^{(2)}_{62}(\varepsilon_i) \propto \begin{cases} 1 & , \ \varepsilon_i \approx \varepsilon_{61} \quad (7.3a) \\ \dfrac{\epsilon_{3p}(\varepsilon_i) + q_{3p}}{\epsilon_{3p}(\varepsilon_i) + i} & , \ \varepsilon_i \approx \varepsilon_{63} \quad (7.3b) \end{cases}$$

in the relevant regions, where

$$\epsilon_n(\varepsilon) = 2\frac{\varepsilon - \varepsilon_n}{\Gamma_n} \tag{7.4}$$

is the reduced energy variable of a resonance $n$ with position $\varepsilon_n$ and width $\Gamma_n$, and $q_n$ is the corresponding Fano profile parameter. Integration over $HH_{63}$ gives the expression

$$\Delta\phi^{\mathrm{At}}_{62}(\varepsilon_e) = -\arg \int_{\mathrm{HH}_{63}} d\varepsilon_i \ \left|\tilde{A}_{\mathrm{IR}}(\varepsilon_e - \varepsilon_i)\tilde{A}_{\mathrm{XUV}}(\varepsilon_i - \varepsilon_0)\right| \ \frac{\epsilon_{3p}(\varepsilon_i) + q_{3p}}{\epsilon_{3p}(\varepsilon_i) + i} \tag{7.5}$$

for the atomic phase of $SB_{62}$, where $\varepsilon_0$ is the ground state energy and $\tilde{A}_{\mathrm{IR}}$ the frequency-distribution of the IR probe vector potential. The result of this equation is shown as a dashed red line in figure 7.8a, where it can be seen to

accurately predict the variation of $SB_{62}$ in the studied energy region.

Turn now to $SB_{64}$, where the case is quite different. As can be seen in figure 7.8b, as $\varepsilon_e$ increases, $\Delta\phi_{64}^{\mathrm{At}}$ first increases by 0.1 rad, before decreasing by 0.2 rad, and finally returning to its original value. This behaviour is both significantly more complex than and qualitatively different from that of $SB_{62}$. Had the only relevant resonance been that found in the shared harmonic ($3p$ in this case), as was the case in Gruson et al. (2016) and Kotur et al. (2016), $\Delta\phi_{64}^{\mathrm{At}}$ would have been an approximate mirror image of $\Delta\phi_{62}^{\mathrm{At}}$. This behaviour follows directly from the definition of the $\Delta\phi_{2n}^{\mathrm{At}}$, and the model-predicted behaviour of $\Delta\phi_{64}^{\mathrm{At}}$ considering only the $3p$ resonance is shown as a dashed red line in figure 7.8b. It is capable of accurately model the general behaviour of $\Delta\phi_{64}^{\mathrm{At}}$ only for $\varepsilon_e < 0.92$ au.

Hence, it can be concluded that more resonances are relevant in describing the behaviour of $\Delta\phi_{64}^{\mathrm{At}}$. In order to avoid having to use an overly complex expression for the model, it is convenient to restrict the problem to the case when only one resonance element is considered in either harmonic path.

Since, for the lower values of $\varepsilon_e$ considered, the qualitatively correct behaviour of $\Delta\phi_{64}^{\mathrm{At}}$ can be predicted considering only the $3p$ resonance, this is the only resonance to be considered when calculating $\mathcal{M}_{64}^{(2)}(\varepsilon_i)$ for $\varepsilon_i \approx \varepsilon_{63}$. Assuming that the same approximation can be made with the $4p$ resonance for the upper harmonic and, analogously to the case of $\mathcal{M}_{62}^{(2)}(\varepsilon_i)$, removing the background from equation 5.29 gives the expressions

$$\mathcal{M}_{64}^{(2)}(\varepsilon_i) \propto \begin{cases} \dfrac{\epsilon_{3p}(\varepsilon_i) + q_{3p}}{\epsilon_{3p}(\varepsilon_i) + i}, \ \varepsilon_i \approx \varepsilon_{63} & \text{(7.6a)} \\ \dfrac{\epsilon_{4p}(\varepsilon_i) + q_{4p}}{\epsilon_{4p}(\varepsilon_i) + i}, \ \varepsilon_i \approx \varepsilon_{65} & \text{(7.6b)} \end{cases}$$

for $\mathcal{M}_{64}^{(2)}(\varepsilon_i)$. From this, the atomic phase can be calculated as

$$\begin{aligned}\Delta\phi_{64}^{\mathrm{At}}(\varepsilon_e) \;=\; &\arg\int_{\mathrm{HH}_{63}} d\varepsilon_i \;\left|\tilde{A}_{\mathrm{IR}}\left(\varepsilon_e-\varepsilon_i\right)\tilde{A}_{\mathrm{XUV}}\left(\varepsilon_i-\varepsilon_0\right)\right| \frac{\epsilon_{3p}(\varepsilon_i)+q_{3p}}{\epsilon_{3p}(\varepsilon_i)+i} \\ &- \arg\int_{\mathrm{HH}_{65}} d\varepsilon_i \;\left|\tilde{A}_{\mathrm{IR}}\left(\varepsilon_e-\varepsilon_i\right)\tilde{A}_{\mathrm{XUV}}\left(\varepsilon_i-\varepsilon_0\right)\right| \frac{\epsilon_{4p}(\varepsilon_i)+q_{4p}}{\epsilon_{4p}(\varepsilon_i)+i}\end{aligned} \;. \tag{7.7}$$

This behaviour is illustrated with a blue dotted line in figure 7.8b. Unlike the red dashed line, it correctly predicts the qualitative behaviour of $\Delta\phi_{64}^{\mathrm{At}}$. Thus it can be seen that the behaviour of $\Delta\phi_{64}^{\mathrm{At}}$ can be explained by considering only the $3p$ and $4p$ resonances. Further discrepancies between the model and ab-initio results can most likely be attributed to contributions from the $4s$ resonance.

The idea that the main contributions to the phase characteristic derives from the $3p$ and $4p$ resonances is further bolstered by figure 7.9, which compares the above presented XCHEM and experimental results with non-physical XCHEM calculations where a significant part of the involved resonances have been artificially removed. In figures 7.9a and 7.9c, it can be seen that removing both the $3p$ and the $4p$ resonance causes significant changes to the sideband phase, unlike what is seen when removing the $4s$ resonance, shown in figure 7.9b. Indeed – removing the $4s$ gives almost the same behaviour for the phase as in $\mathrm{SB}_{62}$!

### 7.2.3 Conclusions

In the present study, RABITT has been used to determine the spectral phases of neon using XUV-IR attosecond interferometric experiments as well as full-electron ab-initio calculations. This was done in energy regions where several resonances are present, resulting in a complex energy-dependence of the atomic phase. The experimental and theoretical results show excellent agreement, validating the XCHEM methodology used to describe the electron correlation

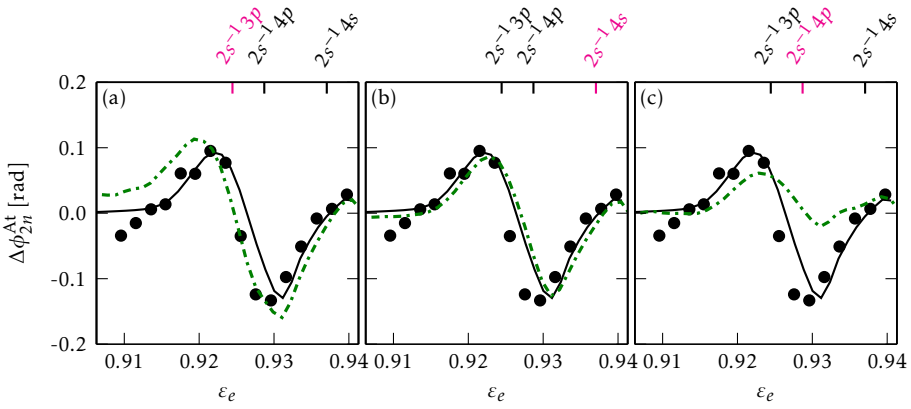


**Figure 7.9:** In black, the RABITT atomic phase difference $\Delta\phi^{\mathrm{At}}_{64}$ of $\mathrm{SB}_{64}$ is shown for experiment (black dots) and XCHEM theory (continuous black line), identically to figure 7.8b. In green, the corresponding result is shown for artificial XCHEM calculations, where the majority contribution of the (a) $2s^{-1}3p$, (b) $2s^{-1}4s$, and (c) $2s^{-1}3p$ resonance, respectively, has been removed. As the resonances were mixed with the continuum, they could not be cleanly removed, and significant components of all resonances remain in all figures. Thus, this should be seen only as a qualitative, not a quantitative picture of resonance influences.

in the studied ionisation continuum. As this is a common scenario in many-electron systems, the development of theory such as XCHEM – capable of describing these systems – is vital.

Further, in systems where ab-initio theory is unavailable, simpler models are needed to interpret and guide experiments. Despite the complex behaviour of the atomic phase observed, here one such model has been used to accurately describe and disentangle the contributions of the autoionising resonances involved.

This work opens the way to the reconstruction of resonant electronic wave packets coherently produced by two-photon ionisations in multi-resonance atomic regions. Thereby it extends the range of applicability of reconstruction methods to more complex cases than those previously available.

# Chapter 8

## Argon

The third and final atomic system discussed in this work is argon. As it was treated before the XCHEM approach, discussed in chapter 4.2, was prepared for accurate ab-initio propagations, no ab-initio calculations are presented in this chapter. Instead, the study presented in chapter 8.1 uses the interferometric models discussed in chapter 5 to study the anisotropy of the atomic time-delay in argon.

The valence shell of argon has the configuration $3s^2 3p^6$. Below the second ($N = 2$) threshold, the ionisation channels $3s^2 3p^5$ with parent ion orientation $m_{\mathrm{PI}} \in \{-1, 0, 1\}$ are open, and the autoionising $3s3p^5 n\ell$ are relevant, where $n$ and $\ell$ respectively denote the excited electron principal quantum number and angular momentum.

## 8.1 Anisotropic Time Delays Near a Resonance

Recent multicolour photoelectron momentum measurements have been used to extract angularly resolved phases and amplitudes of ionising electron wave packets (Laurent et al. 2012; Villeneuve et al. 2017). One study of photoemission delays in helium (Heuser et al. 2016) showed almost no angular dependence, except at large angles relative to the laser polarisation axis. While one-photon ionisation in helium only opens one ionisation continuum, the study employed a multicolour reconstruction of interference between two-photon transitions (RABITT) scheme, resulting in multiple final state symmetries. The observed anisotropy was therefore attributed to phase differences between final interfering quantum states.

The present study considers the effects of correlation effects on the angularly resolved atomic time delay. This is done using extreme-ultraviolet (XUV) infrared (IR) pump-probe RABITT measurements of the region of argon containing the $3s^{-1}n\ell$ (below denoted $n\ell$) series of autoionising resonances. Measured photoelectron angular distributions (PADs) obtained by two-photon absorption are in excellent agreement with previous, static, synchrotron data. The presented results show that the photoemission delays vary strongly with the emission angle, which is caused by interference between ionisation channels of distinct angular momenta. At resonance energies, the relative strength of these channels varies sharply, causing strong variations in the angular and energy dependence of measured ionisation delay. The study was originally published in Nature Communications as Cirelli et al. (2018).

The data presented herein was obtained in two distinct experiments, one carried out at the Swiss Federal Institute of Technology in Zurich (ETH) and one at Lund University. In both experiments, a Ti:Sapphire laser was used to generate infrared pulses with an approximate 30 fs duration and an optimal center wavelength of $\lambda_{\mathrm{IR}} = 780$ nm, corresponding to a frequency of $\omega_{\mathrm{IR}} = 5.84 \cdot 10^{-2}$ au. The Lund experiment also allowed the wavelength to be tuned

up to $\lambda_{\mathrm{IR}} = 794$ nm, corresponding to a frequency of $\omega_{\mathrm{IR}} = 5.74 \cdot 10^{-2}$ au.

The IR beam was split into two beams of distinct intensity. The weaker part had an intensity of $3 \cdot 10^{11}\ \frac{\mathrm{W}}{\mathrm{cm}^2}$, low enough to be approximated in the weak-field limit, and was used as a probe. The more intense part was focused into an argon gas target for the purpose of high-harmonic generation (HHG), resulting in an extreme ultraviolet attosecond pulse train (XUV-APT) with central frequency 1.286 au and spectral envelope full width at half-maximum (FWHM) of 0.441 au, composed of the high harmonics (HH) of the IR. After the HHG, the IR component is removed using an aluminium filter, resulting in a pure XUV pulse.

Both interferometer arms were stabilised during the experiment in order to minimise sources of systematic errors and ensure the stability of the delay in the attosecond range. After recombination, the IR and XUV-APT propagate collinearly onto a toroidal mirror which focuses them onto an argon gas jet inside an electron spectrometer.

In the ETH setup, the spectrometer contains a reaction microscope detector (Ullrich et al. 2003b), which allows for the retrieval of the full 3D momentum vector in coincidence for each emitted electron over the full $4\pi$ solid angle.

The Lund experiment used a velocity-map imaging (VMI) detector (Eppink et al. 1997) to measure the projection of the electron distribution onto a photo-sensitive detector. This technique is well adapted to the geometry of the interaction, when the XUV and IR are chosen to have a common polarisation axis, perpendicular to the detector axis. The 3D electron momentum distributions are obtained by inversion of the 2D projections using the pBasex algorithm (Garcia et al. 2004).

Each ETH value presented is measured using 15 independent datasets, while 10 were obtained in the Lund experiment. Error bars indicate the standard deviation.

Figure 8.1 show measured XUV-APT one-photon spectra from the ETH (in red) and the Lund (in blue) experiments. The spectra span the $n\ell$ series of autoionising resonances. More specifically, $\mathrm{HH}_{17}$ is resonant with the $4p$

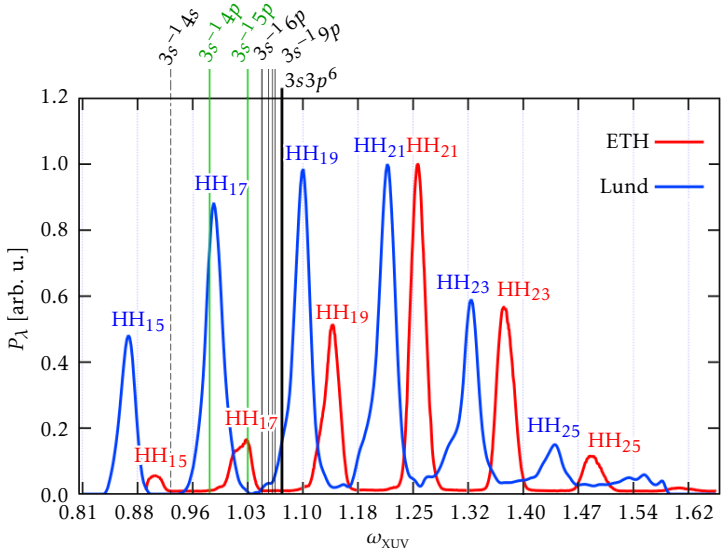


**Figure 8.1:** The spectral distributions of the Lund (blue) and ETH (red) experimental RABITT pump fields. Several $3s^{-1}n\ell$ resonances below the second threshold have been marked with black, vertical dashed ($3s^{-1}4s$) and continuous ($3s^{-1}np$) lines. The corresponding parent ion (PI) has a valence configuration of $3s3p^6$, and the threshold is marked with a thick black line. For both experiments, $HH_{17}$ is resonant with one of the resonances marked in green – $4p$ (at 0.978 au) for ETH and $5p$ (at 1.029 au) for Lund. The abscissa shows the XUV photon energy $\omega_{XUV}$ and the ordinate the photon probability distribution $P_\lambda$. This figure is here republished with modifications from Fig. 1 in Cirelli et al. (2018).

resonance in the Lund experiment and with the $5p$ in the ETH experiment. Below, the influence of these resonances will be discussed.

The two-colour photoelectron spectrum measured by the ETH setup is shown in figure 8.2. In figure 8.2a, the distribution of photoelectrons by emission energy $\varepsilon_e$ is shown.

In RABITT, the atomic emission delay $\tau_{2n}^{\mathrm{At}}$ of the $2nth$ sideband can be calculated as

$$\tau_{2n}^{\mathrm{At}} = -\frac{\phi_{2n+1}^{\mathrm{At}} - \phi_{2n-1}^{\mathrm{At}}}{2\omega_{\mathrm{IR}}}, \tag{8.1}$$

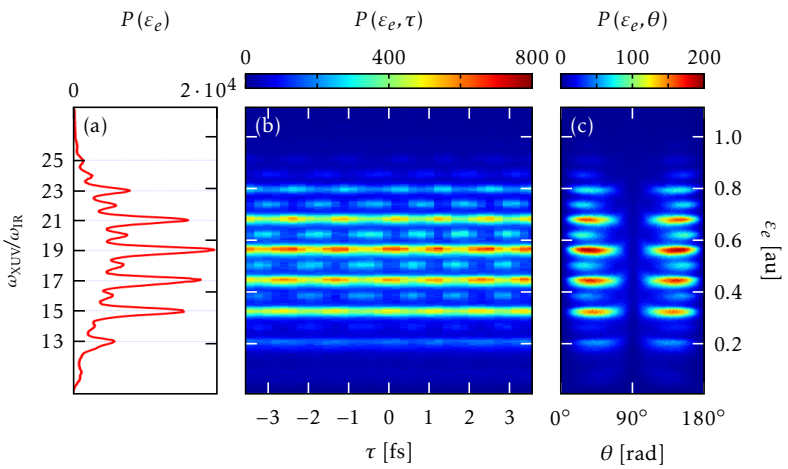


**Figure 8.2:** RABITT spectra obtained using the ETH experimental setup. The photoelectron count $P$ is shown resolved (a) by photoelectron energy $\varepsilon_e$, (b) by both $\varepsilon_e$ and time delay $\tau$, and (c) by both $\varepsilon_e$ and emission angle $\theta$. This figure is here republished with modifications from Fig. 2 in Cirelli et al. (2018).

where $\phi^{\mathrm{At}}_{2n\pm1}$ – the atomic phase – is the argument of the two-photon matrix element averaged over the paths via $\mathrm{HH}_{2n\pm1}$.

The interference of the two paths to the $2nth$ sideband (SB) $\mathrm{SB}_{2n}$ can be studied to measure $\tau^{\mathrm{At}}_{2n}$. This is done by fitting the sideband pump-probe time-delay ($\tau$) oscillation to the equation, equivalent to equation 3.47,

$$I_{2n}(\tau) = \left|\mathcal{A}^{-}_{2n}\right|^2 + \left|\mathcal{A}^{+}_{2n}\right|^2 + \left|\mathcal{A}^{-}_{2n}\mathcal{A}^{+}_{2n}\right| \cos\left(2\omega_{\mathrm{IR}}\left[\tau - \tau^{\mathrm{At}}_{2n} - \tau^{\mathrm{ATP}}_{2n}\right]\right), \tag{8.2}$$

where $\tau^{\mathrm{ATP}}_{2n}$ is the delay associated with the attosecond pulse train (APT) harmonic attochirp and $\mathcal{A}^{\pm}_{2n}$ is the amplitude of the transition via $\mathrm{HH}_{2n\pm1}$. The oscillations predicted by equation 8.2 can be seen for the sidebands in figure 8.2b, where the photoelectron spectrum is resolved by $\tau$.

In this section, the angular dependence of $\tau^{\mathrm{At}}_{2n}$ is studied. As such, the photoelectron spectrum is resolved not only by energy and pump-probe delay, but also by the emission angle $\theta$. Figure 8.2c shows the spectrum resolved by

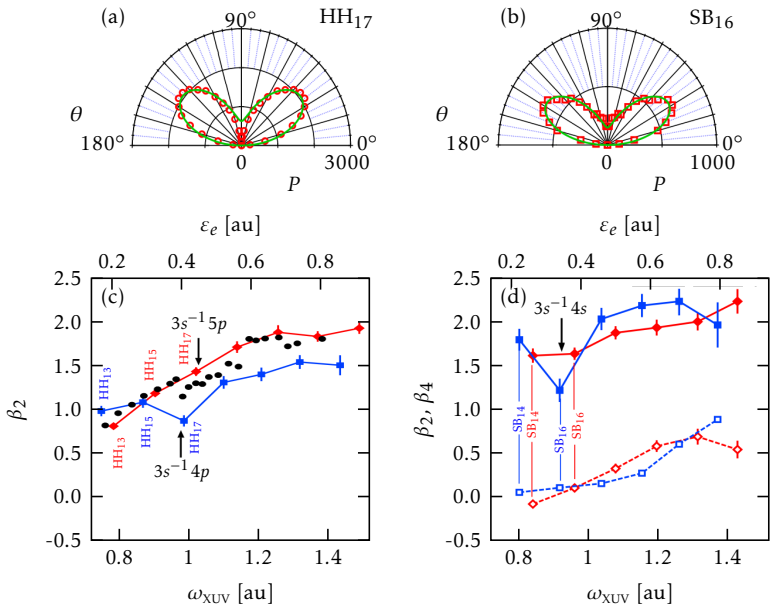


**Figure 8.3:** Angular photoelectron distributions and $\beta_i$ parameters. In (a) and (b) the photoelectron angular distributions (PADs) of electrons corresponding to ETH reaction microscope measurements of $HH_{17}$ and $SB_{16}$ energies, respectively, are illustrated with red dots. The solid green lines correspond to the fit of the sinusoidal HH and SB oscillations, multiplied by $\sin(\theta)$ to account for the detector geometry. In (c) and (d), $\beta_i$ parameters are shown , resolved by photoelectron ($\varepsilon_e$) as well as the excitation energy ($\varepsilon_n$ for the *nth* harmonic or sideband) and $\varepsilon_e$), are shown; measured in the ETH (red) and Lund (blue) experiments, as well as taken from synchrotron data (black dots) taken from (Southworth et al. 1986). In (c), $\beta_2$ is shown for the harmonics, whereas in (d) $\beta_2$ (solid lines) and $\beta_4$ (dashed lines) is given for the sidebands. This figure is here republished with modifications from Fig. 3 in Cirelli et al. (2018).

angle and energy.

### 8.1.1 Delay-Integrated Asymmetry Parameters

Denoting the inclination with respect to the direction of the field $\theta$ and the corresponding azimuth $\varphi$, the differential solid angle has the expression $d\Omega = \sin(\theta)\, d\theta d\varphi$. This allows the angularly resolved photoelectron spectrum to be

written as a function $\frac{\partial P}{\partial \Omega}$. It can be expanded as

$$\frac{\partial P}{\partial \Omega} = \frac{P}{4\pi}\left[1 + \sum_{i=1}^{2\ell_{\max}} \beta_i P_i(\cos(\theta))\right] \tag{8.3}$$

into a series of Legendre polynomials $P_i$ of order $i$ with corresponding coefficients $\beta_i$, where $\ell_{\max}$ is the maximum electron angular momentum considered (Laurent et al. 2012). As the photoelectron can be expected to be symmetric around the axis of the linearly polarised field, the $\beta_i$ parameters can be assumed to be zero for odd values of $i$.

The even $\beta_i$ parameters can be determined from the PES. Figures 8.3a and 8.3b show the PADs obtained from integration of the PES over an energy width of $\sim 2.6 \cdot 10^{-2}$ au. The green lines show the fit of the distributions (equation 8.3 being multiplied by $\sin(\theta)$ to compensate for the factor in the solid angle).

The fitted $\beta_i$ coefficients are also shown in figure 8.3 – in 8.3c for the one-electron case (extracted from the harmonics) and in 8.3d for the two-electron case (extracted from the sidebands). For the one-photon case, only $\beta_2$ is shown, whereas both $\beta_2$ and $\beta_4$ are shown for the two-photon case. Both the ETH (red) and Lund (blue) data compares well to previous synchrotron results taken from Southworth et al. (1986), validating the results of the present study.

For both cases (the one-photon case in figure 8.3c and the two-photon case in figure 8.3d) the $4p$ resonance strongly influences the $\beta_2$ parameter. This can be seen by observing $HH_{17}$ and $SB_{16}$ in the Lund experiment. The $\beta_2$ variation of $SB_{16}$ is larger than that of $HH_{17}$, and may be enhanced by the $4s$ resonance. The effect on $\beta_2$ of the $5p$ resonance, on the other hand, is only weakly observed, resulting in a small shift of $SB_{16}$ in the ETH experiment.

It should be noted that the large HH and IR bandwidths may obscure the effect of the resonances. The $4p$ resonance width of 2.94 au being significantly larger than the 1.05 au width of the $5p$ resonance (Berrah et al. 1996) would explain the difference between the relative strength of the effect caused by the two resonances.

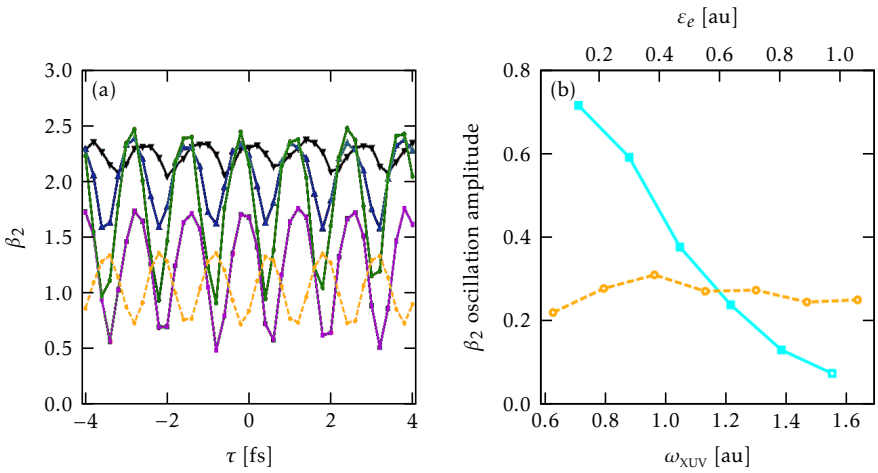


**Figure 8.4:** The time-dependent behaviour of the $\beta_2$ parameters. In 8.4a, the dependence of $\beta_2$ on the time-delay $\tau$ is shown for $HH_{17}$ (yellow), $SB_{14}$ (green), $SB_{16}$ (purple), $SB_{18}$ (blue), and $SB_{22}$ (black); as extracted from the Lund experiment. In 8.4b, the dependence of the $\beta_2$ oscillatory amplitude on energy is given for both the harmonics (yellow) and sidebands (blue). This figure is here republished with modifications from Fig. 4 in Cirelli et al. (2018).

### 8.1.2 Delay-Resolved Asymmetry Parameters

Although the pump-probe methods discussed here provide lower energy resolution than the above presented synchrotron data (Southworth et al. 1986), they have the advantage of being able to provide time-resolved information. In figure 8.4a, the time-dependent behaviour of $\beta_2$ is shown, as a function of the pump-probe time-delay $\tau$. Both the sideband and harmonic $\beta_2$ parameters oscillate with the time-delay, both with the same frequency of $2\omega_{IR}$, although with opposite phase – it being the case in RABITT that sideband maxima coincide with harmonic minima and vice versa. Although the data presented is from the Lund experiment, similar behaviour was observed in the ETH experiment.

The amplitude of the beatings as a function of energy can be seen in figure 8.4b. The sideband $\beta_2$ oscillation amplitude decreases with energy, while the

corresponding parameter for the harmonics remains approximately constant.

### 8.1.3 Angularly Resolved Atomic Delays

Figure 8.5 shows the dependence of the atomic time delay on the emission angle $\theta$ – both for the case of $SB_{14}$ (in figure 8.5a), involving no resonances; and for that of $SB_{16}$ (in figure 8.5b), where the upper harmonic contains the intermediate $5p$ resonance. According to the method discussed by Heuser et al. (2016), the atomic time delay is derived by filtering detected photoelectrons at different emission angles $\theta$. For each value of $\theta$, the sideband population was integrated over a small energy interval of $\sim 2.6 \cdot 10^{-2}$ au and fitted to equation 8.2 in order to obtain $\tau_{2n}$. Thereafter, $\tau_{2n}^{\mathrm{APT}}$ was subtracted in order to calculate $\tau_{2n}^{\mathrm{At}}$. The delay was calculated relative to a reference calculated for angles up to 30° – an range considered large enough to avoid large errors in the reference phase.

The green lines in figure 8.5 are based on the model discussed in chapter 5. Their angular dependence is calculated according to equation 5.39, as

$$\Delta\phi_{2n}^{\mathrm{At}}\left(\hat{\Omega}\right) = \arctan \frac{2\left|\mathcal{A}_{2n,1}^{-}\mathcal{A}_{2n,1}^{+}\right|\sin\left(\Delta\phi_{2n,1}\right) + \left|\mathcal{A}_{2n,0}^{-}\mathcal{A}_{2n,0}^{+}\right|\sin\left(\Delta\phi_{2n,0}\right)}{2\left|\mathcal{A}_{2n,1}^{-}\mathcal{A}_{2n,1}^{+}\right|\cos\left(\Delta\phi_{2n,1}\right) + \left|\mathcal{A}_{2n,0}^{-}\mathcal{A}_{2n,0}^{+}\right|\cos\left(\Delta\phi_{2n,0}\right)}, \quad (8.4)$$

where $\mathcal{A}_{2n,m_{\mathrm{F}}}^{\pm}$ and $\Delta\phi_{2n,m_{\mathrm{F}}}$ are the angularly dependent partial transition amplitudes $\mathcal{A}_{2n}^{\pm}$ and transition phases $\Delta\phi_{2n}$, restricted by the final electron magnetic quantum number $m_{\mathrm{F}}$. In calculating $\mathcal{A}_{2n,m_{\mathrm{F}}}^{\pm}$, the pulse envelopes were assumed to be Gaussian.

As no resonances are present in the case of $SB_{14}$, the matrix element to the final state of energy $\varepsilon_{\mathrm{F}}$ and magnetic quantum number $m_{\mathrm{F}}$, via an intermediate energy $\varepsilon_i$, is calculated as

$$\mathcal{M}_{\mathrm{F},m_{\mathrm{F}}}^{(2)}\left(\varepsilon_i\right) \approx \sum_{\alpha_{\mathrm{I}}} \frac{\overline{\mathcal{O}}_{\alpha_{\mathrm{I}}}^{m_{\mathrm{F}}}\left(\varepsilon_{\mathrm{F}}\right)\mathcal{O}_{0}^{\varepsilon_{\mathrm{F}}\alpha_{\mathrm{I}}}}{\varepsilon_i - \varepsilon_{\mathrm{F}} + i0^{+}} \quad (8.5)$$

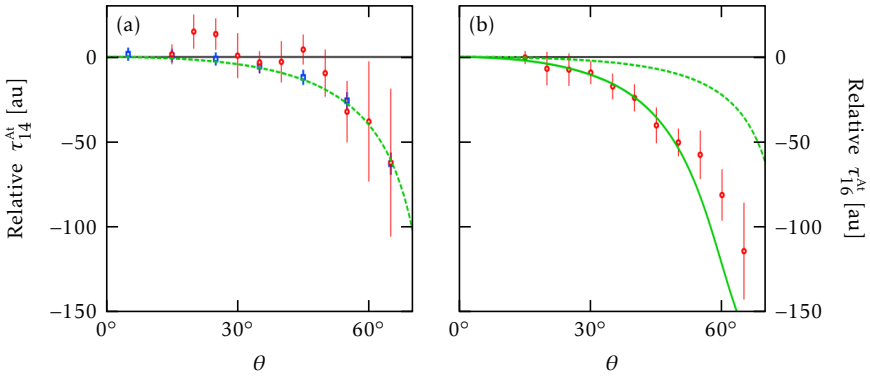


**Figure 8.5:** The angularly resolved emission delays $\tau_{2n}^{At}$ for (a) $SB_{14}$ and (b) $SB_{16}$, relative to those with an emission angle of $\theta \in [0°, 30°]$. The delays are extracted from ETH (red, $\lambda_{IR} = 789$ nm) and, in (a), Lund (blue, $\lambda_{IR} = 789$ nm) data. The error bars indicate the standard deviation, obtained using a series of independent measurements. The green lines show the calculated delays calculated using the theory described in chapter 5. Unlike the dashed lines, which treats the intermediate and final states as smooth continua the solid one takes the $5p$ resonance into account. This figure is here republished with modifications from Fig. 5 in Cirelli et al. (2018).

by taking all intermediate continua $\alpha_I$ into account. The one-photon matrix elements $\mathcal{O}_0^{\varepsilon_I \alpha_I}$ and $\overline{\mathcal{O}}_{\alpha_I}^{m_F}(\varepsilon_F)$ were calculated using a random phase approximation with exchange (RPAE), excluding resonant contributions (Dahlström et al. 2014, 2012b).

In the case of $SB_{16}$, the intermediate $5p$ resonance is present in $HH_{17}$. As such, the upper-harmonic matrix element transversing the intermediate scattering continua containing $5p$ resonance was calculated according to equation 5.29, giving the expression

$$\mathcal{M}_{F,\alpha_I}^{(2)}(\varepsilon_i) = \frac{\epsilon_{5p}(\varepsilon_i) + q_{5p}}{\epsilon_{5p}(\varepsilon_i) + i} \frac{\overline{\mathcal{O}}_{\alpha_I}^{m_F} \mathcal{O}_0^{\alpha_I}}{\varepsilon_i - \varepsilon_F}, \tag{8.6}$$

where the $5p$ Fano profile parameter $q_{5p}$, along with the $5p$ resonance position $\varepsilon_{5p}$ and width $\Gamma_{5p}$, used for calculating the reduced energy variable

$$\epsilon_{5p}(\varepsilon) = 2\frac{\varepsilon - \varepsilon_{5p}}{\Gamma_{5p}}, \tag{8.7}$$

was derived using a multiconfigurational Hartree-Fock (MCHF) approach (Carette et al. 2013).

For both sidebands, $\tau_{2n}^{\mathrm{At}}$ becomes more and more negative as $\theta$ increases. This same tendency was observed by Heuser et al. (2016) for the case of helium. The model accurately reproduces the experimental data. The dependence of $\tau_{2n}^{\mathrm{At}}$ on $\theta$ is much greater for $\mathrm{SB}_{14}$ than $\mathrm{SB}_{16}$. Removing the $5p$ resonance in the model, the $\theta$-dependence of $\tau_{2n}^{\mathrm{At}}$ decreases, as indicated by the dashed line. Hence the resonance is needed to quantitatively describe the behaviour of the delay.

### 8.1.4 Angularly and Spectrally Resolved Atomic Delays

In figure 8.6, the values of $\tau_{2n}^{\mathrm{At}}$ are presented not only resolved by angle, but also by energy. Analogously to figure 8.5, both the cases of $\mathrm{SB}_{14}$ (in figure 8.6a) and $\mathrm{SB}_{16}$ (in figure 8.6b) are considered. The data emanates from the Lund experiment, where $\lambda_{\mathrm{IR}}$ was varied from 780 nm to 794 nm, corresponding to a change in $\omega_{\mathrm{IR}}$ between $5.84 \cdot 10^{-2}$ au and $5.74 \cdot 10^{-2}$ au. The energy range was chosen to have $\mathrm{HH}_{17}$ traversing the $4p$ resonance, allowing it to affect $\mathrm{SB}_{16}$. Here, a different normalisation than that used for 8.5 is applied: Each wavelength is normalised independently with respect to the angularly integrated delays obtained by analysing $\mathrm{SB}_{14}$ and $\mathrm{SB}_{22}$, similarly to the procedure used by Kotur et al. (2016).

The two sidebands display qualitatively different behaviour. In 8.6a, $\mathrm{SB}_{14}$ can be seen to vary only slowly with energy, while, like in figure 8.5, becoming more and more negative as the emission angle increases.

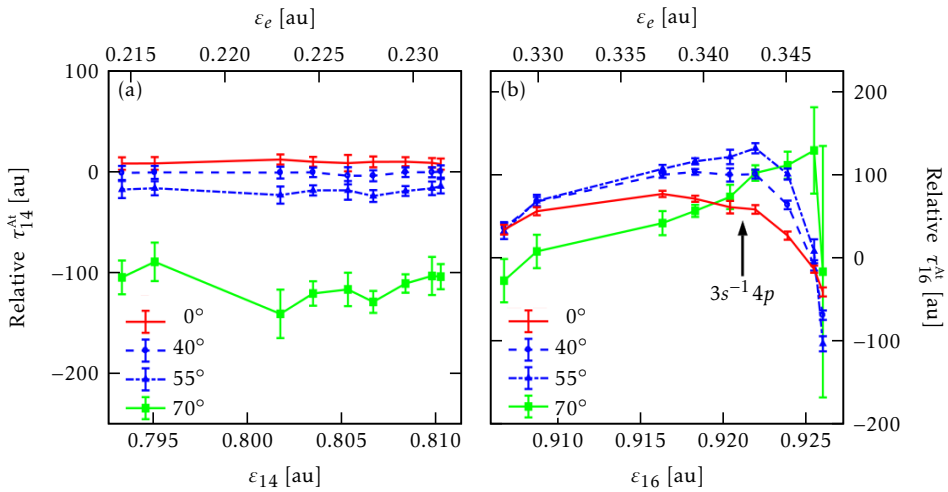


**Figure 8.6:** The emission delays of (a) $SB_{14}$ and (b) $SB_{16}$, measured as part of the Lund experiment, resolved by energy by varying the IR frequency $\omega_{\mathrm{IR}}$. In (b), the $3s^{-1}4p$ resonance is marked, albeit shifted by a factor 16/17 to account for it appearing in $HH_{17}$. The error bars represent the standard deviation, obtained using a series of independent measurements. The ordinate shows both the electron emission energy $\varepsilon_e$ and the excitation energy $\varepsilon_{2n}$ of the $2nth$ harmonic. This figure is here republished with modifications from Fig. 6 in Cirelli et al. (2018).

The behaviour of $SB_{16}$ is significantly more complex. As the energy passes over the $4p$ resonance, a sharp variation of the delay is observed, which would be expected due to the rapid phase shift characteristic of a Fano profile (Carette et al. 2013). The small magnitude of the shift as compared to that reported by Kotur et al. (2016) may be explained by the resonance being obscured due to the large bandwidth of the pulses utilised in the present study.

Interestingly, the angular dependence of the emission delay is here seen to vary strongly with energy in the vicinity of a resonance. The illustrated emission angle curves all appear to cross paths at sideband energies around $\varepsilon_{16} = 0.926$ au. This behaviour is discussed in more detail below.

### 8.1.5 Ionisation Paths and Angle-Dependent Atomic Delays

In order to provide a qualitative explanation of the angularly resolved data in the vicinity of a single intermediate resonance presented above (in figure 8.6b), a model based on simple arguments will presently be considered. The anisotropic delay of the emitted electron is theoretically calculated by averaging the angle-resolved RABITT probability over parent ion (PI) orientations ($m_{\mathrm{PI}} \in \{-1, 0, 1\}$ between the first and second threshold of argon). For the present discussion, however, it suffices to consider the case of $m_{\mathrm{PI}} = 0$.

Figure 8.7a and 8.7b show, respectively, the amplitude and argument of the one-photon matrix element $\mathcal{M}_{\ell_{\mathrm{I}}\varepsilon_{\mathrm{I}}}$ from the $3p$ (ground) state to the continuum of angular momenta $\ell_{\mathrm{I}} \in \{0, 2\}$ and energies $\varepsilon_{\mathrm{I}}$ in the vicinity of the $4p$ resonance. The data has been obtained from a multiconfiguration Hartree-Fock (MCHF) calculation, taken from Carette et al. (2013).

Far from the $4p$ resonance, the $d\varepsilon_{\mathrm{I}}$ channel is dominant with a factor $\sim 5$ in amplitude. Only in the neighbourhood of the $4p$ resonance can it be seen to decrease in amplitude sufficiently for $s\varepsilon_{\mathrm{I}}$ channel to dominate. As the different scattering channels have different angular distributions, the coherent interference of the two channels changes will affect the geometric properties of the emitted photoelectron. The total one-photon matrix element can thus be written as

$$\begin{aligned} \mathcal{M}^{(1)}(\varepsilon_{\mathrm{I}}, \theta) \propto\ & \mathcal{M}_0^{(1)}(\varepsilon_{\mathrm{I}}) \times Y_0^0(\theta) \\ & - \mathcal{M}_2^{(1)}(\varepsilon_{\mathrm{I}}) \times Y_2^0(\theta) \end{aligned} \tag{8.8}$$

for a given $\theta$ and $\varepsilon_{\mathrm{I}}$, where $Y_\ell^m(\theta)$ is the spherical harmonic associated with the angular momentum $\ell$ and magnetic quantum number $m$.

Figure 8.7c shows $\mathcal{M}^{(1)}$ for several values of $\theta$. At small ($\theta \in \{0°, 40°\}$) and large ($\theta = 70°$) values of $\theta$, the phase follows the same trend of the $d$ symmetry, while in-between ($\theta = 55°$) it follows that of the $s$ symmetry. This can be understood when considering that $\theta = 55°$ is close to "the magic angle" of $\theta \approx 54.7°$, for which $Y_2^0(\theta)$ is zero (illustrated by the subfigure insert). Near the

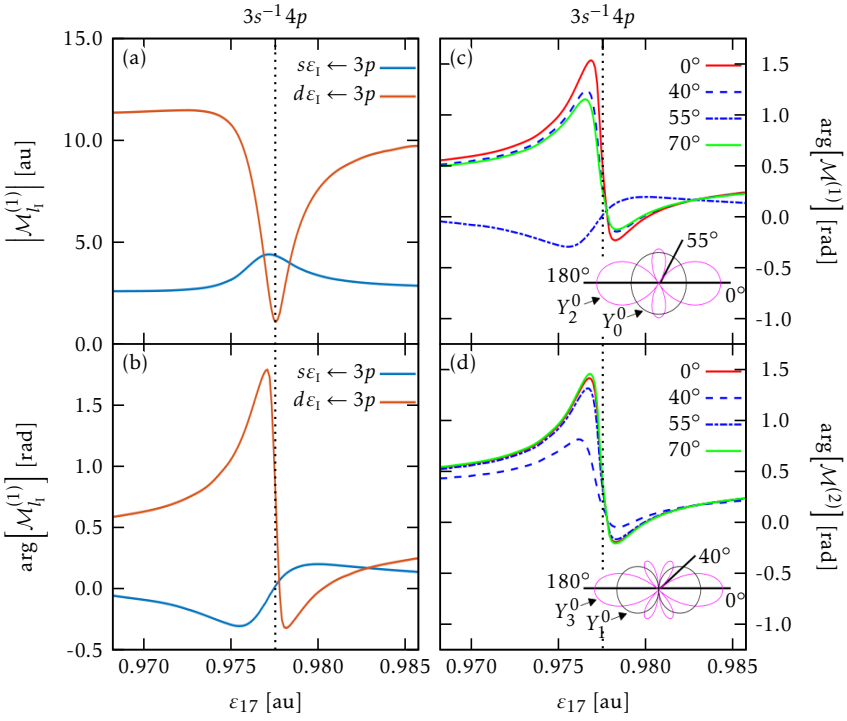


**Figure 8.7:** Amplitudes and phases for the one- and two-photon transition matrix elements from the $3s^{-1}4p$ state, respectively denoted $\mathcal{M}^{(1)}$ and $\mathcal{M}^{(2)}$, calculated using a simple model. In (a) and (b), the (a) amplitude and (b) argument of the partial one-photon matrix element $\mathcal{M}^{(1)}_{\ell_1}$ from the $3p$ state to the intermediate state of angular momentum $\ell_1$ and energy $\varepsilon_1$ are shown. Both potential angular momenta are considered, $s$ ($\ell_1 = 0$) in blue and $d$ ($\ell_1 = 2$) in red. In (c), the phase of the same matrix element, unresolved by symmetry, is shown for several values of the emission angle $\theta$. In (d), the corresponding phases of the two-photon matrix element are shown. In both (c) and (d), the angular distributions for several relevant spherical harmonics $Y^m_\ell(\theta)$ are shown. The abscissa of all figures shows the energy $\varepsilon_{17}$ of $HH_{17}$, which traverses the $4p$ resonance as shown by the dotted lines. This figure is here republished with modifications from Fig. 7 in Cirelli et al. (2018).

resonance, at $HH_{17}$ energy $\varepsilon_{17} \approx 0.978$ au, the amplitude of $\mathcal{M}_2^{(1)}$ is very small. For this reason, $\mathcal{M}^{(1)}$ approaches $\mathcal{M}_0^{(1)}$ and the angular dependence disappears. As can be seen in figure 8.7c, this causes the curves for the different angles to cross, similarly to what was observed in figure 8.6b.

This study aims to determine the angular dependence of atomic photoemission delays using the RABITT technique. RABITT, however, considers two-photon matrix elements, corresponding to a different symmetry than the one-photon ones which have been treated in this section so far. Three different combinations of intermediate ($\ell_\mathrm{I}$) and final ($\ell_\mathrm{F}$) angular momenta are possible: $(\ell_\mathrm{I}, \ell_\mathrm{F}) \in \{(0,1),(2,1),(2,3)\}$. With this in mind, the two-photon matrix element can be written as a sum of the partial matrix elements $\mathcal{M}^{(2)}_{\ell_\mathrm{F},\ell_\mathrm{I}}(\varepsilon_\mathrm{I})$ as

$$\mathcal{M}^{(2)}(\varepsilon_\mathrm{F},\theta) \propto \mathcal{M}^{(2)}_{3,2}(\varepsilon_\mathrm{I})\, Y_3^0(\theta) + \left[\mathcal{M}^{(2)}_{1,2}(\varepsilon_\mathrm{I}) - \mathcal{M}^{(2)}_{1,0}(\varepsilon_\mathrm{I})\right] Y_1^0(\theta), \tag{8.9}$$

analogously to equation 8.8. As the atomic phase $\phi^{\mathrm{At}}_{2n\pm1}$ is defined as the argument of the two-photon matrix element (averaged over the intermediate states, i.e. over $HH_{2n\pm1}$), the angular dependence of $\mathcal{M}^{(2)}(\varepsilon_\mathrm{F},\theta)$ also implies an angular dependence of $\phi^{\mathrm{At}}_{2n\pm1}(\varepsilon_\mathrm{F},\theta)$.

In order to further investigate this matrix element, it is convenient to first treat the simple, non-resonant case. The atomic phase $\phi^{\mathrm{At}}_{2n} = \phi^{\mathrm{cc}}_{2n} + \phi^{\eta}_{2n}$ can be divided into two components – one ($\phi^{\eta}_{2n}$) corresponding to the scattering phase of the intermediate state and one ($\phi^{\mathrm{cc}}_{2n}$) to the IR continuum-continuum transition. The scattering phase varies only slowly with energy when no resonance is present (Marante et al. 2017b), causing the emission and absorption path components to cancel each other out. Hence, $\phi^{\mathrm{cc}}_{2n}$ is dominant.

The upper ($\phi^{\mathrm{cc},+}_{2n}$) and lower ($\phi^{\mathrm{cc},-}_{2n}$) components of $\phi^{\mathrm{cc}}_{2n}$ can be estimated using Wentzel-Kramers-Brillouin (WKB) wavefunctions (Heuser et al. 2016). Within this approximation, the continuum-continuum phases are independent of angular momentum and (approximately) of energy (i.e. $\phi^{\mathrm{cc},-}_{2n} \approx -\phi^{\mathrm{cc},+}_{2n}$, where the sign difference results from the difference of absorption versus emission). This causes $\phi^{\mathrm{At}}_{2n}$ to completely lack angular dependence.

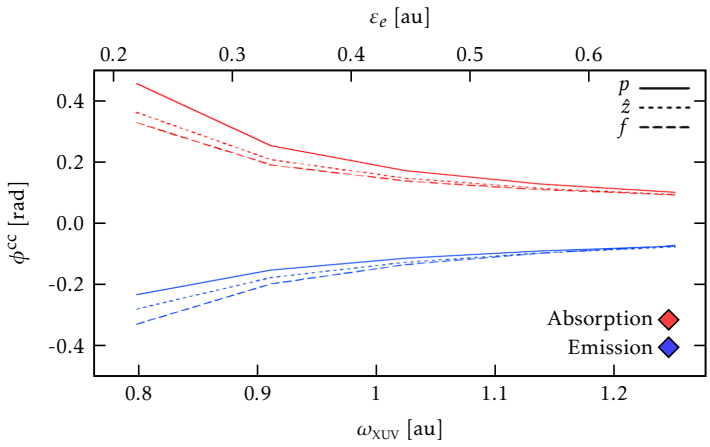


**Figure 8.8:** Theoretical continuum-continuum phases $\phi^{cc}$ for argon for absorption (red) and emission (blue) of an IR photon, calculated using two-photon matrix elements. The curves are shown both for the $p$ (solid) and the $f$ (dashed) symmetry, as well along the polarisation axis $\hat{z}$ of the field (dotted). This figure is here republished with modifications from Supplementary Figure 1 in Cirelli et al. (2018).

The WKB approximation works well for high kinetic energy. This is shown in figure 8.8, as it contains the channel-resolved continuum-continuum phases of argon. They were calculated by subtracting the one-photon matrix element phases from the two-photon ones (the matrix elements being calculated according to the theory described in Dahlström et al. [2014]). The figure shows remarkable agreement with previous exact hydrogen calculations (Dahlström et al. 2013), as the magnitudes of the absorption phase ($\phi_{2n}^{cc,-}$) are slightly larger than those of the emission one ($\phi_{2n}^{cc,+}$), and $\left|\phi_{2n}^{cc,\pm}\right|$ decrease slightly with final angular momentum close to the threshold.

Presently consider the case of a single intermediate resonance, which can be exemplified by (ignoring the $4s$ resonance) $SB_{16}$, as $HH_{17}$ overlaps the $4p$ resonance. Neglecting the angular dependence of the continuum-continuum component of the atomic phase, the phase $\phi_{16}^{At,-}$ of the path via $HH_{15}$ can be used as a reference phase.

By further assuming that the two-photon matrix element is proportional to the one-photon one (i.e. that $\forall \ell_F : \mathcal{M}^{(2)}_{\ell_F,\ell_I} \propto \mathcal{M}^{(1)}_{\ell_I}$), the two-photon ionisation phases have been calculated, and are shown in figure 8.7d. For the two-photon case, the angle follows the pattern of the $d$ symmetry, apart for at $\theta = 40°$, where $Y^0_3$ goes to zero.

Separating it from the case of the one-photon phase presented in figure 8.7c, the two-photon phase is very different to that of the $s$ channel (the red curve in figure 8.7b) for $\theta = 40°$. Instead, it is comprised by the sum $\mathcal{M}^{(2)}_{3,2}(\varepsilon_I) + \mathcal{M}^{(2)}_{1,2}(\varepsilon_I)$ of the terms associated with the $Y^0_1$ term in equation 8.9. Like in the one-photon case, the phases cross at the resonance energy, when the intermediate $d$ transition goes to zero.

Although this model is not capable of explaining the complex behaviour of the experimental data, that is not its purpose. Rather, it illustrates the principle by which interference between ionisation via different symmetries influences the angular dependence of the photoemission delays.

### 8.1.6 Conclusions

In the present study, two-colour XUV-IR RABITT measurements have been used to extract time-dependent as well as angularly and energetically resolved atomic delays in argon. The XUV spectra were chosen to populate the energy region containing the $3s^{-1}n\ell$ series of autoionising resonances. The $3s^{-1}4p$ and $3s^{-1}5p$ resonances in particular can be seen to have a clear effect on the measured atomic delays. The $3s^{-1}4p$ resonance was also, along with the $3s^{-1}4s$ one, observed to have an impact on the anisotropy parameters of the measured spectrum. This is not the case for the $3s^{-1}5p$ resonance, which is significantly narrower than the $3s^{-1}4p$ one.

Further, the results presented demonstrate the sharp phase-distortions characteristic of resonant continua; which, as discussed in chapter 3.2.1, prevent the interpretation of the atomic delay as a Wigner delay. In the present study, these distortions are shown to vary with the photoelectron emission angle. This

anisotropic behaviour can be modeled by using a simple model based on an extension of Fano formalism for resonant continuum to two-photon transitions. In the context of this model, the resonances may be artificially removed, showing that they serve to greatly increase the delay anisotropy.

The angular dependence of the phenomena studied here can be explained as being the result of the coherent interference between several open ionisation channels. Such variations are enhanced near the resonances, where the matrix elements associated with the different channels undergo sharp changes.

# IV Conclusions

# Chapter 9

# Conclusions

This thesis considers the time-dependent, attosecond electron dynamics of atomic systems. Such dynamics are a highly important avenue of study, as electron movement is a driving force in chemical reactions. In order to study such dynamics, a pump-probe approach can be employed – by exposing a system to two distinct laser pulses, separated in time by a variable delay, time-dependent phenomena may be probed. In particular, two pump-probe methods were considered as part of this thesis.

The first method employed is what is known as attosecond transient absorption spectroscopy (ATAS), which conventionally uses a short extreme ultraviolet (XUV) pump and a low-frequency, few-femtosecond probe. A well established method, with an analogous femtosecond counterpart, ATAS is capable of tracking time-resolve electron dynamics and reconstruct electronic wave packets.

ATAS has previously been used to study helium below the second ionisation threshold (Argenti et al. 2015; Ott et al. 2014). This was done using accurate, full-electron, ab-initio pump-probe calculations, implemented using a B-spline basis. Here, a similar theoretical study – using similar pulse parameters and the same basis – was undertaken to probe the same atom above the second threshold, where several ionisation channels are open.

With these pulse parameters, it was possible to induce resonant one-photon transitions between the $3s4p\ ^1P^o$ resonance and lower $3\ell^2\ ^1S^e$ and $3\ell^2\ ^1D^e$ states, where $\ell$ is the angular momentum. Further, two-photon beatings between the $3s4p\ ^1P^o$ and $3s4p\ ^1P^o$ resonances and the lower $^1P^o$ continuum were observed, showing the formation of a probe-induced, multichannel, two-electron correlated wave packet. Similarly to was observed to be the case below the second ionisation threshold, it is thus possible to control the multichannel, two-electron correlated wave packet.

Further, it can be concluded that the opening of additional ionisation channels should pose no major challenge compared to the single-channel case. The only features qualitatively different from what was observed below the second threshold were two-photon beatings between autoionising resonances and the nonresonant continuum. One complication that was observed, however, is the difficulty of unambiguously attributing certain features to specific processes. This may be solved by the addition of a low-frequency component to the pump.

A second atomic system studied using ATAS as part of this thesis is neon. In this case, a two-colour pump was indeed used, the XUV being overlaid with a near infrared (NIR) field of the same frequency as the control pulse. This gave rise to one-photon beatings between the $2s^{-1}3p\ ^1P^o$ autoionising resonance and the nearby $2s^{-1}3s\ ^1S^e$ and $2s^{-1}3d\ ^1D^e$ states.

The study was undertaken using accurate, full-electron, ab-initio pump-probe calculations, with a basis created through the newly developed XCHEM methodology. A previous study (Ding et al. 2016) used a mix of experiment and R-matrix theory to carry out a study with similar laser parameters, observing the same one-photon beatings. The agreement between previous literature data and the current study can be taken as providing validation to the XCHEM methodology.

The results presented here also show signs of one- and two-photon beatings between the $^1P^o$ continuum and higher resonances, like what was observed for helium. More specifically, the one-photon beatings were enhanced by the $2s^{-1}3s\ ^1S^e$ resonance, and the two-photon ones by the $2s^{-1}3p\ ^1P^o$ resonance.

These were not observed in the reference study, which looked only at higher energies.

The second pump-probe method considered herein is reconstruction of attosecond beatings by interference of two-photon transitions (RABITT); which uses a train of extreme ultraviolet attosecond pulses (XUV-APT) as a pump, consisting of the odd harmonics of a low-frequency probe, in order to consider the interference between different ionisation paths. It is capable of obtaining photoemission delays of the order of hundreds of attoseconds.

Using the aforementioned time-dependent XCHEM implementation, a RABITT study of neon was also undertaken as part of this thesis. This was done in multi-resonance energy-regions of neon, resulting in a complex energy-dependence of the measured phases. Both experimental and theoretical results have been presented, showing excellent agreement, and further validating the XCHEM methodology.

Multi-resonance regions have previously not been available to RABITT, due to the difficulty of accurately modeling the associated electron correlation, which would be needed for an accurate theoretical description, necessary to guide experiment. This study thus opens the way for reconstruction of resonant electronic wave-packets coherently produced by two-photon ionisation in such regions, extending the applicability of reconstruction methods such as RABITT.

In order to further understand the contributions of the different states, a simple model, based on an extension of the Fano description of resonant continua to two-photon transitions, was employed. Despite its simplicity, it was capable of accurately predicting the behaviour of the measured spectral phases, and thereby disentangling the contributions of the different involved resonances. Such models are even more useful when more accurate ab-initio calculations are unavailable.

Such was the case for the final study presented in this thesis, which considered the angularly and energetically resolved emission delays in argon near the $3s^{-1}n\ell$ series of resonances using RABITT. Both the $3s^{-1}5p$ and, especially strongly, the $3s^{-1}4p$ resonances were seen to have a clear effect on the measured

atomic delays, and their angular dependence. The $3s^{-1}4p$ resonance was also, along with the $3s^{-1}4s$ one, observed to have an impact on the anisotropy parameters of the measured spectrum. This was not the case for the $3s^{-1}5p$ resonance, which is significantly narrower than the $3s^{-1}4p$ one.

Although the phase varies slowly with energy in smooth continua, it undergoes dramatic changes when a resonance is introduced. These distortions are shown to vary with the photoelectron emission angle.

The model discussed above in the context of neon also here manages to predict the behaviour of the emission delays. In the context of this model, the resonances may be artificially removed, showing that they serve to greatly increase the delay anisotropy.

The observed angular dependence of the emission delays can be explained as the result of the coherent interference between several open ionisation channels. Such variations are enhanced near the resonances, where the matrix elements associated with the different channels undergo sharp changes.

# Chapter 10

## Conclusiones

Esta tesis trata de las dinámicas electrónicas de attosegundo de sistemas atómicos. Como el movimiento de electrones es la fuerza motriz de las reacciones químicas, el estudio de este tipo de dinámicas resulta muy atractivo. Para estudiar este tipo de dinámicas, se pueden utilizar métodos de bombeo y sonda; considerando dos pulsos de láser distintos, separados en el tiempo con un retraso variable, permitiendo la investigación de fenómenos dependientes del tiempo. En esta tesis, dos métodos de bombeo y sonda en particular se han empleado.

El primer método empleado se conoce como espectroscopía de absorción transitoria de attosegundos (ATAS), y como norma general usa un pulso de bombeo corto de radiación ultravioleta extrema (XUV) y una sonda de baja frecuencia y de algunos femtosegundos. Un método sólidamente establecido, con un equivalente análogo en la física de femtosegundos, ATAS es capaz de rastrear dinámicas electrónicas resueltas en el tiempo y reconstruir paquetes de ondas electrónicos.

ATAS ya ha sido usado para estudiar el helio por debajo del segundo umbral de ionización (Argenti et al. 2015; Ott et al. 2014). Esto se hizo usando cálculos ab-initio precisos, considerando todos los electrones y utilizando una base de B-splines. Aquí un estudio teórico semejante – usando semejantes parámetros

de pulso y la misma base – se realizó para investigar el mismo átomo por encima del segundo umbral de ionización, done existen varios canales de ionización.

Con susodichos parámetros de pulso, fue posible provocar "beatings" de un fotón entre la resonancia $3s4p\ ^1P^o$ y estados $3\ell^2\ ^1S^e$ y $3\ell^2\ ^1D^e$ más bajas, donde $\ell$ denota el momento angular. Además, se observaron beatings entre las resonancias $3s4p\ ^1P^o$ y $3s4p\ ^1P^o$ y el continuo $^1P^o$ más bajo, lo cual muestra la formación de un paquete correlacionado multicanal de ondas de dos electrones inducido por la sonda. Tal como fue observado debajo del segundo umbral de ionización, es posible controlar el paquete correlacionado multicanal de ondas de dos electrones.

Además, se puede concluir que la presencia de canales de ionización adicionales no van a suponer ningún problema en comparación con el caso de un único canal abierto. La única característica espectral que cualitativamente separa los dos casos es la presencia de beatings de dos fotones entre estados autoionizantes y el continuo suave. Una complicación observada, sin embargo, es la dificultad de atribuir de modo inequívoco ciertos rasgos espectrales a procesos especificos. Este problema puede ser resuelto con la adición de un componente de baja frecuencia al pulso de bombeo.

El segundo átomo que ha sido investigado usando ATAS en esta tesis es neón. En este caso, un pulso de bombeo de dos colores sí fue utilizado – esté fue era mezclado con un pulso infrarrojo cercano (NIR) de la misma frecuencia que la sonda. Esto causó beatings de un fotón entre la resonancia autoionizante $2s^{-1}3p\ ^1P^o$ y los estados cercanos de $2s^{-1}3s\ ^1S^e$ y $2s^{-1}3d\ ^1D^e$.

El estudio se llevó al cabo usando cálculos ab-initio exactos considerando todos los electrones, con un base generado usando el método recientemente propuesto de XCHEM. En otro estudio (Ding et al. 2016) con parámetros de láser parecidos ya se observaron los mismos beatings, mediante experimentación y calculaciones de matriz R. Todos los rasgos espectrales mencionados en aquel estudio también se observaron aquí. La buena concordancia con el estudio de referencia otorga validez al método de XCHEM.

Los resultados presentados aquí también muestran signos de beatings de

uno y dos fotones entre el continuo $^1P^o$ y resonancias más altas, como lo que fue observado en el helio. Más específicamente, los beatings de un fotón se amplificaron por la resonancia $2s^{-1}3s\ ^1S^e$, y los de dos fotones por la resonancia $2s^{-1}3p\ ^1P^o$. Estos beatings no fueron observados en el estudio referencia, que solo consideraba energías más altas.

El segundo método de bombeo y sonda considerado aquí es reconstrucción de "beatings" de attosegundo por interferencia de transiciones de dos fotones (RABITT); que utiliza como bombeo un tren de pulsos de radiación ultravioleta extrema (XUV-APT), que contiene armónicas impares de la sonda, para considerar la interferencia entre distintos trayectorias de ionización. Es capaz de obtener retrasos de la fotoemisión con una precisión de cientos de attosegundos.

Utilizando la antes mencionada implementación dependiente del tiempo de XCHEM, un estudio de RABITT se ha llevado a cabo como parte de esta tesis. El estudio se realizó en las cercanías de resonancias múltiples, por lo cual había una dependencia compleja de la energía con la las fases obtenidas. Tanto resultados experimentales como teóricos se han presentado. Los resultados teóricos comparan muy bien con las experimentales, dando así validez al método de XCHEM.

Hasta ahora, los métodos interferométricos han estado restringidos a regiones de energíıa de hasta una resonancia, a causa de las dificultades en describir la correlación electrónica, lo cual sería necesario para una descripción teórica fiel que se pueda usar para guiar a los experimentos. Por consiguiente, este estudio abre el camino para la reconstrucción de paquetes de ondas electrónicas producidos por ionización de dos fotones en regiones semejantes, extendiendo la aplicabilidad de métodos de reconstrucción como el RABITT.

Para entender la contribución de las distintas resonancias involucradas, se empleó un modelo sencillo basado en una extensión de la descripción de Fano del continuo resonante a transiciones de dos fotones. A pesar de su simplicidad, fue capaz de predecir con precisión la dependencia energética de la fase, por lo cual, también fue capaz de resolver las contribuciones de las distintas resonancias involucradas. Tal tipo de modelos son aun más útiles

cuando cálculos ab-initio más precisos no son posibles.

Un ejemplo de eso se puede encontrar en el ultimo estudio presente en esta tesis, que uso RABITT para considerar la dependencia angular y energética de retrasos de emisión en argón cerca a la serie $3s^{-1}n\ell$ de estados autoionizantes. Tanto la resonancia $3s^{-1}5p$ como, aún más fuertemente, la $3s^{-1}4p$ afectan considerablemente los retrasos y sus dependencias angulares. Se observó que la resonancia $3s^{-1}4p$, junto con la $3s^{-1}4s$, tienen un efecto en los parámetros de anisotropía del espectro. Lo mismo no se observó con la resonancia $3s^{-1}5p$, que es considerablemente más estrecha que la $3s^{-1}4p$.

A pesar de que la fase varía lentamente en continuos suaves, depende fuertemente de la energía en las cercanías de una resonancia. Estas distorsiones varían mucho con el angulo de emisión.

El modelo, mencionado anteriormente, que se empleó en el contexto del neón también aquí es capaz de predecir el comportamiento de los retrasos de emisión. En el contexto de este modelo, es posible artificialmente quitar las resonancias, mostrando que aumentan significativamente la anisotropía del retraso.

La dependencia angular observada en los retrasos de emisión se puede explicar como el resultado de la interferencia coherente entre varios canales abiertos de ionización. Ese tipo de variaciónes se amplifican cerca se las resonancias, donde los elementos de matriz asociados con los distintos canales están sujetos a cambios fuertes.

# V

# Appendices

# Appendix A

## Atomic Units

Throughout this communication Hartree (1928) atomic units are used unless otherwise stated. Atomic units may be defined by setting $\hbar = m_e = e = 4\pi\epsilon_0 = 1$, where $\hbar$ is the reduced Planck constant, $m_e$ the electron mass, $e$ the elementary charge, and $\epsilon_0$ the vacuum permittivity. In this appendix, several relevant atomic unit conversion factors are given:

| Quantity | Conversion | | | |
|---|---|---|---|---|
| Energy | $E_h = 1\,\text{au} =$ | $\frac{m_e e^4}{(4\pi\epsilon_0\hbar)^2}$ | $= 4.360\times10^{-18}$ | J |
| Length | $a_0 = 1\,\text{au} =$ | $\frac{4\pi\epsilon_0\hbar^2}{m_e e^2}$ | $= 5.292\times10^{-11}$ | m |
| Time | $1\,\text{au} =$ | $\frac{\hbar}{E_h}$ | $= 2.419\times10^{-17}$ | s |
| Velocity | $1\,\text{au} =$ | $\frac{a_0}{\hbar/E_h}$ | $= 2.188\times10^{6}$ | $\frac{\text{m}}{\text{s}}$ |
| Mass | $1\,\text{au} =$ | $m_e$ | $= 9.109\times10^{-31}$ | kg |
| Electric potential | $1\,\text{au} =$ | $\frac{E_h}{e}$ | $= 2.721\times10^{1}$ | V |
| Electric field | $1\,\text{au} =$ | $\frac{E_h}{e a_0}$ | $= 5.142\times10^{11}$ | $\frac{\text{V}}{\text{m}}$ |
| Dipole moment | $1\,\text{au} =$ | $e a_0$ | $= 8.478\times10^{-30}$ | $\text{C}\cdot\text{m}$ |
| Intensity | $1\,\text{au} =$ | $\frac{\epsilon_0 c E_h}{2(e a_0)^2}$ | $= 3.509\times10^{16}$ | $\frac{\text{W}}{\text{cm}^2}$ |

# Appendix B

## Time-Dependent Perturbation Theory

At several points in this thesis, low-order, time-dependent perturbation theory (TDPT) is used to consider the case when the field-free, time-independent, atomic Hamiltonian, $\hat{\mathcal{H}}_0$, is perturbed by a weak, time-dependent potential $\hat{\mathcal{V}}(t)$. Thus, the Hamiltonian can be written on the form

$$\hat{\mathcal{H}}(t) = \hat{\mathcal{H}}_0 + \hat{\mathcal{V}}(t). \tag{B.1}$$

In order to explain the concept of TDPT in more detail, the time-dependent Schrödinger equation (TDSE) first should be considered. Througout this work it has been defined, in what is known as the Schrödinger representation (denoted here with subscript S), as

$$i\frac{\partial}{\partial t}\left|\psi(t)\right\rangle_{\mathrm{S}} = \hat{\mathcal{H}}_{\mathrm{S}}(t)\left|\psi(t)\right\rangle_{\mathrm{S}} \tag{B.2}$$

by applying the Hamiltonian operator $\hat{\mathcal{H}}_{\mathrm{S}}(t)$ to a given ket $\left|\psi(t)\right\rangle_{\mathrm{S}}$. When no external field is present, the ket evolves as

$$\left|\psi(t)\right\rangle_{\mathrm{S}} = \exp\left(-i\hat{\mathcal{H}}_0 t\right)\left|\psi(0)\right\rangle_{\mathrm{S}}. \tag{B.3}$$

With this in mind, the transformation

$$\left|\psi(t)\right\rangle_{\mathrm{D}} = \exp\left(i\hat{\mathcal{H}}_0 t\right)\left|\psi(t)\right\rangle_{\mathrm{S}}, \tag{B.4}$$

to what is known as the Dirac (or interaction) representation (denoted with subscript D), is made. From the definition of the Dirac representation, it follows that as long as $\hat{\mathcal{V}}(t) = 0$, the state kets remain constant over time. The corresponding operator-transformation,

$$\hat{\mathcal{A}}_{\mathrm{D}}(t) = \exp\left(i\hat{\mathcal{H}}_0 t\right) \times \hat{\mathcal{A}}_{\mathrm{S}}(t) \times \exp\left(-i\hat{\mathcal{H}}_0 t\right), \tag{B.5}$$

compensates, keeping the time-dependence of observables consistent between the two representations.

It should be noted that the operator $\hat{\mathcal{H}}_0$, since it commutes with $\exp\left(i\hat{\mathcal{H}}_0 t\right)$, is identical in both representations. This can easily be understood by expanding the Taylor series of $\exp\left(i\hat{\mathcal{H}}_0 t\right)$. For this reason, no subscript is used for $\hat{\mathcal{H}}_0$.

Combining equations B.1 and B.4, it can be seen from the derivation

$$\begin{aligned} i\frac{\partial}{\partial t}\left|\psi\right\rangle_{\mathrm{D}} =& i\frac{\partial}{\partial t}\left[\exp\left(i\hat{\mathcal{H}}_0 t\right)\left|\psi\right\rangle_{\mathrm{S}}\right] \\ =& -\hat{\mathcal{H}}_0 \exp\left(i\hat{\mathcal{H}}_0 t\right)\left|\psi\right\rangle_{\mathrm{S}} + \exp\left(i\hat{\mathcal{H}}_0 t\right)\left[\hat{\mathcal{H}}_0 + \hat{\mathcal{V}}_{\mathrm{S}}\right]\left|\psi\right\rangle_{\mathrm{S}} \\ =& \exp\left(i\hat{\mathcal{H}}_0 t\right)\hat{\mathcal{V}}_{\mathrm{S}} \exp\left(-i\hat{\mathcal{H}}_0 t\right)\left|\psi\right\rangle_{\mathrm{D}} \end{aligned} \tag{B.6}$$

that the Schrödinger-like equation

$$i\frac{\partial}{\partial t}\left|\psi(t)\right\rangle_{\mathrm{D}} = \hat{\mathcal{V}}_{\mathrm{D}}\left|\psi(t)\right\rangle_{\mathrm{D}} \tag{B.7}$$

describes time-evolution in the Dirac representation (Sakurai et al. 2011). Alternatively, the same equation can be rewritten as

$$i\frac{\partial}{\partial t}\hat{\mathcal{U}}_{\mathrm{D}}(t,t_0)\left|\psi(t_0)\right\rangle_{\mathrm{D}} = \hat{\mathcal{V}}_{\mathrm{D}}(t)\hat{\mathcal{U}}_{\mathrm{D}}(t,t_0)\left|\psi(t_0)\right\rangle_{\mathrm{D}}, \tag{B.8}$$

where $\hat{\mathcal{U}}_{\mathrm{D}}(t,t_0)$ is the (Dirac representation) time evolution operator between two times $t_0$ and $t$. Since this relation is independent of the initial ket $\left|\psi(t_0)\right\rangle_{\mathrm{D}}$ and time $t_0$, it is equivalent to

$$i\frac{\partial}{\partial t}\hat{\mathcal{U}}_{\mathrm{D}}(t,t_0) = \hat{\mathcal{V}}_{\mathrm{D}}(t)\hat{\mathcal{U}}_{\mathrm{D}}(t,t_0). \tag{B.9}$$

Together with the initial condition $\hat{\mathcal{U}}_{\mathrm{D}}(t_0,t_0) = \hat{\mathcal{I}}$, where $\hat{\mathcal{I}}$ is the identity operator, (that is, if no time passes, no change occurs to the system) equation B.9 can be integrated between two times $t_0$ and $t_1$ as

$$\hat{\mathcal{U}}_{\mathrm{D}}(t_1,t_0) = \hat{\mathcal{I}} - i\int_{t_0}^{t_1} dt\ \hat{\mathcal{V}}_{\mathrm{D}}(t)\,\hat{\mathcal{U}}_{\mathrm{D}}(t,t_0). \tag{B.10}$$

This can recursively be expanded into a series of terms $\hat{\mathcal{U}}_{\mathrm{D}}^{(n)}(t_1,t_0)$ (Cohen-Tannoudji et al. 1998), as

$$\hat{\mathcal{U}}_{\mathrm{D}}(t_1,t_0) = \sum_{n=0}^{\infty}\hat{\mathcal{U}}_{\mathrm{D}}^{(n)}(t_1,t_0), \tag{B.11}$$

which is known as a Dyson series. The individual terms can be written as

$$\hat{\mathcal{U}}_{\mathrm{D}}^{(n)}(t_1,t_0) = (-i)^n\int_{t_1\geq\tau_n\geq\ldots\tau_2\geq\tau_1\geq t_0} d\tau_n\ldots d\tau_2 d\tau_1\ \hat{\mathcal{V}}_{\mathrm{I}}(\tau_n)\times\cdots\times\hat{\mathcal{V}}_{\mathrm{I}}(\tau_2)\times\hat{\mathcal{V}}_{\mathrm{I}}(\tau_1) \tag{B.12}$$

in the Dirac representation. The *nth* term correpsonds to a total of $n$ applications of $\hat{\mathcal{V}}_{\mathrm{I}}(t)$ to an initial ket $\left|\psi(t_0)\right\rangle$. If $\hat{\mathcal{V}}_{\mathrm{I}}(t)$ is sufficently weak, each iterative application incures a decrease in magnitude, and only a few terms need to be included. This is analogous to the case of a Taylor series. In the Schrödinger

representation,

$$\begin{aligned}\hat{\mathcal{U}}_{\mathrm{S}}^{(n)}(t_1,t_0) = (-i)^n \int_{t_1\geq t_n\geq\cdots\geq t_2\geq t_1\geq t_0} dt_n \ldots dt_2 dt_1 \; \exp\Big(-idt[\,t_1-\tau_n]\hat{\mathcal{H}}_0\Big)\times\hat{\mathcal{V}}_{\mathrm{S}}(\tau_n) \\ \cdots \\ \times\exp\Big(-idt[\tau_3-\tau_2]\hat{\mathcal{H}}_0\Big)\times\hat{\mathcal{V}}_{\mathrm{S}}(\tau_2) \\ \times\exp\Big(-idt[\tau_2-\tau_1]\hat{\mathcal{H}}_0\Big)\times\hat{\mathcal{V}}_{\mathrm{S}}(\tau_1) \\ \times\exp\Big(-idt[\tau_1-\,t_0]\hat{\mathcal{H}}_0\Big)\end{aligned} \tag{B.13}$$

is the equivalent expression.

In order to gain an intuitive understanding of equation B.13, it may be useful to consider the case of an atomic potential, $\hat{\mathcal{H}}_0$, perturbed by an external electric field. For this case, multiplication with $\hat{\mathcal{V}}_{\mathrm{S}}(t)$ corresponds to absorption of one photon. In equation B.13 it can be seen that, by applying $\hat{\mathcal{U}}_{\mathrm{S}}^{(n)}(t_1,t_0)$, the state ket first evolves freely from time $t_0$ to $\tau_1$, absorbs a photon at time $\tau_1$, then again evolves freely until time $\tau_2$, at which point it absorbs a second photon. This process continues until time $t_1$, where a total of $n$ photons have been absorbed. Via integration, it considers all (sequential) values of $\tau_i$, $i\in\{1,\ldots,n\}$. Thus, it can be seen that the $nth$ term in the series corresponds to the $n-$photon process.

# Appendix C

## Numerical Accuracy and Efficiency

The ab-initio propagations utilised in this work rely on a split time-propagation operator

$$\hat{\mathcal{U}}(t;dt) \approx \exp\left[-i\,dt\,\hat{\mathcal{V}}_{\mathrm{CAP}}\right] \tag{C.1a}$$

$$\times \exp\left[-i\frac{dt}{2}\hat{\mathcal{H}}_0\right] \tag{C.1b}$$

$$\times \exp\left[-i\,dt\,A\left(t+\frac{dt}{2}\right)\hat{\mathcal{P}}\right] \tag{C.1c}$$

$$\times \exp\left[-i\frac{dt}{2}\hat{\mathcal{H}}_0\right] \tag{C.1d}$$

initially defined in equation 3.79 for a time step length $dt$. This operator takes into account the field-free propagation by the atomic Hamiltonian $\hat{\mathcal{H}}_0$, the propagation driven by the vector potential $A(t)$ (which include the dipole operator $\hat{\mathcal{P}}$ and the fine-structure constant $\alpha$ in the exponent), and the propagation using the Complex Absorption Potential (CAP) $\hat{\mathcal{V}}_{\mathrm{CAP}}$. This appendix deals with the accuracy of the operator splitting, as well as the time complexity of the split operator components.

## C.1 Accuracy of the Operator Split

For a set of scalars $x$ and $y$, the exponent $e^{x+y}$ may be split into separate components according to the formula $e^{x+y} = e^x e^y$. For two operators $\hat{\mathcal{X}}$ and $\hat{\mathcal{Y}}$, however, the relation $e^{\hat{\mathcal{X}}+\hat{\mathcal{Y}}} = e^{\hat{\mathcal{X}}} e^{\hat{\mathcal{Y}}}$ holds if and only if $\hat{\mathcal{X}}$ and $\hat{\mathcal{Y}}$ commute. Thus, the operator splitting given in equation C.1 holds only approximately.

This can be seen by considering the Taylor expansion. For the exponential of an operator $\hat{\mathcal{X}}$, the Taylor expansion reads

$$\exp\left[\hat{\mathcal{X}}\right] = \sum_{i=0}^{\infty} \frac{1}{i!} \hat{\mathcal{X}}^i. \tag{C.2}$$

Comparing the Taylor expansions of the two expressions $e^{\hat{\mathcal{X}}+\hat{\mathcal{Y}}}$ and $e^{\hat{\mathcal{X}}} e^{\hat{\mathcal{Y}}}$, it can be seen that

$$\begin{aligned}
\exp\left[\hat{\mathcal{X}} + \hat{\mathcal{Y}}\right] &= \hat{\mathcal{I}} + \left(\hat{\mathcal{X}} + \hat{\mathcal{Y}}\right) + \frac{\hat{\mathcal{X}}^2 + \hat{\mathcal{X}}\hat{\mathcal{Y}} + \hat{\mathcal{Y}}\hat{\mathcal{X}} + \hat{\mathcal{Y}}^2}{2} + \dots && \text{(C.3a)} \\
&\neq \hat{\mathcal{I}} + \left(\hat{\mathcal{X}} + \hat{\mathcal{Y}}\right) + \frac{\hat{\mathcal{X}}^2 + 2\hat{\mathcal{X}}\hat{\mathcal{Y}} + \hat{\mathcal{Y}}^2}{2} + \dots \quad . && \text{(C.3b)} \\
&= \exp\left[\hat{\mathcal{X}}\right] \times \exp\left[\hat{\mathcal{Y}}\right] && \text{(C.3c)}
\end{aligned}$$

In fact, two expressions only coincide up to the first-order term, unless $\hat{\mathcal{X}}$ and $\hat{\mathcal{Y}}$ commute, in which case $\hat{\mathcal{X}}\hat{\mathcal{Y}} + \hat{\mathcal{Y}}\hat{\mathcal{X}} = 2\hat{\mathcal{X}}\hat{\mathcal{Y}}$.

### C.1.1 The Strang Splitting

As a initial step, in order to understand the splitting of the operator, consider the operator split which divides the field-free and the field-driven operator, corresponding to equations C.1b–C.1d. It is known as a Strang (1968) splitting, and can be written as

$$\exp\left[\hat{\mathcal{X}}+\hat{\mathcal{Y}}\right] \longrightarrow \exp\left[\tfrac{1}{2}\hat{\mathcal{X}}\right]\times\exp\left[\hat{\mathcal{Y}}\right]\times\exp\left[\tfrac{1}{2}\hat{\mathcal{X}}\right] \tag{C.4}$$

by introducing the shorthand expressions

$$\hat{\mathcal{X}} = -i\,dt\,\hat{\mathcal{H}}_0 \tag{C.5a}$$

$$\hat{\mathcal{Y}} = -i\,dt\,A\left(t+\frac{dt}{2}\right)\hat{\mathcal{P}} \tag{C.5b}$$

for the relevant exponents. Looking at the split Taylor expansion,

$$\begin{aligned}\exp\left[\tfrac{1}{2}\hat{\mathcal{X}}\right]\times\exp\left[\hat{\mathcal{Y}}\right]\times\exp\left[\tfrac{1}{2}\hat{\mathcal{X}}\right] &= \sum_{i=0}^{\infty}\frac{1}{i!}\left(\frac{\hat{\mathcal{X}}}{2}\right)^i\cdot\sum_{j=0}^{\infty}\frac{1}{i!}\hat{\mathcal{Y}}^j\cdot\sum_{k=0}^{\infty}\frac{1}{i!}\left(\frac{\hat{\mathcal{X}}}{2}\right)^k \\ &= \hat{\mathcal{I}}+\left(\hat{\mathcal{X}}+\hat{\mathcal{Y}}\right)+\frac{\hat{\mathcal{X}}^2+\hat{\mathcal{X}}\hat{\mathcal{Y}}+\hat{\mathcal{Y}}\hat{\mathcal{X}}+\hat{\mathcal{Y}}^2}{2} \\ &\quad+\frac{1}{6}\Big[\hat{\mathcal{X}}^3+\tfrac{3}{4}\hat{\mathcal{X}}^2\hat{\mathcal{Y}}+\tfrac{3}{2}\hat{\mathcal{X}}\hat{\mathcal{Y}}\hat{\mathcal{X}}+\tfrac{3}{4}\hat{\mathcal{Y}}\hat{\mathcal{X}}^2 \\ &\qquad+\tfrac{3}{2}\hat{\mathcal{X}}\hat{\mathcal{Y}}^2+\tfrac{3}{2}\hat{\mathcal{Y}}^2\hat{\mathcal{X}}+\hat{\mathcal{Y}}^3\Big]+\ldots\end{aligned} \tag{C.6}$$

and comparing it with equation C.3a, it can be seen that the second-order term now is correct. The third-order term, however, which for $\exp\left[\hat{\mathcal{X}}+\hat{\mathcal{Y}}\right]$ can be calculated as $\frac{1}{6}\left[\hat{\mathcal{X}}^3+3\hat{\mathcal{X}}^2\hat{\mathcal{Y}}+3\hat{\mathcal{X}}\hat{\mathcal{Y}}^2+\hat{\mathcal{Y}}^3\right]$, is correct if and only if – again – $\hat{\mathcal{X}}$ and $\hat{\mathcal{Y}}$ commute. Hence, the Strang splitting is a second order splitting.

### C.1.2 Addition of the CAP

Presently consider the introduction of the Complex Absorption Potential (CAP),

$$\hat{\mathcal{Z}} = -i\,dt\,\hat{\mathcal{V}}_{\mathrm{CAP}}, \tag{C.7}$$

in equation C.1a. After the introduction of this component, the splitting can be written as

$$\exp\left[\hat{\mathcal{X}}+\hat{\mathcal{Y}}+\hat{\mathcal{Z}}\right] \longrightarrow \exp\left[\hat{\mathcal{Z}}\right]\times\exp\left[\tfrac{1}{2}\hat{\mathcal{X}}\right]\times\exp\left[\hat{\mathcal{Y}}\right]\times\exp\left[\tfrac{1}{2}\hat{\mathcal{X}}\right], \tag{C.8}$$

which implies multiplication by $\hat{\mathcal{Z}}$ only from the left.

From the Taylor expansion

$$\begin{aligned}\exp\left[\hat{\mathcal{X}}+\hat{\mathcal{Y}}+\hat{\mathcal{Z}}\right] = \hat{\mathcal{I}} + \left(\hat{\mathcal{X}}+\hat{\mathcal{Y}}+\hat{\mathcal{Z}}\right) + \frac{1}{2}\Big[&\hat{\mathcal{X}}^2+\hat{\mathcal{X}}\hat{\mathcal{Y}}+\hat{\mathcal{Y}}\hat{\mathcal{X}}+\hat{\mathcal{X}}\hat{\mathcal{Z}}+\hat{\mathcal{Z}}\hat{\mathcal{X}}+\\ &\hat{\mathcal{Y}}^2+\hat{\mathcal{Y}}\hat{\mathcal{Z}}+\hat{\mathcal{Z}}\hat{\mathcal{Y}}+\hat{\mathcal{Z}}^2\Big]+\ldots\end{aligned} \tag{C.9}$$

of the non-split operator, it can be seen that the second-order term contains multiplications by $\hat{\mathcal{Z}}$ from the right. Hence, unless the CAP commutes with both $\hat{\mathcal{H}}_0$ and $\hat{\mathcal{P}}$, its introduction implies a lowering of the splitting to the first order.

## C.2 Time Complexity

Numerically, the effect on the time step operator $\hat{\mathcal{U}}(t;dt)$ in equation C.1 on the state ket $|\Psi\rangle$, is treated via the application of a time step matrix $\underline{\mathrm{U}}(t;dt)$ on the state vector

$$\boldsymbol{\Psi} = \begin{bmatrix} c_0 \\ c_1 \\ c_2 \\ \vdots \end{bmatrix}, \tag{C.10}$$

given in the basis of size $N$ of the atomic Hamiltonian matrix $\underline{\mathrm{H}}_0$. Here, the time complexity of the application of the different parts, defined by the splitting in equation C.1, of $\underline{\mathrm{U}}(t;dt)$ is investigated.

### C.2.1 Field-Free Propagation

Initially consider the field-free propagation, discussed in chapter 3.3.1, corresponding to equations C.1b and C.1d. Since the propagation takes place in the eigenbasis of the $N \times N$ matrix $\underline{\mathrm{H}}_0$, the field-free propagator can be written as the diagonal matrix

$$\exp\left(-i\frac{dt}{2}\hat{\mathcal{H}}_0\right) = \begin{pmatrix} e^{-i\frac{dt}{2}\omega_0} & 0 & 0 & \\ 0 & e^{-i\frac{dt}{2}\omega_1} & 0 & \cdots \\ 0 & 0 & e^{-i\frac{dt}{2}\omega_2} & \\ & \vdots & & \ddots \end{pmatrix}. \tag{C.11}$$

Since this matrix is diagonal, it can be applied to $\mathbf{\Psi}$ via the state-wise multiplication

$$\exp\left(-i\frac{dt}{2}\underline{\mathrm{H}}_0\right)\begin{bmatrix} c_0 \\ c_1 \\ c_2 \\ \vdots \end{bmatrix} = \begin{bmatrix} \exp\left(-i\,\frac{dt}{2}\,\omega_0\right)c_0 \\ \exp\left(-i\,\frac{dt}{2}\,\omega_1\right)c_1 \\ \exp\left(-i\,\frac{dt}{2}\,\omega_2\right)c_2 \\ \vdots \end{bmatrix}. \tag{C.12}$$

This is an operation with time complexity of $\mathcal{O}(N)$.

### C.2.2 Field-Driven Propagation

Presently consider the application of the field-driven propagation operator, given in equation C.1c. It is discussed in more detail in chapter 3.3.2. This requires projection into the eigenbasis of the dipole matrix $\underline{\mathrm{P}}$.

#### Using a Krylov Method

Using the Krylov method, with a Krylov space of size $n$, requires the calculation of a set $\{\xi_i,\ i \in \{0,\dots n-1\}\}$ of Krylov vectors, each of which is associated with a help vector $\xi_i'$.

Using the $i-1th$ Krylov vector $\xi_{i-1}$, the $ith$ help vector $\xi_i'$ may be computed as

$$\xi_i' = -i\,dt\,\alpha\ \underline{\mathrm{P}}\ \xi_{i-1} \tag{C.13}$$

according to equation 3.84, by multiplication of the matrix $\underline{\mathrm{P}}$ and subsequent multiplication by the constant $-i\,dt\,\alpha$. The matrix multiplication is of order $\mathcal{O}\left(N^2\right)$, while the scalar multiplication is of order $\mathcal{O}(N)$, for a total time complexity of, for a total $\mathcal{O}\left(N^2+N\right)=\mathcal{O}\left(N^2\right)$.

The $ith$ Krylov vector may now be calculated as

$$\xi_i = \frac{1}{N_i}\left(\xi_i' - \sum_j^{i-1} \xi_j \left\langle \xi_j, \xi_i' \right\rangle\right) \tag{C.14}$$

where $N_i$ is a normalisation constant and $\langle \boldsymbol{x}, \boldsymbol{y} \rangle$ denotes the hermitian inner product of $\boldsymbol{x}$ and $\boldsymbol{y}$. Here, the maximum order of the operations used (the scalar product, the hermitian inner product, vector subtraction, scalar multiplication, calculation of the norm) is $\mathcal{O}(N)$. Thus, each addition of an extra Krylov vector is an operation of total time complexity $\mathcal{O}\left(N^2 + N\right) = \mathcal{O}\left(N^2\right)$.

After the Krylov space is calculated, it is used to diagonalise $\underline{\mathrm{P}}$, which is implemented using the LAPACK (Anderson et al. 1999) ZHEEV routine for hermitian matrices. Although matrix diagonalisation is a heavy process, as it takes place in a limited space of size $n \ll N$, its contribution to the time complexity may be disregarded.

For a maximum Krylov space of size $n_{max}$, the Krylov method is thus of order $\mathcal{O}\left(n_{max} \times N^2\right)$.

#### Exact Solution

The exact implementation of the driven propagation involves projection into the eigenbasis of the dipole matrix $\underline{\mathrm{P}}$. If $\underline{\mathrm{P}}$ has $M$ eigenvectors, this requires $N \times M$ operations, as does the reverse projection. Analogously to the field-free case, the propagation in the basis of $\underline{\mathrm{P}}$ is of order $\mathcal{O}(M)$. This gives a time-complexity of $\mathcal{O}(M \cdot N)$

This is lower than for the Krylov method, especially as $M \leq N$. For reference, diagonalising the $\underline{\mathrm{P}}$ matrix calculated by XCHEM for neon has consistently given the approximate relation $M \approx \frac{2}{3}N$.

### C.2.3 Complex Absorption Potential

Finally, consider the Complex Absorption Potential (CAP) $\hat{\mathcal{V}}_{\text{CAP}}$, discussed in detail in chapter 3.3.3. It is treated analogously to the exact solution of the driven propagation: Denoting the order of $\hat{\mathcal{V}}_{\text{CAP}}$ $K$, projecting into the eigenbasis of $\hat{\mathcal{V}}_{\text{CAP}}$ and back are both operations of order $\mathcal{O}(K \cdot N)$. Once in the eigenspace, the propagation itself is of order $\mathcal{O}(K \cdot N)$. As in the case of the driven propagation, this gives a time complexity of order $\mathcal{O}(K \cdot N)$.

# Bibliography

**Agostini**, **P.** and L. F. DiMauro (May 2004). "The physics of attosecond light pulses". In: *Reports on Progress in Physics* 67.6, pp. 813–855. DOI: 10.1088/0034-4885/67/6/r01. URL: https://doi.org/10.1088%2F0034-4885%2F67%2F6%2Fr01.

**Anderson**, **E.**, Z. Bai, C. Bischof, S. Blackford, J. Demmel, J. Dongarra, J. Du Croz, A. Greenbaum, S. Hammarling, A. McKenney, and D. Sorensen (1999). *LAPACK Users' Guide*. Third. Philadelphia, PA: Society for Industrial and Applied Mathematics. ISBN: 0-89871-447-8 (paperback).

**Aquilante**, **F.**, J. Autschbach, R. K. Carlson, L. F. Chibotaru, M. G. Delcey, L. De Vico, I. Fdez. Galván, N. Ferré, L. M. Frutos, L. Gagliardi, M. Garavelli, A. Giussani, C. E. Hoyer, G. Li Manni, H. Lischka, D. Ma, P. Malmqvist, T. Müller, A. Nenov, M. Olivucci, T. B. Pedersen, D. Peng, F. Plasser, B. Pritchard, M. Reiher, I. Rivalta, I. Schapiro, J. Segarra-Martí, M. Stenrup, D. G. Truhlar, L. Ungur, A. Valentini, S. Vancoillie, V. Veryazov, V. P. Vysotskiy, O. Weingart, F. Zapata, and R. Lindh (2016). "Molcas 8: New capabilities for multiconfigurational quantum chemical calculations across the periodic table". In: *Journal of Computational Chemistry* 37.5, pp. 506–541. DOI: 10.1002/jcc.24221. eprint: https://onlinelibrary.wiley.com/doi/pdf/10.1002/jcc.24221. URL: https://onlinelibrary.wiley.com/doi/abs/10.1002/jcc.24221.

**Argenti**, **L.**, Á. Jiménez-Galán, J. Caillat, R. Taïeb, A. Maquet, and F. Martín (Apr. 2017). "Control of photoemission delay in resonant two-photon

transitions". In: *Phys. Rev. A* 95 (4), p. 043426. DOI: 10.1103/PhysRevA.95.043426. URL: https://link.aps.org/doi/10.1103/PhysRevA.95.043426.

**Argenti, L.** and E. Lindroth (Unpublished). "B-spline close-coupling description of helium ionization".

**Argenti, L.** and R. Moccia (May 2006). "K-matrix method with B-splines: $\sigma_{n\ell}$, $\beta_n$ and resonances in He photoionization below $N = 4$ threshold". In: *Journal of Physics B: Atomic, Molecular and Optical Physics* 39, p. 2773. DOI: 10.1088/0953-4075/39/12/012.

**Argenti, L.**, C. Ott, T. Pfeifer, and F. Martín (Nov. 2012). "Attosecond Transient Absorption Spectroscopy of doubly-excited states in helium". In: *arXiv [physics.atom-ph]*, p. 2566. arXiv: 1211.2566. URL: http://arxiv.org/abs/1211.2566.

**Argenti, L.**, R. Pazourek, J. Feist, S. Nagele, M. Liertzer, E. Persson, J. Burgdörfer, and E. Lindroth (May 2013a). "Photoionization of helium by attosecond pulses: Extraction of spectra from correlated wave functions". In: *Phys. Rev. A* 87 (5), p. 053405. DOI: 10.1103/PhysRevA.87.053405. URL: https://link.aps.org/doi/10.1103/PhysRevA.87.053405.

— (May 2013b). "Photoionization of helium by attosecond pulses: Extraction of spectra from correlated wave functions". In: *Phys. Rev. A* 87 (5), p. 053405. DOI: 10.1103/PhysRevA.87.053405. URL: https://link.aps.org/doi/10.1103/PhysRevA.87.053405.

**Argenti, L.**, Á. Jiménez-Galán, C. Marante, C. Ott, T. Pfeifer, and F. Martín (2015). "Dressing effects in the attosecond transient absorption spectra of doubly excited states in helium". In: *Physical Review A* 91.6, p. 061403.

**Autler S. H. and Townes, C. H.** (Oct. 1955). "Stark Effect in Rapidly Varying Fields". In: *Phys. Rev.* 100 (2), pp. 703–722. DOI: 10.1103/PhysRev.100.703. URL: https://link.aps.org/doi/10.1103/PhysRev.100.703.

**Bachau, H.**, E. Cormier, P. Decleva, J. E Hansen, and F. Mart'in (Dec. 2001). "Applications of B -splines in atomic and molecular physics". In: *Reports on Progress in Physics* 64, p. 1815. DOI: 10.1088/0034-4885/64/12/205.

**Balay**, **S.**, W. D. Gropp, L. C. McInnes, and B. F. Smith (1997). "Efficient Management of Parallelism in Object Oriented Numerical Software Libraries". In: *Modern Software Tools in Scientific Computing*. Ed. by E. Arge, A. M. Bruaset, and H. P. Langtangen. Birkhäuser Press, pp. 163–202.

**Balay**, **S.**, S. Abhyankar, M. F. Adams, J. Brown, P. Brune, K. Buschelman, V. Eijkhout, W. D. Gropp, D. Kaushik, M. G. Knepley, L. C. McInnes, K. Rupp, B. F. Smith, and H. Zhang (2014). *PETSc Users Manual*. Tech. rep. ANL-95/11 - Revision 3.5. Argonne National Laboratory.

**Barreau**, **L.**, **Petersson C. L. M.**, M. Klinker, A. Camper, C. Marante, T. Gorman, D. Kiesewetter, L. Argenti, P. Agostini, J. González-Vázquez, P. Salières, L. F. DiMauro, and F. Martín (June 2019). "Disentangling Spectral Phases of Interfering Autoionizing States from Attosecond Interferometric Measurements". In: *Phys. Rev. Lett.* 122 (25), p. 253203. DOI: 10.1103/PhysRevLett.122.253203. URL: https://link.aps.org/doi/10.1103/PhysRevLett.122.253203.

**Beck**, **A. R.**, B. Bernhardt, E. R. Warrick, M. Wu, S. Chen, M. B. Gaarde, K. J. Schafer, D. M. Neumark, and S. R. Leone (Nov. 2014). "Attosecond transient absorption probing of electronic superpositions of bound states in neon: detection of quantum beats". In: *New Journal of Physics* 16.11, p. 113016. DOI: 10.1088/1367-2630/16/11/113016. URL: https://doi.org/10.1088%2F1367-2630%2F16%2F11%2F113016.

**Ben-Tal**, **N.**, N. Moiseyev, and A. Beswick (Sept. 1993). "The effect of Hamiltonian symmetry on generation of odd and even harmonics". In: *Journal of Physics B-atomic Molecular and Optical Physics - J PHYS-B-AT MOL OPT PHYS* 26, pp. 3017–3024. DOI: 10.1088/0953-4075/26/18/012.

**Berrah**, **N.**, B. Langer, J. Bozek, T. W. Gorczyca, O. Hemmers, D. W. Lindle, and O. Toader (Nov. 1996). "Angular-distribution parameters andR-matrix calculations of Ar resonances". In: *Journal of Physics B: Atomic, Molecular and Optical Physics* 29.22, pp. 5351–5365. DOI: 10.1088/0953-4075/29/22/013. URL: https://doi.org/10.1088%2F0953-4075%2F29%2F22%2F013.

**Burgers**, **A.**, D. Wintgen, and J. .-.-M. Rest (Aug. 1995). "Highly doubly excited S states of the helium atom". In: *Journal of Physics B: Atomic, Molecular and Optical Physics* 28.15, pp. 3163–3183. DOI: 10.1088/0953-4075/28/15/010. URL: http://dx.doi.org/10.1088/0953-4075/28/15/010.

**Busto**, **D.**, L. Barreau, M. Isinger, M. Turconi, C. Alexandridi, A. Harth, S. Zhong, R. J Squibb, D. Kroon, S. Plogmaker, M. Miranda, Á. Jiménez-Galán, L. Argenti, C. L Arnold, R. Feifel, F. Martín, M. Gisselbrecht, A. L'Huillier, and P. Salières (2018). "Time-frequency representation of autoionization dynamics in helium". In: *Journal of Physics B: Atomic, Molecular and Optical Physics* 51.4, p. 044002.

**Caillat**, **J.**, A. Maquet, S. Haessler, B. Fabre, T. Ruchon, P. Salières, Y. Mairesse, and R. Taïeb (Mar. 2011). "Attosecond Resolved Electron Release in Two-Color Near-Threshold Photoionization of $N_2$". In: *Phys. Rev. Lett.* 106 (9), p. 093002. DOI: 10.1103/PhysRevLett.106.093002. URL: https://link.aps.org/doi/10.1103/PhysRevLett.106.093002.

**Carette**, **T.**, J. Dahlström, L. Argenti, and E. Lindroth (Jan. 2013). "The Multi-Configurational Hartree-Fock close-coupling ansatz: application to Argon photoionization cross section and delays". In: *Physical Review A* 87. DOI: 10.1103/PhysRevA.87.023420.

**Cattaneo**, **L.**, J. Vos, M. Lucchini, L. Gallmann, C. Cirelli, and U. Keller (Dec. 2016). "Comparison of attosecond streaking and RABBITT". In: *Opt. Express* 24.25, pp. 29060–29076. DOI: 10.1364/OE.24.029060. URL: http://www.opticsexpress.org/abstract.cfm?URI=oe-24-25-29060.

**Cattaneo**, **L.**, J. Vos, R. Y. Bello, A. Palacios, S. Heuser, L. Pedrelli, M. Lucchini, C. Cirelli, F. Martín, and U. Keller (2018). "Attosecond coupled electron and nuclear dynamics in dissociative ionization of H2". In: *Nature Physics* 14.7, pp. 733–738. ISSN: 1745-2481. DOI: 10.1038/s41567-018-0103-2. URL: https://doi.org/10.1038/s41567-018-0103-2.

**Cavalieri**, **A. L.**, N. Müller, T. Uphues, V. S. Yakovlev, A. Baltuska, B. Horvath, B. Schmidt, L. Blümel, R. Holzwarth, S. Hendel, M. Drescher, U. Kleineberg, P. M. Echenique, R. Kienberger, F. Krausz, and U. Heinzmann (Oct. 2007).

"Attosecond spectroscopy in condensed matter". In: *Nature* 449, p. 1029. URL: https://doi.org/10.1038/nature06229.

**Chen**, **M.-K.** (Dec. 1997). "Doubly excited $^{1,3}S^e$, $^{1,3}P^o$, and $^{1,3}D^e$ resonances in He below the $n = 2$ $He^+$ threhsold". In: *Phys. Rev. A* 56 (6), pp. 4537–4544. DOI: 10.1103/PhysRevA.56.4537. URL: https://link.aps.org/doi/10.1103/PhysRevA.56.4537.

**Chen**, **S.**, M. J. Bell, A. R. Beck, H. Mashiko, M. Wu, A. N. Pfeiffer, M. B. Gaarde, D. M. Neumark, S. R. Leone, and K. J. Schafer (Dec. 2012). "Light-induced states in attosecond transient absorption spectra of laser-dressed helium". In: *Phys. Rev. A* 86 (6), p. 063408. DOI: 10.1103/PhysRevA.86.063408. URL: https://link.aps.org/doi/10.1103/PhysRevA.86.063408.

**Chen**, **S.**, M. Wu, M. B. Gaarde, and K. J. Schafer (Sept. 2013a). "Laser-imposed phase in resonant absorption of an isolated attosecond pulse". In: *Physical Review A* 88.3. DOI: 10.1103/physreva.88.033409. URL: http://dx.doi.org/10.1103/PhysRevA.88.033409.

— (Mar. 2013b). "Quantum interference in attosecond transient absorption of laser-dressed helium atoms". In: *Phys. Rev. A* 87 (3), p. 033408. DOI: 10.1103/PhysRevA.87.033408. URL: https://link.aps.org/doi/10.1103/PhysRevA.87.033408.

**Cheng**, **Y.**, M. Chini, X. Wang, A. González-Castrillo, A. Palacios, L. Argenti, F. Martín, and Z. Chang (Aug. 2016). "Reconstruction of an excited-state molecular wave packet with attosecond transient absorption spectroscopy". In: *Phys. Rev. A* 94 (2), p. 023403. DOI: 10.1103/PhysRevA.94.023403. URL: https://link.aps.org/doi/10.1103/PhysRevA.94.023403.

**Chini**, **M.**, X. Wang, Y. Cheng, and Z. Chang (June 2014). "Resonance effects and quantum beats in attosecond transient absorption of helium". In: *Journal of Physics B: Atomic, Molecular and Optical Physics* 47.12, p. 124009. DOI: 10.1088/0953-4075/47/12/124009. URL: https://doi.org/10.1088%2F0953-4075%2F47%2F12%2F124009.

**Cirelli**, **C.**, C. Marante, S. Heuser, C. L. M. Petersson, Á. J. Galán, L. Argenti, S. Zhong, D. Busto, M. Isinger, S. Nandi, et al. (2018). "Anisotropic photoemission time delays close to a Fano resonance". In: *Nature Communications* 9.1, p. 955. ISSN: 2041-1723. DOI: 10.1038/s41467-018-03009-1. URL: https://doi.org/10.1038/s41467-018-03009-1.

**Cohen-Tannoudji**, **C.**, J. Dupont-Roc, and G. Grynberg (1998). *Atom-Photon Interactions: Basic Process and Appilcations*. Wiley-VCH. ISBN: 9780471293361.

**Corkum**, **P. B.** (1993). "Plasma perspective on strong field multiphoton ionization". In: *Physical review letters* 71.13, p. 1994.

**Dahlström**, **J. M.** and E. Lindroth (June 2014). "Study of attosecond delays using perturbation diagrams and exterior complex scaling". In: *Journal of Physics B: Atomic, Molecular and Optical Physics* 47.12, p. 124012. DOI: 10.1088/0953-4075/47/12/124012. URL: https://doi.org/10.1088%2F0953-4075%2F47%2F12%2F124012.

**Dahlström**, **J. M.**, A. L'Huillier, and A. Maquet (2012a). "Introduction to attosecond delays in photoionization". In: *Journal of Physics B: Atomic, Molecular and Optical Physics* 45.18, p. 183001.

**Dahlström**, **J. M.**, D. Guénot, K. Klünder, M. Gisselbrecht, J. Mauritsson, A. L'Huillier, A. Maquet, and R. Taïeb (2013). "Theory of attosecond delays in laser-assisted photoionization". In: *Chemical Physics* 414, pp. 53–64.

**Dahlström**, **J. M.**, T. Carette, and E. Lindroth (Dec. 2012b). "Diagrammatic approach to attosecond delays in photoionization". In: *Phys. Rev. A* 86 (6), p. 061402. DOI: 10.1103/PhysRevA.86.061402. URL: https://link.aps.org/doi/10.1103/PhysRevA.86.061402.

**Dill**, **D.** (1976). "Fixed-molecule photoelectron angular distributions". In: *The Journal of Chemical Physics* 65.3, pp. 1130–1133. DOI: 10.1063/1.433187. eprint: https://doi.org/10.1063/1.433187. URL: https://doi.org/10.1063/1.433187.

**Ding**, **T.**, C. Ott, A. Kaldun, A. Blättermann, K. Meyer, V. Stooss, M. Rebholz, P. Birk, M. Hartmann, A. Brown, H. V. D. Hart, and T. Pfeifer (Feb. 2016).

"Time-resolved four-wave-mixing spectroscopy for inner-valence transitions". In: *Opt. Lett.* 41.4, pp. 709–712. DOI: 10.1364/OL.41.000709. URL: http://ol.osa.org/abstract.cfm?URI=ol-41-4-709.

**Dirac**, **P. A. M.** (1939). "A new notation for quantum mechanics". In: *Mathematical Proceedings of the Cambridge Philosophical Society* 35.3, pp. 416–418. DOI: 10.1017/S0305004100021162.

**Dunning**, **T. H.** (1989). "Gaussian basis sets for use in correlated molecular calculations. I. The atoms boron through neon and hydrogen". In: *The Journal of Chemical Physics* 90.2, pp. 1007–1023. DOI: 10.1063/1.456153. eprint: https://doi.org/10.1063/1.456153. URL: https://doi.org/10.1063/1.456153.

**Eppink**, **A. T. J. B.** and D. H. Parker (1997). "Velocity map imaging of ions and electrons using electrostatic lenses: Application in photoelectron and photofragment ion imaging of molecular oxygen". In: *Rev. Sci. Instrum.* 68.9, p. 3477. ISSN: 00346748. DOI: 10.1063/1.1148310. URL: http://dx.doi.org/10.1063/1.1148310%20http://scitation.aip.org/content/aip/journal/rsi/68/9/10.1063/1.1148310.

**Fano**, **U.** (Dec. 1961). "Effects of Configuration Interaction on Intensities and Phase Shifts". In: *Phys. Rev.* 124.6, pp. 1866–1878. ISSN: 0031-899X. DOI: 10.1103/PhysRev.124.1866. URL: http://link.aps.org/doi/10.1103/PhysRev.124.1866.

**Feagin**, **J. M.** and J. S. Briggs (Aug. 1986). "Molecular Description of Two-Electron Atoms". In: *Phys. Rev. Lett.* 57, pp. 984–987. DOI: 10.1103/PhysRevLett.57.984.

**Feist**, **J.**, O. Zatsarinny, S. Nagele, R. Pazourek, J. Burgdörfer, X. Guan, K. Bartschat, and B. I. Schneider (Mar. 2014). "Time delays for attosecond streaking in photoionization of neon". In: *Phys. Rev. A* 89 (3), p. 033417. DOI: 10.1103/PhysRevA.89.033417. URL: https://link.aps.org/doi/10.1103/PhysRevA.89.033417.

**Ferray**, **M.**, A. L'Huillier, X. F. Li, L. A. Lompre, G. Mainfray, and C. Manus (Feb. 1988). "Multiple-harmonic conversion of 1064 nm radiation in rare gases".

In: *Journal of Physics B: Atomic, Molecular and Optical Physics* 21.3, pp. L31–L35. DOI: 10.1088/0953-4075/21/3/001. URL: https://doi.org/10.1088%2F0953-4075%2F21%2F3%2F001.

**Fock, V.** (Jan. 1930). "Näherungsmethode zur Lösung des quantenmechanischen Mehrkörperproblems". In: *Zeitschrift für Physik* 61.1, pp. 126–148. ISSN: 0044-3328. DOI: 10.1007/BF01340294. URL: https://doi.org/10.1007/BF01340294.

**Freeman, R. R.**, N. P. Economou, G. C. Bjorklund, and K. T. Lu (Nov. 1978). "Observation of Electric-Field-Induced Resonances above the Ionization Limit in a One-Electron Atom". In: *Phys. Rev. Lett.* 41 (21), pp. 1463–1467. DOI: 10.1103/PhysRevLett.41.1463. URL: https://link.aps.org/doi/10.1103/PhysRevLett.41.1463.

**Freeman, R. R.**, P. H. Bucksbaum, H. Milchberg, S. Darack, D. Schumacher, and M. E. Geusic (Sept. 1987). "Above-threshold ionization with subpicosecond laser pulses". In: *Phys. Rev. Lett.* 59 (10), pp. 1092–1095. DOI: 10.1103/PhysRevLett.59.1092. URL: https://link.aps.org/doi/10.1103/PhysRevLett.59.1092.

**Freeman, R. R.** and P. H. Bucksbaum (Jan. 1991). "Investigations of above-threshold ionization using subpicosecond laser pulses". In: *Journal of Physics B: Atomic, Molecular and Optical Physics* 24.2, pp. 325–347. DOI: 10.1088/0953-4075/24/2/004. URL: https://doi.org/10.1088%2F0953-4075%2F24%2F2%2F004.

**Gapanov, A. V.** and M. A. Miller (1958). "Potential Wells for Charged Particles in a High-Frequency Electromagnetic Field". In: *Zh Éksp. Teor. Fiz* 34. English translation - JETP, Vol. 7, No. 1, p. 168, July 1958, p. 34. DOI: 10.1038/s41567-018-0103-2. URL: http://www.jetp.ac.ru/cgi-bin/e/index/r/34/1/p242?a=list.

**Garcia, G. A.**, L. Nahon, and I. Powis (2004). "Two-dimensional charged particle image inversion using a polar basis function expansion". In: *Review of Scientific Instruments* 75.11, pp. 4989–4996. DOI: 10.1063/1.1807578.

eprint: https://doi.org/10.1063/1.1807578. URL: https://doi.org/10.1063/1.1807578.

**García, I. S.** (1992). "Metodos de cuadrado integrable para el estudio de colisiones con multiples canales abiertos. Aplicacion a la fotoionizacion del He". PhD thesis. Cantoblanco (Madrid): Universidad Autónoma de Madrid, Departamento de Química.

**Goulielmakis, E.**, Z.-H. Loh, A. Wirth, R. Santra, N. Rohringer, V. S. Yakovlev, S. Zherebtsov, T. Pfeifer, A. M. Azzeer, M. F. Kling, S. R. Leone, and F. Krausz (Aug. 2010). "Real-time observation of valence electron motion." In: *Nature* 466.7307, pp. 739–43. ISSN: 1476-4687. DOI: 10.1038/nature09212. URL: http://www.nature.com/doifinder/10.1038/nature09212%20http://www.ncbi.nlm.nih.gov/pubmed/20686571.

**Gruson, V.**, L. Barreau, Á. Jiménez-Galan, F. Risoud, J. Caillat, A. Maquet, B. Carré, F. Lepetit, J.-F. Hergott, T. Ruchon, L. Argenti, R. Taïeb, F. Martín, and P. Salières (2016). "Attosecond dynamics through a Fano resonance: Monitoring the birth of a photoelectron". In: *Science* 354.6313, pp. 734–738. ISSN: 0036-8075. DOI: 10.1126/science.aah5188. eprint: http://science.sciencemag.org/content/354/6313/734.full.pdf. URL: http://science.sciencemag.org/content/354/6313/734.

**Guénot, D.**, D. Kroon, E. Balogh, E. W. Larsen, M. Kotur, M. Miranda, T. Fordell, P. Johnsson, J. Mauritsson, M. Gisselbrecht, K. Varjù, C. L. Arnold, T. Carette, A. S Kheifets, E. Lindroth, A. L'Huillier, and J. M. Dahlström (2014). "Measurements of relative photoemission time delays in noble gas atoms". In: *Journal of Physics B: Atomic, Molecular and Optical Physics* 47.24.

**Haessler, S.**, B. Fabre, J. Higuet, J. Caillat, T. Ruchon, P. Breger, B. Carré, E. Constant, A. Maquet, E. Mével, P. Salières, R. Taïeb, and Y. Mairesse (July 2009). "Phase-resolved attosecond near-threshold photoionization of molecular nitrogen". In: *Phys. Rev. A* 80 (1), p. 011404. DOI: 10.1103/PhysRevA.80.011404. URL: https://link.aps.org/doi/10.1103/PhysRevA.80.011404.

**Hammond**, **T. J.**, S. Monchocé, C. Zhang, G. G. Brown, P. B. Corkum, and D. M. Villeneuve (Dec. 2016). "Femtosecond time-domain observation of atmospheric absorption in the near-infrared spectrum". In: *Phys. Rev. A* 94 (6), p. 063410. DOI: 10.1103/PhysRevA.94.063410. URL: https://link.aps.org/doi/10.1103/PhysRevA.94.063410.

**Hartree**, **D. R.** (1928). "The Wave Mechanics of an Atom with a Non-Coulomb Central Field. Part I. Theory and Methods". In: *Mathematical Proceedings of the Cambridge Philosophical Society* 24.1, pp. 89–110. DOI: 10.1017/S0305004100011919.

**Hartree**, **D. R.** and W. Hartree (1935). "Self-consistent field, with exchange, for beryllium". In: *Proceedings of the Royal Society of London. Series A - Mathematical and Physical Sciences* 150.869, pp. 9–33. DOI: 10.1098/rspa.1935.0085. eprint: https://royalsocietypublishing.org/doi/pdf/10.1098/rspa.1935.0085. URL: https://royalsocietypublishing.org/doi/abs/10.1098/rspa.1935.0085.

**Hättig**, **C.**, W. Klopper, A. Köhn, and D. P. Tew (2011). "Explicitly correlated electrons in molecules". In: *Chemical reviews* 112.1, pp. 4–74.

**Heinrich-Josties**, **E.**, S. Pabst, and R. Santra (Apr. 2014). "Controlling the $2p$ hole alignment in neon via the $2s$-$3p$ Fano resonance". In: *Phys. Rev. A* 89 (4), p. 043415. DOI: 10.1103/PhysRevA.89.043415. URL: https://link.aps.org/doi/10.1103/PhysRevA.89.043415.

**Herrick**, **D. R.**, M. E. Kellman, and R. D. Poliak (Oct. 1980). "Supermultiplet classification of higher intrashell doubly excited states of $H^-$ and He". In: *Phys. Rev. A* 22, pp. 1517–1535. DOI: 10.1103/PhysRevA.22.1517.

**Herrick**, **D. R.** and O. Sinanoğlu (Jan. 1975). "Comparison of doubly-excited helium energy levels, isoelectronic series, autoionization lifetimes, and group-theoretical configuration-mixing predictions with large-configuration-interaction calculations and experimental spectra". In: *Phys. Rev. A* 11, pp. 97–110. DOI: 10.1103/PhysRevA.11.97.

**Herrmann**, **J.**, M. Weger, R. Locher, M. Sabbar, P. Rivière, U. Saalmann, J.-M. Rost, L. Gallmann, and U. Keller (Oct. 2013). "Virtual single-photon

transition interrupted: Time-gated optical gain and loss". In: *Phys. Rev. A* 88 (4), p. 043843. DOI: 10.1103/PhysRevA.88.043843. URL: https://link.aps.org/doi/10.1103/PhysRevA.88.043843.

**Heuser, S.**, Á. Jiménez Galán, C. Cirelli, C. Marante, M. Sabbar, R. Boge, M. Lucchini, L. Gallmann, I. Ivanov, A. S. Kheifets, J. M. Dahlström, E. Lindroth, L. Argenti, F. Martín, and U. Keller (Dec. 2016). "Angular dependence of photoemission time delay in helium". In: *Phys. Rev. A* 94 (6), p. 063409. DOI: 10.1103/PhysRevA.94.063409. URL: https://link.aps.org/doi/10.1103/PhysRevA.94.063409.

**Huppert, M.**, I. Jordan, D. Baykusheva, A. von Conta, and H. J. Wörner (Aug. 2016). "Attosecond Delays in Molecular Photoionization". In: *Phys. Rev. Lett.* 117 (9), p. 093001. DOI: 10.1103/PhysRevLett.117.093001. URL: https://link.aps.org/doi/10.1103/PhysRevLett.117.093001.

**Jiménez-Galán, Á.**, L. Argenti, and F. Martín (2013). "The soft-photon approximation in infrared-laser-assisted atomic ionization by extreme-ultraviolet attosecond-pulse trains". In: *New Journal of Physics* 15.11, p. 113009.

**Jiménez-Galán, Á.**, F. Martín, and L. Argenti (Feb. 2016). "Two-photon finite-pulse model for resonant transitions in attosecond experiments". In: *Phys. Rev. A* 93 (2), p. 023429. DOI: 10.1103/PhysRevA.93.023429. URL: https://link.aps.org/doi/10.1103/PhysRevA.93.023429.

**Jordan, I.**, M. Huppert, S. Pabst, A. S. Kheifets, D. Baykusheva, and H. J. Wörner (Jan. 2017). "Spin-orbit delays in photoemission". In: *Phys. Rev. A* 95 (1), p. 013404. DOI: 10.1103/PhysRevA.95.013404. URL: https://link.aps.org/doi/10.1103/PhysRevA.95.013404.

**Kaldun, A.**, A. Blättermann, V. Stooß, S. Donsa, H. Wei, R. Pazourek, S. Nagele, C. Ott, C. D. Lin, J. Burgdörfer, and T. Pfeifer (2016). "Observing the ultrafast buildup of a Fano resonance in the time domain". In: *Science* 354.6313, pp. 738–741. ISSN: 0036-8075. DOI: 10.1126/science.aah6972. eprint: https://science.sciencemag.org/content/354/6313/738.full.pdf. URL: https://science.sciencemag.org/content/354/6313/738.

**Kaldun, A.**, C. Ott, A. Blättermann, M. Laux, K. Meyer, T. Ding, A. Fischer, and T. Pfeifer (Mar. 2014). "Extracting Phase and Amplitude Modifications of Laser-Coupled Fano Resonances". In: *Phys. Rev. Lett.* 112.10, p. 103001. ISSN: 0031-9007. DOI: 10.1103/PhysRevLett.112.103001. URL: http://link.aps.org/doi/10.1103/PhysRevLett.112.103001.

**Kheifets, A. S.** (June 2013). "Time delay in valence-shell photoionization of noble-gas atoms". In: *Phys. Rev. A* 87 (6), p. 063404. DOI: 10.1103/PhysRevA.87.063404. URL: https://link.aps.org/doi/10.1103/PhysRevA.87.063404.

**Kotur, M.**, D. Guénot, Á. Jiménez-Galán, D. Kroon, E. W. Larsen, M. Louisy, S. Bengtsson, M. Miranda, J. Mauritsson, C. L. Arnold, S. E. Canton, M. Gisselbrecht, T. Carette, J. M. Dahlström, E. Lindroth, A. Maquet, L. Argenti, F. Martín, and A. L'Huillier (Feb. 2016). "Spectral phase measurement of a Fano resonance using tunable attosecond pulses". In: *Nature Communications* 7. Article, p. 10566. URL: https://doi.org/10.1038/ncomms10566.

**Krause, J. L.**, K. J. Schafer, and K. C. Kulander (June 1992). "High-order harmonic generation from atoms and ions in the high intensity regime". In: *Phys. Rev. Lett.* 68 (24), pp. 3535–3538. DOI: 10.1103/PhysRevLett.68.3535. URL: https://link.aps.org/doi/10.1103/PhysRevLett.68.3535.

**Laurent, G.**, W. Cao, H. Li, Z. Wang, I. Ben-Itzhak, and C. L. Cocke (Aug. 2012). "Attosecond Control of Orbital Parity Mix Interferences and the Relative Phase of Even and Odd Harmonics in an Attosecond Pulse Train". In: *Phys. Rev. Lett.* 109 (8), p. 083001. DOI: 10.1103/PhysRevLett.109.083001. URL: https://link.aps.org/doi/10.1103/PhysRevLett.109.083001.

**Lewenstein, M.**, P. Balcou, M. Y. Ivanov, A. L'Huillier, and P. B. Corkum (Mar. 1994). "Theory of high-harmonic generation by low-frequency laser fields". In: *Phys. Rev. A* 49 (3), pp. 2117–2132. DOI: 10.1103/PhysRevA.49.2117. URL: https://link.aps.org/doi/10.1103/PhysRevA.49.2117.

**Lin, C. D.** (Mar. 1984). "Classification and supermultiplet structure of doubly excited states". In: *Phys. Rev. A* 29 (3), pp. 1019–1033. DOI: 10.1103

/PhysRevA.29.1019. URL: https://link.aps.org/doi/10.1103/PhysRevA.29.1019.

— (1986). "Doubly Excited States, Including New Classification Schemes". In: *Adv. At. Mol. Phys.* 22, pp. 77–142. DOI: 10.1016/S0065-2199(08)60335-8.

**Lindroth**, **E.** and L. Argenti (2012). "Atomic resonance states and their role in charge changing processes". In: *Adv. Quantum Chem.* 63. DOI: 10.1016/B978-0-12-397009-1.00005-9. URL: http://www.sciencedirect.com/science/article/pii/B9780123970091000059.

**Locher**, **R.**, L. Castiglioni, M. Lucchini, M. Greif, L. Gallmann, J. Osterwalder, M. Hengsberger, and U. Keller (2015). "Energy-dependent photoemission delays from noble metal surfaces by attosecond interferometry". In: *optica* 2.5, pp. 405–410.

**Lucchini**, **M.**, L. Castiglioni, L. Kasmi, P. Kliuiev, A. Ludwig, M. Greif, J. Osterwalder, M. Hengsberger, L. Gallmann, and U. Keller (2015). "Light-matter interaction at surfaces in the spatiotemporal limit of macroscopic models". In: *Physical review letters* 115.13, p. 137401.

**Mairesse**, **Y.**, A. de Bohan, L. J. Frasinski, H. Merdji, L. C. Dinu, P. Monchicourt, P. Breger, M. Kovačev, R. Taïeb, B. Carré, H. G. Muller, P. Agostini, and P. Salières (2003). "Attosecond Synchronization of High-Harmonic Soft X-rays". In: *Science* 302.5650, pp. 1540–1543. ISSN: 0036-8075. DOI: 10.1126/science.1090277. eprint: https://science.sciencemag.org/content/302/5650/1540.full.pdf. URL: https://science.sciencemag.org/content/302/5650/1540.

**Marante**, **C.**, L. Argenti, and F. Martín (July 2014). "Hybrid Gaussian–*B*-spline basis for the electronic continuum: Photoionization of atomic hydrogen". In: *Phys. Rev. A* 90 (1), p. 012506. DOI: 10.1103/PhysRevA.90.012506. URL: https://link.aps.org/doi/10.1103/PhysRevA.90.012506.

**Marante**, **C.**, M. Klinker, I. Corral, J. González-Vázquez, L. Argenti, and F. Martín (2017a). "Hybrid-Basis Close-Coupling Interface to Quantum Chemistry Packages for the Treatment of Ionization Problems". In: *Journal*

*of Chemical Theory and Computation* 13.2. PMID: 28058835, pp. 499–514. DOI: 10.1021/acs.jctc.6b00907. eprint: https://doi.org/10.1021/acs.jctc.6b00907. URL: https://doi.org/10.1021/acs.jctc.6b00907.

**Marante**, **C.**, M. Klinker, T. Kjellsson, E. Lindroth, J. González-Vázquez, L. Argenti, and F. Martín (Aug. 2017b). "Photoionization using the xchem approach: Total and partial cross sections of Ne and resonance parameters above the $2s^2 2p^5$ threshold". In: *Phys. Rev. A* 96 (2), p. 022507. DOI: 10.1103/PhysRevA.96.022507. URL: https://link.aps.org/doi/10.1103/PhysRevA.96.022507.

**Martín**, **F.**, H. Bachau, P. Galan, A. Riera, and M. Yáñez (1991). "Electron correlation properties of doubly excited states. Berylliumlike vs heliumlike systems". In: *The Journal of Chemical Physics* 94.7, pp. 5011–5020. DOI: 10.1063/1.460536.

**McPherson**, **A.**, G. Gibson, H. Jara, U. Johann, T. S. Luk, I. A. McIntyre, K. Boyer, and C. K. Rhodes (Apr. 1987). "Studies of multiphoton production of vacuum-ultraviolet radiation in the rare gases". In: *J. Opt. Soc. Am. B* 4.4, pp. 595–601. DOI: 10.1364/JOSAB.4.000595. URL: http://josab.osa.org/abstract.cfm?URI=josab-4-4-595.

**Menzel**, **A.**, S. P. Frigo, S. B. Whitfield, C. D. Caldwell, and M. O. Krause (Sept. 1996). "Partial photoionization cross sections and photoelectron angular distributions for double excitations up to the N=5 threshold in helium". In: *Phys. Rev. A* 54 (3), pp. 2080–2090. DOI: 10.1103/PhysRevA.54.2080. URL: https://link.aps.org/doi/10.1103/PhysRevA.54.2080.

**Min**, **G.**, Z. Lin-Fan, L. Cun-Ding, and X. Ke-Zun (Oct. 2008). "Optically Forbidden Excitations of 2s Electron of Neon Studied by Fast Electron Impact". In: *Chinese Physics Letters* 25.10, pp. 3646–3648. DOI: 10.1088/0256-307x/25/10/034. URL: https://doi.org/10.1088%2F0256-307x%2F25%2F10%2F034.

**Moccia**, **R.** and P. Spizzo (Mar. 1991). "Helium photoionization between the N=2 and N=3 thresholds including angular distribution and resonance

properties: A K-matrix $L^2$ basis-set calculation". In: *Phys. Rev. A* 43 (5), pp. 2199–2214. DOI: 10.1103/PhysRevA.43.2199. URL: https://link.aps.org/doi/10.1103/PhysRevA.43.2199.

**Moore**, **L. R.**, M. A. Lysaght, J. S. Parker, H. W. van der Hart, and K. T. Taylor (Dec. 2011). "Time delay between photoemission from the 2*p* and 2*s* subshells of neon". In: *Phys. Rev. A* 84 (6), p. 061404. DOI: 10.1103/PhysRevA.84.061404. URL: https://link.aps.org/doi/10.1103/PhysRevA.84.061404.

**Neppl**, **S.**, R. Ernstorfer, A. L. Cavalieri, C. Lemell, G. Wachter, E. Magerl, E. M. Bothschafter, M. Jobst, M. Hofstetter, U. Kleineberg, J. V. Barth, D. Menzel, J. Burgdörfer, P. Feulner, F. Krausz, and R. Kienberger (Jan. 2015). "Direct observation of electron propagation and dielectric screening on the atomic length scale". In: *Nature* 517, p. 342. URL: https://doi.org/10.1038/nature14094.

**Nikolopoulos**, **L. A. A.** and P. Lambropoulos (Feb. 2001). "Multichannel theory of two-photon single and double ionization of helium". In: *Journal of Physics B: Atomic, Molecular and Optical Physics* 34.4, pp. 545–564. DOI: 10.1088/0953-4075/34/4/304. URL: https://doi.org/10.1088%2F0953-4075%2F34%2F4%2F304.

**Ohlén**, **G.** (2005). *Kvantvärldens fenomen : teori och begrepp*. Ed. by Studentlitteratur. First. Studentlitteratur AB. ISBN: 9789144034508.

**Ott**, **C.**, A. Kaldun, P. Raith, K. Meyer, M. Laux, Y. Zhang, S. Hagstotz, T. Ding, R. Heck, and T. Pfeifer (May 2012). "Quantum Interferometry and Correlated Two-Electron Wave-Packet Observation in Helium". In:

**Ott**, **C.**, A. Kaldun, P. Raith, K. Meyer, M. Laux, J. Evers, C. H. Keitel, C. H. Greene, and T. Pfeifer (2013). "Lorentz Meets Fano in Spectral Line Shapes: A Universal Phase and Its Laser Control". In: *Science* 340.6133, pp. 716–720. ISSN: 0036-8075. DOI: 10.1126/science.1234407. eprint: http://science.sciencemag.org/content/340/6133/716.full.pdf. URL: http://science.sciencemag.org/content/340/6133/716.

**Ott**, **C.**, A. Kaldun, L. Argenti, P. Raith, K. Meyer, M. Laux, Y. Zhang, A. Blättermann, S. Hagstotz, T. Ding, R. Heck, J. Madroñero, F. Martín, and T. Pfeifer (Dec. 2014). "Reconstruction and control of a time-dependent two-electron wave packet". In: *Nature* 516.7531, pp. 374–378. DOI: 10.1038/nature14026. URL: http://dx.doi.org/10.1038/nature14026.

**Palatchi**, **C.**, J. M. Dahlström, A. S. Kheifets, I. A. Ivanov, D. M. Canaday, P. Agostini, and L. F. DiMauro (2014). "Atomic delay in helium, neon, argon and krypton". In: *Journal of Physics B: Atomic, Molecular and Optical Physics* 47.24.

**Paul**, **P. M.**, E. S. Toma, P. Breger, G. Mullot, F. Augé, P. Balcou, H. G. Muller, and P. Agostini (2001). "Observation of a Train of Attosecond Pulses from High Harmonic Generation". In: *Science* 292.5522, pp. 1689–1692. ISSN: 0036-8075. DOI: 10.1126/science.1059413. eprint: http://science.sciencemag.org/content/292/5522/1689.full.pdf. URL: http://science.sciencemag.org/content/292/5522/1689.

**Pazourek**, **R.**, S. Nagele, and J. Burgdörfer (Aug. 2015). "Attosecond chronoscopy of photoemission". In: *Rev. Mod. Phys.* 87 (3), pp. 765–802. DOI: 10.1103/RevModPhys.87.765. URL: https://link.aps.org/doi/10.1103/RevModPhys.87.765.

**Petersson**, **C. L. M.**, L. Argenti, and F. Martín (2017). "Attosecond transient absorption spectroscopy of helium above the N= 2 ionization threshold". In: *Physical Review A* 96.1, p. 013403. DOI: 10.1103/PhysRevA.96.013403. URL: https://journals.aps.org/pra/abstract/10.1103/PhysRevA.96.013403.

**Pollard**, **W. T.** and R. A. Mathies (1992). "Analysis of Femtosecond Dynamic Absorption Spectra of Nonstationary States". In: *Annual Review of Physical Chemistry* 43.1. PMID: 1463575, pp. 497–523. DOI: 10.1146/annurev.pc.43.100192.002433.

**Rost**, **J. M.**, K. Schulz, M. Domke, and G. Kaindl (Nov. 1997). "Resonance parameters of photo doubly excited helium". In: *Journal of Physics B: Atomic, Molecular and Optical Physics* 30.21, pp. 4663–4694. DOI: 10.1088

/0953-4075/30/21/010. URL: http://dx.doi.org/10.1088/0953-4075/30/21/010.

**Saad**, **Y.** (1992). "Analysis of Some Krylov Subspace Approximations to the Matrix Exponential Operator". In: *SIAM Journal on Numerical Analysis* 29.1, pp. 209–228. DOI: 10.1137/0729014. eprint: https://doi.org/10.1137/0729014. URL: https://doi.org/10.1137/0729014.

**Sabbar**, **M.**, S. Heuser, R. Boge, M. Lucchini, T. Carette, E. Lindroth, L. Gallmann, C. Cirelli, and U. Keller (Sept. 2015). "Resonance Effects in Photoemission Time Delays". In: *Phys. Rev. Lett.* 115 (13), p. 133001. DOI: 10.1103/PhysRevLett.115.133001. URL: https://link.aps.org/doi/10.1103/PhysRevLett.115.133001.

**Sakurai**, **J.** and J. Napolitano (2011). *Modern Quantum Mechanics*. Addison-Wesley. ISBN: 9780805382914.

**Santra**, **R.**, V. S. Yakovlev, T. Pfeifer, and Z.-H. Loh (Jan. 2011). "Theory of attosecond transient absorption spectroscopy of strong-field-generated ions". In: *Physical Review. A* 83. DOI: 10.1103/PHYSREVA.83.033405.

**Schafer**, **K. J.**, B. Yang, L. F. DiMauro, and K. C. Kulander (Mar. 1993). "Above threshold ionization beyond the high harmonic cutoff". In: *Phys. Rev. Lett.* 70 (11), pp. 1599–1602. DOI: 10.1103/PhysRevLett.70.1599. URL: https://link.aps.org/doi/10.1103/PhysRevLett.70.1599.

**Schrödinger**, **E.** (Dec. 1926). "An Undulatory Theory of the Mechanics of Atoms and Molecules". In: *Phys. Rev.* 28 (6), pp. 1049–1070. DOI: 10.1103/PhysRev.28.1049. URL: https://link.aps.org/doi/10.1103/PhysRev.28.1049.

**Schultze**, **M.**, M. Fieß, N. Karpowicz, J. Gagnon, M. Korbman, M. Hofstetter, S. Neppl, A. L. Cavalieri, Y. Komninos, T. Mercouris, C. A. Nicolaides, R. Pazourek, S. Nagele, J. Feist, J. Burgdörfer, A. M. Azzeer, R. Ernstorfer, R. Kienberger, U. Kleineberg, E. Goulielmakis, F. Krausz, and V. S. Yakovlev (2010). "Delay in Photoemission". In: *Science* 328.5986, pp. 1658–1662. ISSN: 0036-8075. DOI: 10.1126/science.1189401. eprint: https://

science.sciencemag.org/content/328/5986/1658.full.pdf. URL: https://science.sciencemag.org/content/328/5986/1658.

**Schulz, K.**, M. Domke, R. Püttner, A. Gutiérrez, G. Kaindl, G. Miecznik, and C. H. Greene (1996). "High-resolution experimental and theoretical study of singly and doubly excited resonances in ground-state photoionization of neon". In: *Physical Review A* 54.4, p. 3095.

**Slater, J. C.** (Nov. 1929). "The Theory of Complex Spectra". In: *Phys. Rev.* 34 (10), pp. 1293–1322. DOI: 10.1103/PhysRev.34.1293. URL: https://link.aps.org/doi/10.1103/PhysRev.34.1293.

**Smith, F. T.** (Apr. 1960). "Lifetime Matrix in Collision Theory". In: *Phys. Rev.* 118 (1), pp. 349–356. DOI: 10.1103/PhysRev.118.349. URL: https://link.aps.org/doi/10.1103/PhysRev.118.349.

**Southworth, S. H.**, A. C. Parr, J. E. Hardis, J. L. Dehmer, and D. M. Holland (1986). "Calibration of a monochromator/spectrometer system for the measurement of photoelectron angular distributions and branching ratios". In: *Nuclear Instruments and Methods in Physics Research Section A: Accelerators, Spectrometers, Detectors and Associated Equipment* 246.1-3, pp. 782–786.

**Stark, J.** (1913a). "Observation of the Separation of Spectral Lines by an Electric Field". In: *Nature* 92.2301, pp. 401–401. ISSN: 1476-4687. DOI: 10.1038/092401b0. URL: https://doi.org/10.1038/092401b0.

— (1913b). "Beobachtungen über den Effekt des elektrischen Feldes auf Spektrallinien". In: *Sitzungsberichte der Königlichen Preußischen Akademie der Wissenschaften*, pp. 932–946.

**Strang, G.** (Sept. 1968). "On the Construction and Comparison of Difference Schemes". In: *Journal on Numerical Analysis* 5.3, pp. 506–517. DOI: 10.1137/0705041.

**Svanberg, S.** (1991). *Atomic and Molecular Spectroscopy: Basic Aspects and Practical Applications*. Ed. by A. L. Schawlow and K. Shimoda. Fourth. Springer. ISBN: 9783540203827. DOI: 10.1007/978-3-642-18520-5.

**Swoboda**, **M.**, T. Fordell, K. Klünder, J. M. Dahlström, M. Miranda, C. Buth, K. J. Schafer, J. Mauritsson, A. L'Huillier, and M. Gisselbrecht (Mar. 2010). "Phase Measurement of Resonant Two-Photon Ionization in Helium". In: *Phys. Rev. Lett.* 104 (10), p. 103003. DOI: 10.1103/PhysRevLett.104.103003. URL: https://link.aps.org/doi/10.1103/PhysRevLett.104.103003.

**Tanner**, **G.**, K. Richter, and J.-M. Rost (Apr. 2000). "The theory of two-electron atoms: between ground state and complete fragmentation". In: *Rev. Mod. Phys.* 72 (2), pp. 497–544. DOI: 10.1103/RevModPhys.72.497. URL: https://link.aps.org/doi/10.1103/RevModPhys.72.497.

**Tao**, **Z.**, C. Chen, T. Szilvási, M. Keller, M. Mavrikakis, H. Kapteyn, and M. Murnane (2016). "Direct time-domain observation of attosecond final-state lifetimes in photoemission from solids". In: *Science* 353.6294, pp. 62–67. ISSN: 0036-8075. DOI: 10.1126/science.aaf6793. eprint: https://science.sciencemag.org/content/353/6294/62.full.pdf. URL: https://science.sciencemag.org/content/353/6294/62.

**Ullrich**, **J.**, R. Moshammer, A. Dorn, R. Dörner, L. P. H. Schmidt, and H. Schmidt-Böcking (Sept. 2003a). "Recoil-ion and electron momentum spectroscopy: reaction-microscopes". In: *Rep. Prog. Phys.* 66.9, pp. 1463–1545. ISSN: 0034-4885. DOI: 10.1088/0034-4885/66/9/203. URL: http://stacks.iop.org/0034-4885/66/i=9/a=203?key=crossref.4f0ed0c11253bbad6096727290d95871.

**Ullrich**, **J.**, R. Moshammer, A. Dorn, R. Dörner, L. P. H. Schmidt, and H. Schmidt-Böcking (2003b). "Recoil-ion and electron momentum spectroscopy: reaction-microscopes". In: *Reports on Progress in Physics* 66.9, p. 1463.

**Villeneuve**, **D. M.**, P. Hockett, M. J. J. Vrakking, and H. Niikura (2017). "Coherent imaging of an attosecond electron wave packet". In: *Science* 356.6343, pp. 1150–1153. ISSN: 0036-8075. DOI: 10.1126/science.aam8393. eprint: https://science.sciencemag.org/content/356/6343/1150.full.pdf. URL: https://science.sciencemag.org/content/356/6343/1150.

**Wang**, **X.**, M. Chini, Y. Cheng, Y. Wu, X.-m. Tong, and Z. Chang (June 2013). "Subcycle laser control and quantum interferences in attosecond photoabsorption of neon". In: *Phys. Rev. A* 87.6, p. 063413. ISSN: 1050-2947. DOI: 10.1103/PhysRevA.87.063413. URL: http://link.aps.org/doi/10.1103/PhysRevA.87.063413.

**Werner**, **H.-J.**, P. J. Knowles, G. Knizia, F. R. Manby, and M. Schütz (2012). "Molpro: a general-purpose quantum chemistry program package". In: *Wiley Interdisciplinary Reviews: Computational Molecular Science* 2.2, pp. 242–253. DOI: 10.1002/wcms.82. eprint: https://onlinelibrary.wiley.com/doi/pdf/10.1002/wcms.82. URL: https://onlinelibrary.wiley.com/doi/abs/10.1002/wcms.82.

**Wigner**, **E. P.** (Apr. 1955). "Lower Limit for the Energy Derivative of the Scattering Phase Shift". In: *Phys. Rev.* 98 (1), pp. 145–147. DOI: 10.1103/PhysRev.98.145. URL: https://link.aps.org/doi/10.1103/PhysRev.98.145.

**Wu**, **M.**, S. Chen, S. Camp, K. J. Schafer, and M. B. Gaarde (2016). "Theory of strong-field attosecond transient absorption". In: *Journal of Physics B: Atomic, Molecular and Optical Physics* 49.6, p. 062003.

**Zatsarinny**, **O.** and K. Bartschat (May 2013). "TheB-splineR-matrix method for atomic processes: application to atomic structure, electron collisions and photoionization". In: *Journal of Physics B: Atomic, Molecular and Optical Physics* 46.11, p. 112001. DOI: 10.1088/0953-4075/46/11/112001. URL: https://doi.org/10.1088%2F0953-4075%2F46%2F11%2F112001.

# Index


Argon, 137–154
ATAS, 17–33, 106–114, 117–123
  Beatings, 28–30, 121
  Bidimensional spectrum, 24–26, 112–113, 121–123
  Field, 17–18
  Resonance profile buildup, 30–33, 121
  Spectral features, 26–33
  Transient spectrum, 18–25, 109–111, 119–121
Autler-Townes splitting, 27–28

Basis, 73–74
  B-spline, 75–82
  XCHEM, *see* XCHEM
Boundary conditions, 49, 58, 70
  Dirichlet, 58, 70

Complex absorption potential, 49, 58–63
  Anatomy, 58–59
  Interpretation, 60–63

Dipole, 23, 27, 41, 49
  Eigenbasis, 54, 57
  Response, 22–69
  Selection rules, 37
Dirac representation, 170
Dyson series, 171

Emission time delays, 44–47
  Wigner, 46–47, 151

Gauge
  Length, 22
  Velocity, 22–24, 40, 48, 49, 65

Hamiltonian, 40, 48–49, 169
  Complex absorption component, *see* Complex absorption potential
  Eigenbasis, 49, 51
  Interaction term, 40, 49, 172
  Quenched, 59, 61
Helium, 105–114
High harmonic, 36–39
High harmonic generation, 34–38

Interaction representation, *see* Dirac representation

Krylov method, 48, 52–56, 178–179
  Convergence, 54–56
  Subspace, 53

Maxwell's equations, 20

Neon, 115–135

Operator Splitting, 49–51, 173–176
  Strang, 50, 175

Perturbation theory
  Time dependent, 40–42, 169–172
Photo-electron spectroscopy, 40, 64, 69–71
Ponderomotive energy, 35

Rabi-frequency, 27
RABITT, 34–47, 89–90, 127–135, 138–154
  Anisotropic, 138–154
  Field (probe), 36, 38
  Field (pump), 36, 37
  Path interference, 38, 42–44, 89–90
  Phase, 38, 40–47, 89–101
  Phase (atomic), 43–44, 89–101
  Phase (attochirp), 43–44
  Phase convention, 43–44
Rotating wave approximation, 27

Schrödinger equation
  Time-dependent, 48, 169
Schrödinger representation, 169
Sideband, 38
  Intensity, 38
Stark effect, 27, 30

Three-step model, 35–36
Time Complexity, 176–180
Time propagation, 48–63, 173–180
  Ab-initio, 48–63
  Field-driven, 52
  Field-free, 41, 51, 58, 169, 172
  Numerical, 48–63
Transient absorption spectroscopy, 18–24, 40, 64–69

XCHEM, 83–87, 179
  GABS, 85–87